Spatial Profiling Using a Time of Flight Diagnostic and Applications of Deuterium-Deuterium Fusion in Inertial Electrostatic Confinement Fusion Devices

David C. Donovan

May 2011

UWFDM-1392

Ph.D. thesis.

FUSION TECHNOLOGY INSTITUTE

UNIVERSITY OF WISCONSIN

MADISON WISCONSIN

Spatial Profiling Using a Time of Flight Diagnostic and Applications of Deuterium-Deuterium Fusion in Inertial Electrostatic Confinement Fusion Devices

David C. Donovan

Fusion Technology Institute
University of Wisconsin
1500 Engineering Drive
Madison, WI 53706

http://fti.neep.wisc.edu

May 2011

UWFDM-1392

Ph.D. thesis.

SPATIAL PROFILING USING A TIME OF FLIGHT DIAGNOSTIC AND APPLICATIONS OF DEUTERIUM-DEUTERIUM FUSION IN INERTIAL ELECTROSTATIC CONFINEMENT FUSION DEVICES

by

David C. Donovan

A dissertation submitted in partial fulfillment of

the requirements for the degree of

Doctor of Philosophy

(Nuclear Engineering & Engineering Physics)

at the

University of Wisconsin – Madison

2011

Abstract

The Inertial Electrostatic Confinement (IEC) Fusion Research Group at the University of Wisconsin – Madison utilizes IEC devices as small-scale neutron generators using D-D fusion to create 2.45 MeV neutrons for the purpose of detecting clandestine material. Detection of explosives in particular can be accomplished using thermal neutron capture methods to identify characteristic nitrogen signatures in explosive material. Initial proof-of-principle experiments have demonstrated that IEC devices are capable of producing a sufficiently high neutron flux to detect nitrogen-based explosives utilizing source strengths of roughly 5×10^7 neutrons/second. Research has been conducted to expand upon the proof-of-principle experiments of an IEC device to detect explosives in order to increase reliability of detection, decrease interrogation time, and increase the steady-state operational time. These goals were furthered by optimizing the detection setup, which involves increasing the number of detectors and improving the detector configuration, as well as the placement and thickness of the shielding and moderator.

Efforts have also been made to increase the neutron production rate of the device. The record UW IEC steady-state neutron production rate is currently 2.2×10^8 neutrons/second. Optimization studies have varied the configuration and design of the electrodes and have resulted in system configurations with up to 50 percent higher neutron production rates than have previously been utilized. A new feedthrough design has been constructed that is intended to increase the maximum operating voltage from 175 kV with the previous feedthrough to 300 kV in order to make use of the recently upgraded 300 kV, 200 mA power supply. Neutron production rates scale almost linearly with both current and voltage, so the higher current and voltage ranges attainable with the new supply and feedthrough will allow the IEC device to be operated at higher neutron producing regimes than have ever before been achieved.

The optimization efforts involve the use of several new diagnostic tools developed at UW, which are the Fusion Ion Doppler (FIDO) Diagnostic and the Time of Flight (TOF) Diagnostic. FIDO provides the energy spectra of the charged fusion products and reactants created in the IEC device. The FIDO Diagnostic was originally only capable of studying D-D fusion, but with recent advancements is now able to study both D-D and D-^{3}He fusion. The TOF Diagnostic provides spatial information along with the energy resolution of where the fusion reactions are occurring in the IEC device. This diagnostic has been taken from concept to full utilization. This has involved the implementation of high precision timing electronics, alignment systems, data acquisition software, computational post-processing methods for analysis, as well as all the necessary upgrades to the experimental facility to accommodate such a highly sensitive diagnostic.

The TOF Diagnostic has uncovered previously unknown characteristics of the spatial distribution of fusion reactions in a spherically gridded IEC device. A significant rise in the concentration of fusion events was found outside of the anode, which is believed to be due in part from negative ions fusing with the background gas. The effects on the spatial distribution of fusion reactions from slight non-concentricities of the spherical electrodes and the placement of the ion sources have been investigated. More insight has also been gained regarding the existence and significance of microchannels of fusion reactants and electrons that emanate from potential variations between the wires of the cathode. The FIDO and TOF Diagnostics have proven to be valuable additions to the study of IEC devices and have greatly advanced IEC operation and theory.

Acknowledgments

First and foremost, I would like to thank my advisor, Professor Gerald Kulcinski, whose wisdom and guidance have shaped me into the scientist that I am today. I would also like to thank Professor John Santarius, with whom I have had countless stimulating discussions that have been instrumental to my work and understanding of my field of research. The research described in this work could only have been possible with the support and collaboration of the entire UW IEC Research Group with whom I have had the privilege of working. This includes Professor Gil Emmert, Robert Ashley, Richard Bonomo, Dr. Gregory Piefer, Dr. Ross Radel, Dr. Brian Egle, Dr. Samuel Zenobia, Eric Alderson, John Sorebo, Gabriel Becerra, Carlos Paz-Soldan, Lauren Garrison, Craig Schuff, Aaron McEvoy, Peter Rusch, and Logan Campbell. I would like to extend a special acknowledgement to Dr. David Boris, without whose groundbreaking work in the field of IEC research, my work would not have been possible. I would like to thank the entire Fusion Technology Institute for working to create an environment designed to promote learning and the advancement of science, particularly Joan Welc-Lepain, Dennis Bruggink, and Nancy Griego.

This work represents the culmination of an academic journey that has taken over two decades to complete. I could not hope to list all those who have helped me along the way, but from my first lessons on addition and subtraction to my advanced graduate courses in nuclear engineering, every step in my path has led to the one after it, so I would like to thank all those who have contributed to my education and helped me to reach this accomplishment. Of course, reaching this point in my life was not only an academic challenge, but also a personal journey, so I would like to thank all of my friends and colleagues for their support and contributions.

Finally, I would like to thank my family. Since I was a child, I have always had overwhelming support and encouragement from my loved ones. They instilled in me the desire to take advantage of all the opportunities that are available to expand my understanding of the world around me. My parents, James and Anglia, created an environment that always made me feel supported in every aspect of my life and encouraged me to push my boundaries and always strive to better myself. My entire family has always reassured me with their unfailing belief that I could succeed, even when it was difficult to believe it myself. Everything that I have become is due to that encouragement and support, and everything that I will accomplish in the future will be a testament to the strength I was given by my family.

Table of Contents

Table of Figures

Table of Tables

1 Introduction

The University of Wisconsin-Madison Inertial Electrostatic Confinement (IEC) Fusion Research Group has been studying the design and operation of IEC devices for over 15 years for utilization in a variety of near term applications. Small scale fusion reactors such as the IEC devices have a number of important applications that make use of the high energy neutrons produced from D-D or D-T fusion and the high energy protons produced from D-He^3 fusion. IEC devices have the added benefit over most other fusion systems in that they are capable of running steady-state or pulsed, depending on the application. One such application for a compact fusion system is the detection of nitrogen-based explosives, which use the energetic neutrons to produce characteristic gamma rays in an interrogation sample that can be used to identify the high nitrogen and oxygen contents of most explosives.

Explosive detection techniques using thermal neutron capture have already been developed and deployed at screening facilities at high traffic locations such as airports. Many of the current neutron activation systems utilize Cf-252 as their neutron source with source strengths on the order of 5×10^8 neutrons/second [1,2]. These sources are compact and produce reliably steady neutron fluxes, which make them attractive for portable interrogation setups. However, using a radioactive isotope requires constant shielding of the source even when the system is not in operation, and when detecting explosives there is the added risk of detonating an explosive device during interrogation causing the destruction and dispersal of the radioactive isotopes creating a radiological health risk. In the case of the D-D fusion sources, radiation is only produced while the system is operating and poses no radiological risk if the system is damaged during the accidental detonation of an explosive device. Previous experiments utilizing

IEC devices with source strengths on the order of 5×10^7 neutrons/second have been used to successfully detect the nitrogen signature in explosive material at the University of Wisconsin-Madison [3] and at Kyoto University [4]. These were proof-of-principle experiments, and in order to determine whether an IEC neutron source can be competitive with the currently available radioactive isotope sources used for explosive detection, further optimization of the IEC neutron source as well as the detector setup are required in order to achieve a clearer and more definitive explosive signature in a shorter interrogation time.

The detection of explosives can be separated into the neutron source and the detector setup. The detector setup consists of everything outside of the source including the gamma ray detectors, shielding, moderator, and interrogation sample. Experiments have already been conducted focusing on the thickness and placement of the moderator and shielding, as well as the detector configurations, all of which are discussed in Chapter 6. After a series of initial experiments, it was determined that a stronger neutron source could bring about the greatest improvement of the detection abilities. As was mentioned, previous IEC explosive detection experiments performed by other researchers have used source strengths on the order of 5×10^7 neutrons/second. Currently, the record steady-state neutron production rate for the UW IEC devices is 2.2×10^8 neutrons/second, and most commercially available radioactive isotope neutron sources produces at least 5×10^8 neutrons/second.

In order to increase the neutron yield of the IEC sources, a series of optimization and parameterization experiments has been conducted. The operating parameters of the IEC such as deuterium pressure, cathode voltage, and ion current have been studied with regard to their effect on neutron production rates. Optimization efforts have also taken place by studying the IEC electrode configuration and design, specifically how the separation distance between the electrodes and the design of the cathode affects neutron production rates. Preparations have also been made for the utilization of a new higher capacity power supply. The successful utilization of this new supply requires better practices for conditioning the devices for high voltage operation as well as significant upgrades to the high voltage components of the IEC device, particularly the high voltage feedthrough. For this purpose, a new feedthrough design capable of increasing the maximum voltage capabilities of the IEC device by at least 50 percent has been constructed. Neutron production rates in the IEC have been shown to scale nearly linearly with both voltage and current, so these conditioning efforts and other upgrades to allow the system to run at higher voltage and current levels will be a very important part of reaching the goal of a higher neutron production rate. Further discussion of these experiments and upgrades to the IEC can be found in Chapters 7 and 8.

In order to fully understand the effect that varying operating and system parameters has on the IEC, several different diagnostics are necessary to observe more than just the overall neutron rates. The Fusion Ion Doppler (FIDO) Diagnostic is capable of collecting energy spectra of the fusion products with enough accuracy to observe the Doppler shift of the products, which then also provides the energy spectra of the fusion reactants. The FIDO Diagnostic has already been implemented with considerable success and has been utilized to understand the reason behind the change in neutron rates seen in the optimization studies. The FIDO Diagnostic was used to analyze many of the optimization studies discussed in this work. Previously, the FIDO Diagnostic has only been capable of studying D-D fusion reactions. An advancement upon the FIDO design is detailed in this work that has been constructed and implemented, which will allow FIDO to now be used to study D-D or D-^{3}He fusion.

Another very important tool is the Time of Flight (TOF) Diagnostic, which combines two identical FIDO setups to not only measure the fusion reactant and product energy spectra, but also utilizes the time of flight of the fusion products to determine the spatial location of the fusion reactions within the IEC device. This diagnostic has been utilized on a variety of different configurations and has yielded previously unknown and unpredicted information about the spatial profile of the fusion reactions in a spherically gridded IEC devices. There have been a variety of attempts in the past to spatially profile IEC devices, but the TOF Diagnostic is the first tool to directly measure individual fusion reactions to create profiles, thereby removing the need to make many of the previous assumptions about the structure to perform an analysis. The TOF Diagnostic has a spatial resolution on the order of centimeters, which is far greater than any similar tool used to profile an IEC device. Another unique feature of the TOF Diagnostic is its ability to collect both spatial location and fusion product energies simultaneously, which provides fusion reactant energy spectra in every spatial bin.

The goal of these diagnostics was to use them to better understand the IEC, and then use that understanding to predict the ideal operating configurations to maximize steady-state neutron production rates. These diagnostic tools directly serve to further the optimization and parameterization efforts by providing additional information on how the system is affected as parameters and system configurations are varied. The profiles collected offer one of the best methods discovered thus far of comparing experimental data and theoretical modeling, which further aides the ability to predict optimal operating regimes for the IEC devices. This thesis details the large amount of progress that has been made by the author in the understanding of the spherically gridded IEC devices through the use of these diagnostic tools, and describes the many new pathways that have been uncovered to learning aspects of IEC operation that have never before been studied.

Chapter 1 References

1 U.S. Congress, Office of Technology Assessment (1991). *Technology Against Terrorism: The Federal Effort, OTA-ISC-481*. Washington, D.C., U.S. Government Printing Office

2 Twomey, T. R., Caffrey, A. J., Chichester, D. L., (2007). Nondestructive identification of chemical warfare agents and explosives by neutron-generator driven PGNAA. INL/CON-07-12304

3 Wehmeyer, A. L. (2005). The detection of explosives using an inertial electrostatic confinement D-D fusion device. (Masters thesis, University of Wisconsin – Madison)

4 Yoshikawa, K., Masuda, K., *et al.* (2007). Research and development of humanitarian landmine detection system by a compact discharge-type fusion neutron source. Proceedings of SPIE 2007, 6553, 65531S

2 Evolution of the Understanding of the IEC

2.1 History of the IEC

Inertial electrostatic confinement (IEC) fusion utilizes electrostatic forces to accelerate charged particles to fusion relevant energies (tens to hundreds of keV) towards a central focal point in order for them to collide with other particles and fuse. The concept of using electrostatic fields to confine charged particles began with the work of Elmore, Tuck, and Watson [1] in the late 1950's in which they proposed confining a plasma at thermonuclear temperatures using electrons accelerated radially inward from a spherical surface. This work was closely followed by that of Farnsworth [2], who in the late 1950's and early 1960's conceived, and shortly thereafter patented, the concept of electrostatically accelerating ions rather than electrons towards a central focus in order to cause interactions among the fast particles. Farnsworth created a spherical IEC device in which the electrostatic potential well was created by a highly transparent spherical cathode, which caused the positively charged ions to accelerate down the negative potential well towards the cathode. The purpose of this device was to create a core at the center of the sphere with a significantly higher density of fast particles than the surrounding volume in which collisions and fusion could occur.

Hirsch was contracted by Farnsworth to further study the spherical IEC concept and in 1967 he began publishing findings from his own experiments [3,4,5]. Hirsch reported producing up to approximately $5x10^7$ n/s steady-state from D-D fusion reactions and $3x10^9$ n/s steady-state from D-T fusion reactions at 150 kV cathode potential and 10 mA ion current [3]. The work of Farnsworth and Hirsch inspired a number of other researchers around the country to begin studying various aspects of IEC technology. The formation and structure of the potential well was of particular interest and was studied, among others, by Swanson [6], Dolan [7], Hu & Klevans [8], Black & Klevans [9], and Black & Robinson [10]. However, by the end of the 1970's, most researchers had come to the conclusion that the spherical gridded IEC devices, as designed at that time, would not be capable of producing more energy from fusion than what they consumed. Among the primary concerns was that the cathode itself would never survive the intense heat created by a sufficiently powerful fusion burn in an IEC device that would allow an IEC fusion power plant to be possible.

In 1983, a possible solution for this problem arose when Bussard came up with the idea for the Polywell™ design for IEC fusion [11]. This work was also done in collaboration with theoretical modeling performed by Krall [12]. This design does not utilize electrode grids to create a potential but instead uses magnetic fields to confine electrons in the center of the device creating a region of negative charge that accelerates the ions towards the central focus. After this discovery, IEC research was revisited at several new sites around the United States and various other locations around the world.

Bussard's Polywell™ experiments were cut short due to a reorganization of priorities at DARPA, which was the governmental organization financing the research, resulting in a loss of funding for the project. However, by this time various other research institutions in the United States had already begun programs to once again examine the gridded IEC devices, this time for a different purpose than energy production. IEC devices were studied for use as generators of neutrons and charged particles, which were emitted as products of the fusion reactions. IEC research was initiated at the University of Illinois (UIUC) in around 1989 by Miley, Gu, and Nadler, *et al* [13]. Some of their early work was focused on studying electrostatic potential profiles within an IEC device, but by the mid 1990's they had begun to focus on using IEC devices as neutron generators. After graduation from UIUC, Nadler continued his work at Idaho National Lab (INL) where he studied electrostatic potential profiles using a collimated proton detector [14]. Nadler began working at INL with Anderl and in 1995 they proposed using small-scale IEC devices for non-destructive evaluation of materials, which was conducted in conjunction with the work at UIUC [15].

Research was initiated in around 1993 at the University of Wisconsin-Madison in the form of theoretical and experimental research under Kulcinski, Santarius, and Fonck. Thorson and Fonck [16,17,18,19] began their experimental work studying the potential structures inside the cathode as well as the radial profile of fusion events in a spherical gridded IEC. After the graduation of Thorson in 1996, IEC research at UW-Madison began looking into several different near term applications of IEC devices, some including the use of the D-^{3}He reaction, which is discussed in further detail in Section 2.2.

Barnes and Nebel created several new IEC concepts at Los Alamos National Laboratory beginning in around 1993 with the Penning Trap design [20] and later the Periodically Oscillating Plasma Sphere (POPS) in 1998 [21]. The IEC concept was also investigated with the idea of applying it to space propulsion at the Marshal Space Flight Center in Huntsville, AL by Hrbud in 2001 [22]. In only the last few years, several IEC research projects were conducted at the Massachusetts Institute of Technology [23,24] and the University of Missouri – Columbia [25], and an independent research project was conducted at Georgia Institute of Technology [26].

At nearly the same time as most of the modern US programs began, IEC research groups began to arise internationally as well. Preliminary research studies were initiated in Japan at Osaka University in 1992 [27], and IEC programs eventually arose at Kyoto University in 1996

[28], the Tokyo Institute of Technology in 2000 [29], Kansai University in 2000 [30], and Kyushu University in 2001 [31]. The Japanese have studied both D-D and, recently, D-^{3}He fusion in an IEC and have examined the potential for several different near term applications of IEC neutron sources, particularly the detection of landmines [32]. Programs have also been more recently initiated in South Korea at Seoul National University and Hanyang University [33], and spectroscopy research on IEC devices has been conducted at the University of Sydney [34,35] in Australia beginning in around 2000.

2.2 IEC Research at the University of Wisconsin – Madison

IEC research at the University of Wisconsin began in the early 1990's in the Fusion Technology Institute under Kulcinski, Santarius, and Fonck, and Thorson was the first graduate student to work on this research beginning in around 1994 [16]. Thorson studied a variety of aspects of a spherical gridded IEC device including the potential structure of the core, the radial profile of the fusion reactions, the optimization of system configurations, and the parameterization of system variables such as voltage and current. After the completion of Thorson's PhD thesis, the UW IEC research program began to examine other applications of the IEC fusion concept. The research topics since then have focused on a variety of areas that encompass both near term applications of IEC technology, as well as answering fundamental questions about how the IEC operates.

Most of the near term applications involve using the IEC as a neutron or charged particle generator, which result from the fusion of D-D or D-^{3}He, respectively. These applications include detection of explosive material [36] and highly enriched uranium (HEU) [37], as well as the production of medical isotopes [38,39,40]. For these applications, the maximum possible particle flux out of the chambers is desired, so efforts have been constantly underway to increase the fusion rate. This has led to a variety of optimization and parameterization studies, which will be discussed in greater detail in later chapters. The proof of principle experiments for the detection of explosives and HEU have already been accomplished. They have also demonstrated that the current IEC technology is within the minimum range to produce results that indicate that it could potentially be competitive with other neutron generator technologies on the market with further optimization and study. However, while the current detection methods may only require a factor or 2 or 3 increase in neutron rates to become viable, the medical isotope production methods would need several orders of magnitude increase in particle flux in order to approach commercial viability. Another near term application of IEC technology does not actually involve fusion, but instead uses the IEC as an ion accelerator for the purpose of testing materials [39,37,41]. Materials testing for other large scale, high power fusion reactors around the world is a very important task, and the IEC offers the potential of testing various materials at reasonably high particle fluxes in order to determine their resilience to the bombardment.

As was indicated before, important research on the fundamental operation of the IEC and its various operating regimes has also been studied. Low-pressure experiments have been performed on the IEC through the use of a helicon ion source [42]. The ^3He-^3He fusion reaction has been measured in this low pressure operating mode [42]. The use of focused ion beams to create a converged core of fusion reactants has been studied and experiments were able to successfully recreate the original Hirsch results, which have not been reproduced since the experiments were first conducted in the 1960's but still hold the record for highest energy efficiency with regard to fusion production rates in an IEC device. These new experiments offered extensive insight into the dominant types of fusion in these converged ion beam devices [43]. A variety of diagnostic methods have also been developed and tested including methods for studying the various regions of the IEC in which fusion occurs [44], spectroscopic [45] measurements of the helicon ion source, and Langmuir probe [46] measurements of the ion source region. Finally, the IEC theory regarding the atomic [47] and molecular [48] effects have been advanced to the point that computational models of the device have begun to match experimental data.

2.3 Sources of Fusion in the IEC

The understanding of the internal operations of the gridded spherical IEC devices has evolved quite significantly since their discovery by Farnsworth in the early 1960's. IEC theory began with the most basic model for the operation of a gridded IEC device, known as the collisionless model. In this model, the assumptions are made that there are no collisions with background particles or the electrodes in the system and that the electrostatic forces only cause an acceleration of the ions in the radial direction, resulting in a current of monoenergetic ions accelerating towards a single focus. Up until the time of Thorson's work at UW-Madison in the early 1990's, the collisionless model was still being used as the starting point for building all other IEC theory. The most widely held belief in the IEC community as a result of this model was that nearly all fusion in an IEC device was occurring in a dense core of nearly monoenergetic fast ions that forms at a focal point at the center of the spherical electrodes. This is what is known as the converged core concept. Experiments performed by Thorson were among the first to question the idea of a converged core being entirely responsible for the fusion occurring in a gridded spherical IEC device.

There are several assumptions made in the collisionless model that result in inconsistencies with actual experiments. The largest inconsistency is that collisions with background particles can be neglected. The previous assumption was that the system is either a perfect vacuum or is at such low pressure that collisions with background neutrals can be neglected and only collisions with other fast ions are important. In reality, the IEC devices are not run in a perfect vacuum void of background neutrals, and even the lowest pressure operations typically have approximately three to four orders of magnitude higher background neutral density than fast ion density. As a result, it is more likely that fast ions travelling back and forth through the core will collide with a background neutral before they hit another fast ion. Fusion reactions that occur as a result of these types of collisions are known as beam-background fusion, where beam refers to the fast ions accelerating towards the core. Those collisions that do manage to occur between two fast ions are known as beam-beam collisions.

The likelihood of a beam-background collision resulting in fusion depends, amongst other factors, upon the energy of the fast ion, which then determines the fusion reactivity. The chart of fusion reactivity cross-sections can be found below in Figure 2.1.

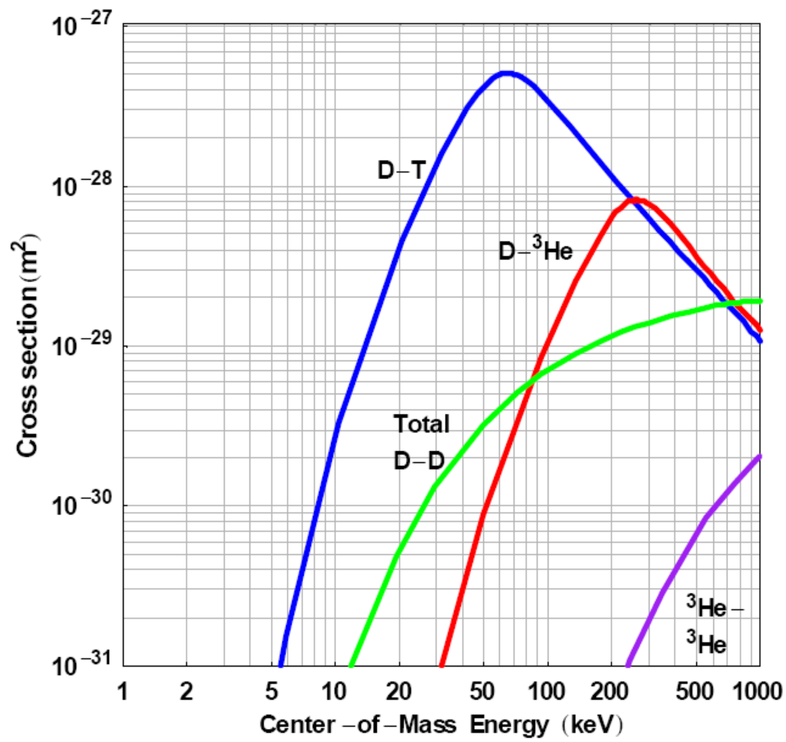

Figure 2.1 : Fusion reactivity cross-sections of various relevant fusion reactions [49,50].

As can be seen from the figure, the fusion cross-section for D-D fusion increases with increasing center-of-mass energy for the center-of-mass energies of interest. Typically, deuterium particles must be accelerated to center-of-mass energies on the order of 10 to 100 keV before they are likely to fuse during a collision. Many fast ions collide with background particles before they have been accelerated to these fusion relevant energies. Another possible result of a beam-background reaction other than fusion is a charge exchange reaction. Charge exchange involves the transfer of an electron from a cold neutral atom or molecule to a fast ion, resulting in the creation of a fast neutral and a cold ion. Charge exchange can occur either as a result of a collision, or if a fast ion travels close enough to a neutral atom to pull off one of its electrons. Charge exchange in an IEC device was discussed by Hirsch [3] and in the work of

Black and Klevans [9] in 1973 where they calculate how charge exchange reactions result in the creation of a population of fast neutrals and the spreading of the ion energy spectrum. Thorson's work in 1996 expanded on the importance of charge exchange in an IEC device. He developed a series of calculations that took into account the probability of an accelerating ion colliding with a background neutral or grid wire as it traversed the radius of the device. Thorson's experiments were performed on a spherical gridded IEC device with a cathode radius of 5 cm, and an anode radius of 20 cm. For the purpose of his calculations, he assumed roughly 2 mTorr of background deuterium pressure and a cathode voltage of 35 kV. His calculations indicated that over 75% of the original ions created in the source region are converted to fast neutrals after only one pass through the IEC, and that nearly two-thirds of all fusion occurring in the device is caused by fast neutrals rather than fast ions [17]. More recent work by Emmert and Santarius [47,48] includes the effects of atomic and molecular processes in an IEC device and will be discussed in more detail later in Section 2.8.

Other important sources of collisions and fusion reactions in a gridded IEC device are the electrode grids, particularly the cathode. Typical grid transparencies are on the order of 85 to 95 percent, so there is usually on average only approximately a 10 percent chance that the fast ions will collide with the grids. However, these collisions are still important to take into account in the calculations since the grids can become implanted with gas particles resulting in embedded fusion reactions occurring in the grid wires when they are struck by fast particles. The electrodes can then act as a sink for fast particles as well as a source of fusion reactions through the embedded fusion that occurs. These types of collisions are known as beam-target collisions, in which the target refers to a surface implanted with fusion relevant gas particles.

2.4 Radial Profiling of the Fusion Reactions in a Spherical Gridded IEC

One of the primary goals of Thorson's work was to experimentally identify where each type of fusion reaction was occurring in a gridded spherical IEC device, as well as what portion of the total fusion rate each type of reaction contributed. In order to accomplish this, a radial profile of the fusion reactions had to be measured in order to determine where the fusion was occurring in the chamber, and then determine which fusion reactions were responsible for the rates in each region. In order to accomplish this, Thorson used a collimated proton detector [17] in a similar manner as was presented several years earlier by Nadler [51]. A surface barrier diode detector was placed at the end of a 10 cm long, 1 cm diameter stainless steel tube. The tube acts to collimate the incoming protons by eliminating all those that do not travel in a nearly parallel path relative to the tube because all other trajectories would result in a collision with the side of the tube. This creates a cone of detectable volume that the proton detector can see from the chamber. The setup used by Thorson can be seen in Figure 2.2 below.

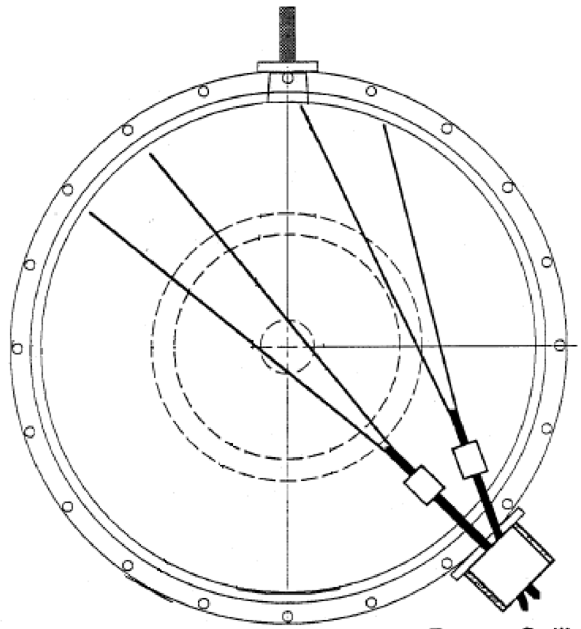

Figure 2.2 : Diagram of Thorson experimental setup for proton collimator diagnostic [17].

The collimated detector was attached to a bellows assembly that allowed for it to be rotated in order to look at different solid angle views of the chamber. An 18 μm thick aluminum film was placed over the end of the collimator tube to protect the detector from the plasma, and a 25 μm thick film of lead was placed in front of the detector to attenuate soft x-rays created in the chamber. Using this setup, Thorson took proton counts at a range of angles through the chamber. The results are shown below in Figure 2.3.

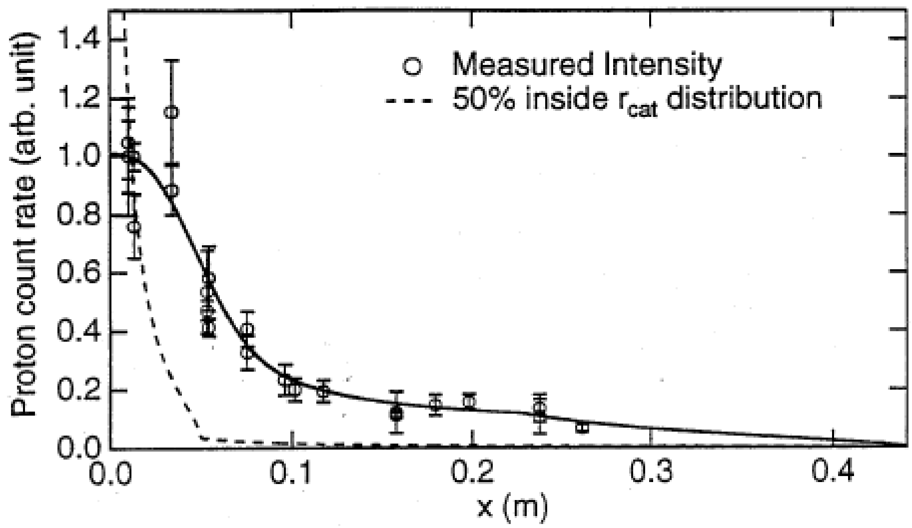

Figure 2.3 : Collimated proton detector measurements at varying radii across a gridded spherical IEC device [17].

The values in the figure above represent the integral number of proton counts in each chord through the chamber. Thorson then applied a spline fit to the above data and performed an Abel inversion. To perform the spline fit and the Abel inversion, several assumptions had to be made. Among those assumptions were that the reactivity outside the anode decreases as $1/r^2$. Inside the anode, he assumed that the radial profile could be estimated as being similar to a polynomial function. This was based upon the idea that the volume source would have contributed a significant portion of the neutron rates, which are in that case proportional to r^2. The Abel inversion is a widely recognized method, particularly in astronomy and plasma science, that is used to determine the radial profile of an approximately spherical or cylindrical object using only a finite number of data points taken as integrated counts along chords through the radial profile [52].

This method is typically considered to be quite reliable in obtaining a reasonable approximation of the profile of a radially symmetric object, though there are a few important caveats to keep in mind. First, the Abel inversion does not produce unique solutions, and the process requires the user to make an assumption on what the basic shape of the profile looks like in order to create an equation based on a series of discrete data points. With no unique solution, it cannot be confirmed whether or not the assumed function used to model the data points is the most accurate one possible. Usually the profile is assumed to be some sort of polynomial in nature, or that it fits a recognized distribution function. These approximations are typically sufficiently accurate to develop a reasonably complete profile. However, it is difficult to predict deviations from these recognized functions such as sudden peaks or valleys within the profile that do not match a typical distribution or polynomial function. Another drawback is that the Abel inversion is very sensitive to error in the data points collected. This is due to the fact that it is not the magnitude of the data points themselves that is used in the inversion but rather the magnitude of the slope between the points since the Abel inversion uses the derivative of the function [df(r)/dr] that is used to model the collected data rather than the function itself [f(r)]. This makes it even more important to ensure that the experimental data collected has very little error.

The resulting function created from the Abel inversion was volume integrated over r to give the percentage of total fusion reactions occurring within r. The results of this technique are shown in Figure 2.4.

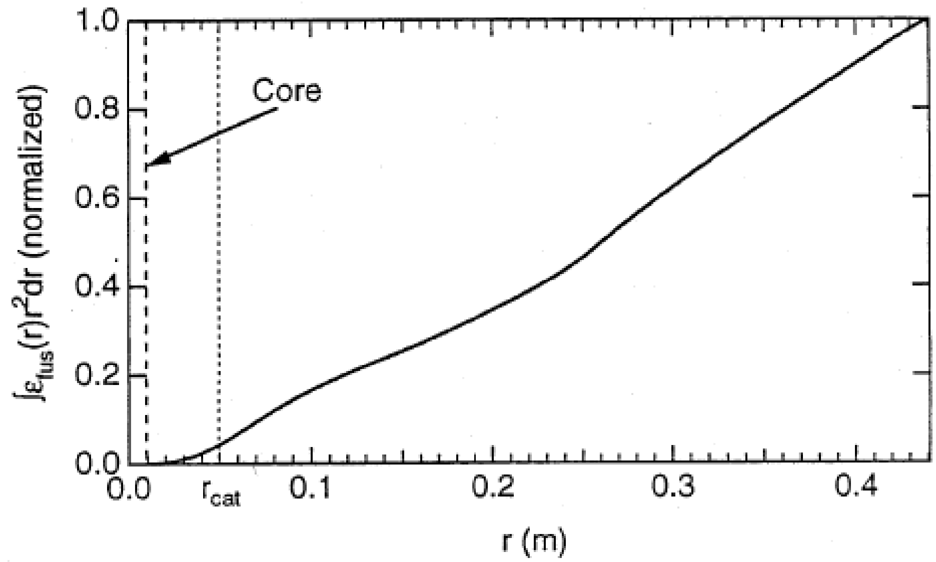

Figure 2.4 : Integrated Abel-inverted radial reactivity profile of gridded spherical IEC device [17].

As can be seen from the results shown above, only a very small percentage of the total number of fusion reactions occurring in the device are inside the core. According to the integrated Abel inverted profile, less than 10% of the fusion reactions occur inside the cathode. These results were among the first indications that the gridded spherical IEC devices were not getting converged core, or at the very least that the core was not responsible for a majority of the fusion occurring in the device. As was previously mentioned, all theorists before Thorson predicted that nearly all fusion in an IEC device should occur in a dense core in the middle of the device, and the results of Thorson's experiments contradicted that assumption and created a new picture of what was happening inside an IEC.

2.5 Further Development of Fusion Source Regions

After the work of Thorson, much more attention began to be paid to the importance of the other sources of fusion in the IEC outside of the core, primarily the beam-background and beam-target reactions. Nearly a decade later, another diagnostic method for studying the radial profile of a gridded IEC device known as the eclipse disc diagnostic was developed at UW-Madison by Ashley, Murali, and Cipiti [53,54,55]. The IEC device was divided into three different regions with regard to where the dominant sources of fusion were occurring. The three regions were the Converged Core, Volume, and Embedded source regions, and they can be seen below in Figure 2.5.

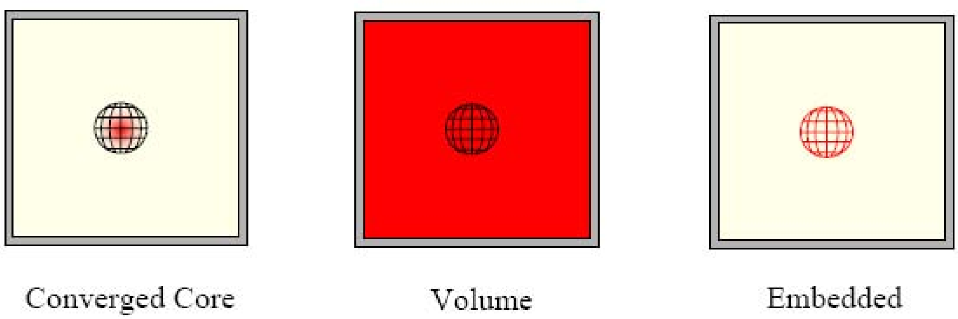

Figure 2.5 : Source regions for fusion reactions within a gridded spherical IEC device (regions of fusion are marked in red) [55].

The converged core region is made up primarily of beam-beam and beam-background fusion reactions caused by the fast ions all converging at the central focus of the system and colliding either with other fast ions or more likely with the background neutrals. The volume source region is composed of fast neutral-background collisions, which would theoretically occur somewhat uniformly throughout the volume of the chamber since the fast neutrals, once created, would not experience any electrostatic force and thus travel in a straight line to a wall, reacting at all points along the line with a constant probability of fusion with a background gas molecule. The embedded source region consists of the beam-target reactions that occur as a result of fast particles colliding with the surface of the cathode grid and fusing with embedded gas particles within a few μm of the surface. The eclipse disc experiments determined the extent to which each of these fusion source regions contributed to the total fusion rates.

The basic design of the eclipse disc diagnostic is to place a circular piece of aluminum directly in front of the collimated proton detector on a plane that is normal to the detector's line of sight. The purpose of this is to eclipse a portion of the view of the detector in order to block D-D protons and reduce the energy of D-^{3}He protons for a region of interest. Three different sized discs were placed interchangeably outside the anode and used to examine each source region separately, and a small disc was also scanned across the cathode region. The discs were all thick enough to stop the 3 MeV fusion protons created in the D-D fusion reaction. A drawing of the setup constructed is shown in Figure 2.6.

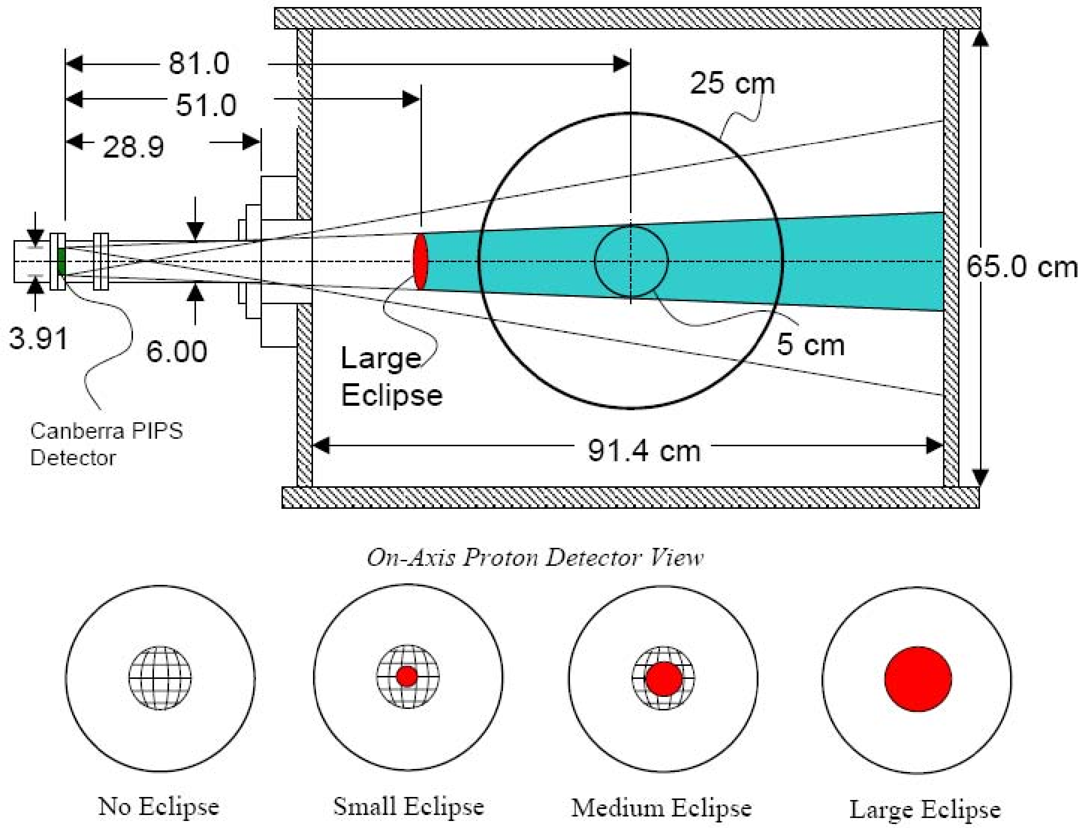

Figure 2.6 : Eclipse disc diagnostic setup including portions of detector view blocked by the various discs [55].

A measurement was first taken with no disc in place, providing the total fusion rate occurring in the line of sight of the collimated proton detector. The small disc was then put into place, which was just large enough to cover up the core, thereby eliminating the contribution from the converged core source region. The medium disc was just large enough to fit within the radius of the cathode so that nearly all the volume inside the cathode could be omitted but a portion of the cathode wires could still be seen, which provided a total fusion count that excluded everything inside the cathode but still included some of the beam-target source region from the cathode wires. The large disc blocked out the entire cathode, which removed the embedded and converged core source regions completely and left only the volume source region contribution from the rest of the chamber.

One issue with the eclipse disc setup was that the discs not only blocked out the intended region, such as the core or the cathode, but it also blocked out all the volume source region behind the disc. This meant that when the small disc was used, both the converged core source region and a portion of the volume source region were blocked out, so the magnitude of the contribution from converged core could not be accurately determined without knowing how much the volume source was also contributing in that region. This issue was resolved by taking an off-axis measurement with the collimated proton detector, similar to what was done by Thorson. Since the volume source region was theoretically uniform across the volume of the chamber, the proton detector could be rotated to look at a solid angle that did not include any of the cathode. This would allow a measurement of the number of fusion reactions occurring due to the volume source within a given volume, which was the volume of the solid angle view of the detector. The value taken from these off-axis measurements for the fusions reactions per volume contributed by the volume source were then used with the eclipse disc measurements to determine how much of the fusion reactions obstructed by the disc were caused by volume source reactions as compared to converged core or embedded fusion.

The measurements from the eclipse disc and off-axis experiments were analyzed and the contribution from each source region within the solid angle volume of the detector was calculated. These measurements were then converted to the contribution of each source region to the total amount of fusion occurring in the chamber using a scaling function developed based upon the view factor of the detector and the geometry of the chamber [55]. The results of D-D experiments are shown below in Table 2.1 and D-^{3}He experiments are shown in Table 2.2.

	Converged Core	Embedded	Volume
Raw Counts	74%	14%	12%
Total Rate	22%	8%	70%

Table 2.1 : Results of eclipse disc and off-axis experiments on D-D fusion reactions including raw counts collected in solid angle view of detector and the corresponding scaled contribution from total fusion reactions in entire device [55].

	Converged Core	Embedded	Volume
Raw Counts	10%	90%	Negligible
Total Rate	5%	95%	Negligible

Table 2.2 : Results of eclipse disc and off-axis experiments on D-^{3}He fusion reactions including raw counts collected in solid angle view of detector and the corresponding scaled contribution from total fusion reactions in entire device [55].

It is important to note that although the volume source is only responsible for 12% of the fusion reactions occurring in the solid angle view of the on-axis detector, it is responsible for 70% of the total fusion reactions occurring in the entire device. This is because all other fusion occurring outside of the view of the detector is created from the volume source. So when the raw counts are scaled to the total fusion rate created within the chamber, the volume source, though more diffuse than the converged core or embedded sources, makes up a very large portion of the total fusion rate created in the device. These results are in a reasonable level of agreement with those of Thorson. Thorson calculated that less than 10% of all fusion was occurring inside the cathode and the results shown above indicate that the converged core region inside the cathode could be responsible for around 22% of the total fusion rate. However, both agree that the core is not responsible for the majority of the fusion reactions in the chamber, which further disproves the converged core theory within this range of operating pressures.

2.6 Embedded D-D and D-^{3}He Fusion

Cipiti also conducted a series of experiments to better gauge the significance of the beam-target fusion reactions in an IEC device [39]. The first set of experiments involved constructing new tungsten-rhenium grids, and then running these new “virgin” grids in the IEC and measuring the increase in fusion rates with each successive run. The purpose of these experiments was to show that as the new grid was exposed to more deuterium, the wires would become increasingly implanted with embedded deuterium atoms until it reached a saturation point. By measuring the fusion rate, Cipiti was hoping to gauge the level of increase of beam-target fusion events, which would then correspond to the increased amount of embedded atoms in the grid. The results of this set of experiments found an undetectable change in rates over time while the new grid was operated in the device using only deuterium. When ^{3}He was used, though, a significant increase in rates was seen on a new grid as run time went on until an eventual saturation point was reached. This was one of the first demonstrations of the difference in fusion regimes between using D-D and D-^{3}He fuels due to the significance of the beam-target reactions for each, which can be seen in Table 2.1 and Table 2.2.

Another set of experiments was performed on embedded fusion rates, this time using several solid cathodes instead of wire grids. Three solid spherical cathodes approximately 2.5 cm in diameter were machined out of tungsten, titanium, and molybdenum [55]. By using solid cathodes instead of grids, any converged core or other effects inside the cathode are removed and any change in rates due to the embedded fusion would be more significantly noticeable. These experiments were also able to test the effectiveness of various materials at retaining deuterium or helium-3 atoms in an IEC device. For the D-D fusion case, the results indicated that the solid cathodes consistently produced around four to ten times lower levels of fusion reactions than the spherical grids under the same conditions. The tungsten sphere produced the highest D-D fusion rates, followed by molybdenum, and finally by titanium.

The difference in rates for the different materials is most likely due to the fact that titanium has the highest diffusivity for deuterium of all the elements used, which means that the deuterium could more easily diffuse in and out of the sphere making it more difficult to build up a dense layer of embedded deuterium atoms. Molybdenum and tungsten have much lower diffusivities, so a higher concentration of embedded deuterium is able to build up before it saturates.

Once again, the effects on D-^{3}He fusion reactions were much more significant, which appears to be the result of the ability of ^{3}He to be retained by materials as opposed to deuterium. An order of magnitude increase in D-^{3}He fusion rates was observed when deuterium was run after ^{3}He was implanted when compared to running ^{3}He after the target was saturated in deuterium, indicating that ^{3}He implants and is retained in the cathode material much more effectively than does deuterium. Once again, the tungsten produced the highest fusion rates, followed by molybdenum and titanium. These experiments served to not only further the understanding of the importance of embedded fusion reactions in an IEC device, but also began to quantify the difference in various materials and different types of fusion reactions as they pertain to embedded fusion. Particularly, the importance of the ability of ^{3}He to implant in surfaces would warrant a serious consideration in the design of a D-^{3}He IEC device as opposed to a D-D device.

2.7 Advancing the Use of Diagnostics in IEC Devices – Work of Masuda, *et al*

Several years after the work done by Ashley, Murali, and Cipiti on the eclipse disc diagnostic, another diagnostic tool was developed in 2006 by Masuda, Fujimoto, and Yoshikawa [56, 57] using methods similar to both the collimated proton and eclipse disc diagnostics. The experimental setup used in these experiments is shown below in Figure 2.7.

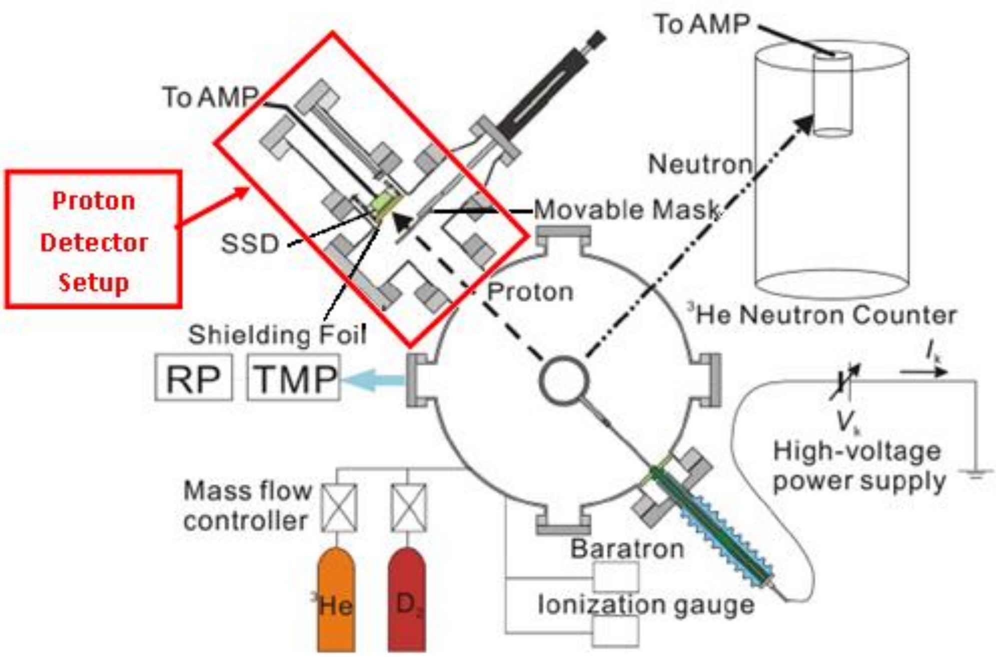

Figure 2.7 : Experimental setup used by Masuda, et al., highlighting proton diagnostic configuration [56].

The experimental setup for these experiments consisted of a 17 cm radius spherical chamber, which served as the anode, and a 3 cm radius spherical cathode grid. The system was run at cathode voltages up to 60 kV and ion currents up to 3 mA with pressures up to 10 mTorr. A Li-implanted Si-doped diode detector was used in these experiments, capable of measuring energies up to and including the 14.7 MeV proton emitted by the D-^{3}He fusion reaction. As in previous experimental setups, a thin metallic foil was placed in front of the solid state detector (SSD) in order to protect it from the plasma and shield some of the soft x-rays emitted from the chamber. The unique aspect of this setup was that a linearly movable mask was used that could be moved back and forth across a path directly in front of the line of sight of the proton detector. Three different sized masks were used with diameters of 25, 34, and 37 mm. This is similar to the eclipse disc diagnostic used earlier at UW-Madison, except in this case the masks are placed inside the collimating channel instead of inside the chamber, and they now have the ability to scan across the profile of the chamber in order to provide integrated proton measurements of collimated chords to back out a radial profile. This provided an additional benefit that the unmasked collimated proton detector did not have, which is that the masked collimated detector was capable of focusing on aspects of the chamber that were not inherently spherically symmetric, such as the high voltage feedthrough.

Fujimoto [57] used the masked collimated proton detector for this purpose in order to determine the amount of embedded D-^{3}He fusion occurring in the feedthrough. To do this, Fujimoto made another addition to this setup, which was the ability to move the SSD azimuthally with respect to the center of the IEC. The result of this setup was that the masks and the SSD could be aligned in a manner such that collimated proton measurements were able to be taken that included only the volume of the cathode at one extreme, and only the feedthrough at the opposite extreme. This allowed for the contribution of the cathode volume and the feedthrough to be evaluated separately in order to gauge both of their significances to the total fusion rate in the chamber. The results of these experiments for D-^{3}He fusion reactions matched those of Cipiti reasonably well, showing that nearly 99% of all D-^{3}He fusion was occurring within the cathode and on the cathode wires as compared to 95% found by Cipiti.

2.8 Theoretical Modeling of the IEC – Work of Emmert and Santarius

Most of the discussion thus far has focused upon experimental work that has been performed regarding the radial profile of a gridded spherical IEC device, but not much has yet been said about the theoretical work regarding the internal workings of an IEC. The primary reason is that it has only been within the last few years that the theoretical modelings of an IEC device has begun to match the experimental data within a reasonable level of precision. The work referred to here is that of Emmert and Santarius [47,48] of UW-Madison. For the last several years, they have been developing a computer code that can simulate the operation of a gridded IEC device at moderate pressures (0.1 to 10 mTorr). Particular attention has been paid to the molecular composition of the source region (D_2, D^+, D_2^+, D_3^+) as well as the importance of charge exchange, dissociation, and ionization reactions and their effects on the softening of the resulting ion energy spectra. This code has been developed in conjunction with experimental work done on gridded IEC devices at UW-Madison, which has allowed for a direct comparison of theoretical and experimental data.

One element of this model is the molecular composition mix of the source region. The source region for the IEC devices discussed here consists of the region outside of the anode where the filaments ionize the background deuterium that is pumped into the device. Based upon the existing molecular ionization and collision cross section data, it was estimated that the molecular ratios of the various ions are approximately 70% D_3^+, 25% D_2^+, and 5% D^+ ions [46] Each of these species has collision cross sections that quantify both the probability of a collision with another particle in the system, as well as the possible results of what will happen to the particle after the collision occurs. The possible outcomes of collisions with other particles for each ion species are shown in Figure 2.8 below.

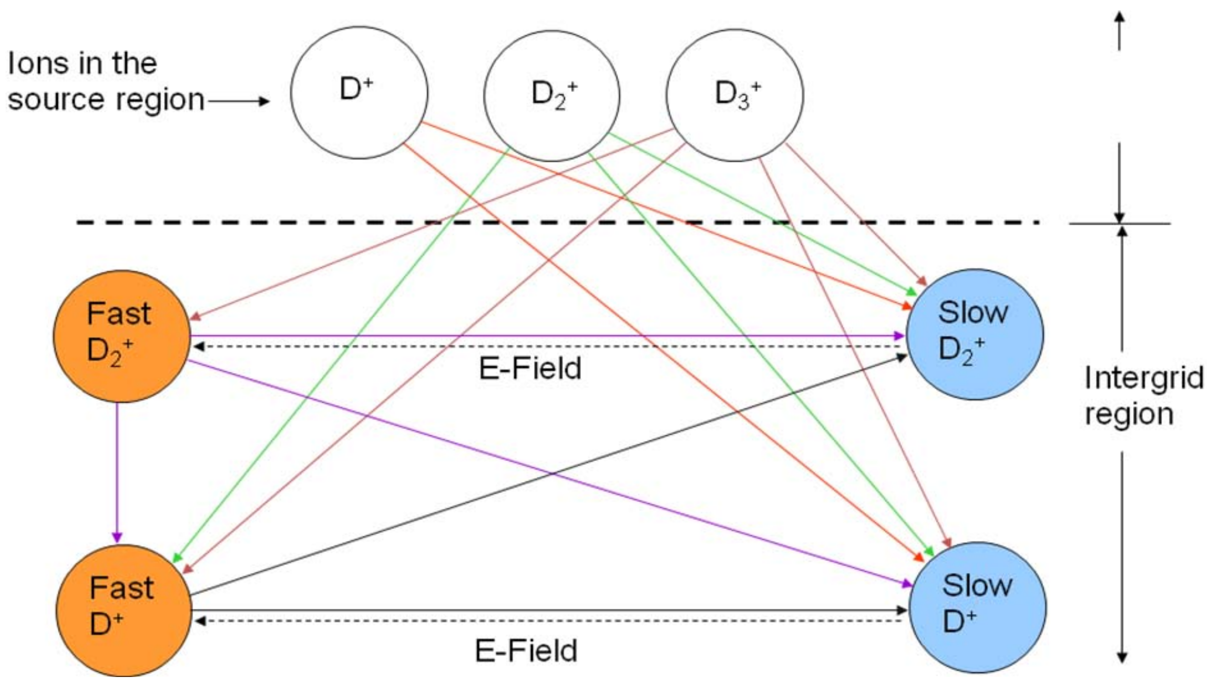

Figure 2.8 : Possible outcomes of collisions of various ion species with a neutral background gas molecule [58].

In the context of this discussion, "fast" refers to high energy particles (those at fusion relevant energies) and "slow" refers to low energy particles. As has already been discussed, the most likely target for a fast particle to collide with is a background neutral. When this occurs, a number of results are possible including charge exchange, dissociation, ionization, or inelastic scattering. The end result, though, is going to be one of the options shown in the figure above in the blue and orange bubbles. This figure serves to demonstrate all the likely outcomes of a collision of each of the ion species with a neutral background has molecule, and all of these possibilities were taken into account in the theoretical modeling along with the corresponding cross section for each reaction.

After defining the composition of the source region and taking into account all of the relevant types of collisions that the ions may experience, the code was used to determine the ion energy spectrum at the cathode radius and the total neutron production rate of the device. Multiple series of simulations were performed that varied parameters such as pressure, cathode radius at constant anode radius, and the source region ion mix. The ion energy spectra created by the program were able to clearly indicate the presence of ion energy peaks at the full energy (determined by the potential on the cathode) as well as at 1/2, 1/3, and 2/3 of the full energy. A calculated sample spectrum is shown in Figure 2.9.

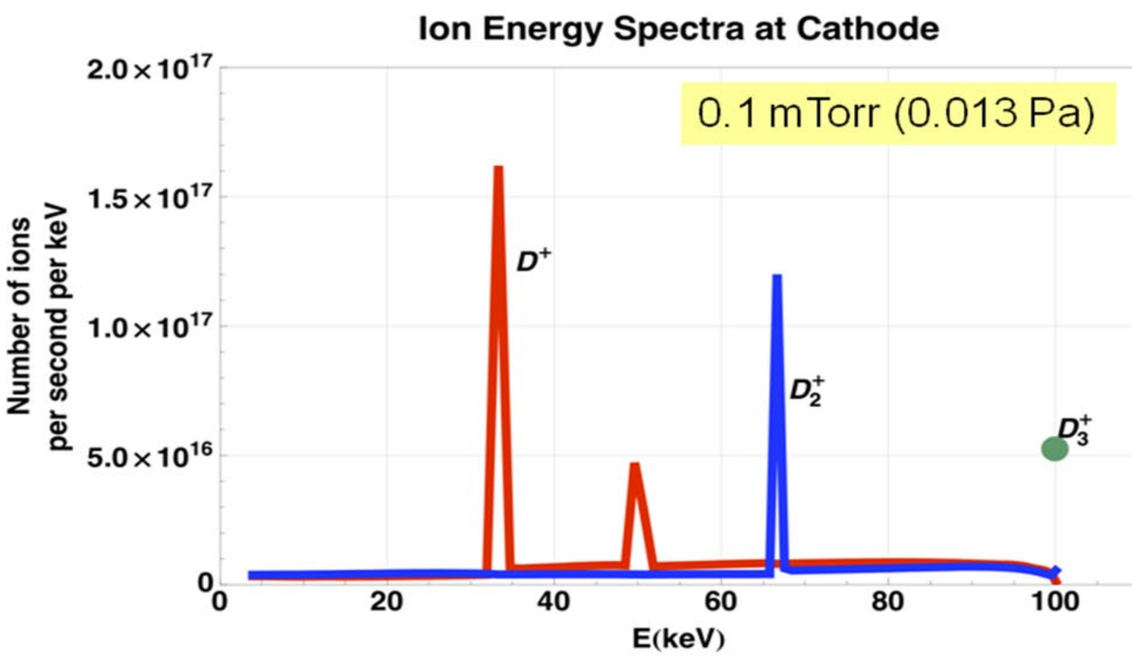

Figure 2.9 : Theoretical ion energy spectra at cathode for 0.1 mTorr deuterium pressure, 100 kV, 60 mA, r_c=0.1 m, r_a=0.2 m, Source: 0.06 D^+, 0.23 D_2^+, 0.71 D_3^+ [59].

The spectra shown above indicate the importance of the collisions in the ion energy spectra. Very few full energy particles (100 keV in this case) actually create fusion reactions at the cathode, most collide along the way and only make it there with a fraction of their full energy.

At 2 mTorr, many of the ions from the source region could potentially make it all the way to the cathode, pass through the core, and then back out the other side of the cathode, at which point they are accelerated back toward the core where they can possibly pass back through another time before they cause a fusion reaction. However, whenever a collision occurs within the anode radius, the ions may still be able to make multiple passes through the core, but they have less energy, and the resulting energy spectra is softened.

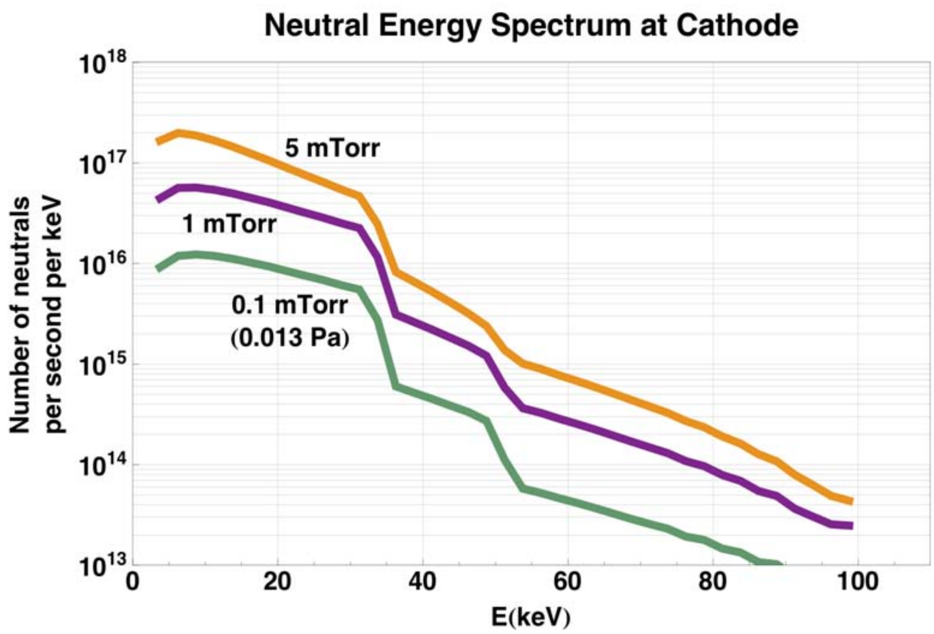

Figure 2.10 : Fast neutral energy spectra at cathode for varying pressure of deuterium at 100 kV, 60 mA, Cathode Radius = 10 cm, Anode Radius = 20 cm, Source D^+ : D_2^+ : D_3^+ = 0.06 : 0.23 : 0.71 [59].

The fast neutral population has a soft spectrum as well, as can be seen in Figure 2.10. Although in the case of fast neutrals, increasing the pressure actually increases the number of fast particles as opposed to the fast ion energy spectra in which increasing pressure results in fewer fast ions. Once again, it appears that the majority of the fusion reactions occur by particles with energies well below the energy corresponding to the voltage difference between the anode and cathode. The fast neutrals have nearly the same probability of running into background neutrals as the fast ions. The fast neutrals are also quite often created in the intergrid region between the anode and cathode, which means that they are usually unable to reach their full energy by the time they reach the cathode even without collisions. This indicates that whether it is fast ions or fast neutrals causing the fusion in an IEC device, the majority of the fast particles are only at a fraction of the full applied voltage difference between the anode and cathode. This is a significant development in understanding the relationship between applied voltage and fusion rates in an IEC device at moderate pressures. These results also magnified the importance of charge exchange reactions and other types of background collisions because of their obvious effect on softening the energy spectrum of the fast particles.

Chapter 2 References

1 Elmore, W. C., Tuck, J. L., Watson, K. M. (1959). On the inertial-electrostatic confinement of a plasma. *Physics of Fluids*, Vol. 2, 239

2 Farnsworth, P. T. (1962). *Electric Discharge Device for Producing Interactions between Nuclei*. Patent Number: 3,258,402. June 28, 1966

3 Hirsch, R. L. (1967). Inertial-electrostatic confinement of ionized fusion gases. *Journal of Applied Physics*, *38*(11), 4522-4534

4 Hirsch, R. L. (1967). Highly efficient, inexpensive, medium current ion source. *Review of Scientific Instruments*, 38(5), 621-624

5 Hirsch, R. L. (1968). Experimental studies of a deep, negative, electrostatic potential well in spherical geometry. *Physics of Fluids*, 11(11), 2486-2490

6 Swanson, D. A., *et al.* (1973). Potential well structure in an inertial electrostatic plasma confinement device. *Physics of Fluids*, 16(11), 1939-1945

7 Dolan, T. J., Verdeyen, J. T., Meeker, D. J., Cherrington, B. E. (1972). Electrostatic-inertial plasma confinement. *Journal of Applied Physics*, 43(4), 1590-1600

8 Hu, K. M., Klevans, E. H. (1974). On the theory of electrostatic confinement of plasmas with ion injection. *Physics of Fluids*, **17**, 227-231

9 Black, W. M., Klevan, E. H. (1974). Theory of potential-well formation in an inertial electrostatic confinement device. *Journal of Applied Physics*, **45**, 2502

10 Black, W. M., Robinson, J. W. (1974). Measuring rotationally symmetric potential profiles with an electron-beam probe. *Journal of Applied Physics*, 45(6), 2497-2501

11 Bussard, R. W. (1985). *Method and Apparatus for Controlling Charged Particles.* Patent Number: 4,826,646. May 2, 1989

12 Bussard, R. W., Krall, N. A. (1994). Inherent characteristics of fusion power systems: physics, engineering, and economics. *Fusion Technology*, 26 (4), 1326-1336

13 Miley, G. H., *et al*. (1991). Inertial electrostatic confinement: an approach to burning advanced fuels. *Fusion Technology*, 19, 840

14 Nadler, J. H., Gu, Y. B., Miley, G. H. (1992). Potential profile measurement using a collimated proton detector in spherical inertial-electrostatic plasma confinement. *Review of Scientific Instruments* 63 (10), 4810-4812

15 Anderl, R. A., Hartwell, J. K., Nadler, J. H., *et al.* (1995). Development of an IEC neutron source for NDE. *Fusion Engineering*, 16th IEEE/NPSS Conference, 1482-1485

16 Thorson, T. A., Durst, R. D., Fonck, R. J., Foucher, B. S., Wainwright, L. P. (1995). Initial results from the Wisconsin spherically convergent ion focus experiment. Presented at 1995 IEEE International Conference on Plasma Science

17 Thorson, T. A. (1996). Ion flow and fusion reactivity characterization of a spherically convergent ion focus. (PhD dissertation, University of Wisconsin – Madison)

18 Thorson, T. A., Durst, R. D., Fonck, R. J., Wainwright, L. P. (1997). Convergence, electrostatic potential, and density measurements in a spherically convergent ion focus. *Physics of Plasmas*, 4(1), 4-15

19 Thorson, T. A., Durst, R. D., Fonck, R. J., Sontage, A. C. (1998). Fusion reactivity characterization of a spherically convergent ion focus. *Nuclear Fusion*, 38(4), 495-507

20 Barnes, D. C., Nebel, R. A., Turner, L. (1993). Production and application of dense penning trap plasmas. *Physics of Fluids B*, 5(10), 3651

21 Nebel, R. A., Barnes, D. C. (1998). The periodically oscillating plasma sphere. *Fusion Technology*, 34, 28-45

22 Hrbud, I. (2001). IEC Research Status at MSFS. Presented at 3rd US-Japan Exchange on IEC, March 22-23, 2001, Huntsville, AL

23 McGuire, T. J. (2007). Improved lifetimes and synchronization behavior in multi-grid inertial electrostatic confinement fusion devices. (PhD dissertation, Massachusetts Institute of Technology)

24 Dietrich, C. C. (2007). Improving particle confinement in inertial electrostatic fusion for spacecraft power and propulsion. (PhD dissertation, Massachusetts Institute of Technology)

25 Meyer, R. (2007). Inertial electrostatic confinement: theoretical and experimental studies of spherical devices. (PhD dissertation, University of Missouri – Columbia)

26 Seltzman, A. (2008). Design of an actively cooled grid system to improve efficiency in inertial electrostatic confinement fusion reactors. (Masters thesis, Georgia Institute of Technology)

27 Mima, K., Yoshikawa, K., Morimiya, O., *et al.* (1992). Preliminary studies of direct energy conversion in a D-^{3}He inertial confinement fusion reactor. *Fusion Technology*, 22 (1), 56-65

28 Ohnishi, M., *et al.* (1996). Correlation between potential well structure and neutron production in inertial electrostatic confinement fusion. *Institute of Advanced Energy Research Report*, Kyoto University, ISSN 1342-3185

29 Matsuura, H., *et al.* (2000). Ion distribution function and radial profile of neutron production rate in spherical inertial electrostatic confinement plasmas. *Nuclear Fusion*, 40(12), 1951

30 Ohnishi, M., *et al.* (2000). Beam optics in inertial-electrostatic confinement fusion. *Review of Scientific Instruments*, 71(2), 1210

31 Yamauchi, K., *et al.* (2001). Neutron production characteristics and emission properties of spherically convergent beam fusion. *Fusion Technology,* 39(3), 1182

32 Yoshikawa, K., Masuda, K., *et al.* (2005). Research and development of a compact fusion neutron source for humanitarian landmine detection. Presented at 20th IAEA Fusion Energy Conference, IC/P6-54

33 Park, M. J. (2003). RF plasma ion sources of compact neutron generators. Presented at 6th US-Japan Workshop on IEC, October 20-21, 2003, Tokyo, Japan

34 Khachan, J., *et al.* (2003). Spatial distribution of ion energies in an electrostatic confinement device. *Physics of Plasmas*, 10(3), 596-599

35 Kipritidis, J., Khachan, J. (2008). Application of Doppler spectroscopy in H_2 to the prediction of experimental D(d,n)^{3}He reaction rates in an inertial electrostatic confinement device. *The American Physical Society, Physics Review E*, 79(2), 026403-1-8

36 Wehmeyer, A. L. (2005). The detection of explosives using an inertial electrostatic confinement D-D fusion device. (Masters thesis, University of Wisconsin – Madison)

37 Radel, R. F. (2007). Detection of highly enriched uranium and tungsten surface damage studies using a pulsed inertial electrostatic confinement fusion device. (PhD dissertation, University of Wisconsin – Madison)

38 Weidner, J. W. (2003). The production of ^{13}N from inertial electrostatic confinement fusion. (Masters thesis, University of Wisconsin-Madison)

39 Cipiti, B. B. (2004). The fusion of advanced fuels to produce medical isotopes using inertial electrostatic confinement. (PhD dissertation, University of Wisconsin – Madison)

40 Egle, B. J. (2007). Comparison of cylindrical and spherical geometry in a new inertial electrostatic confinement device. Poster Presented at 9th US-Japan Workshop, Argonne National Lab, IL

41 Zenobia, S. J. (2007). Ion implantation effects on carbon-carbon velvet. Poster presented at 9th US-Japan Workshop at Argonne National Lab, IL

42 Piefer, G. R. (2006). Performance of a low-pressure, helicon driven IEC ^{3}He fusion device. (PhD dissertation, University of Wisconsin – Madison)

43 Egle, B. J. (2010). Nuclear Fusion of Advanced Fuels Using Converging Focused Ion Beams. (PhD dissertation, University of Wisconsin-Madison)

44 Murali Subramanian, Krupakar (2004). Diagnostic study of steady-state advanced fuel (D-D and D-^{3}He) fusion in an IEC device. (PhD dissertation, University of Wisconsin – Madison)

45 Alderson, E. C., *et al.* (2007). Spectroscopic diagnosis of plasma in the IEC. Poster presented at 9th US-Japan Workshop, Argonne National Lab, IL

46 Boris, D., Emmert, G. (2006). Plasma characteristics of the ion source region in the University of Wisconsin IEC device. American Physical Society 48th Annual Meeting of the Division of Plasma Physcs, October 30, 2006

47 Emmert, G. A., Santarius, J. F. (2010). Atomic and molecular effects on spherically convergent ion flow I: single atomic species. *Physics of Plasmas, 17,* 013502

48 Emmert, G. A., Santarius, J. F. (2010). Atomic and molecular effects on spherically convergent ion flow II: multiple molecular species. *Physics of Plasmas, 17,* 013503

49 Bosch, H. S., & Hale, G. M. (1992). Improved formulas for fusion cross-sections and thermal reactivities. *Nuclear Fusion, 32*(4), 611-31

50 Junker, M, d'Alessandro, A., Zavatarelli, S., Arpesella, C., Bellotti, E., *et al.* (1998). Cross section of ^{3}He(^{3}He, 2p)^{4}He measured at solar energies. *Physical Review C,* 57, 2700

51 Nadler, J. H., Gu Y. B., Miley, G. H. (1992). Potential profile measurements using a collimated proton detector in spherical inertial-electrostatic plasma confinement. *Review of Scientific Instruments* **63,** 4810

52 Lochte-Holtgreven, W. (Editor) (1968). *Plasma Diagnostics*. North-Holland Publishing Company, 184-186

53 Ashley, R. P., Kulcinski, G. L., Santarius, J. F., Krupakar Murali, S., Piefer, G. R., Cipiti, B. B., Radel, R. F., Weidner, J. W. (2003). Recent progress in steady state fusion using D-^{3}He. *Fusion Science and Technology*, 44, 564

54 Krupakar Murali, S., Cipiti, B. B., Santarius, J. F., Kulcinski, G. L. (2006). Study of fusion regimes in an inertial electrostatic confinement device using the new eclipse disc diagnostic. *Physics of Plasmas*, 13, 053111

55 Cipiti, B. B. (2004). The fusion of advanced fuels to produce medical isotopes using inertial electrostatic confinement. (PhD dissertation, University of Wisconsin – Madison)

56 Masuda K., Yoshikawa, K., Ohishi, T., Ogawa, S. Zen, H., Takamatsu, T. (2006). Spatial distribution of D-D/D-^{3}He advanced fuels fusion reactions in an inertial electrostatic confinement fusion device. Proceedings of 21st IAEA Fusion Energy Conference, IAEA-CN-149 / IC / P7-9

57 Fujimoto, T., Oishi, T., Zen, H., Masuda, K., Yoshikawa, K. (2007). Intensity distribution of D-3He fusion reaction rate in an IEC device. *Fusion Engineering*, SOFE 2007, 1-4

58 Emmert, G. A., Santarius, J. F. (2008). Integral transport approach for molecular processes in IEC devices. Powerpoint Presentation, Proceedings of 10th US-Japan IEC Conference, Kyoto, Japan

59 Santarius, J. F., Emmert, G. A. (2008). Parametric exploration of moderate-pressure IEC device operation. Powerpoint Presentation, Proceedings of 10th US-Japan IEC Conference, Kyoto, Japan

3 Previous Optimization and Parameterization Efforts

Over the first few decades of IEC research, the majority of the research and experimentation was aimed at proof of principle experiments on various IEC devices and establishing some basic theory that could describe the operation of the IEC. A number of experiments were attempting to discover new modes of operation in an IEC in order to seek orders of magnitude gains in fusion reaction rates. Therefore, much of the early work focused on studying the electric potential and ion density structure of the core region. It was not until the rebirth of IEC technology in the 1990's, particularly with the work of the UW IEC group, that individuals began to realize the importance of other sources of fusion events in IEC devices, particularly the beam-background and fast neutral-background fusion reactions in the volume source. Once the various sources of fusion were put into perspective with regard to their respective contributions to the total fusion rate, efforts began to parameterize the operating conditions and optimize various components of the IEC in order to maximize the contribution of each type of fusion so as to increase the total fusion rate.

In nearly all IEC devices, there are several parameters that can be varied during operation, each of which has a noticeable impact on the fusion rate in the chamber. The most important of these parameters are the cathode voltage, ion current, and feed gas background pressure. In any IEC experiment, it is essential to understand how each of these parameters affects the operation of the device, particularly in order to be able to reach a desired neutron production rate. It is typically standard practice to perform scans of each of these parameters in which the neutron rates produced within the chamber are recorded for a range of values of each variable quantity. Recording neutron production rates alone during these scans can provide valuable information regarding the capabilities for producing fusion in the IEC devices. However, to get a more complete picture of how each parameter is affecting the internal operations of the IEC device, the energy spectra of the fast particles are also very important. Only within the last few years have there been concerted efforts to collect and study these spectra both experimentally and in theoretical models.

Outside of the operating parameters, there are a number of hardware components of the IEC chamber that can also be varied. The largest amount of study has been devoted to the design of the electrodes which, in the context of the discussion presented here, are the spherical grids. The cathode in particular is one of the most important components of the IEC, and other than the fact that nearly all IEC research utilizes highly transparent spherical grids (typically greater than 85% transparency); there is otherwise quite a variety in the design and construction of cathodes. Among the quantities varied in the design of the cathodes are geometry of the wires, material, number of channels, methods of construction, diameter of the electrodes, and transparency (all are still varied in the 85-95% range). A final area of optimization that has begun to be explored more recently has been the relative diameter of the cathode to that of the anode and the separation distance between the two.

3.1 Thorson Optimization Studies

Thorson conducted deuterium IEC experiments in the early 1990's that varied cathode material, wire spacing, transparency, and size. All of these experiments were intended to optimize the system with regard to neutron production rates. All the cathodes were constructed using wire of varying thicknesses and all were in the latitude/longitude (lat/long) geometry. The lat/long geometry is designed just as the name entails, it is made up of a series of latitudinal and longitudinal wires, sometimes also known as the geodesic or globe geometries. The other geometry typically used is the symmetric geometry, which is made up of a series of triangular holes that are symmetrically placed on all sides of the sphere created by using only rings of wire the same diameter as the sphere. Figure 3.1 shows the difference between the symmetric and the lat/long geometries.

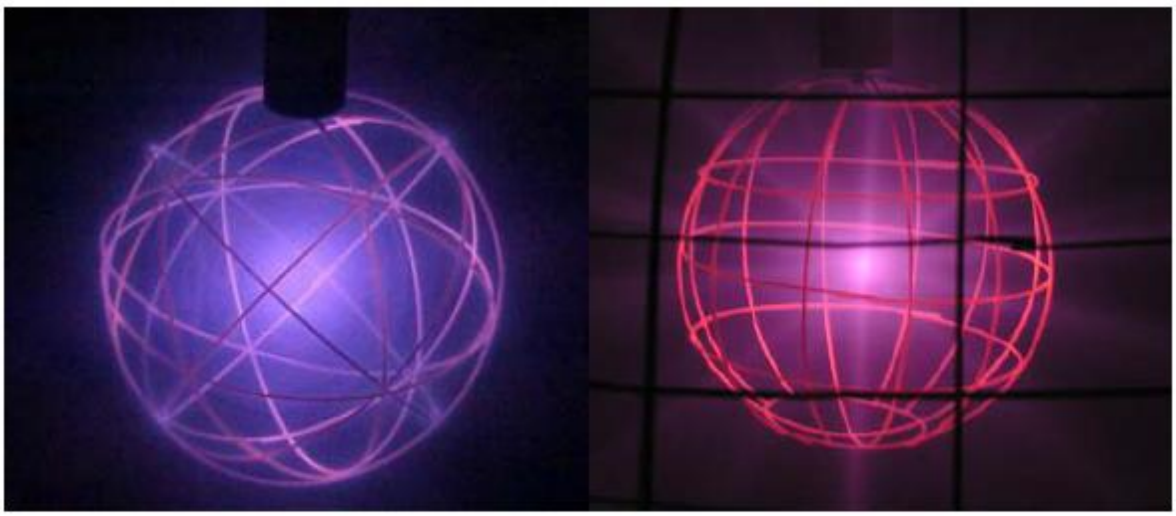

Figure 3.1 : Photos of symmetric (left) and lat/long (right) cathodes in operation [1].

The materials tested by Thorson were tungsten, titanium, and stainless steel. As has already been discussed, the physical presence of the cathode can result in a contribution to the total fusion rate from the embedded fusion occurring in the wires. The material properties of the cathode determine the extent to which the energetic deuterium atoms can become trapped in the first few microns of the cathode surface. These three materials have very different trapping properties at low temperatures, but at high temperatures the properties of all three are much more similar. As a result, when the three different cathodes were operated and brought to temperatures on the order of 2000 K, they showed no significant variation in neutron production rates [2]. However, it should be noted that these were D-D experiments, and deuterium typically has low retention abilities in most materials as opposed to ^{3}He, which was discussed in Section 2.6.

Thorson varied the transparency of the grids by constructing three cathodes with the same number of latitude and longitude wires, but the wires had varying thicknesses. The resulting cathodes had transparencies of 91, 94, and 96 percent. The transparency is defined as the percentage of the surface area of the sphere that is not obstructed by material. It was originally believed that increasing the transparency of the cathode would increase the lifetime of the energetic ions by providing less area with which the ions could collide. All three cathodes tested had a diameter of 10 cm, 45 degree spacing between the wires, and scans were collected for the range of 20 to 40 kV at roughly 2 mTorr of deuterium pressure. The results indicated no appreciable change in neutron rates between the three cathodes and it was concluded that the transparency in the range 91 to 96 percent had no significant effect on neutron production.

The mesh spacing of the grids was compared by constructing two different cathodes with a different number of wires, but also of different wire thicknesses in order to maintain roughly the same transparency of 91 percent. The resulting cathodes had a wire spacing of 22.5 and 45 degrees. The mesh spacing is dictated by the number of wires used to construct the grid and it is a measure of the number of holes between the wires. Slight dips in the potential are believed to occur in these holes between the wires, and it is also theorized that microchannels of counter-flowing ion and electron currents can then focus in the middle of the holes. The original hypothesis was that by increasing the number of holes, focusing of the microchannels could be improved and greater convergence could be achieved in the core, resulting in higher fusion rates.

However, the results of the comparison between the two cathodes indicated a negligible difference in neutron rates between the two cathodes over a range of operating conditions. Thorson concluded that mesh spacing did not have an appreciable impact on neutron rates.

The only cathode parameter that had any noticeable impact on neutron rates throughout the course of these experiments was the size of the cathode. By increasing the size of the cathode, it was believed that the path length of the fast ions could be increased by giving them a longer distance to travel inside the cathode at their full energy, thereby increasing the probability of fusion with background neutrals. Three cathodes were constructed with radii of 2.5, 5, and 10 cm. All three cathodes had a transparency of roughly 91 percent and they were all operated at 20 mA, 1.9 mTorr of background deuterium pressure, and over a voltage range of 20 to 45 kV. The results indicated only a very slight increase in neutron rates when the radius was increased from 2.5 to 5 cm. However, an increase of up to 50 percent in neutron rates was seen when the radius was increased from 5 to 10 cm. This indicated a clear dependence of the neutron rates on the size of the cathode.

3.2 Demora Cathode Optimization Studies

Slightly before IEC research was initiated at the University of Wisconsin – Madison, another research group had begun similar studies at the University of Illinois at Urbana-Champaign (UIUC). One such study conducted by Demora, *et al.* [3] at UIUC focused upon the design of the cathode and its effects on the neutron production rates of an IEC device. During the course of these experiments, 8 cathodes were constructed and operated with 2 different sized anodes creating a total of 10 operating configurations. The physical specifications of the cathodes are shown in Table 3.1.

Cathode	Diameter (cm)	Wire Thickness (cm)	Geometric Transparency	Material	Anode Diameter (cm)
A	4.35	0.081	0.87	Stainless Steel	30, 23.5
B	3.0	0.081	0.81	Stainless Steel	30, 23.5
C	5.6	0.081	0.9	Stainless Steel	30
D	3.1	0.051	0.89	Stainless Steel	30
E	3.9	0.102	0.81	Stainless Steel	23.5
F	4.1	0.102	0.82	Stainless Steel	23.5
G	4.2	0.071	0.88	Tantalum	30
H	3.4	0.025*	0.86	Tantalum	30

Table 3.1 : Physical specifications of cathodes used in Demora experiments [3].

* Grid H made of a 0.025 cm thick tantalum ribbon that was 0.32 cm wide

In Thorson's experiments, the anode was a highly transparent spherical wire grid, similar to the cathode, only larger and at ground potential. In Demora's experiments, the spherical chamber wall acted as the anode, and two different sized chambers were used so that configurations could be created that had a 23.5 or 30 cm diameter anode. All of the cathodes constructed for Demora's experiments were of the symmetric geometry, as opposed to the lat/long geometry that Thorson used. As one may notice from examining the specifications listed in Table 3.1, there was quite a variety of cathode and anode specifications that were tested. This large variety of parameters actually makes it a bit more difficult to identify trends based on any one variable alone. The same geometry and mesh spacing were used for constructing all of the cathodes, so those variables were not considered among these experiments. The parameters varied here were the size, transparency, material, and the separation distance between the anode and cathode. No two cathodes made were of exactly the same size, and nearly none of the cathodes had the same transparency.

The analysis performed on these results involved comparing the neutron production rates of each of these configurations on a single plot for various points over a range of voltage and current levels. An attempt was then made to develop a best-fit equation of the data points that could factor in all of the variable quantities previously mentioned, which could then accurately predict the neutron outputs of each configuration. The final result of this analysis was an equation that was dependent on three variables: anode diameter, cathode diameter, and current. Demora's final equation for the spherical IEC neutron yield correlation was:

$$N \approx 7.4 \cdot 10^5 \cdot \{\text{Current}\} \cdot \{\text{Anode Diameter}\} \cdot \{\text{Material Constant}\} \cdot \exp(-0.141 \cdot \{\text{Cathode Diameter}\}) \text{ [neutrons/second]}$$

In order to perform this analysis, a number of assumptions had to be made regarding the role of each variable in the production of neutrons. Over the course of the decade since these experiments took place though, several of these assumptions have been found to be inaccurate in modeling an IEC device, which calls into question the validity of the above formula. The first assumption that has been demonstrated recently to be false is that all the ions that reach the cathode have the same energy as the cathode potential. The theoretical work of Emmert and Santarius discussed in Section 2.8 and more recent experimental work that will be discussed in a later section indicate that a spectrum of ion energies is created and the majority of fast particles have less than a third of the full energy applied to the cathode. This discovery would greatly influence any scaling laws that are attempting to be applied to cathode voltage.

Another assumption was that the neutron rate simply scales linearly with the diameter of the anode. This is an oversimplified assumption on the importance of volumetric fusion occurring between the grids. More recent experiments, which will be discussed in a later section and which have studied the effect of three different anode sizes on a cathode of constant radius, have indicated that the effect of the anode size on neutron production does not scale in a simple linear fashion. A final assumption was that the transparency of the cathode had no significant impact on the neutron rates as long as it was in the range of 75 to 95 percent transparent. This assumption was based upon the idea that nearly all ions existed only in the microchannels formed in the middle of the holes in the grids. Therefore, as long as the transparency was in the above mentioned range then there was no appreciable likelihood that the fast particles would come close to the grid wires. Thorson also believed that the transparency of the grid had a negligible impact on neutron rates, so this assumption may perhaps be valid. As was pointed out previously, the assumption about the transparency having a negligible effect on neutron rates may be correct, but further testing would most likely still be valuable.

Outside of the experimental data collected on these various cathode and anode combinations, the SIMION code was also run that used the same assumptions mentioned above. SIMION is a software package that is used to calculate the trajectory of charged particles in electric and magnetic fields [4]. The best fit equation created by the code has similar dependencies as the model created based on experimental data. They both showed a dependence primarily on the cathode diameter, and they indicated that decreasing the diameter could increase the neutron rates. Thorson also found that the only parameter of the cathode that had a significant effect on neutron rates was the cathode size, but he found that the opposite trend was true, which was that increasing the cathode diameter resulted in an increase in neutron rates. The neutron yield equation developed by Demora needs to be revisited and updated taking into account the new developments that have occurred that effect some of the assumptions made. However, the data collected is still valuable and can be analyzed again. All of the cathodes constructed had a diameter within the range of 3.0 to 5.6 cm, which is somewhat smaller than the cathodes used by most other IEC research groups. As a result, the neutron production rates of these small cathodes can be studied more in the future to examine the possibility that even if neutron rates decrease as the cathode size is decreased, there may be a range of diameters in the range studied here in which a slight increase in rates can be seen as the diameter decreases beyond a certain critical radius.

3.3 Wehmeyer and Radel Optimization Efforts

Optimizations studies were once again performed at the University of Wisconsin – Madison beginning in 2004 with the work of Wehmeyer [1] and Radel [5]. The purpose of these experiments was to maximize the neutron production of a spherical IEC device for use in active interrogation methods for detecting clandestine materials. Wehmeyer conducted experiments that varied the cathode geometry, material, and size. These were the first experiments that made a direct comparison between the lat/long and symmetric geometries. The difference between the two geometries is primarily the shape of the holes between the wires. As can be seen from the photos of the two geometries in Figure 3.1, the symmetric geometry creates triangular holes while the lat/long creates trapezoidal holes. The potential is believed to drop slightly between the wires causing potential valley structures, so a difference in the shape of the holes in the grid could result in the formation of different potential structures between the grid wires, which would then affect the way in which ion channels form between the wires.

The experiments were conducted with the intention of determining whether the difference in the shape of the potential structures created by the two different shaped holes in the grids was significant enough to create a noticeable difference in neutron production rates. Both cathodes had a radius of 10 cm and were operated over a higher range of voltages (60 to 120 kV) relative to the Thorson experiments, and a current range of 20 and 70 mA, all at around 2 mTorr of deuterium pressure. The result of these experiments indicated that there was no appreciable difference (less than 5% variation) in neutron rates at all points studied in the voltage and current ranges [1]. It should be noted that these experiments were apparently conducted without regard for the number of holes in the cathode or the transparency. Further study could possibly look into characterizing the effect of each of those variables in conjunction with the geometry. However these initial estimates indicate that there is most likely no fundamental difference in operational capabilities of these two types of geometries that could result in an appreciable difference in neutron rates.

The cathode material studies conducted by Wehmeyer tested the difference in neutron production rates of a pure tungsten and a tungsten-rhenium alloy wire cathode. Tungsten was chosen as a material to make cathodes out of due to its very high melting point of nearly 3700 K, and correspondingly its low thermionic emission rate. However, tungsten is also very brittle and the tungsten wire is quite difficult to bend and mold into a spherical grid. Rhenium has a slightly lower melting point than tungsten of around 3450 K, but it is also much more ductile. Tungsten-rhenium alloys are intended to provide the high heat capacity of tungsten with the ductility of rhenium. The wire used to make the grids discussed here are a 75 percent tungsten, 25 percent rhenium mixture.

This materials testing was performed in order to determine whether there would be any appreciable gain in neutron rates by moving from a tungsten-rhenium cathode to a pure tungsten cathode that would warrant the negative consequences of more difficult construction practices necessary with the more brittle pure tungsten wire. Two 10 cm diameter cathodes were constructed using the same geometry, number of holes, and transparency; the only difference was the material. Both cathodes were once again operated in the range of 60 to 120 kV and 20 to 70 mA at 2 mTorr deuterium pressure. The results indicated that there was no appreciable difference (less than 8 percent variation) in neutron production rates throughout the range of voltage and current levels between the two different material cathodes [1].

The next study by Wehmeyer and Radel was another revisiting of the size of the cathode. This time, the experiments tested the difference in neutron production rates between a 10 cm and a 20 cm diameter cathode. Both cathodes were of a lat/long geometry, made of tungsten-rhenium wire, and the experiments were all run using the same 50 cm diameter spherical anode grid and operated at 2 mTorr of deuterium pressure. The results indicated that the 20 cm cathode performed on average 21 percent better with regard to neutron production rate as compared to the 10 cm cathode [1]. At the time, it was believed that the reason for this increase was that by increasing the diameter of the cathode, the energetic ions had less distance to travel in the region between the anode and cathode and more distance to travel at their full energy inside the cathode. This effectively increased the total fast ion path length, which would have increased the probability of beam-background fusion in the cathode.

Referring back to Table 2.1, Cipiti believed that 22 percent of the total D-D fusion rate in the IEC chamber came from the Converged Core source region, which includes the beam-background, and to a much lesser extent the beam-beam, fusion reactions in the core region of the device. Wehmeyer conjectured that by doubling the size of the cathode, the path length of the energetic ions inside the cathode is also doubled. That would then double the number of beam-background fusion events inside the cathode, which would in turn result in nearly another 22 percent increase in neutron rates that was originally predicted by Cipiti. Since the actual experimental increase found by Wehmeyer and Radel was roughly 21 percent, this was accepted as being quite close to the prediction by Cipiti.

At roughly the same time as these experiments, Radel also conducted a series of experiments that examined the importance of the separation distance between the cathode and the anode [5]. He tested two different anode/cathode configurations, which were a 10 cm diameter cathode, 50 cm diameter anode case and a 20 cm diameter cathode, 40 cm diameter anode case. The motivation for these experiments came from the idea that by shortening the distance between the electrodes, the distance that the ions have to travel from the source region to the cathode to reach their full energy would also be shortened. By decreasing the path length the ions have to travel to reach their full energy, the number of opportunities for a beam-background collision in the intergrid region is also reduced. Therefore it was believed that by moving to a shorter distance between the grids, the number of charge-exchange reactions that serve to diminish the ion energy spectrum could be decreased and there would be more high energy fast particles reaching the inner-cathode region.

The experiments were conducted in 2.5 mTorr of deuterium pressure, 30 mA of ion current, and over a range of 30 to 130 kV of cathode voltage. The results indicated that the 20 cm diameter cathode/40 cm diameter anode configuration produced nearly double the neutron rates of the 10 cm diameter cathode/50 cm anode diameter configuration over the entire range of voltages. It was actually with the 20 cm diameter cathode/40 cm diameter anode configuration that the highest steady-state neutron record to date of 2.2×10^8 n/s was achieved at 165 kV, 68 mA, and 3.1 mTorr of deuterium pressure [5]. These experiments served to prove that the separation distance between the electrodes had a definite impact on neutron production rate. Further experiments would still be needed to better understand this relationship, such as varying the size of one electrode while holding the other one constant, and then varying the size of the electrodes but maintaining the same separation distance to attempt to determine both the effect of electrode size and absolute separation distance on neutron production rates.

The final study on optimization conducted by Radel working with Rusch [6] did not actually involve varying any system parameter, but instead entailed adding a new element to the IEC device, which was the use of titanium coating of the internal surfaces of the IEC device. Titanium is able to capture and retain hydrogen species in its matrix at low temperatures and therefore acts to increase the embedded fusion in the surfaces it coats by loading it with deuterium particles that can then fuse with incoming fast particles. The chamber wall, in particular, is constantly bombarded by fast neutral atoms and molecules, created by charge exchange and disassociation reactions, which are not driven towards the center of the chamber by electrostatic forces so they travel out of the chamber in all directions. For the purpose of these experiments, a minimum of 0.3 μm of titanium was deposited on all surfaces of the chamber including the walls, anode, and cathode. Deuterium gas was introduced during the titanium deposition in order to saturate the titanium matrix with deuterium atoms.

After the titanium coating was complete, the IEC chamber was operated at 2.5 mTorr of deuterium pressure, 30 mA of ion current, and over a range of 30 to 100 kV of cathode potential. The results were a 35 to 70 percent increase in neutron production rates over the voltage range studied as compared to the identical system operated before the titanium coating. The titanium had an obvious and immediate effect on neutron production rates due to the increased beam-target embedded fusion reactions on the internal surfaces of the IEC device.

Despite this obvious gain in neutron rates, there were several unforeseen side effects of the titanium coating that had a lasting impact. The most important lesson learned from this experience was that the cathode should not be coated with titanium along with the rest of the chamber. Despite all attempts at uniform deposition of all surfaces, the titanium coating thickness was not even everywhere, resulting in the formation of peaks and valleys in the coating. The titanium also has a tendency to flake off creating additional peaks and minute sharp points over all the surfaces. This is not as severe an issue on the walls or anode since they are at ground potential and the potential gradient is weaker at the anode, but the cathode is at tens to hundreds of kilovolts of potential, which means that any small peaks become prime sites for arcing. The titanium coated cathode was found to be extremely unstable at higher voltages due to frequent high voltage arcs occurring in the system, and was almost inoperable beyond 100 kV. Multiple attempts were made to clean the cathode and remove the titanium, but they were unsuccessful and the cathode was deemed unusable and had to be replaced.

Another side effect is that although titanium coating has become a relatively common technique within the plasma community, and particularly fusion, experiments, the long term effects of titanium coating in a system are still relatively uncertain. The titanium changes the properties of the surfaces of the device and also introduces additional impurities into the vacuum environment, which cannot be perfectly predicted regarding their impact on the operation of the device. Therefore, the titanium coating is an obviously effective tool at gaining immediate increases in neutron production rates, but the application of this tool must be carefully considered and the long term effects must be realized before it can be used reliably.

3.4 Theoretical Work of Emmert & Santarius

The final work to be discussed on the topic of optimization of an IEC device is that of Emmert and Santarius [7,8]. Some of the details of the theoretical and computational work they have done have already been discussed in the previous chapter, and now the focus will be upon some of the specific modeling they have done regarding the parameterization and optimization of various components of a spherical IEC device. The optimization efforts discussed here focus upon the separation distance between the anode and cathode and its effect on neutron production rates. This study was carried out in two ways, first by varying the cathode radius while keeping the anode radius constant, then by varying the anode radius while keeping the cathode radius constant.

For the first model, the anode radius was held constant at 20 cm while the cathode radius was varied between 5 and 19 cm. The model assumed a voltage of 100 kV and a current of 60 mA, and the deuterium pressure was varied from 1 to 4 mTorr [9]. The results indicated that the neutron rates steadily increased as the cathode radius increased, and there was up to around a 50 percent increase in neutron rates between the 5 cm diameter cathode and the 19 cm diameter cathode over the entire pressure range. Another input for the model was the composition of the source region, which in this case was 6 percent D_1^+, 23 percent D_2^+, and 71 percent D_3^+. The resulting ion energy spectra and ion mix at the cathode were also analyzed in the results, creating plots like the one found in Figure 2.9 for cathode radii of 5, 10, and 15 cm. In each of the ion energy spectrum plots, there were distinct peaks at 1/3, 1/2, and 2/3 of the full energy, representing the contribution of each ion species at the cathode after they have been broken up in the intergrid region.

When comparing the 5 and 10 cm radii cases, it was found that the peaks of the 10 cm case were nearly twice as high as the peaks of the 5 cm case, indicating that there were more high energy fast ions reaching the cathode in the 10 cm case. However, there was only a slight increase in the height of the peaks between the 10 and 15 cm radii cases. This indicates that decreasing the separation distance between the grids does seem to result in more high energy ions reaching the cathode, but that the number of fast ions does not scale linearly with the separation distance. The effect seems to taper off as the separation distance becomes very small. The energy spectra of the fast neutrals were also studied at the cathode for the different cathode radii. It was found that varying the cathode radius had a negligible impact on the neutral energy spectra.

In the second case, the cathode radius was held constant at 10 cm while the anode radius was varied between 11 and 50 cm. The same conditions as before were used, except only the 2 mTorr case was examined. In this case, it was found that varying the radius of the anode while keeping cathode radius constant had very little impact on neutron production rates. Only a very slight decrease in neutron rates was seen as the anode radius, and correspondingly the separation distance between the grids, was increased. This indicates that it is not merely the relative difference between the electrodes that makes a difference, but also the absolute size of the cathode. This model predicts that larger cathode size and smaller separation between the electrodes is the ideal combination for maximizing neutron production rates.

Efforts have also been made to utilize these computational models to predict how the applied cathode voltage affects the ion species mix at the cathode. It has been experimentally confirmed that the neutron rates increase as the applied cathode voltage increases, but little attention has thus far been paid to observing how the fast particle energy spectra and the ion species mix at the cathode varies with the voltage. The initial modeling that has been performed indicates that the dominant ion species varies as the voltage is increased, which is demonstrated in Figure 3.2.

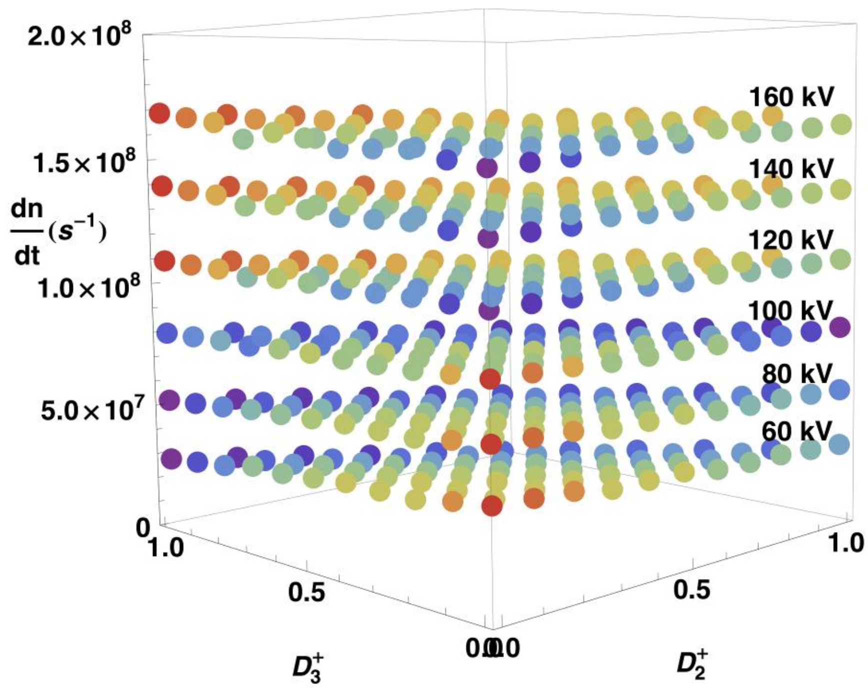

Figure 3.2 : Ion species mix at the cathode over a range of voltages and at 2 mTorr deuterium pressure, 60 mA ion current, cathode radius of 10 cm, anode radius of 20 cm (color scheme: purple is minimum, red is maximum) [9].

In the figure above, the horizontal planar axis is made up of the percentage of the ion species that is either D_2^+ or D_3^+, which are indicated on the sides of the figure. The total species mix for this model is made up only of D_1^+, D_2^+, or D_3^+, which means that whatever fraction is missing after adding up the D_2^+ and D_3^+ contributions marked on the axes is from the D_1^+ contribution. What the figure indicates is that at around 100 kV, the dominant ion species in the mix switches rather abruptly from D_1^+ to D_3^+ at the cathode. This effect has yet to be confirmed experimentally, but it is possible to measure this ratio with some of the new diagnostic tools available, which will be discussed in a later chapter. Nevertheless, this is a valuable new means of analyzing how the variation of different parameters affects the fusion rate in the IEC device, and as it evolves it can be combined with experimental data to predict optimal configurations and settings for IEC devices.

Chapter 3 References

1 Wehmeyer, A. L. (2005). The detection of explosives using an inertial electrostatic confinement D-D fusion device. (Masters dissertation, University of Wisconsin – Madison)

2 Thorson, T. A. (1996). Ion flow and fusion reactivity characterization of a spherically convergent ion focus. (PhD dissertation, University of Wisconsin – Madison)

3 Demora, J. M. (1999). Cathode grid optimization studies for the spherical inertial electrostatic confinement device. (Masters dissertation, University of Illinois at Urbana-Champaign)

4 Collected from internet, March 21, 2009: http://simion.com/

5 Radel, R. F. (2007). Detection of highly enriched uranium and tungsten surface damage studies using a pulsed inertial electrostatic confinement fusion device. (PhD dissertation, University of Wisconsin – Madison)

6 Rusch, P. E., Radel, R. F., Kulcinski, G. L. (May 2007). Vapor Deposition in IEC to Increase Neutron Production. Powerpoint Presentation, Proceedings of 9th US-Japan IEC Conference, Argonne National Laboratory, Argonne, IL

7 Emmert, G. A., Santarius, J. F. (2009). Atomic and molecular effects on spherically convergent ion flow I: single atomic species. In preparation

8 Emmert, G. A., Santarius, J. F. (2009). Atomic and molecular effects on spherically convergent ion flow II: multiple molecular species. In preparation

9 Santarius, J. F., Emmert, G. A. (2008). Parametric exploration of moderate-pressure IEC device operation. Powerpoint Presentation, Proceedings of 10th US-Japan IEC Conference, Kyoto, Japan

4 Previous Research on Detection of Explosives

Improvised explosive devices (IEDs) have been one of the largest threats to domestic and international security over the past few decades. A large variety of IEDs have been developed, many of which require relatively little expertise to construct and utilize components that can be obtained on the open market. This makes it very difficult to determine where IEDs are being manufactured, which makes it even more difficult to thwart their use before they leave for their destination. The IEDs must therefore be identified while in transit, or at their destination before they have been detonated. Attempts are made to accomplish this by setting up explosive screening stations in high traffic locations such as airports, train stations, shipping ports, and other high profile buildings or points of infrastructure. In order to serve this purpose, a variety of explosive screening methods and technologies have been developed to counter the IED threat.

4.1 Methods of Explosive Detection

The goals of any system for detecting clandestine material are a high level of reliability, minimal time necessary for interrogation, and as little disturbance to the object being scanned as possible. In the case of scanning for explosive material, the issue of non-destructive evaluation (NDE) is particularly important as there is always the risk of inadvertently detonating the device during a search. There are two categories of explosives detection known as bulk and trace detection, both of which are capable of scanning the contents of a sealed object without having to physically disturb the object. Bulk detection involves either indirect detection of explosive devices through imaging of key components such as detonators or explosive charges, or direct detection of the chemical or dielectric properties of the explosive material itself. Trace detection involves the detection of characteristic vapors or particles emitted from an explosive device. Both of these categories contain a variety of different detection techniques, many of which are displayed in Figure 4.1 and Figure 4.2.

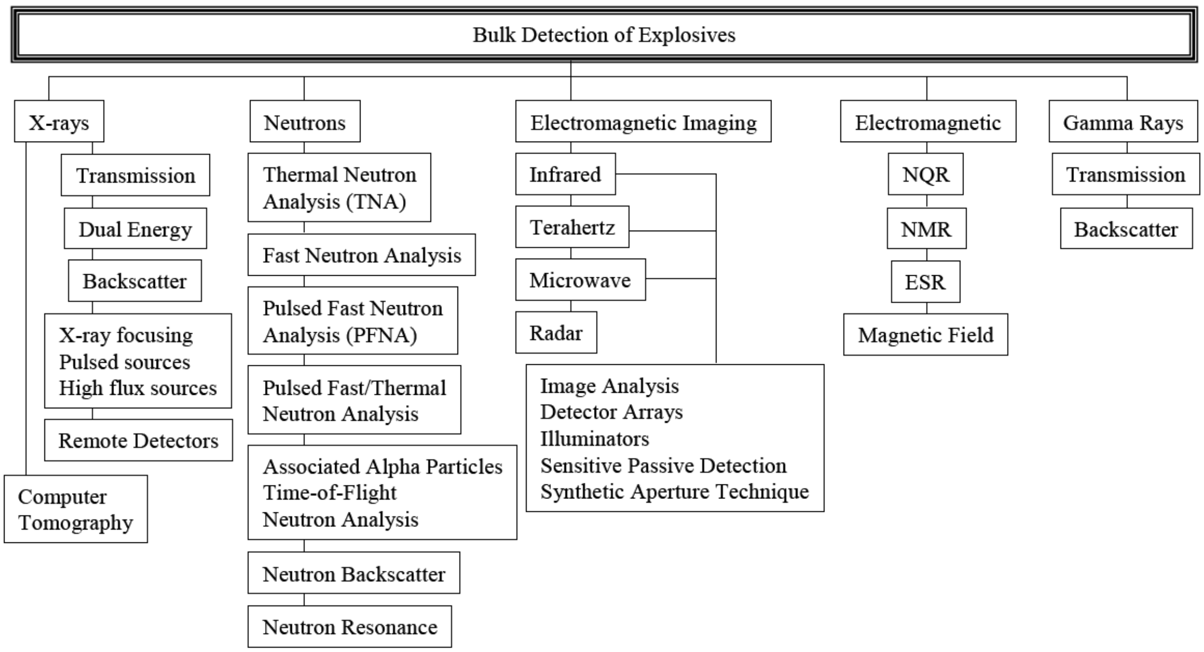

Figure 4.1 : Bulk explosives detection methods [1]. (NQR = Nuclear Quadrupole Resonance; NMR = Nuclear Magnetic Resonance; ESR = Electron Spin Resonance)

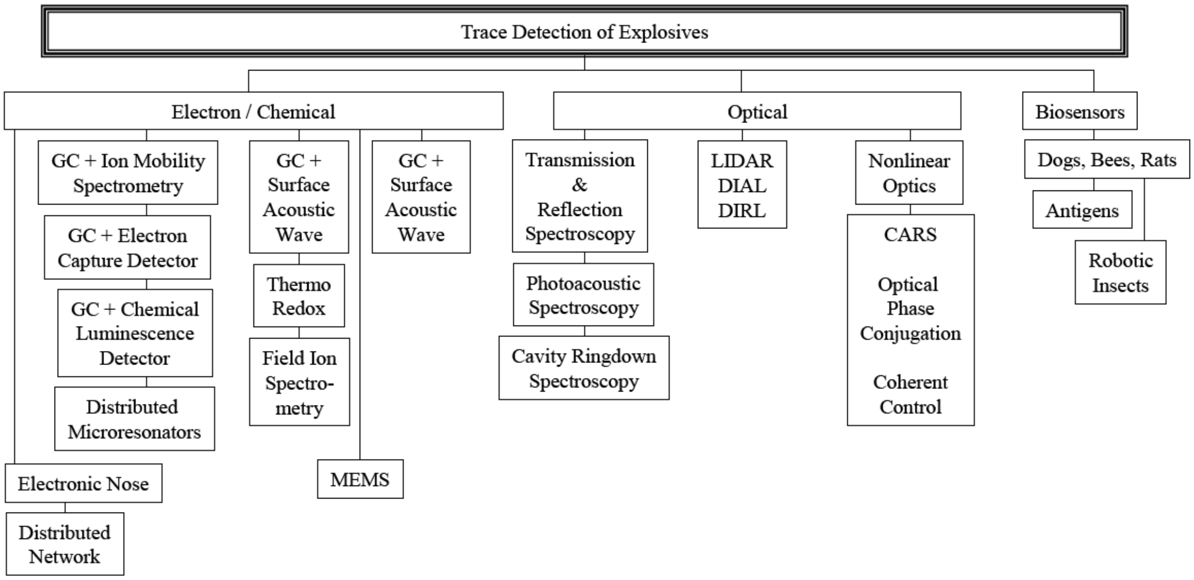

Figure 4.2 : Trace explosive detection methods [1].

4.2 Explosives Detection using Neutrons

For the purposes of this report, only the bulk detection methods using neutrons will be discussed. The differences that are most relevant to this discussion between the various detection methods utilizing neutrons are whether the neutrons used are fast or thermal, and whether the neutron source is pulsed or steady-state.

4.2.1 Fast vs. Thermal Neutron Analysis

Thermal neutrons have an energy range typically on the order of 0.1 to 1 eV, while fast neutrons are in the above 1 MeV energy range. Thermal neutron analysis (TNA) of materials involves the capture of a thermalized neutron by the nucleus of an atom, which excites the nucleus and subsequently causes the emission of a gamma ray. The energy of this emitted gamma ray is determined by the difference in energy between the excited and ground states of the nucleus. Every element has a characteristic gamma ray energy that it emits from which it can be identified [2]. Neutrons for TNA are typically emitted from a source as fast neutrons, and then they are directed through some sort of moderating material such as paraffin or heavy water (anything with a high H or D concentration) so that the neutrons can scatter off the atoms in the moderator and be slowed to thermal energies.

Fast neutron analysis (FNA) involves using the fast neutrons directly from the source without thermalizing. The fast neutrons bombard the sample being interrogated and inelastically collide with the atomic nuclei, which once again causes the emission of a characteristic gamma ray. In order for a gamma ray to be emitted, the colliding neutron must have greater energy than the excitable nuclear levels of the interacting nuclei, which is on the order of several MeV [2].

The decision to use TNA or FNA depends upon what elements are attempting to be detected and the energy of the neutrons emitted from the source. As for the elements to be detected, Table 4.1 lists some of the most common explosive materials and their chemical compositions.

Explosives Based on Nitrogen	Formula	wt% C	wt% H	wt% N	wt% O	sum N+O
Ammonium Nitrate (AN)	$H_4N_2O_3$	0	5.04	35.01	59.97	94.98
Ammonium Picrate (Expl D)	$C_6H_6N_4O_7$	29.28	2.46	22.76	45.5	68.26
Cyclonite (RDX)	$C_3H_6N_6O_6$	16.22	2.72	37.84	43.22	81.06
Ethylenediamine Dinitrate	$C_2H_{10}N_4O_6$	12.91	5.42	30.1	51.58	81.68
Guanidine Nitrate	$CH_6N_4O_3$	9.84	4.95	45.89	39.32	85.21
Hexamethylenetriperoxide Diamine	$C_6H_{12}N_2O_6$	34.62	5.81	13.46	46.11	59.57
Hexanitrohexaazaisowurtzitane	$C_6H_6N_{12}O_{12}$	16.45	1.38	38.36	43.82	82.18
Hydrazine nitrate	$H_5N_3O_3$		5.3	44.2	50.09	94.29
Mannitol hexanitrate	$C_6H_8N_6O_{18}$	15.94	1.78	18.59	63.69	82.28
Monomethylamine Nitrate	$CH_4N_2O_3$	13.05	4.38	30.43	52.14	82.57
Nitrocellulose	$C_6H_7N_3O_{11}$	24.24	2.37	14.14	59.23	73.37
Nitroglycerine (NG)	$C_3H_5N_3O_9$	15.87	2.22	18.5	63.41	81.91
Nitrotriazolone (NTO)	$C_2H_2N_4O_3$	18.47	1.55	43.08	36.9	79.98
Octogen (HMX)	$C_4H_8N_8O_8$	16.22	2.72	37.84	43.22	81.06
Pentaerythritol Tetranitrate (PETN)	$C_5H_8N_4O_{12}$	19	2.55	17.72	60.73	78.45
Picric Acid	$C_6H_3N_3O_7$	31.46	1.32	18.34	48.88	67.22
Tetrazene	$C_2H_8N_{10}O$	12.77	4.29	74.44	8.5	82.94
Tetryl	$C_7H_5N_5O_8$	29.28	1.76	24.39	44.58	68.97
Trinitrobenzene (TNB)	$C_6H_3N_3O_6$	33.82	1.42	19.72	45.05	64.77
Trinitrotolouene (TNT)	$C_7H_5N_3O_6$	37.02	2.22	18.5	42.26	60.76
Triaminoguanidine Nitrate (TAGN)	$CH_9N_7O_3$	7.19	5.43	58.67	28.72	87.39
Triaminotrinitrobenzene (TATB)	$C_6H_6N_6O_6$	27.92	2.34	32.55	37.19	69.74
1,3,3-Trinitroazetidine (TNAZ)	$C_3H_4N_4O_6$	18.76	2.1	29.17	49.98	79.15
Trinitrochlorobenzene	$C_6H_2ClN_3O_6$	29.11	0.81	16.97	38.78	55.75
Trinitropyridine	$C_5H_2N_4O_6$	28.05	0.94	26.17	44.84	71.01
Urea Nitrate	$CH_5N_3O_4$	9.76	4.09	34.14	52	86.14
Average (%)		**20.29**	**2.98**	**30.81**	**46.14**	**76.95**
Standard Deviation		**$\pm$8.15**	**$\pm$1.38**	**$\pm$11.01**	**$\pm$8.01**	**$\pm$8.47**

Table 4.1 : Common explosive material and their chemical compositions [1].

As can be seen from the list above, the most important elements for explosives detection are carbon, hydrogen, nitrogen, and oxygen.

The most common sources of neutrons for detection are naturally radioactive isotopes or a D-D or D-T fusion source. Typically Cf-252 is the radioactive isotope of choice because it is reasonably long-lived (half life of 2.645 years) and produces a reliably steady neutron flux for a small amount of weight (2.314×10^6 n s^{-1} μg^{-1}) [3]. The average emitted neutron energy of Cf-252 is 2.1 MeV and the most probable energy is 0.7 MeV. One example of a neutron analysis method that uses Cf-252 is the Portable Isotropic Neutron Spectroscopy (PINS) device developed at Idaho National Lab [4]. The PINS system is a portable diagnostic device for detecting the contents of unknown armaments and uses 10 µg of Cf-252, which produces approximately 2.3×10^7 n/s and requires between 100 to 1000 seconds to obtain an identifiable signature.

The D-D fusion reaction creates, as one of its products, a 2.45 MeV neutron. The D-T fusion reaction produces a 14.1 MeV neutron. The problem with both Cf-252 and D-T fusion is that they involve the use of radioactive isotopes (tritium has a half-life of 4500 days and emits 18.7 keV beta rays), which means that the sources must be shielded at all times, even when not in use. A further danger of using radioactive material as part of the detection setup is that if the explosive device being interrogated is inadvertently detonated, then the radioactive material may also be dispersed turning an explosive device into a radiological hazard. A D-D fusion source will only emit radiation when in use, but at all other times the only source of radiation is from neutron activation of the chamber walls.

Another difference between these sources is related to the energy of the neutrons emitted, which determines the probability of an inelastic scattering event creating a gamma ray when the neutron strikes a nucleus. The cross sections for these inelastic scattering events for carbon and oxygen are shown in Figure 4.3 and Figure 4.4, respectively.

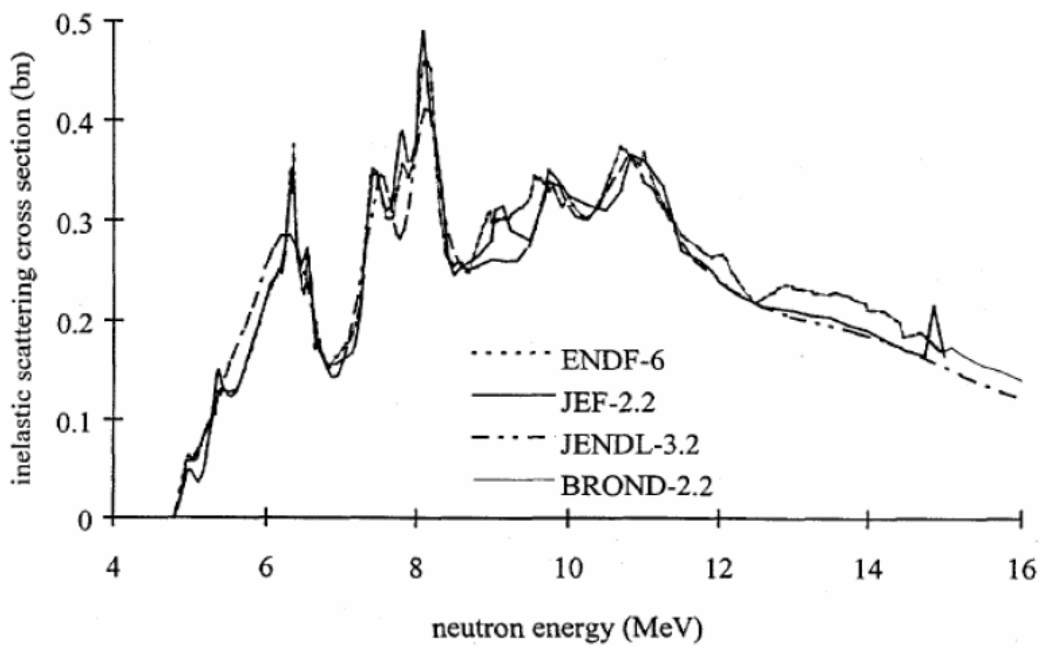

Figure 4.3 : Inelastic scattering cross section to the first excited state of ^{12}C [5].

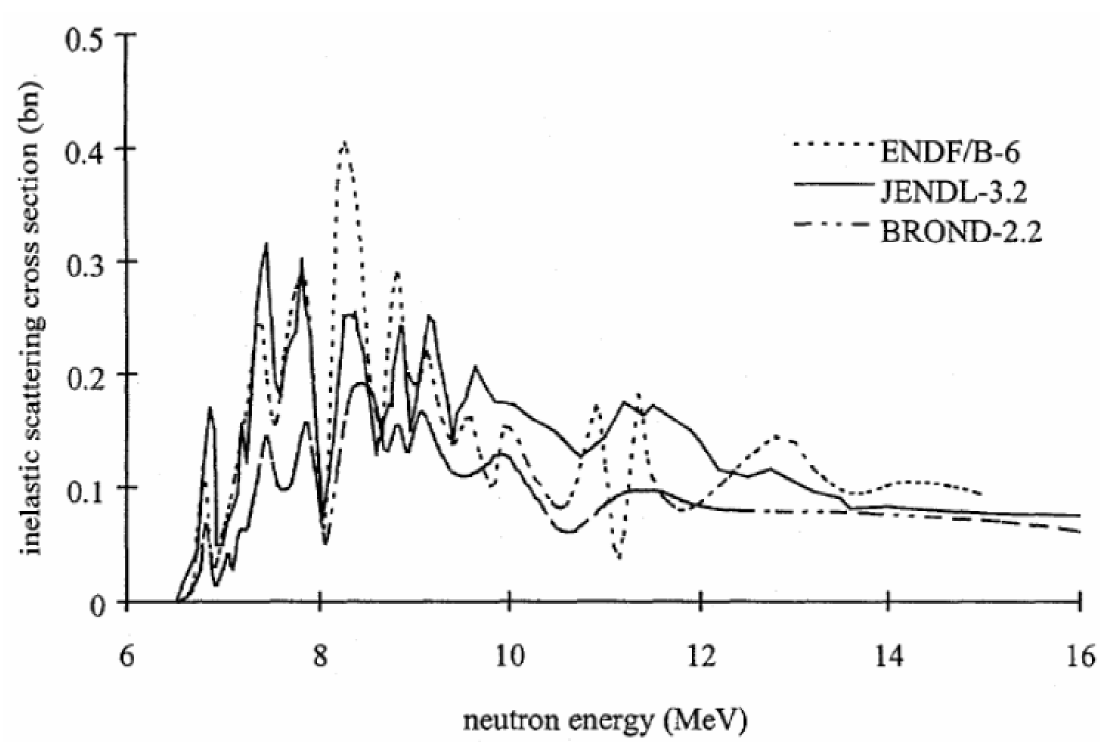

Figure 4.4 : Inelastic scattering cross sections to the 2nd excited state of ^{16}O [5]

The cross section plots indicate that there is no significant probability of an inelastic scattering event creating a gamma ray for neutron energies less than 5 MeV for carbon and 7 MeV for oxygen. This means that of the types of sources previously listed, only the 14.1 MeV neutrons produced by the D-T fusion source are capable of identifying carbon and oxygen using FNA.

The neutrons produced by the Cf-252 and D-D fusion source can both still be used for TNA. The neutron capture cross section plots for C, H, N, and O are shown in Figure 4.5, Figure 4.6, Figure 4.7, and Figure 4.8, respectively. The energy of the 2.45 MeV D-D neutron and the commonly recognized energy of a thermal neutron (0.0253 eV) are both marked on all the plots.

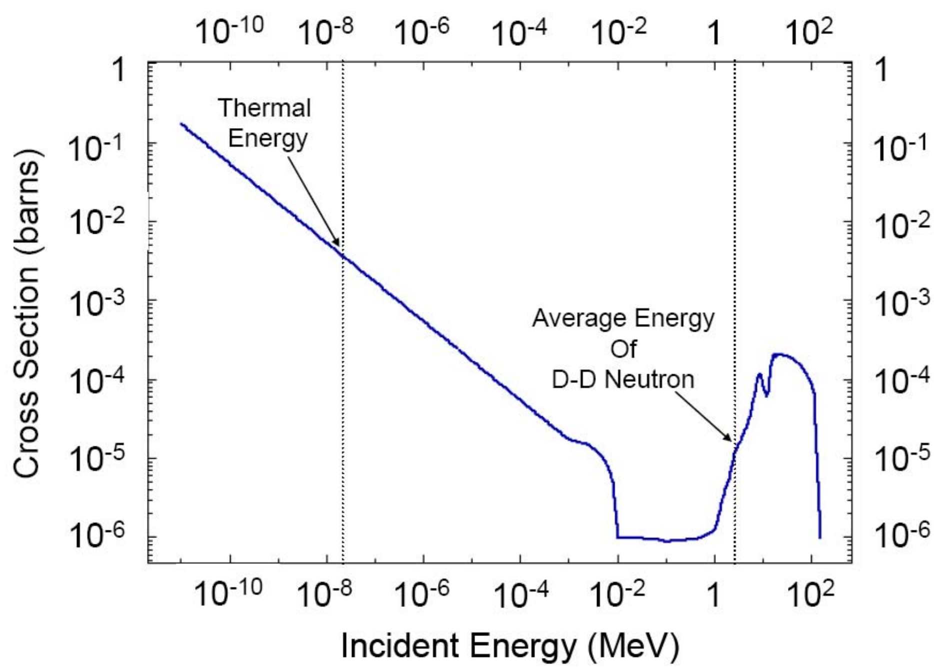

Figure 4.5 : Neutron capture cross section for carbon [6].

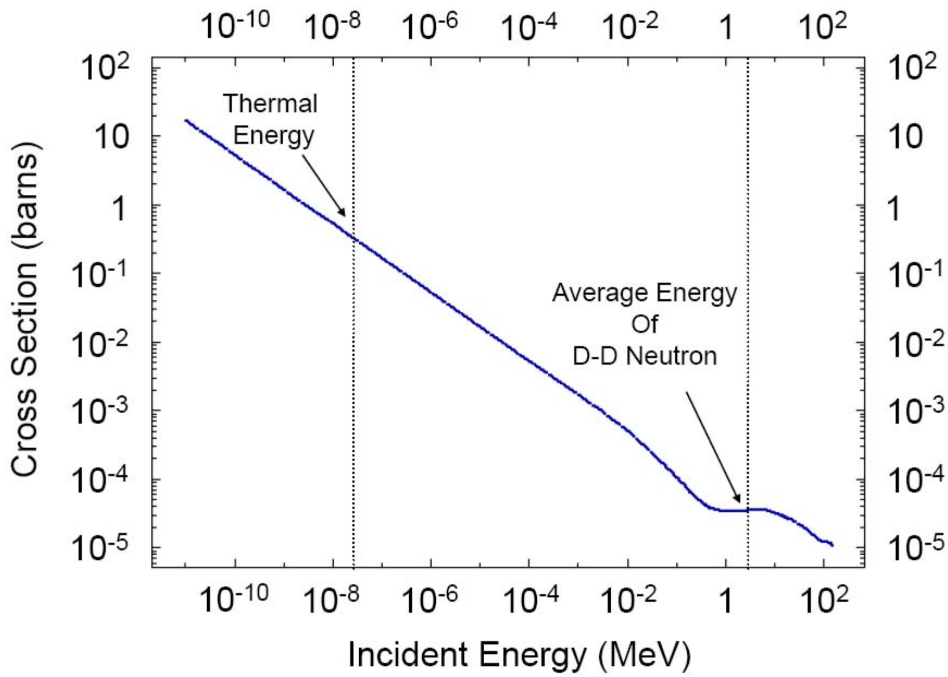

Figure 4.6 : Neutron capture cross section for hydrogen [6].

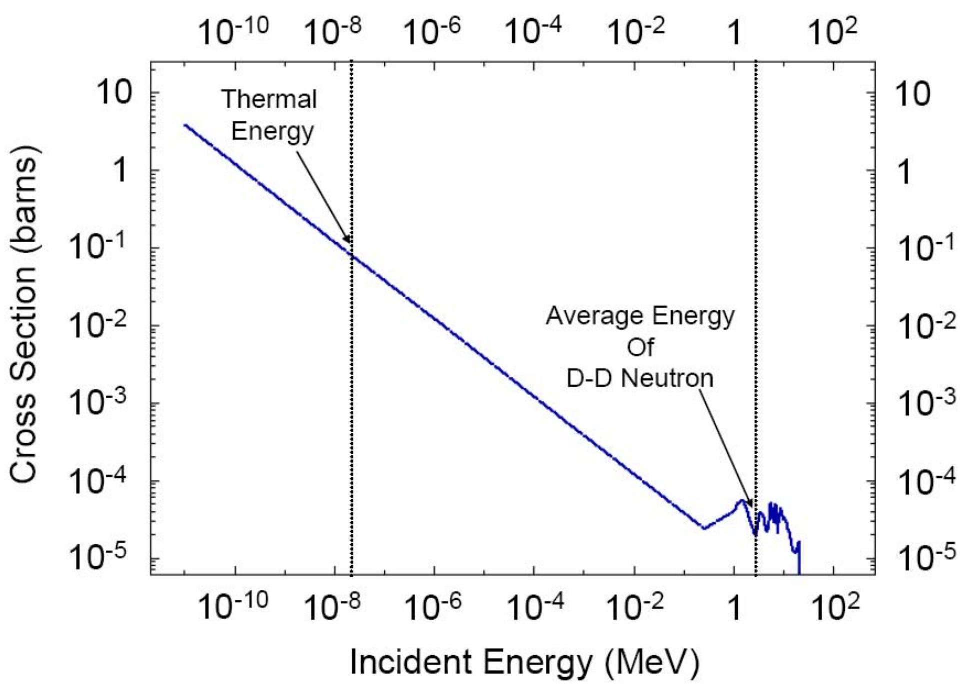

Figure 4.7 : Neutron capture cross sections for nitrogen [6].

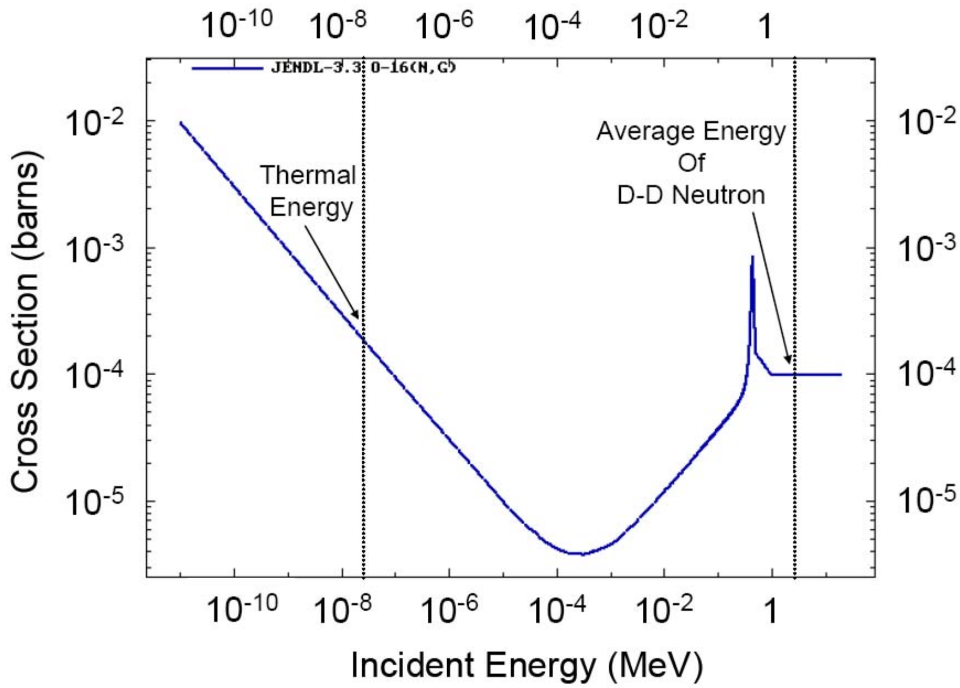

Figure 4.8 : Neutron capture cross sections for oxygen [6].

The cross sections of the four elements at the thermal energy of 0.0253 eV are listed below in Table 4.2.

Element	Cross Section (mb)
Carbon	3.51
Hydrogen	332.6
Nitrogen	79.5
Oxygen	0.19

Table 4.2 : Neutron capture cross sections at incident neutron energy of 0.0253 eV [7].

Carbon and oxygen have a significantly lower neutron capture cross section at thermal energies as compared to nitrogen and hydrogen. As a result of these low cross sections, TNA is not an effective means of detecting carbon and oxygen. Therefore, when scanning for explosive material, nitrogen and hydrogen can both be detected using thermal neutrons created from either a radioactive source, such as Cf-252, or a D-D fusion source. However, in order to detect carbon and oxygen, the 14.1 MeV neutrons of the D-T fusion source are required for FNA.

4.2.2 Pulsed vs. Steady-State Neutron Sources

Steady-state neutron sources produce a constant flux of neutrons, while pulsed neutron sources emit short bursts of neutrons for a preset duration at regular, periodic time intervals. TNA and FNA can both be done steady-state, but there is also the option of using them in a pulsed mode for Pulsed Fast Neutron Analysis (PFNA) or Pulsed Fast/Thermal Neutron Analysis (PFTNA) [1]. The value of pulsing the neutron source is that it allows time of flight measurement of the gamma rays provided enough detectors are used, which can provide a three dimensional map of where the signature is being emitted from in the sample. The quick burst of neutrons from the pulse bombards the sample and immediately produces the characteristic gamma rays. The gamma ray detectors must pick up the signal and record the length of time after the pulse that the signal was detected in order to calculate the distance to the source of the gamma rays based on the time it took the gamma rays to arrive at the detectors. All this must happen before the next pulse of neutrons reaches the sample. Detectors can be positioned around the sample in order to get a three dimensional coordinate of where the gamma rays are being emitted.

PFNA is only used to detect the elements with high inelastic scattering cross sections for fast particles, such as carbon and oxygen [8]. PFTNA was developed in order to also detect the elements that only respond to thermal neutron capture, such as nitrogen and hydrogen. PFTNA uses a neutron source that creates sufficiently fast neutrons to detect the carbon and oxygen signature the same as FNA, but between the pulses the fast neutrons are given sufficient time to scatter around in the sample until they have lost enough energy to be useful for TNA. A PFTNA system was developed at Western Kentucky University known as Pulsed Elemental Analysis (PELAN) that successfully detected the C, H, N, and O signatures in several varieties of high explosives using a pulsed D-T neutron source [9].

4.3 Using an IEC as a Neutron Source for Neutron Activation Analysis

There are a variety of recognized methods for creating neutrons for detecting explosives. As was previously mentioned, the most common means for producing neutrons for this purpose are radioactive isotopes such as Cf-252, or a D-D/D-T fusion source. Radioactive isotopes are typically small and produce a reliable steady-state flux of neutrons. However, the isotope must be shielded when not in use and there is the constant safety and security risk of properly controlling a small, highly portable radioactive source. Fusion sources have the benefit of being able to be turned off when not in use, and in the case of D-D fusion sources, there is no radiological risk when the source is not in operation.

Cf-252 is one of the most commonly used radioisotope for this application and its neutron emission rate is 2.314×10^6 neutrons/(sec*microgram) with a half-life of 2.645 years and a specific activity of 0.536 mCi/microgram. The neutron energy spectrum produces a most probable neutron energy of 0.7 MeV and an average energy of 2.1 MeV [10]. The current price for Cf-252 at the time of the writing of this document is $265/microgram, not including the necessary encapsulation and transportation fees, which depend on the amount ordered and location to be delivered, or the expense of disposing of the source [11]. Estimated cost for a loaned Cf-252 source, which is reclaimed for proper disposal at end of use, in sufficient quantities for explosives detectection is on the order of \$20,000 to \$30,000. The proof of principle experiments conducted thus far for TNA methods using non-IEC neutron sources, such as the PINS system mentioned previously, have all had neutron production rates in the range of approximately $1x10^6$ to $5x10^8$ n/s [4,12]. Current IEC technology is capable of producing steady state D-D neutron production rates of approximately $2x10^8$ n/s, which means that IEC sources can potentially become competitive with other commercial neutron sources [13]. Even before these record IEC neutron production rates were achieved, several different research institutions around the world had begun testing the viability of using an IEC source to detect explosive material. One of the first references to the possibility of using an IEC for the purpose of detecting explosives using either D-D or D-T fusion neutrons was made by Nadler and Miley, *et al.* at the University of Illinois at Urbana-Champaign in 1995 [14]. Several years later, experiments using D-D fusion neutrons had begun at the University of Wisconsin – Madison [15] and at Kyoto University [16] to perform proof-of-principle experiments on the possibility of using an IEC for TNA.

4.3.1 UW-Madison Explosives Detection Experiments

Research was undertaken at the UW-Madison IEC group by Wehmeyer to perform a proof-of-principle experiment to demonstrate that an IEC could be used to detect the nitrogen signature of an explosive material [15]. As was previously mentioned, nitrogen is one of the four most commonly found elements in any explosive material, particularly military grade explosives. One of the characteristic gamma rays produced by the thermal neutron capture of ^{14}N occurs at 10.829 MeV [17], which is uniquely high in energy, placing it well beyond the typical range of background soft x-ray noise. It is also one of the highest energy characteristic gamma rays produced by any element. This means that there is very little chance of confusing signals in the range of the nitrogen gamma ray with those of other elements, which adds to the reliability of the detection method. Finally, nitrogen is not commonly found in most commercial products. Figure 4.9 below shows a list of various materials along with the atomic fractions of the four common explosive elements.

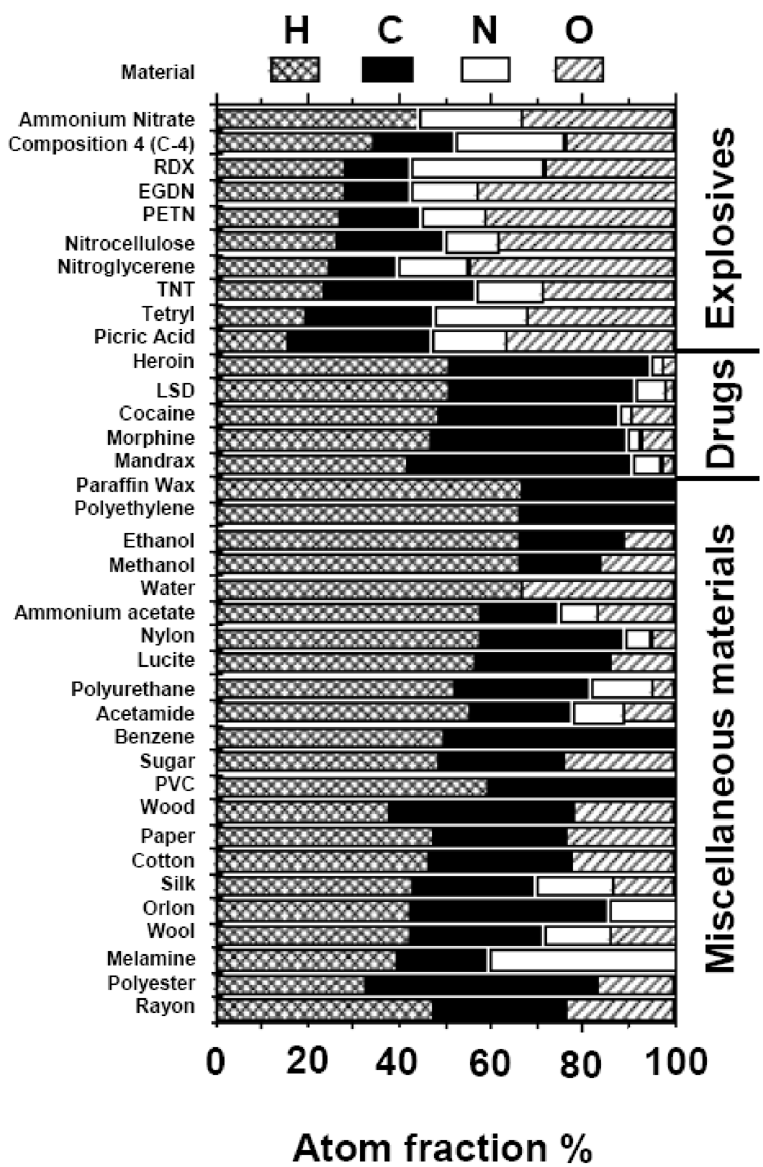

Figure 4.9: Atomic fractions of C, H, N, O for various materials [18].

As can be seen from the figure, very few materials other than explosives have an atomic fraction of nitrogen greater than 10 percent. Carbon and hydrogen both make up a significant percent of the total atomic fraction in many different materials, making it more difficult to conclusively identify an explosive material based on the identification of just those elements. The oxygen content in most commercial materials is also consistently lower than the amounts found in explosive devices, which makes it a useful marker for identifying suspicious material. However, as was mentioned before, detection of oxygen requires the use of a D-T fusion source which requires significantly more radiation shielding both during operation and when not in use. As a result, nitrogen was chosen as the best candidate for performing proof-of-principle explosives detection experiments using an IEC.

The experiments of Wehmeyer were performed using a spherically gridded IEC device known as HOMER (described in further detail in Chapter 6), which was contained in a cylindrical aluminum chamber 65 cm high and 91 cm in diameter that utilized highly transparent grids for both the anode and cathode. The anode was 50 cm in diameter, constructed of stainless steel wire, and kept at ground potential. Experiments were performed on cathode diameters of either 10 or 20 cm, various materials for the wires were used, and the cathode voltage range was 40 to 185 kV of negative potential. Typical base pressure was on the order of 10^{-7} Torr and operating pressure was in the range of 2 to 2.5 mTorr of background deuterium. Ionization of the background deuterium was accomplished using 200 W tungsten light bulb filaments. Ion current was in the range of 30 to 75 mA. At the time of these experiments, this system was capable of producing neutron rates up to 1.8×10^{8} n/s, however most explosive detection experiments were operated in the range of 5×10^{7} to 6.5×10^{7} n/s [15].

Detection of gamma rays was accomplished using two different types of NaI scintillator detectors. The first was a 3” x 3” NaI(T1) Ortec Detector, Model Number 905-4. When initial attempts to detect a discernable nitrogen gamma ray signature failed, the decision was made to switch to a larger detector. An 8” diameter x 4” thick NaI(T1) detector was implemented, which provided a significantly larger volume NaI crystal for detecting the nitrogen signature. However, although the large detector had a higher efficiency of detecting signals, it had poorer energy resolution causing the peaks to lose their definition, so the decision was then made to go back to the 3” x 3” NaI(T1) detector after improvements to the detection configuration were made.

NaI scintillator crystals are commonly used for the purpose of gamma ray detection because they have a reasonably high efficiency and unlike other detectors, such as solid state detectors, they do not require cooling. However, when the NaI crystals are exposed to high fluxes of neutrons, the neutrons cause activation of the ^{128}I atoms in the crystal through thermal neutron capture by the ^{127}I atoms. The unstable ^{128}I has a half-life of 24.99 minutes and produces beta rays with a spectrum of energies up to 2.119 MeV, and a gamma ray spectrum with energies up to 1.434 MeV [19]. These signals are too low to interfere with the nitrogen signature, but create excess low energy noise that can potentially overshadow the hydrogen signature, which occurs at 2.223 MeV [17]. It is therefore important to shield the detectors from thermal neutrons.

However, it is important to note that the iodine in the crystals is only activated by thermal neutrons. Therefore, moderation of the neutrons between the neutron source and detector must be avoided to minimize the number of fast neutrons being thermalized. The neutron capture cross sections for ^{127}I are shown in Figure 4.10 below, and from the chart it is clear that the probability of capture decreases as the neutron energy increases. It is also important to note the resonance region in the 10 to 1000 eV range, which requires a careful monitoring of the level of thermalization experienced by the neutrons in order to avoid this range.

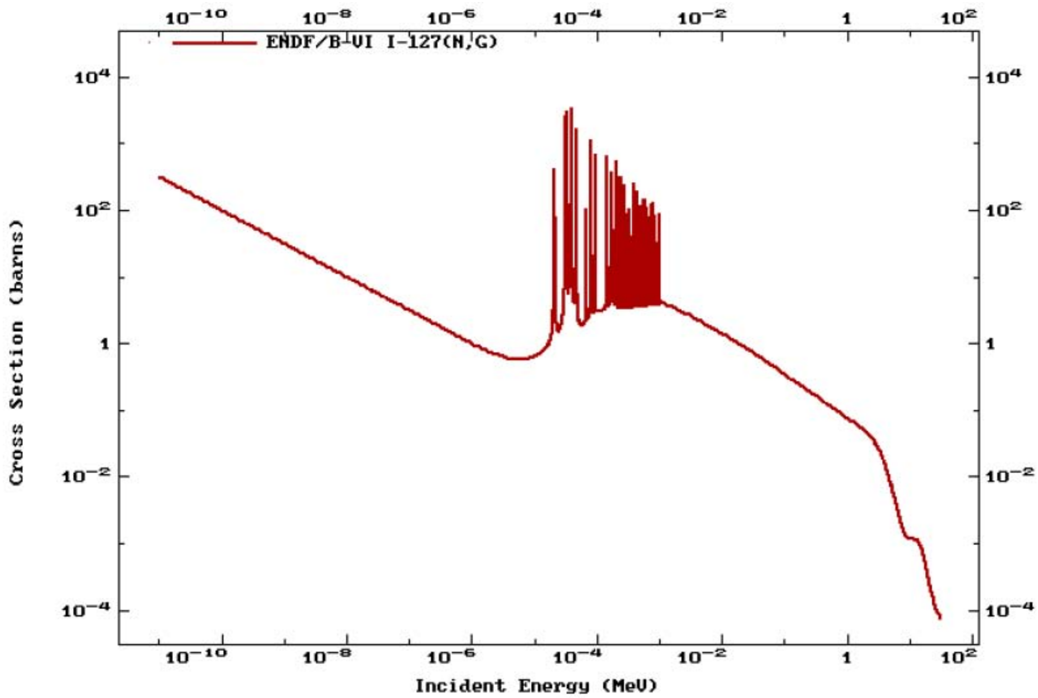

Figure 4.10 : Neutron capture cross sections for ^{127}I [6].

In the experiments conducted by Wehmeyer, the detector was always placed in a direct line with the source and the interrogation sample. The neutrons were intentionally being moderated before they reached the sample because thermal neutrons were required to produce the gamma rays. As a result, the detector was also being bombarded with thermal neutrons since it was always behind the sample. Attempts were made by Wehmeyer to shield the detector from the neutrons using cadmium, since Cd has the property of being able to absorb thermal neutrons. However, the detector still received an appreciable dose of thermal neutrons and the resulting spectra detected by the NaI crystals contained a significant amount of low-level noise, making the hydrogen peak more difficult to discern. A possible improvement on this design would be to remove the detector from the path of neutrons behind the sample and the moderating material so as to minimize the number of thermal neutrons reaching the detector, which was later tested by the author and described in Chapter 6.

The interrogation sample used for these experiments was Composition-4 (C-4) explosives. C-4 is typically composed of approximately 90% RDX ($C_3H_6N_6O_6$) and the other 10% is a binding agent. The resulting chemical composition for the sample used for the experiments was believed to be $C_{1.82}H_{3.54}N_{2.46}O_{2.51}$ [15]. The experimental setup used for the experiments was changed several times, but the basic design can be seen in Figure 4.11 and Figure 4.12.

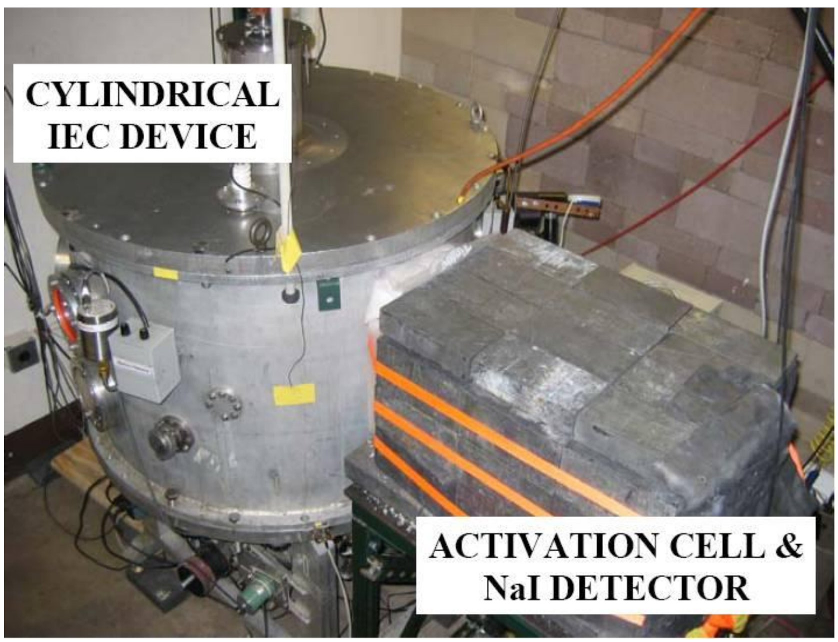

Figure 4.11 : UW IEC chamber and Wehmeyer explosive detection setup [15].

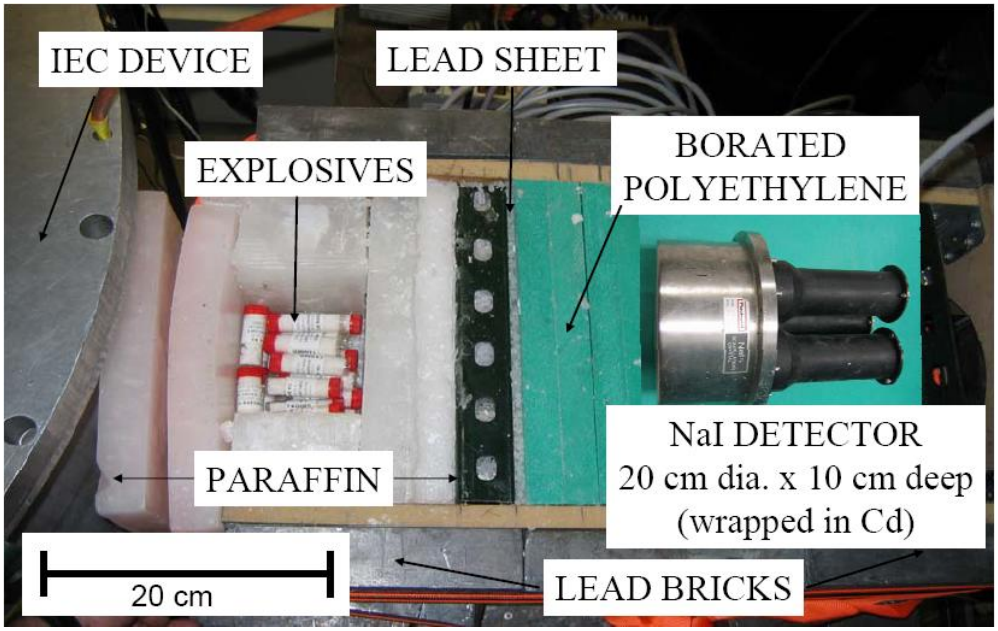

Figure 4.12 : Wehmeyer explosive detection experimental setup (UW(C-4)DET-03) [15].

All experimental setups had every component of the system in a direct line starting from the source of the neutrons, which is symmetric about the center of the cylindrical chamber of the IEC device. The items in this line, beginning from the source and moving outward were the following:

1. Aluminum wall of the chamber (~2.5 cm thick)
2. Moderator (Paraffin Wax) to thermalize the neutrons before reaching the sample
3. Interrogation Sample (C-4)
4. More moderator to scatter neutrons back into sample
5. Lead Sheet (0.32 cm thick) to shield the NaI detector from soft x-rays from the chamber

6. Borated Polyethelene to either absorb or further thermalize the thermal neutrons so that they would be of low enough energy to be absorbed by the cadmium shell around the NaI detector

7. NaI Detector, wrapped in Cd

The entire setup, except for the side facing the chamber, was enclosed in a housing made up of 5 cm thick lead bricks to shield the detector setup from background noise created in the surrounding room. MCNP calculations were performed to determine the optimal moderator thickness and the maximum allowable distance the detector could be from the sample in order to detect the nitrogen signature. Experiments were performed at 130 kV cathode voltage, 60 mA ion current, which produced 6×10^7 n/s. Due to a lack of sufficient cooling and a steadily increasing amount of dead time on the NaI detectors due to iodine activation, the run time was limited to approximately 10 minutes at these conditions. The sample used was 480 grams of C-4, and the detector was given 600 seconds of live count time, which corresponded to approximately 660 seconds real time due to the 10% dead time on the detectors. The experiment was repeated for the same length of time without the C-4 present for comparison. The results are shown in Figure 4.13.

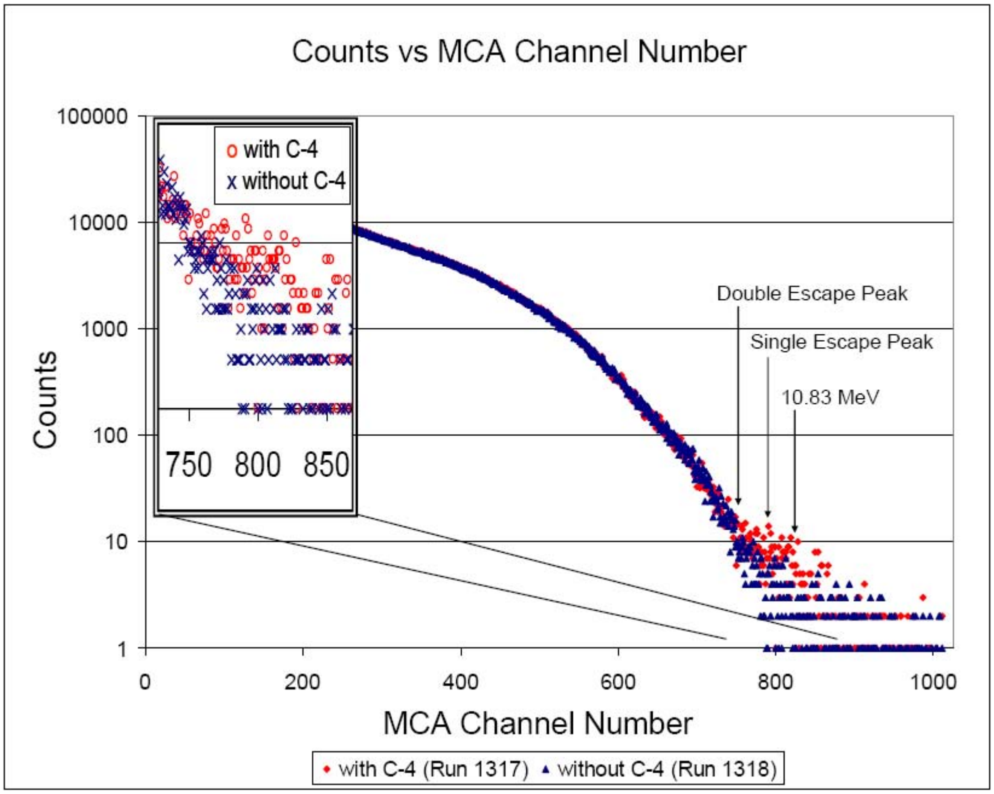

Figure 4.13 : Wehmeyer C-4 explosive detection experimental results ($6x10^7$ n/s; 600 sec count time) [15].

The low energy noise created by soft x-rays emitted from the chamber and from activation of the NaI crystals made the hydrogen peak at 2.223 MeV indiscernible. The lower level of the detector was therefore set above the range of the hydrogen peak in order to minimize dead time. The range in which the nitrogen signature was expected to occur was between channels 815 and 830. Within this range, a total of 33 counts were collected without C-4 present and 89 counts were collected with C-4 present. Wehmeyer also believed he could discern the single and double escape peaks of the 10.83 MeV nitrogen gamma ray, identified in Figure 4.13, which are inherent properties of NaI scintillator crystals caused by pair production and subsequent escape of photons created by electron-positron annihilations.

For these levels, statistics dictate that a minimum of 29 counts above the “without C-4” case be present in order to obtain a greater than 95% certainty that the nitrogen signature was not produced by statistical error, and Wehmeyer detected 56 counts above the “without C-4 case”. This indicates that there was a greater than 95% chance that this proof-of-principle experiment detected the nitrogen signature of C-4, marking the first time ever recorded that an IEC device was successfully used to detect explosive material.

4.3.2 Kyoto University Explosives Detection Work

In 1999, the IAEA initiated a Coordinated Research Program (CRP) on the “Application of Nuclear Techniques to Anti-Personnel Landmine Identification” [20] in an effort to develop technologies that could be used to clean up the abandoned land mines scattered across Afghanistan. The CRP lasted until 2003 and involved research groups from 14 different nations. In 2002, Japan began its own agreements with Afghanistan to offer humanitarian aid in the form of assisting to clean up the landmines utilizing the findings of the IAEA study and the resources available at their academic institutions. As a part of this humanitarian effort, the IEC research group at Kyoto University under Yoshikawa began their efforts to construct a system for detecting landmines using an IEC neutron source [16].

For the purpose of these experiments, a special chamber was designed that had a 25 cm inner diameter and a 5 cm thick water jacket surrounding nearly the entire surface except for a nozzle at the bottom. A schematic of the chamber is shown in Figure 4.14. The chamber wall acts as the anode and is kept at ground potential and a 9.5 cm diameter cathode is used.

Figure 4.14 : IEC chamber used at Kyoto University for detection of landmines [21].

The water jacket serves the dual purpose of cooling the device as well as reflecting the neutrons so that they are directed out of the nozzle at the bottom of the chamber. Experiments indicated that the neutron flux out of the nozzle was almost beam-like with greater than twice the neutron flux density in the beam as compared to the flux emitted by a system without a reflecting jacket. Neutron production rates were also found to decrease as the temperature of the chamber increases, which emphasizes the importance of effective cooling. Figure 4.15 demonstrates the effects of temperature on neutron production rates.

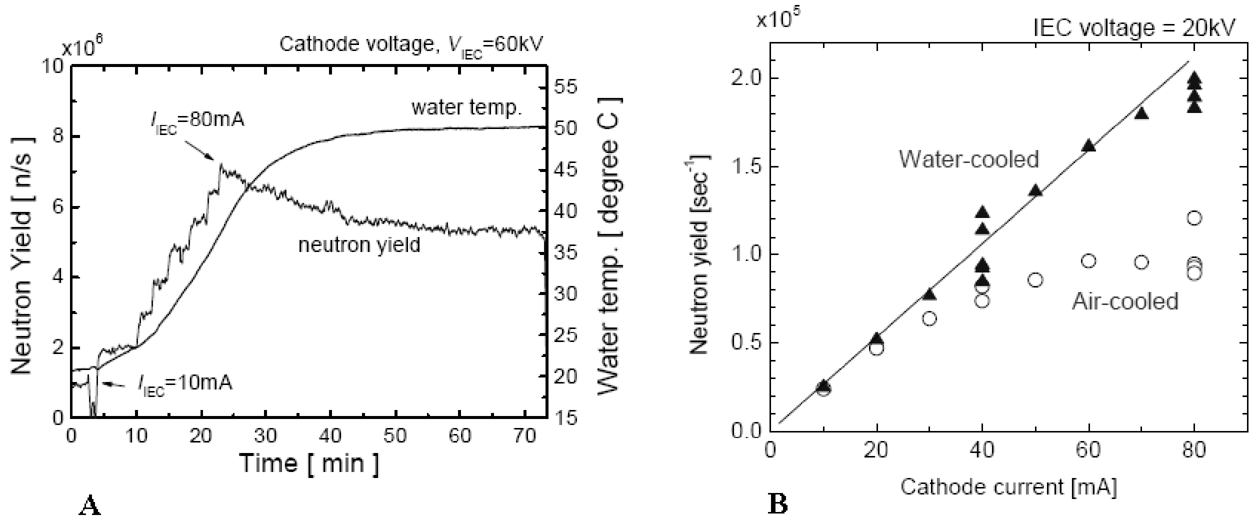

Figure 4.15 : A. (Left) Neutron rate vs. Time demonstrating drop in rates as temperature increases. B. (Right) Neutron rates vs. current for water-cooled as compared to air-cooled systems [21].

The figures above indicate a correlation between a decrease in neutron rates as temperature increases as well as the benefit of using a water-cooled system as compared to an air-cooled system with regard to neutron production.

This system was designed to detect the 10.83 MeV gamma ray produced by the activation of nitrogen in the explosive material. The detector setup developed was known as the Bismuth-Germanium-Oxide-Sodium-Iodide (BGO-NaI) Combined Scintillation (dual) sensor, and its purpose was to allow well-collimated detection of highly energetic gamma rays. This system uses the method of anti-coincidence counting to detect both the energy and directionality of an incoming gamma ray. A schematic of the detector setup along with a diagram of the anti-coincidence method are shown in Figure 4.16.

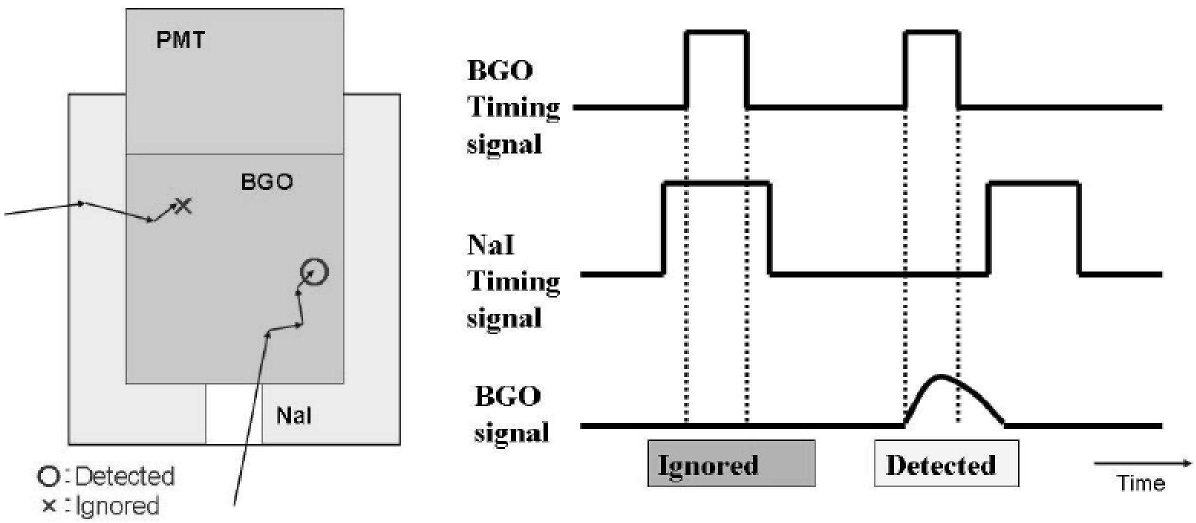

Figure 4.16 : Schematic of BGO-NaI Combined Scintillator (Left) and diagram of anti-coincidence counting method (Right) [21].

The cylindrical BGO scintillator is placed inside an annular-shaped NaI(T1) scintillator. There is a small hole at the bottom of the NaI scintillator through which gamma rays can travel and reach the BGO crystal without passing through the NaI crystal. The anti-coincidence method can then be used to determine whether a signal was detected on both the NaI detector and the BGO detector, or just the BGO detector alone. If the count shows up on both detectors, then it is ignored because it came from some other direction than the one at which the detector is attempting to look. If the count only shows up on the BGO detector, then that means the gamma ray must have come from a direction that sent it through the small hole in the NaI detector, and the count is recorded. This setup allows not only for the energy resolution of the gamma rays from the BGO scintillator, but also ensures that the only counts recorded are being emitted from the direction in which the detector is pointed. A total of three of these BGO-NaI detectors were used in order to both increase the solid angle of detection and attempt to determine an approximate location and distance from the source of the signature by using the directionality of all three detectors. There was also a layer of LiF and Pb used between the neutron source and the detectors in order to minimize activation of the NaI crystals. LiF was chosen because it has very good moderating and neutron absorbing properties.

Several different nitrogen-rich materials were used as the interrogation sample during these experiments including RDX, TNT, and melamine. Since these experiments were intended to determine the effectiveness of using this system on detecting landmines, the moderator used to thermalize the neutrons was soil, and varying moisture contents were tested to simulate different conditions in the field. Results are shown in Figure 4.17 for two cases using 100 g and 300 g of RDX. These experiments were run using a neutron production rate from the source of approximately 1×10^7 n/s for a count time of 1500 seconds. The sample was placed 30 cm from the center of the IEC device and the detectors were positioned 12 cm away from the sample.

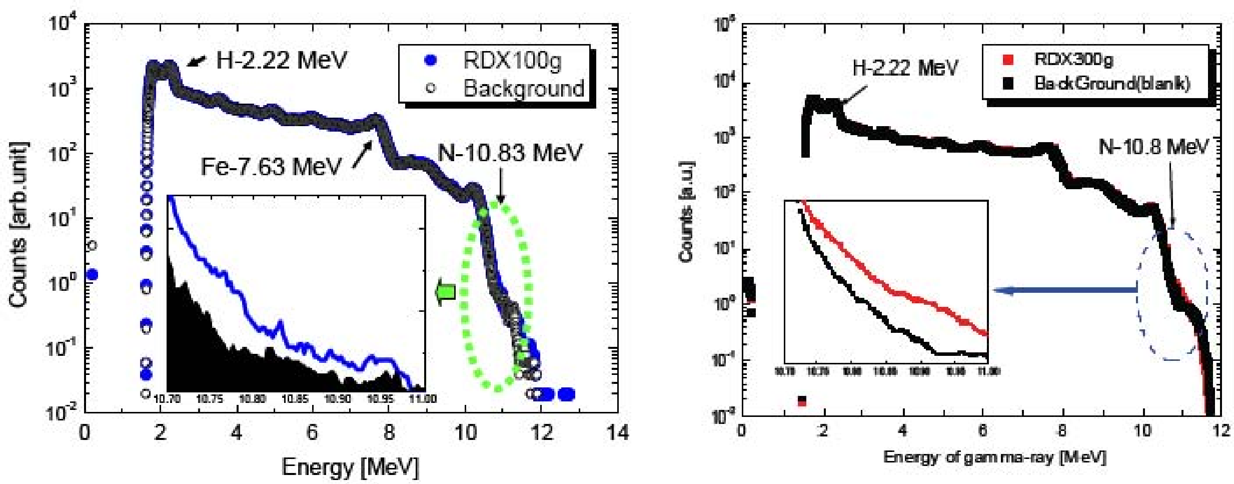

Figure 4.17 : Resulting gamma ray spectra collected by BGO detector of explosive detection setup using 100 g RDX (Left) and 300 g RDX (Right), ~1×10^7 n/s D-D source, 1500 sec count time [22].

The results indicate excess counts in the 10.7 to 11.0 MeV region of the gamma ray spectrum for the case of the sample being present as compared to it not being present. The IEC research group at Kyoto University conducted 231 experimental tests to detect either TNT or RDX, during which they varied the weight of the sample, as well as the depth and moisture content of the soil covering the sample. Out of these 231 tests, the average success rate of detecting the sample was roughly 80 percent. The highest success rates were for the higher mass samples, buried at the lowest depth under the least moisture content soil.

Chapter 4 References

1 National Research Council of the National Academies (2004). *Existing and Potential Standoff Explosion Techniques*. The National Academies Press, Washington, D. C.

2 Gozani, T. (1994). Novel applications of fast neutron interrogation methods. *Nuclear Instruments and Methods in Physics Research A*, 353, 635-640

3 Martin, R. C., Knauer, J. B., Balo, P. A. (2000). Production, distribution, and applications of californium-252 neutron sources. *Applied Radiation and Isotopes*, 53, 785-792

4 Twomey, T. R., Caffrey, A. J., Chichester, D. L., (2007). Nondestructive identification of chemical warfare agents and explosives by neutron-generator driven PGNAA. INL/CON-07-12304

5 Smith, D. L., Micklich, B. J. (2000). Nuclear data needs for non-intrusive inspection. Presented at the International Atomic Energy Agency Advisory Group Meeting on Long Term Needs for Nuclear Data Development, Vienna, Austria, November 28-December 1, 2000, OSTI Identifier 772110, Report Number ANL/TD/CP-103535

6 ENDF/B-VI (1999). Evaluated nuclear data file. National Nuclear Data Center, Brookhaven National Laboratory, United States. Internet: http://www.nndc.bnl.gov

7 Choi, H. D., *et al.* (2006). Database of prompt gamma rays from slow neutron capture for elemental analysis. International Atomic Energy Agency, Vienna, Austria

8 Brown, D. R., Gozani, R., *et al.* (1994). Application of pulsed fast neutrons analysis to cargo inspection. *Nuclear Instruments and Methods in Physics Research, Section A*, 353, 684-688

9 Vourvopoulos, G., Womble, P.C. (2001). Pulsed fast/thermal neutron analysis: a technique for explosives detection. *Talanta*, 54, 459-468

10 Martin, R. C., Knauer, J. B., Balo, P. A. (1999). Production, Distribution, and Applications of Californium-252 Neutron Sources. Presented at IRRMA ’99 4th Topical Meeting on Industrial Radiation and Radioisotope Measurement Applications, Raleigh, NC, Extracted from the Internet at : http://www.orau.org/ptp/PTP%20Library/library/Subject/Neutrons/californium.pdf

11 Ferren, M., Isotopes Business Office, Oak Ridge National Lab, Obtained through official request for price quotation (January 2011)

12 U. S. Congress, Office of Technology Assessment (1991). *Technology Against Terrorism: The Federal Effort*, *OTA-ISC-481*, U.S. Government Printing Office, Washington, D.C.

13 Radel, R. F. (2007). Detection of highly enriched uranium and tungsten surface damage studies using a pulsed inertial electrostatic confinement fusion device. (PhD dissertation, University of Wisconsin – Madison)

14 Anderl, R. A., Hartwell, J. K., Nadler, J. H., Demora, J. M., Stubbers, R. A., Miley, G. H. (1995). Development of an IEC neutron source for NDE. *Fusion Engineering*, 16th IEEE/NPSS Symposium, 2, 1482-1485

15 Wehmeyer, A. L. (2005). The detection of explosives using an inertial electrostatic confinement D-D fusion device. (Masters thesis, University of Wisconsin – Madison)

16 Yoshikawa, K., Masuda, K., *et al.* (2005). Research and development of a compact fusion neutron source for humanitarian landmine detection. Presented at 20th IAEA Fusion Energy Conference, IC/P6-54

17 Molnár, G. L., *et al.* (2004). *Handbook of Prompt Gamma Activation Analysis*. Kluwer Academic Publishers, Dordecht, The Netherlands

18 Buffler, A. (2004). Contraband detection with fast neutrons. *Radiation Physics and Chemistry*, 71, 853-861

19 Retrieved from Internet on April 5, 2009, http://www.nndc.bnl.gov/chart/

20 Csikai, J. (editor), *et al.* (2004). Application of nuclear techniques to anti-personnel landmines identification. *Applied Radiation and Isotopes*, 61, 1

21 Yoshikawa, K., Masuda, K., *et al.* (2007). Research and development of humanitarian landmine detection system by a compact discharge-type fusion neutron source. Proceedings of SPIE 2007, 6553, 65531S

22 Yoshikawa, K., Masuda, K., *et al.* (2007). Research and development of the humanitarian landmine detection system by a compact fusion neutron source. 2007 IEEE Nuclear Science Symposium Conference Record, N24-2

5 Timeline of Research

The research discussed in this report can be divided into five categories relating to the study and operation of a spherically gridded IEC device. Those five categories are:

1. Detection of Explosive Material
2. Optimization and Parameterization of the IEC Device
3. Design and Construction of the 300 kV High Voltage Feedthrough
4. Utilization of Adjustable Arm for Fusion Ion Doppler (FIDO) Diagnostic
5. Radial Profiling and Characterizing of the IEC Device using the Time of Flight (TOF) and FIDO Diagnostics

The first experiments conducted were intended to improve upon the proof-of-principle experiments to detect explosive material originally conducted at UW-Madison by Wehmeyer [1]. Initial experiments resulted in detection of the hydrogen peak at 2.223 MeV and utilization of three NaI detectors instead of only one as in previous experiments. Attempts were made to achieve a detectable nitrogen signature in less than 5 minutes, since all previous detection was done over a period of 10 minutes. It was realized that higher neutron fluxes were necessary to minimize interrogation time. These experiments coincided with a neutron rate optimization study being conducted on the same IEC device by Radel [2] and Rusch [3] to examine the effect of coating the walls and electrodes with titanium in order to improve the embedded fusion rates. These experiments resulted in an immediate increase in neutron rates, but also caused the 20 cm diameter cathode grid exposed to the coating to become unusable due to an unforeseen amount of high voltage arcing during operation as a result of flaking and uneven coating of the titanium on the cathode.

The loss of the original cathode inadvertently brought about the beginning of the optimization and parameterization studies of the IEC device, particularly how the design and configuration of the electrodes affects neutron production rates. The initial cathode constructed had fewer wires than the one that had been decommissioned as a result of the titanium coating. The reason for the new cathode design was to determine the effect of increasing the transparency, as a result of fewer wires being present, on neutron production rates. The experiments indicated that the new cathode had lower fusion rates than the previous cathode even under pre-titanium conditions. Additional wires were added to the cathode, and an immediate increase in neutron rates of 20 to 30 percent, depending on the configuration, was detected during experiments. This obvious effect of the number of cathode grid wires on the neutron rates prompted further investigation of how much the neutron rates could be increased by optimizing the design of the cathode, and eventually resulted in the construction of a four different 20 cm diameter cathodes. These studies produced a cathode, known as the 13/32 cathode (described in further detail in Section 7.3.2), that had higher average neutron rates than a replica of the original cathode that was disabled by titanium, which made it the highest neutron producing cathode ever utilized in the UW-IEC group.

During the course of these cathode studies, the effect of varying the anode diameter while maintaining a constant cathode diameter was also studied. The separation distance between the anode and cathode had an even greater impact on the neutron rates than the design of the cathode. The studies resulted in the implementation of a higher neutron producing configuration than had previously been utilized. To assist in finding an explanation for why separation distance had such a noticeable impact on neutron rates, a new diagnostic tool was utilized capable of measuring the energy spectra of the fast particles in the system. The Fusion Ion Doppler (FIDO) diagnostic, developed by Boris [4], was able to measure the Doppler shift of the fusion products with sufficient accuracy that the center of mass energy of the fusion reactants could be determined. Using this tool, not only could the change in neutron rates between the different anode/cathode configurations be measured, but also the change in the fast particle energy spectra. An advancement was made upon the FIDO diagnostic that was designed and constructed by the author, which is the Adjustable FIDO arm. The original FIDO collimator channel was only capable of studying D-D fusion products, but could not detect the 14.7 MeV protons created from the D-^{3}He reaction. The Adjustable FIDO Arm was created to allow for the collimator channel to be modified while under vacuum in order to go between detecting D-D and D-^{3}He fusion products without having to disrupt the experiment.

FIDO by itself was capable of measuring the energy spectra of the fast particles causing fusion in the solid angle cone of visibility of the detector. Another concept, originally proposed by Piefer and Boris, involved the use of the FIDO setup to allow for both energy resolution and spatial location of fusion reactions occurring in a line through the IEC device [5]. The new tool created from the FIDO components is known as the Time of Flight (TOF) diagnostic. The TOF tool uses high precision timing electronics to detect the arrival of fusion products in two FIDO detector setups, one on each side of the IEC device. The time difference between the arrivals can be used to determine where along the line of sight of the detectors the fusion event occurred, and the original FIDO detectors can still determine the center-of-mass velocity of the fusion reactants. This TOF diagnostic can be used to measure and then calculate the spatial and energy distributions of fusion reactions in an IEC device for various configurations. The TOF Diagnostic was taken from concept to construction and implementation by the author of this work. With these new radial profiles, the understanding of the internal operations of the IEC device can be greatly increased, which can lead to a significant potential for further optimization with regard to maximizing the steady-state neutron production rate.

Another new addition that was made to the IEC experimental capabilities was a 300 kV, 200 mA power supply to replace the original 200 kV, 75 mA power supply. Previous parameterization studies on the IEC device have repeatedly demonstrated that the neutron production rates scale roughly linearly with both ion current and cathode voltage. The new power supply has the capability to allow the IEC devices to reach higher neutron production rates than have ever before been demonstrated. However, the implementation of this supply and subsequent conditioning of the IEC devices to be able to operate at the higher power conditions will require significant upgrades to the system. Upgrades to the IEC device have taken place as well as various improvements to the conditioning methods, quality of the high voltage surfaces, and the design of the high voltage insulating stalk. The most significant advancement required in order to utilize the new power supply and take advantage of its full voltage range is a new high voltage feedthrough. The previous feedthrough design made from stainless steel has demonstrated capabilities up to 175 kV. A new design has been introduced by the author and constructed primarily from quartz and PVC, which should allow operation up to 300 kV. The details of this new feedthrough design can be found in Chapter 8.

Chapter 5 References

1 Wehmeyer, A. L. (2005). The detection of explosives using an inertial electrostatic confinement D-D fusion device. (Masters thesis, University of Wisconsin – Madison)

2 Radel, R. F. (2007). Detection of highly enriched uranium and tungsten surface damage studies using a pulsed inertial electrostatic confinement fusion device. (PhD dissertation, University of Wisconsin – Madison)

3 Rusch, P. E., Radel, R. F., Kulcinksi, G. L. (2007) Vapor deposition in IEC to increase neutron production. Proceedings of 9th US-Japan IEC Conference, Argonne National Lab, IL

4 Boris, D. (2008). Diagnosing the high energy deuterium spectra in IEC devices using Doppler shifted fusion products. Proceedings of 10th US-Japan IEC Conference, Kyoto, Japan

5 Piefer, G. R., Boris, D. R. (2007). Coincidental time of flight diagnostic for spatially resolving fusion reactions. Invention Disclosure Report, Provisional Patent Application

6 Research Progress on Detection of Explosives

6.1 Description of IEC Experimental Facility

The experiments discussed herein on using an IEC device to detect explosive materials began at the UW IEC Research Group in the fall of 2006. All experiments have been conducted on the IEC device known as HOMER. HOMER is a spherically gridded IEC device that is contained in a cylindrical aluminum chamber. The chamber is 65 cm in height and 91 cm in diameter. A schematic of HOMER is shown in Figure 6.1.

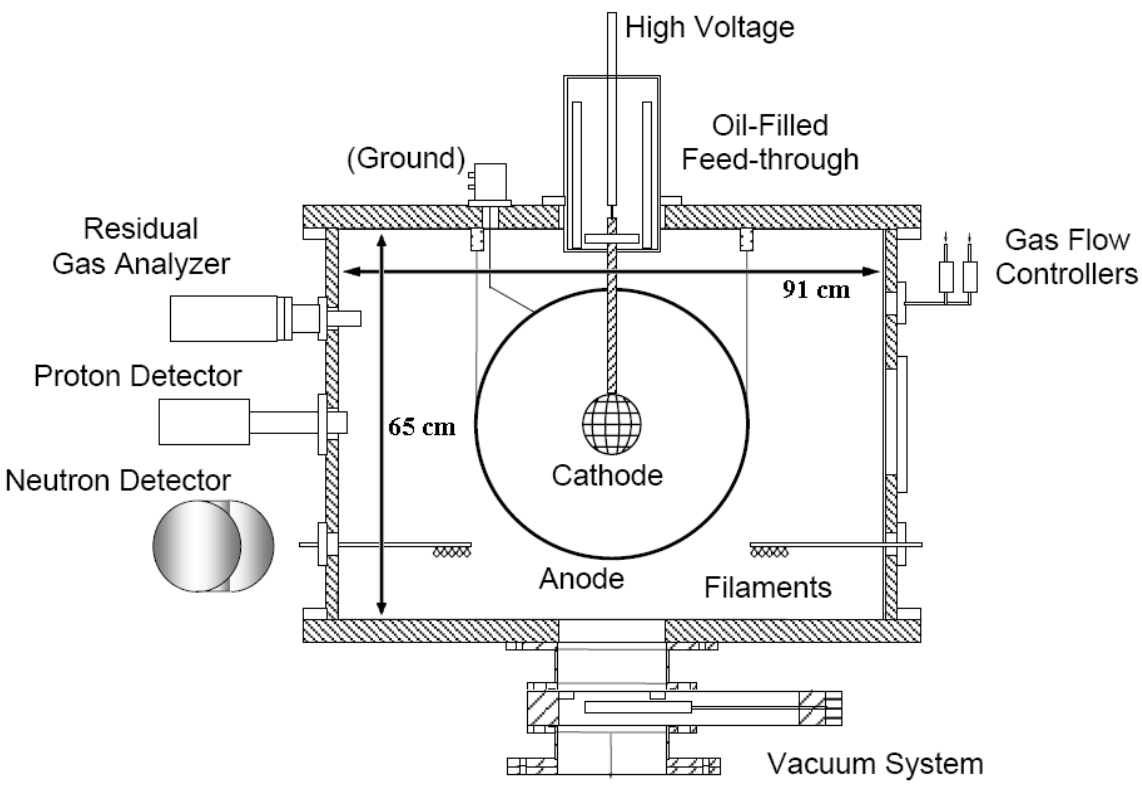

Figure 6.1 : Schematic of IEC device HOMER.

Base pressures in the range of low 10^{-6} to high 10^{-7} Torr are achieved in HOMER using a Leybold Trivac® rotary vane roughing pump to bring the pressure down to roughly $5x10^{-2}$ Torr, and then a 500 L/s Varian turbo pump brings the pressure down the rest of the way. Base pressure measurement is accomplished using an MKS® ion gauge. HOMER is capable of operating with either deuterium, helium-3, or both, but all of the experiments discussed here only involve the use of deuterium gas. Typical background deuterium pressure during operation is in the range of 1 to 4 mTorr, which is regulated using a MKS Mass-Flo® controller.

Ionization of the deuterium gas is provided by a collection of 200 W tungsten light bulb filaments at six sites evenly spaced around the inside of the chamber, outside of the anode. The filaments thermionically emit electrons when heated, which ionize surrounding gas particles. The filament power is controlled using a variac power supply and a negative bias of roughly 100 V is applied to the filaments in order to accelerate the electrons away from the filaments and into the surrounding gas. An additional grounded cylindrical mesh fencing roughly 60 cm in diameter is placed around the anode in order to prevent the negative potential of the cathode (on the order of 100 kV) from affecting the much smaller negative potential on the filaments.

For all experiments before the summer of 2009, the cathode potential was provided by a Hipotronics® Model 8200-75 high voltage power supply rated up to 200 kV and 75 mA. Before reaching the cathode, the high voltage lines pass through a series of resistors whose combined resistance is 250 kΩ, which are contained in a drum of high voltage capacity oil. The resistors limit current transients during high voltage arcs and other surges, which serves the dual purpose of preventing the power supply from shutting down from small arcs as well as protecting the supply from high voltage feedback. However, these resistors also result in a voltage drop between the supply and the cathode that must be taken into account, which is equal to the current multiplied by 250 kΩ. The high voltage cable then is connected to a molybdenum conducting rod in the high voltage feedthrough at the top of the chamber. The molybdenum rod was placed inside an insulating boron-nitride rod in order to prevent shorting to the ground potential on the chamber.

All of the explosives detection experiments were conducted using what is known as the W-7 configuration, which consisted of a 20 cm diameter cathode and a 40 cm diameter anode. The W-7 cathode was made of 75% tungsten/25% rhenium wire and was of the lat/long geometry, discussed previously in Chapter 3. It had 11 latitude and 24 longitude wires, with an effective transparency of 93% and a total of 252 holes between the wires. This configuration was operated at settings up to 170 kV and 70 mA. However, typical operation for explosives detection experiments was on the order of 120 kV and 60 mA, which produced roughly 1.0×10^8 n/s during steady-state operation. At these settings, operation time was determined by the temperature of the chamber, which was limited to 70 degrees Celsius in order to protect the rubber vacuum fittings and glass windows. The chamber was water-cooled by copper tubing wrapped around the outside of the chamber and air-cooled by fans positioned around the chamber. With these cooling elements in place, operation time at 120 kV, 60 mA was typically on the order of 25 to 30 minutes.

Neutron detection is accomplished using a ^{3}He proportional counter, which is housed in a paraffin filled aluminum cylinder. The neutron detector is calibrated using a plutonium-beryllium neutron source obtained from the UW Reactor Lab, which emits neutrons at a constant rate with an average energy of approximately 4.2 MeV. The gamma ray detectors used for these experiments are the same model as the one used by Wehmeyer during the original proof-of-principle experiments, which was a 3” x 3” NaI(T1) Ortec Detector, Model Number 905-4 [1].

A total of three of these detectors have been used as part of the current experimental setup, but they were used independently and their signals were not combined together to give a cumulative reading. These detectors were each equipped with an all-in-one microBase, which contains the photomultiplier tube base, preamplifier, amplifier, high voltage power supply, and multichannel analyzer with a USB interface. The detector and microBase are shown in Figure 6.2.

Figure 6.2 : Ortec NaI detector with microBase [2].

6.2 Improvements on Proof-of-Principle Experiments

The original goal of the explosives detection experiments was to expand upon the proof-of-principle experiments conducted by Wehmeyer and advance the technique. The objectives were to obtain a clearer and more definitive explosive detection signature, shorter interrogation time, and the simultaneous detection of the hydrogen peak for possible use in identifying the explosive based upon the relative amounts of nitrogen and hydrogen in the sample. The first step was a redesign of the detection setup in order to address several issues that had been identified with the previous system.

The original Wehmeyer system had significant low level noise issues due to incomplete shielding of the detectors and excessive activation of iodine in the NaI crystals. This noise was sufficiently high during the original experiments to completely overwhelm the hydrogen peak at 2.223 MeV during high power and neutron flux operation and make it unrecognizable. The issue of activating the iodine was caused by high thermal neutron flux on the NaI crystals, which was due to the fact that the detector was placed in a direct line starting at the IEC source and going through the moderator and the interrogation sample, as was discussed in Section 4.3.1. In order to prevent the neutrons form being thermalized before they reached the crystals, the detectors had to be moved out of the line of neutrons behind the moderator. To resolve this issue, a detector stand was constructed that allowed for the detectors to be placed in a plane that was normal to the line of neutrons streaming from the chamber. The three detectors were oriented in a cross on this plane with the interrogation sample placed directly in the middle, as shown in Figure 6.3. The placement of the detector stand in front of HOMER is shown in Figure 6.4, demonstrating how the NaI detectors have been moved from behind the moderator to the side of it to minimize thermal flux reaching the detectors.

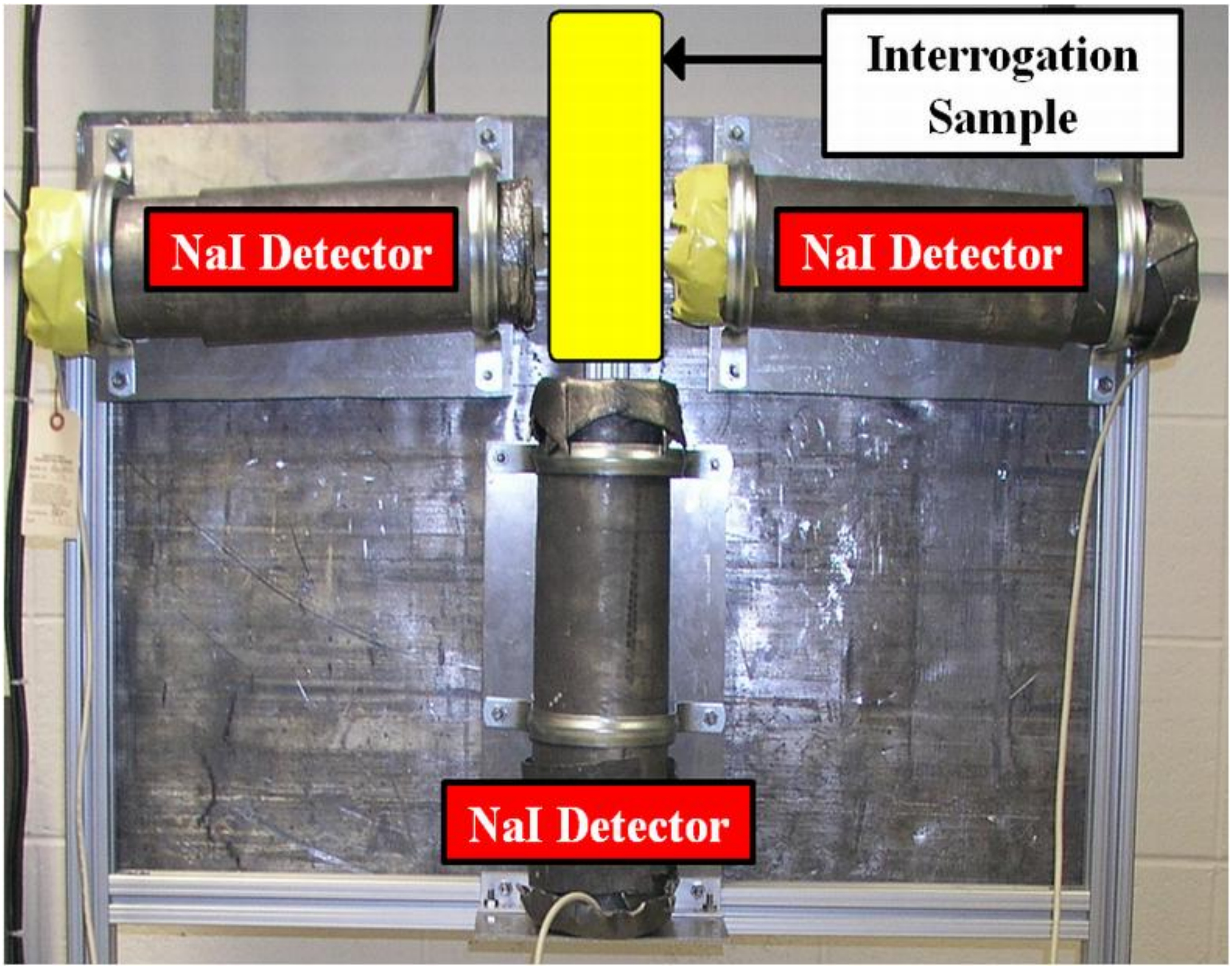

Figure 6.3 Detector stand for explosives detection with three NaI detectors oriented in plane normal to the line of neutrons from the source.

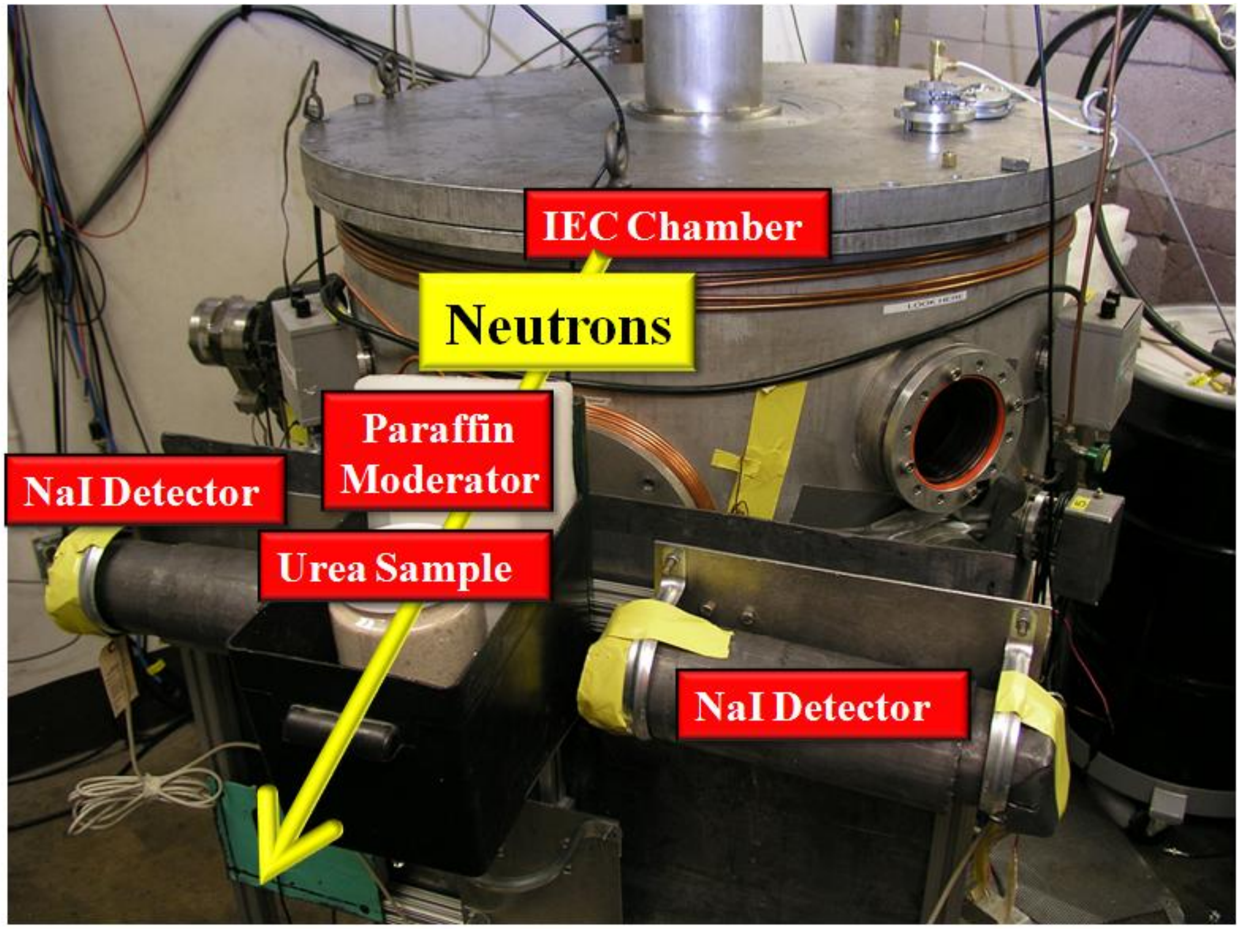

Figure 6.4 : Detector stand in place next to IEC chamber; detectors are out of neutron line with moderator.

The low level x-ray noise is emitted primarily from the chamber wall as the secondary electrons created on the cathode stream through and scattered off the atoms in the wall and caused the emission low energy photons. The intensity of this low-level noise is dependent upon the power and neutron flux of the system, and sufficient noise could be created at levels as low as 10^6 n/s, which occurred at roughly 40 kV, 30 mA, to overshadow the hydrogen peak. During the proof-of-principle experiments, primary shielding from x-rays was provided by a 0.32 cm thick sheet of lead placed between the detector and the chamber. Since the detector was originally in the line of neutrons behind the sample, additional sheets of lead could not be added without losing an increasing amount of the gamma ray signature emitted from the source, so the low level noise simply had to be tolerated. A housing of 5 cm thick lead bricks was also built around all other sides of the detector other than the one facing the chamber to shield from x-rays coming from other directions. These bricks were sufficiently thick to stop any x-rays that could have been emitted by the chamber, but the cracks between the bricks caused gaps in the shielding through which x-rays could still get through.

When the detectors were moved out of line behind the interrogation sample and moderator, the detector face looking at the sample was no longer also facing the chamber wall. This allowed for the body of the detector, and the NaI crystal in particular, to be shielded more than the side facing the sample without losing any additional gamma ray counts emitted from the sample. A 0.32 cm thick cylindrical lead sleeve was placed around the entire body of the detector. An additional 0.32 cm lead jacket was then wrapped around the section of the detector that contained the NaI crystal. Lead caps, also 0.32 cm thick, were placed on both ends of the sleeve, which completely sealed the detector from any direct line of sight. Finally, a 0.32 cm lead sheet was then mounted on the detector stand between the detectors and the IEC chamber. This resulted in minimum of 0.32 cm of lead surrounding all surfaces of the detector, and up to 0.96 cm of lead surrounding the NaI crystal. The shielded detector can be seen in Figure 6.5.

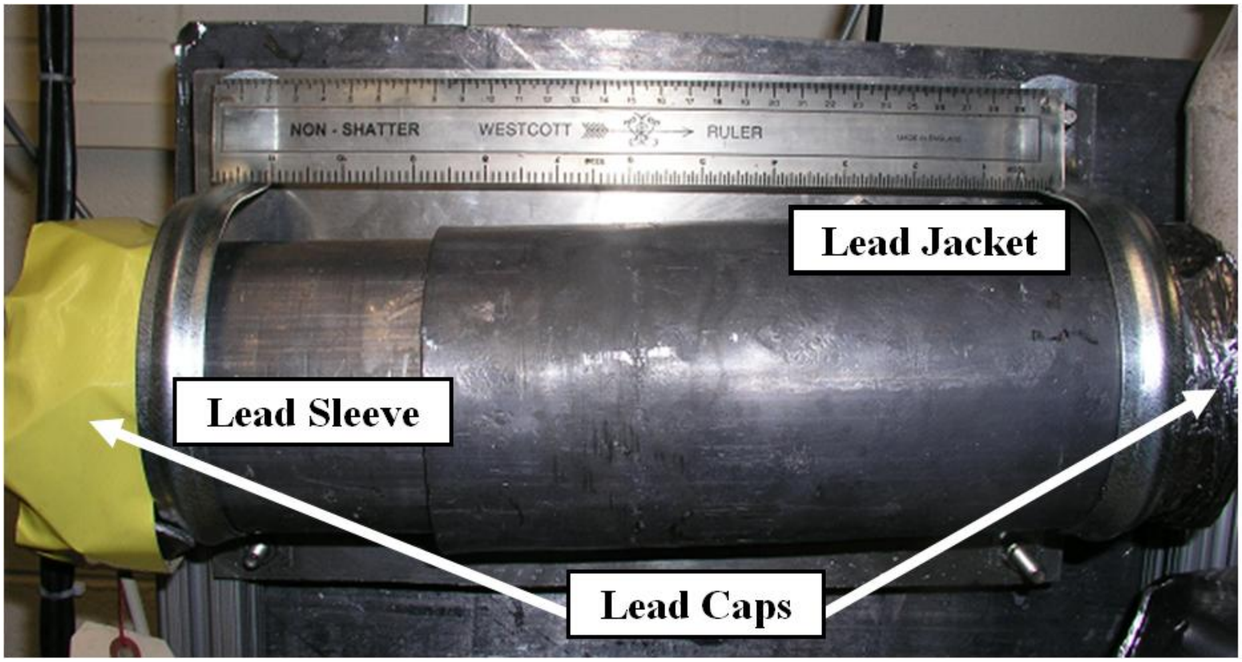

Figure 6.5 : NaI detector shielded in Pb sheets.

Moving the detector faces from the line of neutrons and from behind the moderator, along with the increased amount of shielding around each detector, resulted in a significant decrease in low-level background noise and allowed for the hydrogen peak to be readily visible at 2.223 MeV. The results of the shielding experiments are shown in Figure 6.6. The shielding significantly decreases the level of noise providing much more definition to the peaks throughout the spectrum, but especially in the low level region around the hydrogen gamma ray peak.

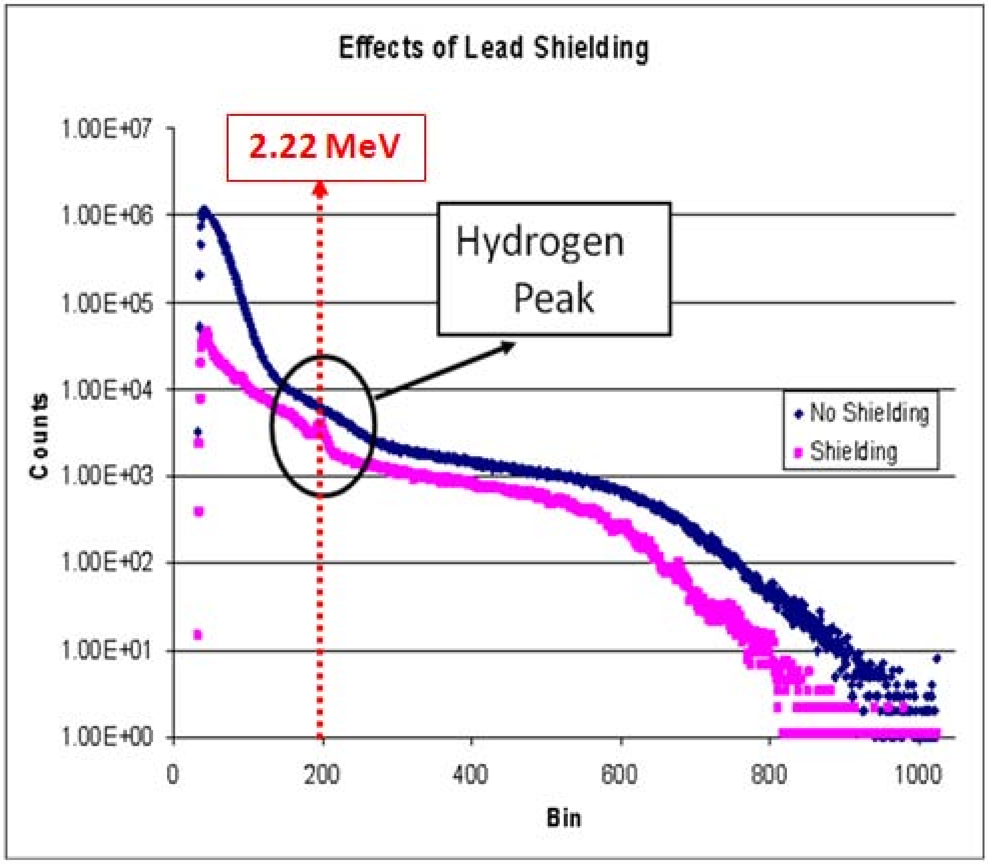

Figure 6.6 : Energy spectra collected from NaI detector placed out of line of neutrons behind moderator with and without shielding. IEC operated at 120 kV cathode potential, 60 mA cathode current, and 2 mTorr of background deuterium pressure.

6.3 Elements of Explosive Detection Setup

For the experiments discussed here, the interrogation sample used has been urea. Urea is an organic compound commonly used as a fertilizer with chemical formula, $(NH_2)_2CO$. It contains roughly 45% nitrogen by mass, giving it one of the highest nitrogen contents of nearly any nitrogeneous fertilizer in common use. Roughly 600 grams of C-4 still remains as the property of the UW IEC Research Group, originally acquired by Wehmeyer for the purpose of the proof-of-principle experiments. However, urea was chosen as the interrogation sample for the initial experiments to avoid any additional safety risks inherent with working with high explosives. The C-4 is kept in a secure facility until such time as the detector setup has been configured properly to be able to detect the urea.

The moderator chosen for these experiments has been paraffin wax ($C_{25}H_{52}$), which is a commonly used moderator because of its high hydrogen content. The best neutron moderating material contains a high atomic fraction of low-Z elements, and hydrogen is the lowest-Z element. Heavy water would theoretically be a better moderator for these experiments because deuterium has the unique property of being able to thermalize neutrons without absorbing them. However, heavy water is considerably more difficult and expensive to obtain than paraffin and has not yet been available at the UW IEC Research Group for experimentation. The moderator serves the purpose of converting the fast neutron flux from the D-D fusion reactions in the IEC into a thermal neutron flux for the purpose of neutron capture by the nitrogen atoms in the sample. However, the moderator not only thermalizes the neutrons, it also absorbs a certain amount of them, which is detrimental to detection because the highest thermal neutron flux possible on the sample is desired in order to achieve the largest gamma ray signature. Therefore there is an optimal thickness at which point thermalization and absorption are balanced and the maximum number of thermal neutrons is able to reach the interrogation sample.

6.4 Experimental Procedure and Preliminary Results

The experiments were performed by first putting the sample to be interrogated in place, Urea in this case, and operating the IEC at 120 kV, 60 mA to produce a neutron production rate of roughly 1.0×10^8 n/s. Over the course of approximately 15 minutes, several gamma ray energy spectra were collected with length ranging from 2 to 4 minutes. The IEC was then shut off, the sample removed, and then the IEC was turned back on for the same conditions and the same gamma ray energy spectra were collected without the sample present. A sample gamma ray energy spectra can be seen in Figure 6.7.

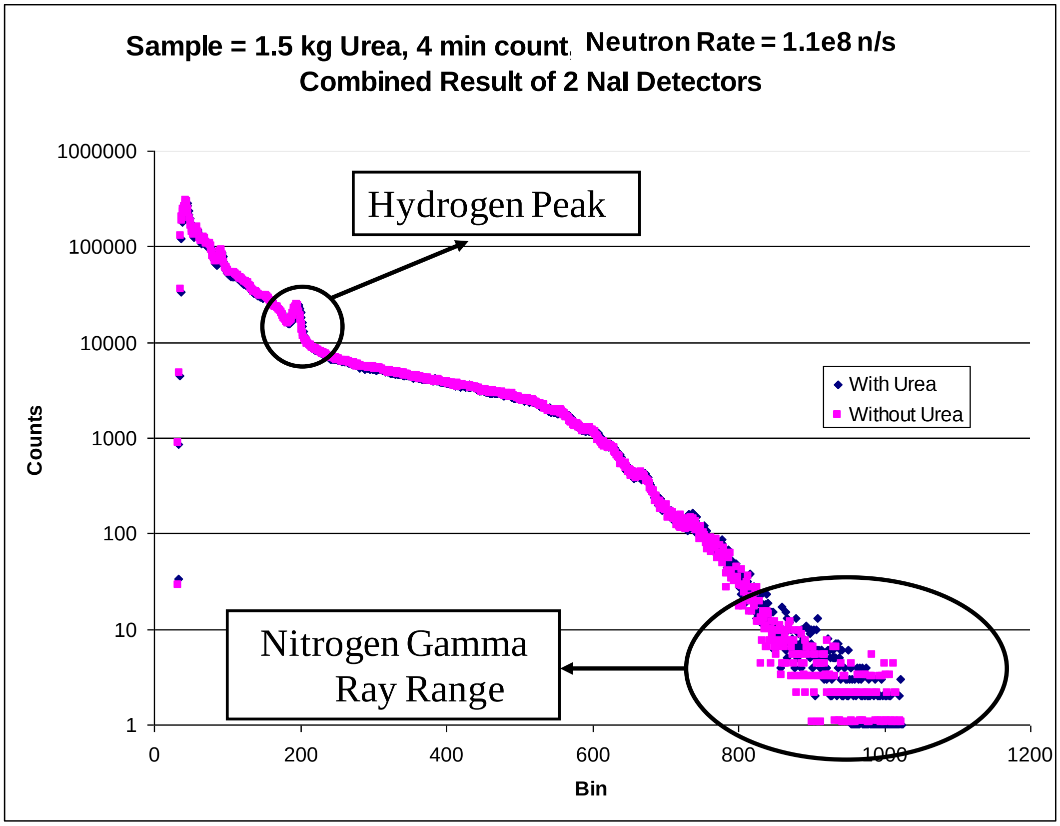

Figure 6.7 : Preliminary results of explosive detection setup.

Preliminary experiments showed repeatable counts above background in the high energy ranges for the case with urea as opposed to without. However, it was deemed that higher neutron fluxes were necessary to effectively distinguish a clear nitrogen signature well beyond the levels of statistical uncertainty. This led to an in depth examination of the workings of the IEC device in order to determine ways in which to increase neutron production rates. The efforts taken to further optimize and parameterize the system became an entirely new direction for research, the details of which are described in the following chapters.

6.5 Computational Modeling of Explosives Detection Setup

The experimental setup described has also been studied using computational modeling. The code package chosen to model this experimental setup was the discrete ordinates transport code system known as the Diffusion Accelerated Neutral Particle Transport Code System, or DANTSYS. This code package was written to solve the time-independent, multigroup discrete ordinates form of the Boltzmann transport equation in a variety of geometries. It uses the discrete ordinates method to approximate the angular variation of particle distributions in combination with the diamond difference method for the discretization of phase space. The discrete ordinates approximation can be used to give fairly accurate approximations of neutronics calculations in much less time than it would take, for example, a Monte Carlo calculation to run.

The purpose of this simulation is to determine the optimal thickness of moderator to create the maximum thermal neutron flux bombarding the interrogation sample. The neutron source can essentially be treated as one dimensional since the neutrons are emitted radially from the source, but the code also has some 2D capabilities to account for scattering of the neutrons, which can divert them from their radial path. For the purpose of this modeling, the IEC is treated as an isotropically emitting point source of 2.45 MeV neutrons at a rate of $2.0\text{x}10^8$ neutrons per second located at the center of the cathode, even though in reality it takes more the form of a volume source. However, since the purpose of this setup is to determine optimal moderator thickness, only the energy of the neutrons from the source is of great importance.

The simulation was run a total of ten times for a range of moderator thicknesses from 2.5 cm to 25 cm in 2.5 cm increments. When the thickness of the moderator was increased, the sample was moved farther away from the source. Therefore, greater thickness meant that the sample was receiving a smaller percentage of the neutrons being isotropically emitted from the source due to the $1/r^2$ fall off of the neutron flux. The way the geometry of this problem was set up, there are eight fine mesh cells in the sample region, each cell representing another length interval into the sample. For each of the different thickness runs, the thermal flux in each of the eight fine mesh cells in the sample region was recorded. The final results are shown in Figure 6.8 below.

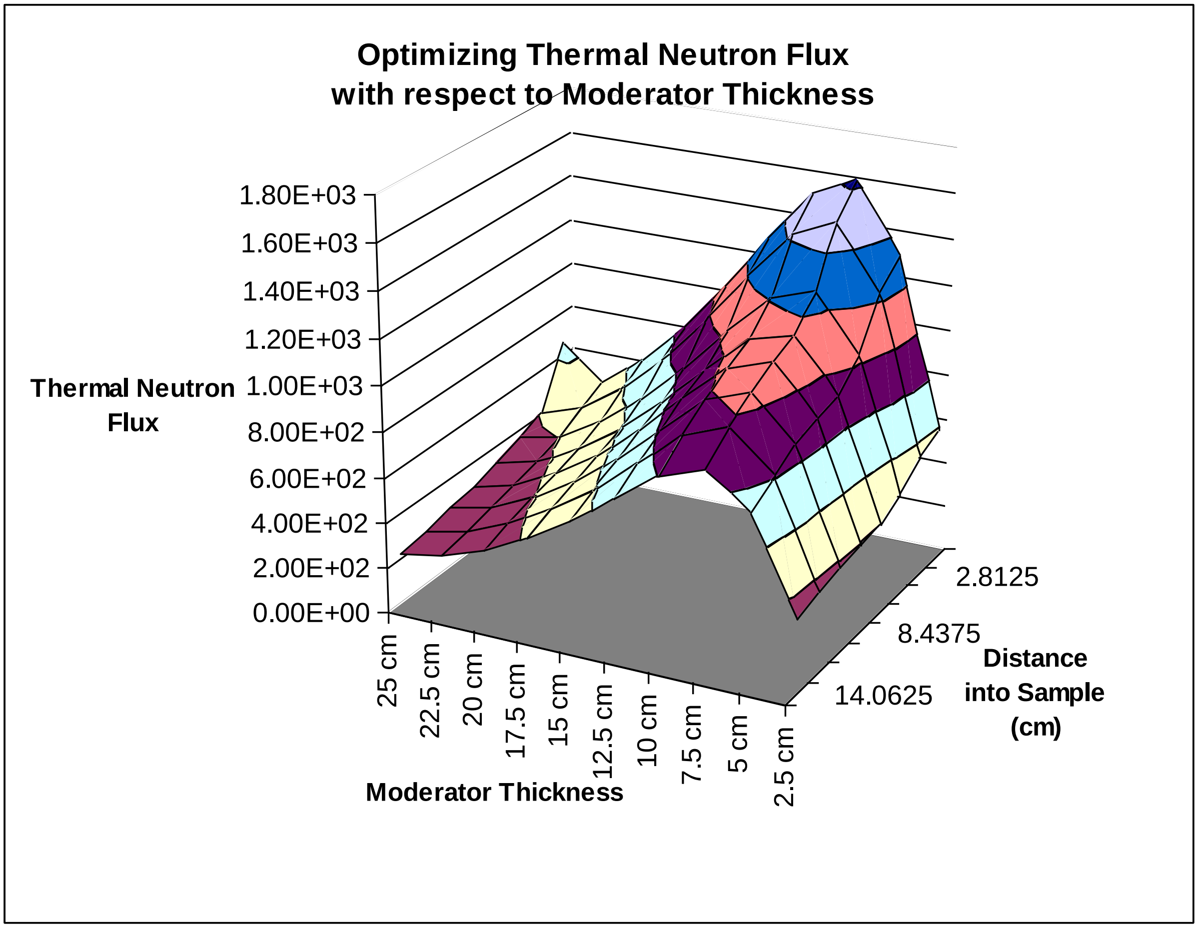

Figure 6.8 : Results of DANTSYS simulations demonstrating optimal moderator thickness.

As can be seen from Figure 6.8, there is an obvious peak in the curve that represents the optimal moderator thickness to achieve the maximum thermal neutron flux in the sample. For these input conditions, the optimal thickness occurs at roughly 7.5 cm. Anything less than this and the neutrons are not slowed down enough to offer sufficient thermal neutron flux. Anything more than this results in too many of the neutrons being scattered or absorbed before they reach the sample, once again resulting in lower total flux at the sample.

Chapter 6 References

1 Wehmeyer, A. L. (2005). The detection of explosives using an inertial electrostatic confinement D-D fusion device. (Masters thesis, University of Wisconsin – Madison)

2 Obtained from Internet on March 9, 2009: www.ortec-online.com

7 Research Progress on Optimization and Parameterization

Experiments discussed here regarding the optimization and parameterization of the IEC device, HOMER, began in May of 2007. The explosives detection experiments being conducted at the time had not yet produced a sufficiently detectable nitrogen signature from the interrogation sample. Various improvements were still being made upon the explosive detection setup, but one focus in particular was to increase the neutron output of the IEC device in order to increase the flux of neutrons available to interrogate a sample. The system operating parameters that were analyzed were background deuterium pressure, cathode voltage, and ion current. Preparations were made for HOMER to operate at higher voltage and current conditions in expectation of a higher capacity power supply. Various system components were optimized with regard to neutron production, particularly the design and configuration of the electrodes.

7.1 Parameterization

Parameterization studies have been performed in the past on HOMER by researchers such as Wehmeyer [1] and Radel [2]. These studies have involved tracking neutron production rates with regard to cathode voltage and current, background pressure, and electrode design and configuration, some of which is discussed in Chapter 3. The experiments conducted by the author and detailed below are intended to confirm and expand upon these initial results in an effort to better understand how to achieve higher neutron production rates.

7.1.1 Pressure

The operating pressure of the system is affected by the base pressure of the vacuum inside the chamber, the pumping speed, and the rate at which gas is fed into the system. Typical base pressure in HOMER is on the order of 7×10^{-7} to 5×10^{-6} Torr. A low base pressure is essential in order to minimize the amount of impurity gases in the system. To maintain a low base pressure, all vacuum components must be thoroughly cleaned and properly handled in order to minimize the amount of water vapor and other impurities that can outgas from the components in a low pressure environment. Cleaning and handling procedures have been adopted for the vacuum chambers, which will be discussed in greater detail in the Section 7.2.2.

During an experimental run, the operating pressure is controlled by the rate at which fuel gas is flowed into the system. For these experiments, the fuel gas is ultra high-purity deuterium. Pressure scans were performed on two different configurations, the 20 cm diameter cathode/30 cm diameter anode and 20 cm diameter cathode/40 cm diameter anode configurations. In both cases, the pressure was varied from 1 to 4 mTorr at two different voltage/current levels, which are labeled in the figures. The results of these pressure scans can be seen in Figure 7.1 and Figure 7.2 below.

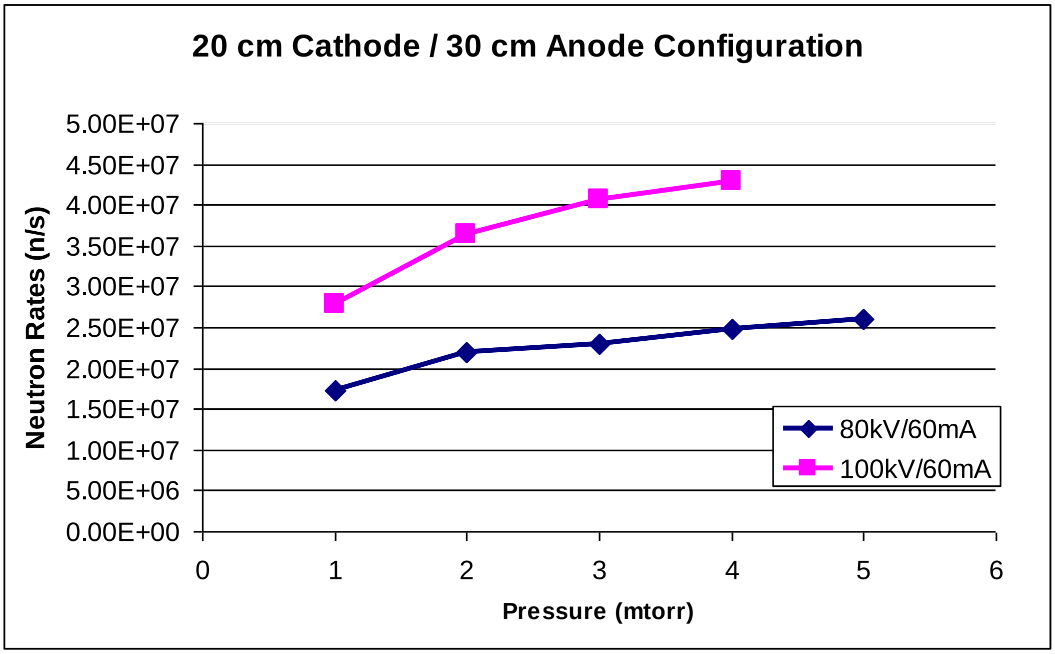

Figure 7.1: Pressure scans on 20 cm cathode/30 cm anode configurations.

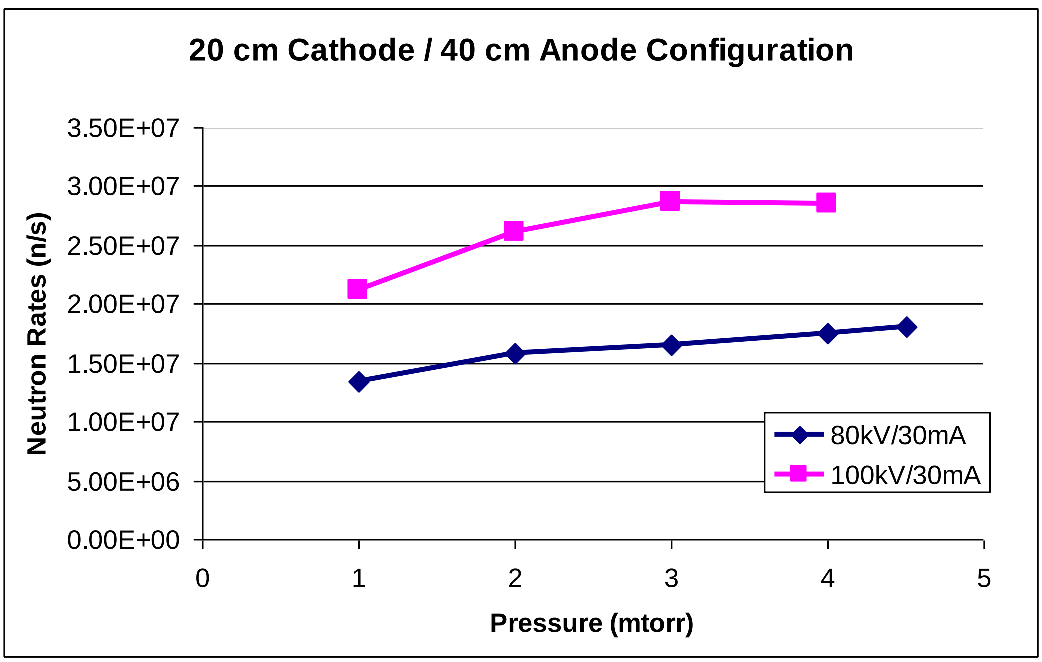

Figure 7.2: Pressure scans on 20 cm cathode/40 cm anode configurations.

The pressure was only varied up to roughly 4 mTorr because beyond that level the plasma goes into glow discharge mode and the current can then no longer be effectively controlled by adjusting the filament power. The higher the voltage level, the sooner the glow discharge mode is reached. This is why in the above figures, the 100kV data was only recorded up to 4 mTorr while the 80kV data extends into the 4.5 to 5 mTorr range.

As can be seen from the figures, in each case the neutron rates increase as pressure increases. This indicates that when trying to achieve maximum neutron rates it is best to operate the system at as high of pressure as possible without reaching glow discharge mode. Typical operating pressure is at around 2.5 mTorr, so by increasing that pressure from 2.5 mTorr up to 3.0 to 3.5 mTorr, an increase in neutron production rates on the order of 5 to 10 percent could be achieved.

7.1.2 Voltage and Current

The neutron production rates of HOMER are mostly dependent upon the voltage and current. It is by tuning these two parameters that the largest differences are seen and for the ranges in which HOMER is operated, higher voltage and higher current means higher neutron rates.

The voltage of the system determines the potential of the cathode and therefore the magnitude of the acceleration of the positively charged ions towards the negatively charged cathode. The experimental data collected on neutron rates with respect to voltage and current in the system is reasonably well matched by a second order polynomial function. The results are shown in Figure 7.3 and Figure 7.4. The best fit line is only slightly greater than linear, and the relationship between neutron rates and voltage is dependent upon several other variables, such as collisions with background particles that soften the fast particle spectrum, which is dependent upon background pressure. However, it appears that based upon the data collected, for every increase in voltage, at least an equal increase in neutron rates can be expected.

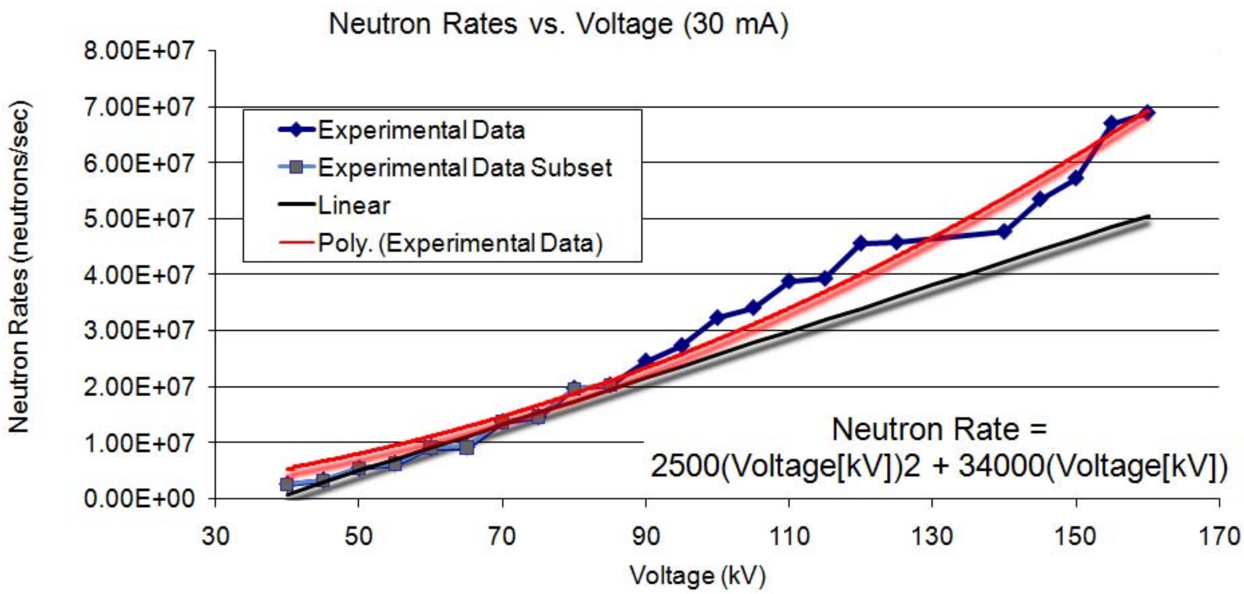

Figure 7.3: Experimental data of neutron rates vs. voltage at 30 mA with second order polynomial best fit line.

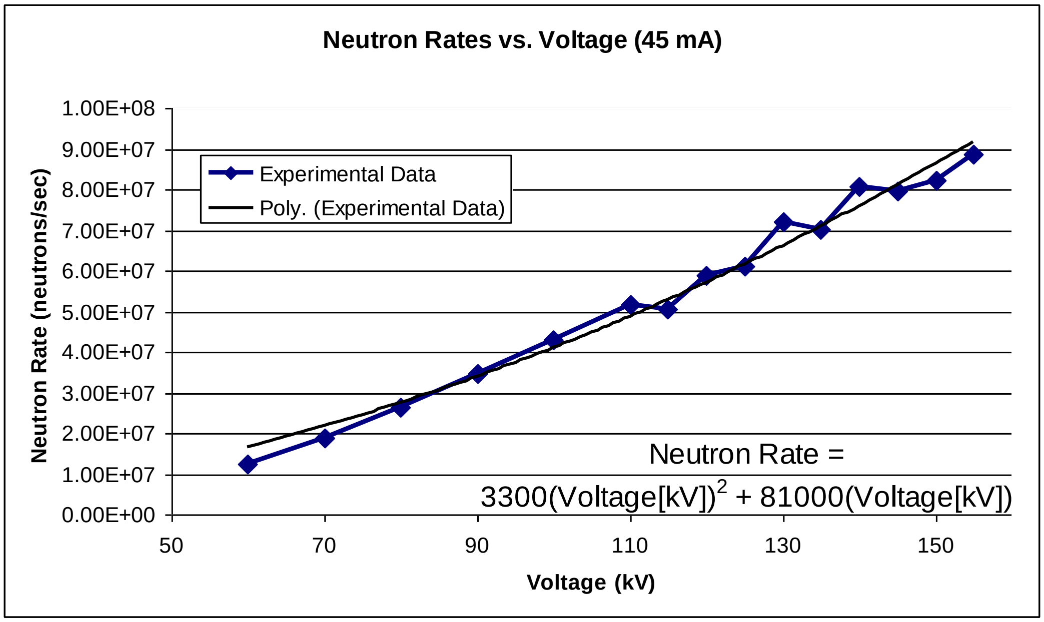

Figure 7.4: Experimental data of neutron rates vs. voltage at 45 mA with second order polynomial best fit line.

Similar results were taken tracking the effect of neutron rates on current. In this case, the relationship between the two is more linearly proportional. Typically HOMER is only operated at 30, 45, or 60 mA. Figure 7.5 shows the factor increase in neutron rates for a corresponding factor increase in current for a variety of voltage levels. The results are also shown in Table 7.1.

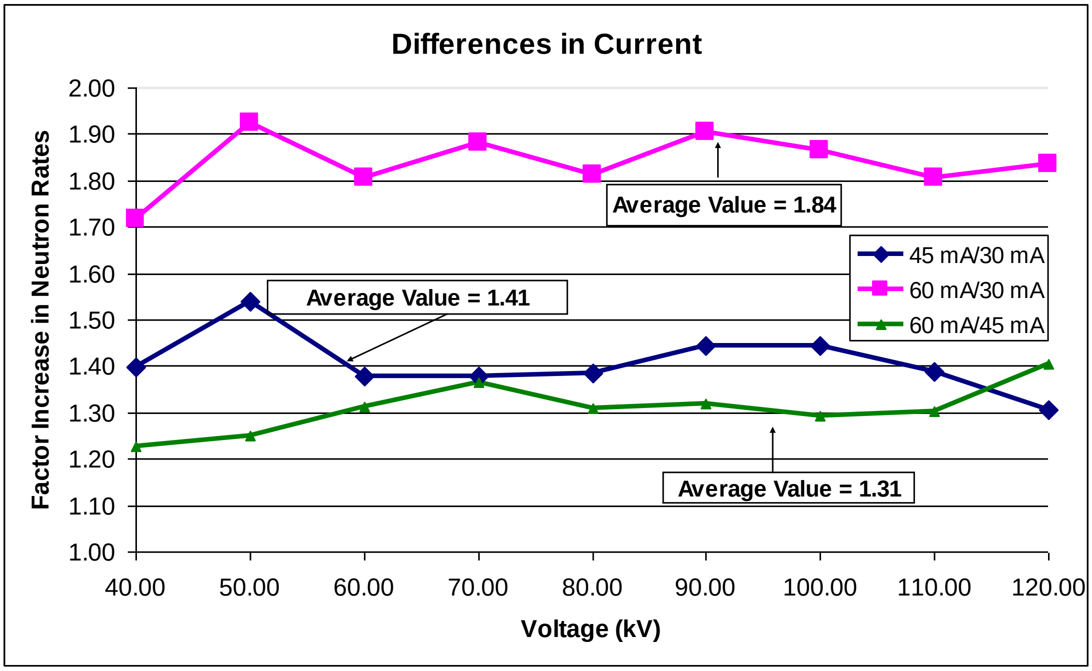

Figure 7.5: Ratio of neutron rates between 30, 45, and 60 mA at a range of voltages.

	Ratio between Current Levels	Average Ratio between Corresponding Neutron Rates (over 40-120 kV)	Proportionality Factor
45mA/30mA	1.5	1.41	0.94
60mA/30mA	2.0	1.84	0.92
60mA/45mA	1.33	1.31	0.98

Table 7.1: Changes in Neutron Rates Due to Changes in Current.

The Proportionality Factor indicates the slope of the linear relationship between the neutron rates and the current. The most conservative estimate of this would indicate that for a 100 percent increase in current, at least a 90 percent increase in neutron rates can be expected for this pressure and anode-cathode configuration.

7.2 High Voltage Conditioning

7.2.1 Overview

From the results displayed thus far, it is evident that the largest increase in rates can be achieved by increasing the current and voltage. In order to do this, a power supply must exist that can meet these higher current and voltage needs. Also, the system must be conditioned to be able to handle the extremely high voltage and high power.

All experiments conducted thus far have used a power supply with a maximum voltage of 200 kV and a maximum current of 75 mA. Operation of this power supply is not typically recommended for consistent use above 90 percent of its maximum rating. To achieve higher voltage and current levels, a higher capacity power supply is required. For this purpose, a new power supply was contracted and constructed by Phoenix Nuclear Labs. Construction of the supply was completed in the summer of 2009, and the supply has a capability of 300 kV and 200 mA. A variety of improvements have been made on HOMER and its operating practices aimed at preparing HOMER to run reliably at much higher current and voltage levels in expectation of this new supply. The areas improved included cleanliness of the vacuum system, design of the high voltage insulating stalks, support for the grids, cooling of the chamber, and condition of the high voltage feedthrough and conductor.

7.2.2 Cleaning

In order to maintain an acceptable base pressure, it is very important to make sure that all components entering a low pressure system are thoroughly cleaned in order to minimize the amount of impurities. Water vapor and other gases have a tendency to outgas from solid materials in high vacuum environments and can be very detrimental to the base pressure of the chamber. Cleanliness is very important in high voltage environments as well. Any peaks or imperfections on the surfaces of materials at high voltages can act as extremely high electric field points at which high voltage arcing is much more likely to occur. Impurities on surfaces can also change conductivities and dielectric strengths of materials, and even slight variations in these quantities at such high voltages can be catastrophic.

In order to ensure as clean a system as possible, several new measures were taken that include ultrasonic cleaning, electropolishing, and glow discharge cleaning. Ultrasonic cleaners use ultrasound frequencies in a fluid to clean materials by vibrating them until the superfluous material is shaken off. Several different fluids are used in the ultrasonic cleaning procedure. The four step cleaning process used in the following order is trichloroethylene, acetone, methyl alcohol, distilled water. When possible, components are then baked out in a high temperature oven to release any residual water vapor.

Electropolishing is a process that involves cleaning peaks and impurities off of a surface by dissolving it in an electrolyte solution using an electric current. Conductive materials, often metals, are treated as the anode and immersed in an electrolyte solution. The solution is typically made of concentrated acidic solutions that combine to form a viscous mixture such as sulfuric and phosphoric acid. Another electrode is then placed in the electrolyte solution and acts as the cathode. A DC current is then applied to the anode and the peaks on the surface are oxidized in the solution and dissolved away. Electropolishing is therefore able to not only dissolve impurities from a surface, but also dissolve away imperfections on the surface that could potentially act as focal points for high electric fields in a high voltage environment. This can also be a very abrasive process on some materials and is not recommended for all components.

For example, it was implemented with some success on the high voltage feedthrough made of stainless steel, which is in an extremely high electric field area and must be as smooth as possible. However, when electropolishing was done on the molybdenum rod used as the high voltage conductor, it resulted in making the surface of the conductor rougher and, in the end, less effective at high voltages.

Cleaning of the inside of HOMER can be accomplished using a glow discharge. A glow discharge is performed by providing a low voltage (on the order of 10 to 100 V) to an electrode in a gas pressure of 5 to 10 mTorr in order to cause a breakdown in the gas and create a plasma. The energetic ions in the plasma are then able to bombard the area surrounding the electrodes and essentially burn off many of the substances on the surface and release some of the impurities trapped in the walls. The electrodes used to perform the glow discharge are the six filaments that are spaced evenly around the chamber, which allowed a significant portion of the surface area of the walls to be cleaned.

These methods together allowed cleaning of the chamber walls as well as the various removable components inside the vacuum system, which is very helpful at lowering the impurity levels in the vacuum and the base pressure of the system. It also provides a way to remove many of the sharp edges and imperfections on some of the various high voltage components, which helps to minimize the amount of high voltage arcing that leads to shut down of the power supply during operation.

7.2.3 Stalk Design

One of the most persistently difficult parts of the entire IEC system to maintain is the insulating stalk that covers the high voltage conductor between the feedthrough in the roof of the chamber and the cathode. In the last five years of operation, over fifty different stalks have been designed and built for the IEC chambers, with each one having lifetimes varying from several weeks to over two years. The insulating stalk is essential to steady state operation of the device at high voltages because it shields the high voltage feedthrough from the surrounding ground potential of the anode and the walls of the chamber and prevents direct arcing between the two. With the stalk in place, the easiest path for the arc to take is often either up the outside surface of the stalk or directly between the anode and cathode. Both of those options do not typically begin to occur until the 100 kV range is reached as opposed to operation without the stalk, which can not reach higher than a few tens of kilovolts in cathode potential. The current stalks are made of 2.5 cm diameter boron nitride rods obtained from Saint-Gobain Crystals.

There are a variety of failure mechanisms for these stalks. The most common type of failure is when a pin sized hole is blasted away through the diameter of the stalk, which then offers a direct line for arcing between the conductor and ground and prevents further high voltage operation. These pinhole failures often occur over time as arcs occur inside the stalk and attempt to reach the grounded anode or chamber on the other side of the stalk. When the failure points are analyzed, a treeing effect around the failure hole is often found where arcs had been blasting away channels in the boron nitride until one channel finally makes it all the way through to the surface and allows an easy path to ground that all future arcs then take. The most common location for these pinhole failures is at the high voltage feedthrough on the lid of the chamber, which is grounded and made of stainless steel. This is the region of the stalk that is closest to a grounded surface. Pinholes failures have been seen to occur, though, throughout the length of the stalk. A diagram of the feedthrough can be seen in Figure 7.6.

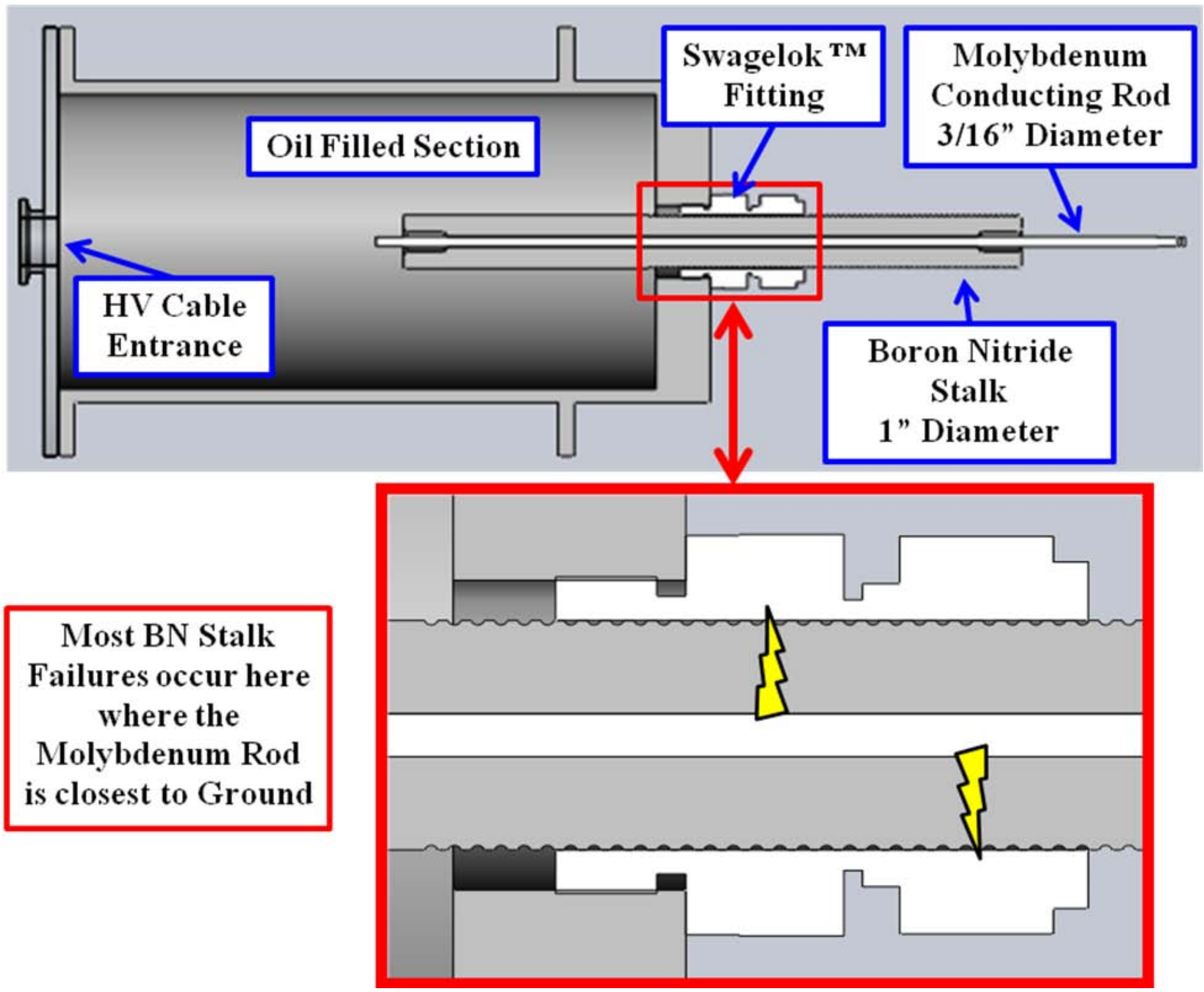

Figure 7.6 Original high voltage feedthrough for HOMER.

The stalks are possibly the most important component of the system that must be considered before HOMER is taken to much higher voltages. During the last few years of operation, a variety of improvements have been made to achieve higher lifetimes and reliability from the stalks. The high voltage feedthrough on HOMER is filled with a high voltage capacity oil that immerses the non-vacuum side of the boron nitride stalk in order to mitigate surface break down. On several occasions, the oil has been found to migrate through the highly porous boron nitride and breach the vacuum. To solve this problem, a new type of coating was applied to the outside of the section of the boron nitride rod that was exposed to the oil. The coating is known as PYRO-ML® and it provides a vacuum sealed barrier that is impenetrable to most fluids and also has a very high heat capacity. Several layers of the coating are baked on to the surface before it is inserted into the feedthrough. Since the onset of its use there have been no additional cases of oil seeping through the insulator.

Another factor that was found to greatly affect stalk lifetime was the rate at which voltage is increased on new stalks as they are conditioned for high voltages. The stalks must be conditioned in a slow and deliberate manner to ensure that the boron nitride has time to outgas as much of the trapped impurities as it can and to allow the stalk to become accustomed to higher voltage levels gradually. A conditioning rate of 5 to 10 kV per hour of run time is optimal for achieving the longest lifetimes and highest voltage capabilities for a stalk. This results in a somewhat slower, but much more reliable method of preparing new stalks for higher voltage conditions.

Previous stalk designs were constructed by taking the boron nitride rod and boring out a hole with diameter slightly larger than the diameter of the conducting rod through the center of the diameter of the boron nitride rod. Small indentations were carved into the outside surface of the boron nitride rod in order to increase the surface path length that the arcs had to travel to reach the ground at the top of the rod. The conducting rod made of molybdenum was then fit snuggly into the boron nitride rod so that it protrudes slightly at both ends in order to reach the cathode on one end and the high voltage connection from the power supply on the other end. The end of the rod that made the connection with the cable from the power supply was not in vacuum and was covered in vacuum sealant. This design was in use for several years, with the longest lasting stalk of this design having a lifetime of roughly 11 months.

However, these stalks were not believed to be capable of reaching the desired voltage levels of 300 kV. Boron nitride was chosen for its very high dielectric strength, which makes it a very good insulator, but a vacuum is an even better insulator. A new stalk design was implemented that was intended to minimize the amount of dielectric material around the conductor as much as possible but still provide that barrier to the path of direct arcing through the plasma between the conductor and ground. The new design involved boring out a 1.25 cm diameter channel from the dielectric material of the boron nitride and replacing it with a vacuum region, which greatly minimizes the maximum electric field surrounding the conductor. The differences between the old solid stalk and the new hollow stalks can be seen in Figure 7.7.

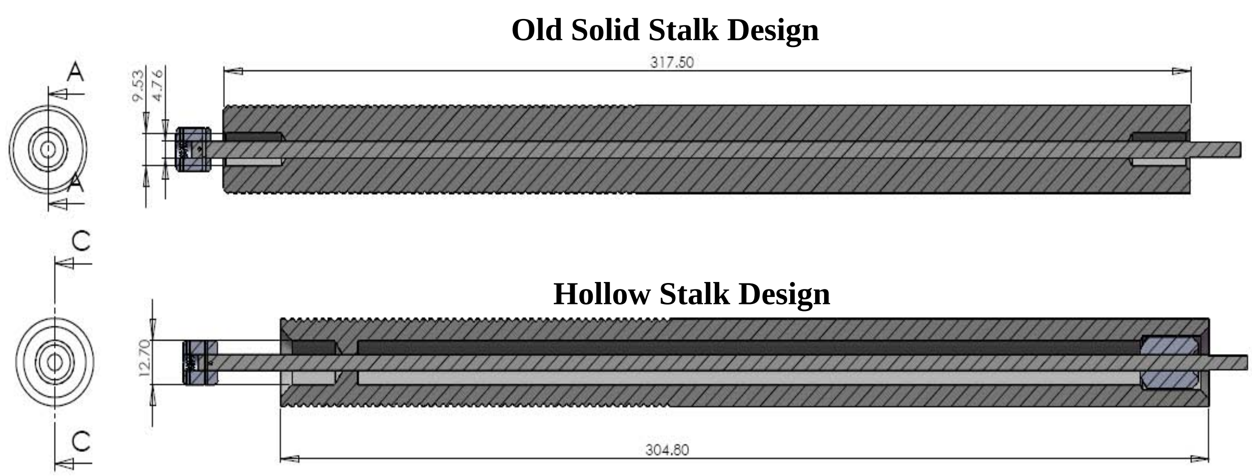

Figure 7.7: Comparison of old solid stalk design and new hollow design (units in mm).

After several variations on the hollow stalk design, it was able to reach 160 kV and 30 mA, and maintain that level for up to 5 minutes without a large arc, which was a significant improvement over previous operating conditions, which typically were unable to last more than a minute at these levels. The hollow stalk design was deemed a successful improvement and has become the preferred design.

7.2.4 Cooling of Chamber

An inevitable product of increased current and voltage on the system is increased heating of the chamber and all of the components. At higher voltage and current levels two other effects occur, which are that the total neutron flux increases and the ion velocity increases. The increased neutron flux results in more neutrons slowing down and losing their energy to the walls of the chamber. The increased ion velocity once again results in more energy being deposited in the walls of the chamber, but more importantly also in the wires of the cathode. The increased amount of energy being deposited on the cathode due to the fast ion bombardment and the increased current from the power supply causes the cathode to heat up until it glows white hot.

The walls are heated primarily through the radiative heating from the cathode and rises on the order of 20 to 25 degrees Celsius during a typical high power run with the 200 kV power supply. Cooling of the chamber thus far has been performed by two methods, which have been water cooling and air cooling. Air cooling is accomplished by high capacity fans that force air over the chamber. Water cooling is performed by wrapping 0.625 cm inner diameter copper tubing around the outside of the vacuum chamber, and cool water is pumped through the lines.

In preparation for the new 300 kV power supply, cooling abilities on HOMER were improved by nearly doubling the length of copper cooling lines from 15 to roughly 28 meters. The ability to cool the system is one of the primary limiting factors in the length of a run at higher power levels. The cooling efforts initiated thus far are aimed at cooling the outside of the chamber, which decreases the risk of various electronics and vacuum seals on the chamber being damaged. However, no systems have been installed to attempt to cool the cathode or any components on the inside of the chamber. The additional cooling ability added from the increased length of copper lines will help to increase run time at higher power levels. However, the runs at voltages above 200 kV and currents above 100 mA will still most likely be limited to lengths on the order 5 to 10 minutes with the current cooling abilities. These short runs should still be sufficient to gauge the capabilities of the system at those levels with regard to neutron rates. For the future, if longer run times are desired a different level of cooling would most likely need to be put in place.

7.2.5 High Voltage Feedthrough and Conductor

The final area that was improved in an effort to prepare for higher voltage and current levels is the high voltage connection to the grids. The two most important aspects of this connection with regard to arcing that have been recognized thus far are the conducting molybdenum rod inside the stalk and the high voltage feedthrough. The conducting rod was chosen to be made out of molybdenum due to the element's very high melting point and very low coefficient of thermal expansion, both of which make it ideal for extremely high heat conditions. Since the conducting rod is placed at hundreds of kilovolts of potential, the smallest sharp point, scratch or irregularity on the rod can act as a focal point for arcs and be very detrimental to the system. The rod must therefore be smoothed and polished as thoroughly as possible.

The high voltage feedthrough is positioned in a 17.8 cm diameter hole in the center of the lid of the chamber. The feedthrough acts to allow the conducting rod in the insulating stalk to penetrate into the chamber while forming a vacuum seal around the surface. A schematic of the location of the feedthrough on the chamber is shown in Figure 7.8.

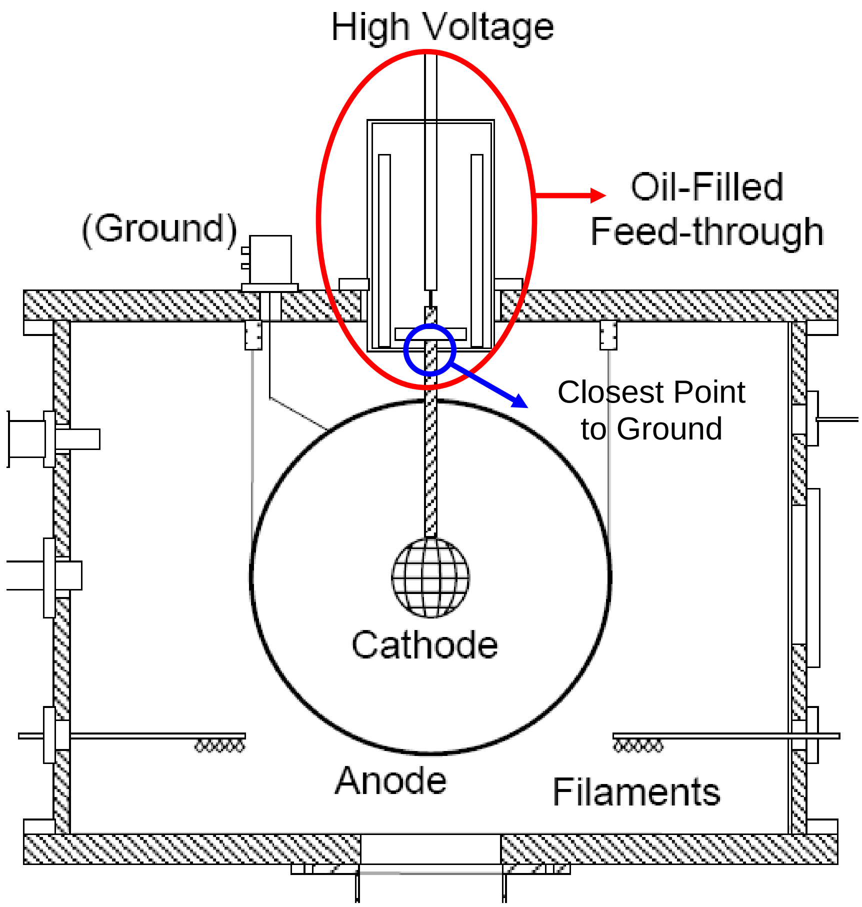

Figure 7.8: Schematic of HOMER and location of high voltage feedthrough as well as closest point to ground in high voltage system.

Also shown in Figure 7.8 is the location of the closest point between ground potential and the high voltage. This occurs at the threaded collar that protrudes from the bottom of the feedthrough through which the stalk is placed and then secured in place using a nylon ferrule that is compressed by a hexagonal nut on that threaded collar. The electric field intensity is highest in this region because it is the closest distance to ground that the high voltage experiences. As was mentioned previously, the highest number of pinhole failures on the stalks occurs in this region. One factor that greatly increases the intensity of electric field points on these surfaces is once again any types of peaks or irregularities. The feedthrough has been electropolished, ultrasonically cleaned, and the collar through which the insulating stalk is placed has been honed until all signs of imperfections have been removed.

A further upgrade to the high voltage feedthrough that was designed by the author is to utilize non-conductive components made of quartz or PVC, which is discussed in a later chapter. By changing the material from stainless steel to a non-conductive material, the closest point to ground is then significantly farther away and could theoretically drastically reduce the amount of arcing and stalk failures that normally occur at these high field intensity locations. An upgrade to the feedthrough would also allow the opportunity to improve the method in which the stalk is installed and secured into the feedthrough.

7.3 Optimization

7.3.1 Titanium Coating

Previous experiments had been undertaken by Radel and Rusch to vapor deposit titanium on inner surfaces and electrodes of HOMER (see Section 3.3). It was believed that this Ti coating could bring about an immediate increase in neutron production rates in HOMER. The titanium was coated onto the walls of the vacuum vessel as well as the anode and cathode using vapor deposition of titanium cartridges. The deposition was performed at roughly 30 volts and 40 amps of current with a background deuterium pressure of 3.75 mTorr over a period of 19 hours. The desired result was a minimum thickness of the coating of 0.3 μm. In order to measure the results of the coating, microscope slides were left in the chamber in different locations so that they could be removed and tested to determine the minimum coating thickness in the chamber as well as the uniformity of the coating throughout the chamber. After the process was complete, the coating thickness on the walls was found to be around 0.3 to 0.4 µm. The first venting of the chamber up to atmosphere after the coating was done using deuterium gas to ensure that the titanium was able to absorb as much deuterium as possible before it was exposed to the air. The results of the titanium coating process are shown in Figure 7.9.

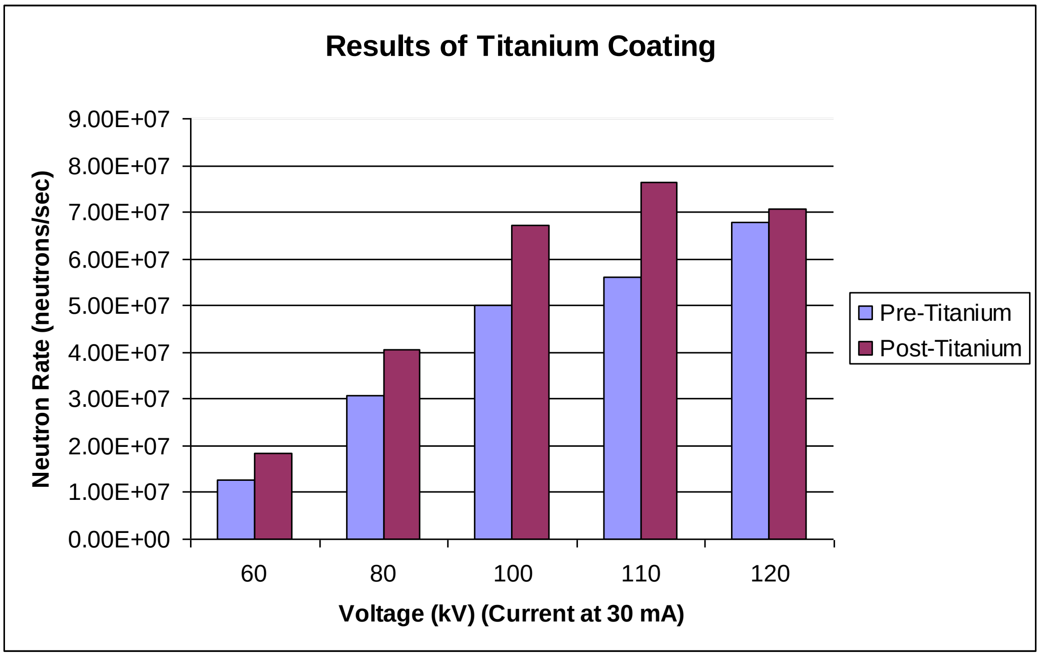

Figure 7.9: Change in neutron rates due to titanium coating of vacuum chamber.

The introduction of the titanium coating in the system provided up to a 35 percent increase in neutron rates at some voltage levels. The reason the increase in rates does not appear as large at the 120 kV level is actually indicative of an adverse side effect of the titanium coating that was not originally predicted. When Ti was deposited in the chamber, the 40 cm diameter anode and the 20 cm diameter cathode, both of which were part of the W-7 configuration, were left inside. The reason why they were exposed to the titanium deposition was that it was believed that the grids could then store more deuterium and increase the amounted of embedded fusions even further. The side effect of coating the grids was that the cathode became much more uncooperative at high voltages as a result of excessive arcing.

What is believed to have happened was that the deposition causes a rough, uneven coating of titanium to form all over the grids. The titanium coatings also have a tendency to flake off over time, which would have caused additional non-uniformities to form. These peaks on the grids act as extremely high electric field points when high voltage is applied, which then increased the amount of high voltage arcing between the anode and cathode. At voltages beyond 100 kV, steady state operation became extremely difficult due to the constant shutdowns of the power supply from the high voltage arcs. Initially it was attempted to remove the titanium coating from the cathode using electropolishing. These attempts were unsuccessful though, and the W-7 cathode had to be retired. It was with the W-7 cathode that the record neutron rate of 2.22e8 n/s was achieved. The cathode was retired because of the titanium coating, which later made it unavailable to directly compare against the other titanium free grids that were constructed. The 40 cm anode that was also coated in titanium did not seem to be adversely affected since it was kept at ground potential so there was no risk of high electric field points occurring, and as a result it was able to be kept in use. Coating with titanium can be a very effective tool for increasing neutron rates, but simple precautions need to be taken, such as removing the cathode during vapor deposition.

7.3.2 Cathode Grid Design

The forced retirement of the W-7 cathode necessitated the construction of a new cathode grid for operation. This event inadvertently began a series of experiments that focused upon how the design of the cathode affects neutron production rates in an IEC device. All of the cathodes constructed were made of 75% W/25% Re wire in the lat/long geometry. There were two factors to the design of the cathodes that were considered during this study which were, the transparency of the grids and the number of electrostatic potential valleys. The transparency is the measure of the surface area of the sphere that is not obstructed by wire. The original hypothesis was that a higher transparency would be better for increasing neutron rates because with less of the surface area of the sphere obstructed, more ions would be able to reach the center of the system without colliding into a wire. The electrostatic potential valleys occur in the holes between the grid wires and represent a minimum in the magnitude of the potential at the center of the holes and a maximum in potential at the wires. It was believed that smaller holes between the wires would result in a higher minimum potential in the potential valleys because the wires would be closer together and allow for a less dramatic drop off in potential. By maintaining this higher potential through the region between the wires it was believed that greater acceleration of the ions towards the center could be achieved. Also, with more holes around the grid the ions would theoretically be more focused towards the center of the sphere, thereby increasing the probability of collisions in the exact center of the spherical system. To vary these two grid parameters, the number of latitude and longitude wires was varied as well as the thickness of wire. A total of four cathodes were constructed and tested, all with varying levels of transparency and number of potential valleys.

In order to construct multiple grids with a variety of different wire configurations, a new method had to be developed that allowed for the template on which the grids were constructed to be varied without great difficulty. Styrofoam spheres were found to be an effective means of creating inexpensive and easily altered templates for constructing the grids. There is a large availability of Styrofoam balls in diameters of 20 and 30 cm at low cost. The construction process of the grids is displayed in

Figure 7.10.

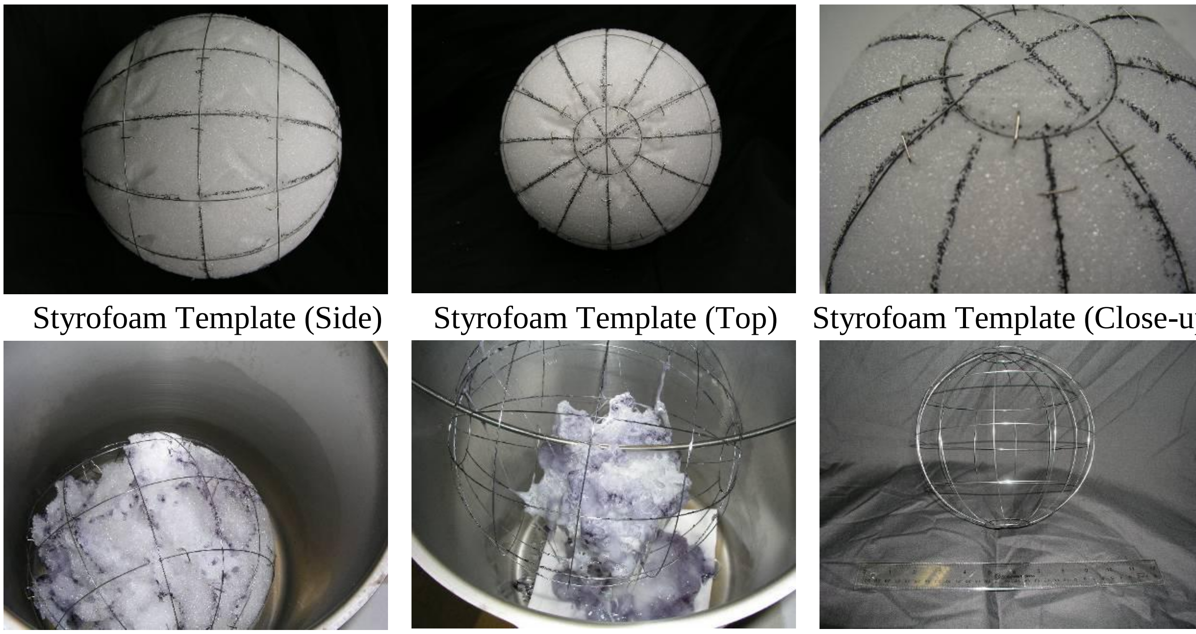

Styrofoam Template (Side) Styrofoam Template (Top) Styrofoam Template (Close-up)

Dissolving Styrofoam Using Acetone Dissolving Styrofoam Using Acetone Completed Grid

Figure 7.10: Construction of 20 cm diameter grids.

The desired lat/long configuration for the grid was drawn onto the surface of the Styrofoam spheres. The wire was then wrapped around the sphere over the drawn template and pinned into place. The thickness of the wire used was either 0.0762 cm diameter or 0.0508 cm diameter or both, depending on the amount of transparency desired for the grid. After all the overlapping wires had been spot welded together, the Styrofoam sphere was dissolved using acetone. The grid was then cleaned and ready for use. This construction method was used to make a total of four 20 cm diameter grids and one 30 cm diameter grid.

Each grid is characterized by the number of latitude and longitude wires it has. The details of the four cathodes constructed are listed in Table 7.2, and photos of each cathode can be seen in Figure 7.11. The 11/24 cathode constructed for these experiments is a replica of the 11/24 cathode used as part of the W-7 configuration that obtained the record neutron production rates.

Grid	**Configurations in which Cathode was Used**	**Number of Latitude Wires**	**Number of Longitude Wires**	**Transparency**	**Number of Potential Valleys (Holes)**
5/12	W-11	5	12	96.77%	72
9/12	W-11a, W-13	9	12	95.53%	120
11/24	W-7, W-16	11	24	92.95%	288
13/32	W-14, W-15	13	32	92.01%	448

Table 7.2 : Details of cathodes constructed for optimization studies

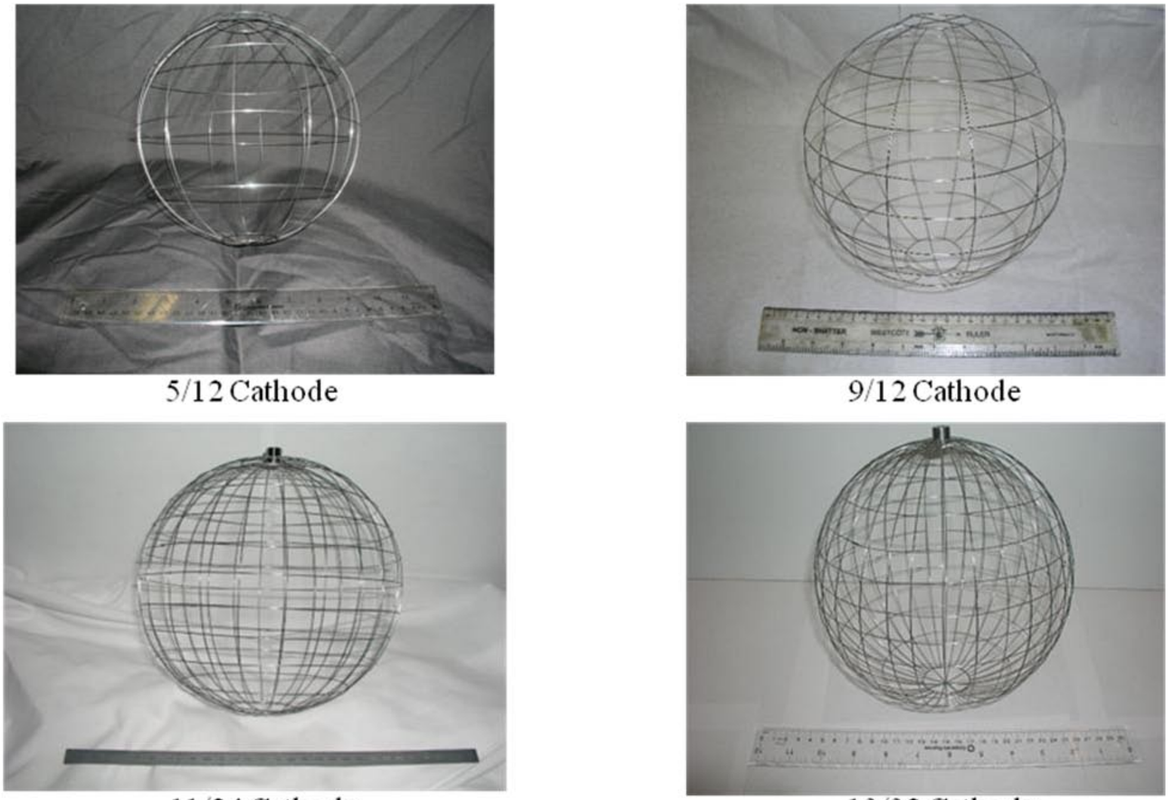

5/12 Cathode 9/12 Cathode

11/24 Cathode 13/32 Cathode

Figure 7.11 : 20 cm diameter cathodes constructed for optimization studies

The cathodes are electrically connected to the high voltage cable coming from the power supply through a 0.65 cm diameter molybdenum rod. In the past, various methods have been developed to attach the cathode to the conducting rod including threading the rod or attempting to weave grid wires through a hole in the conducting rod to hold it in place. However, these efforts had only limited success because molybdenum is not very easily threaded, and attempting to weave the grid wires through a hole in the rod led to insufficient stability for the grid and a lack of repeatability of ensuring that it was oriented in the same place every time it was installed. If the cathode is inadequately connected to the conducting rod, then the electrostatic forces applied during operation can pull the cathode off center and destroy the symmetry of the device.

The 11/24 and 13/32 cathodes had an additional improvement made upon them to deal with this instability, which was a molybdenum nut that was permanently woven into the top of the cathode. This nut could slip over the conducting rod and be held in place with a pin. A photo of the nut and its placement on the cathode can be seen in Figure 7.12. This addition ensured that the cathode was always oriented in the same plane whenever it was installed, and it offered sufficient stability to prevent the cathode from being pulled off center by the electrostatic forces.

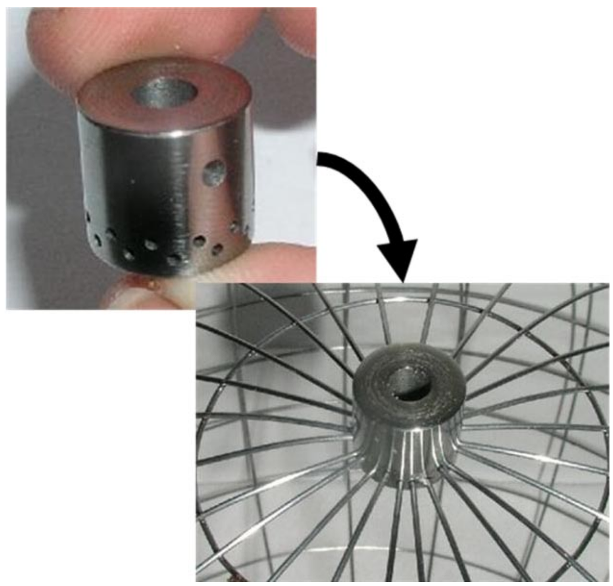

Figure 7.12 : Molydebum nut used to attach cathode grid to high voltage molydenum conducting rod.

Experiments were performed using the four 20 cm diameter cathodes with either the 40 or 50 cm diameter anode. All other variables in the system other than the cathode were kept the same for each configuration as best as possible. Absolute control over the system variables was not realistic as the vacuum had to be broken and the grids removed when changing out the cathode. The exposure to atmosphere when vacuum is broken adds additional impurities into the chamber, although RGA scans were taken at different intervals to ensure that the background air and water vapor levels in the chamber were not above normal, and that there were no additional anomalous impurities in the system. Measurements were taken between the grids to center the cathode directly in the middle of the anode, but the grids do have minor imperfections that lead to slight offsets of the grids causing minor differences between configurations every time the grids are put back into place. Typically the effects of the small variations in these less controlled variables have been found to be negligible with regard to neutron rates.

The four grids were not run directly one after another, there were also several other varieties of experiments and minor improvement that were taking place on HOMER at the same time as the grid studies. The effect of each addition on neutron rates was carefully monitored to ensure that it did not adversely affect the results obtained for the grid studies. One of the additional sets of experiments that was taking place during these cathode studies was designed to test the effect of the separation distance between the grids on the neutron production rates, which will be discussed in the next section. Since each grid was not tested in sequence directly one after another, several “bridge” cases had to be studied to link together the results of all four cathodes. The bridge cases were those experiments in which the only element changed in the system between the two sets of experiments was the cathode. Using these cases, each cathode had a direct relationship with regard to differences in neutron rates to the one before it and the one after it, allowing for all four to be compared without performing them in sequence. Each of the cathode/anode configurations had its own designation based upon the order in which it was run. The details of the different configurations are shown in Table 7.3 below.

Configuration	Cathode	Anode
W-11	5/12 Grid (20 cm diameter)	40 cm diameter
W-11a	9/12 Grid (20 cm diameter)	40 cm diameter
W-12	9/12 Grid (20 cm diameter)	30 cm diameter
W-13	9/12 Grid (20 cm diameter)	40 cm diameter
W-14	13/32 Grid (20 cm diameter)	40 cm diameter
W-15	13/32 Grid (20 cm diameter)	50 cm diameter
W-16	11/24 Grid (20 cm diameter)	50 cm diameter

Table 7.3 : Details of cathode/anode configurations used during the course of these experiments.

The majority of additions or alterations to HOMER made during the course of these experiments were minor and were deemed to have a negligible influence on neutron production rates in the system. The only significant change to the system occurred when the anode diameter was changed, which as was already said was part of an additional study on the effect of the separation distance between the electrodes on neutron production rates. However, even though the anode diameter was changed between different cathodes, there are bridge cases between each cathode in series to make sure that they are each directly comparable to the one tested before it.

The results of the cathode studies experiments can be portrayed by first comparing each of the three bridge cases between the three cathodes. The three cases that will be analyzed are the comparisons of the W-11 and W-11a configurations, the W-13 and W-14 configurations, and the W-15 and W-16 configurations. The results of the three cases are shown in Figure 7.13, Figure 7.14, and Figure 7.15.

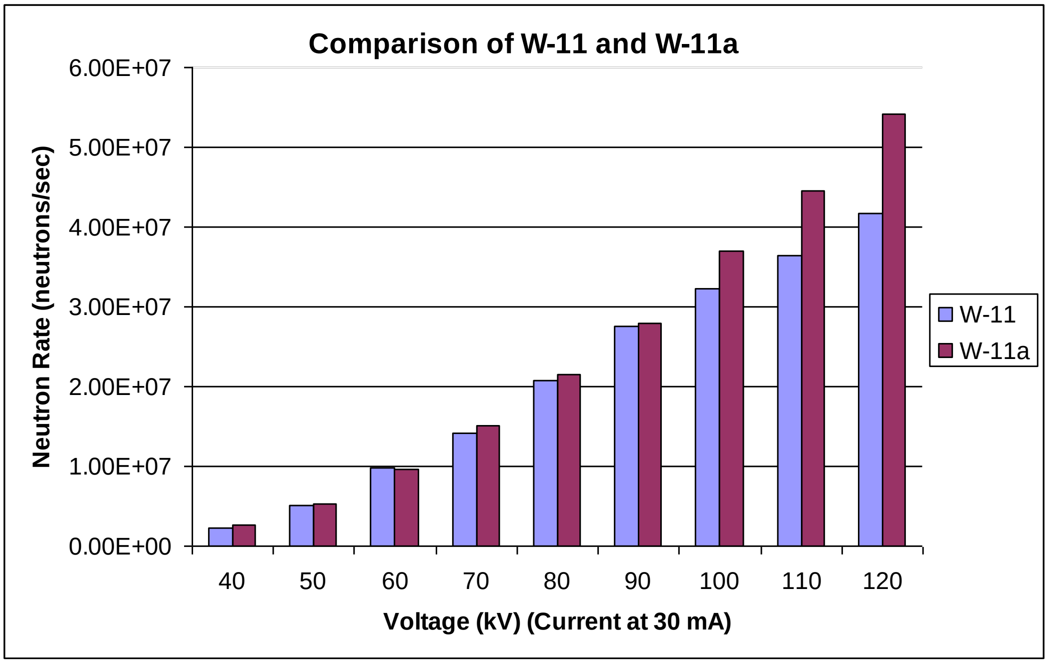

Figure 7.13: Comparison of neutron rates between 5/12 cathode in W-11 and 9/12 cathode in W-11a configurations.

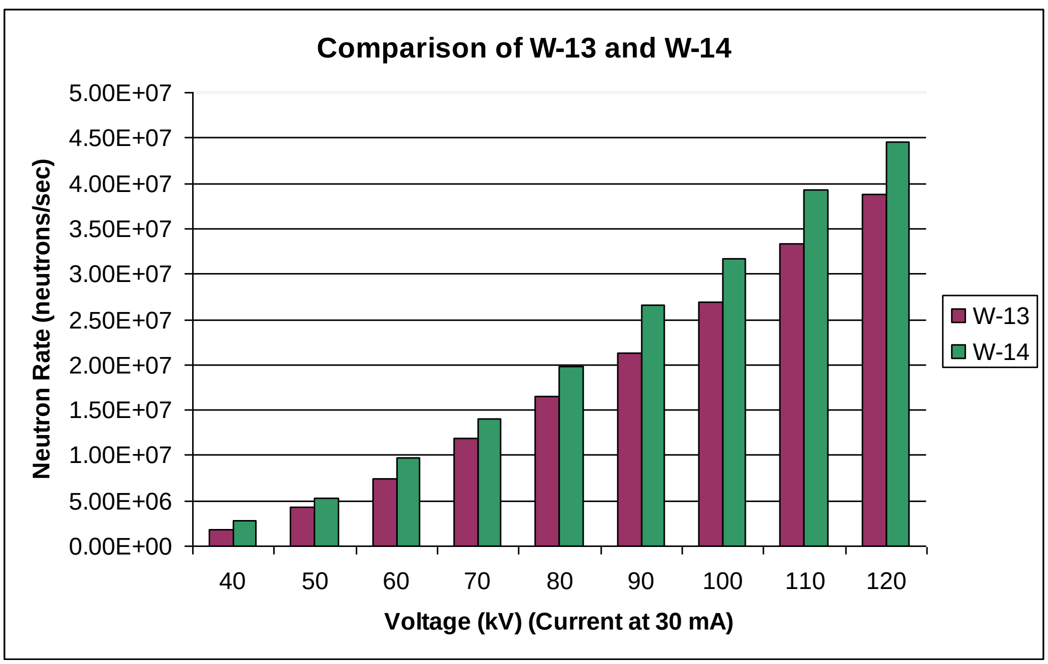

Figure 7.14: Comparison of neutron rates between 9/12 cathode of W-13 and 13/32 cathode of W-14 configurations.

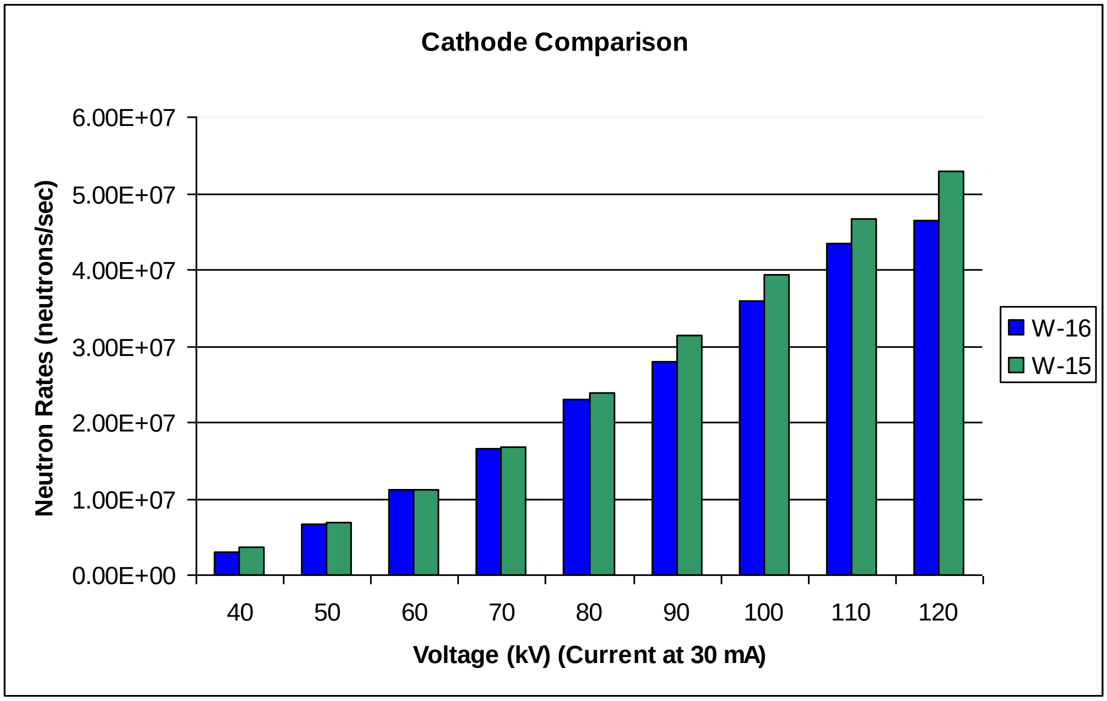

Figure 7.15: Comparison of neutron rates between 11/24 cathode of W-16 and 13/32 cathode of W-15 configurations.

As can be seen from these results, there is a noticeable trend in which the neutron production rates increase with each instance of increasing the number of wires on the cathode. A significant jump in rates was seen between the W-11 and W-11a cathodes, which were the first two cathodes tested. The only difference between the W-11 and W-11a configurations is that the cathode in W-11a had four more latitude wires than the cathode in the W-11 configuration. These additional wires, and the resulting increase in the number of potential valleys, the fact that the potential valleys have become shallower due to shortening the distance between the minimum potential and the wires, and the decrease in transparency, caused up to a 30 percent increase in neutron rates at the higher voltage levels. In the second case, we once again see that adding more wires to the cathode results in higher neutron rates. There is up to a 15 percent increase in neutron rates at the higher voltage levels for the 13/32 cathode over the 9/12 cathode. The third case shows a slightly smaller, but still consistent, increase in neutron rates for the 13/32 cathode over the 11/24 cathode in the range of 10 to 15 percent. A final comparison between the average difference in neutron rates between all four cathodes can be made using the bridging cases to relate the neutron production capacity of all the cathodes to the highest producing cathode, which was the 13/32 cathode. The results are shown in Figure 7.16.

Transparency	96.7%	95.5%	93.0%	92.0%
Potential Valleys	72	120	288	448

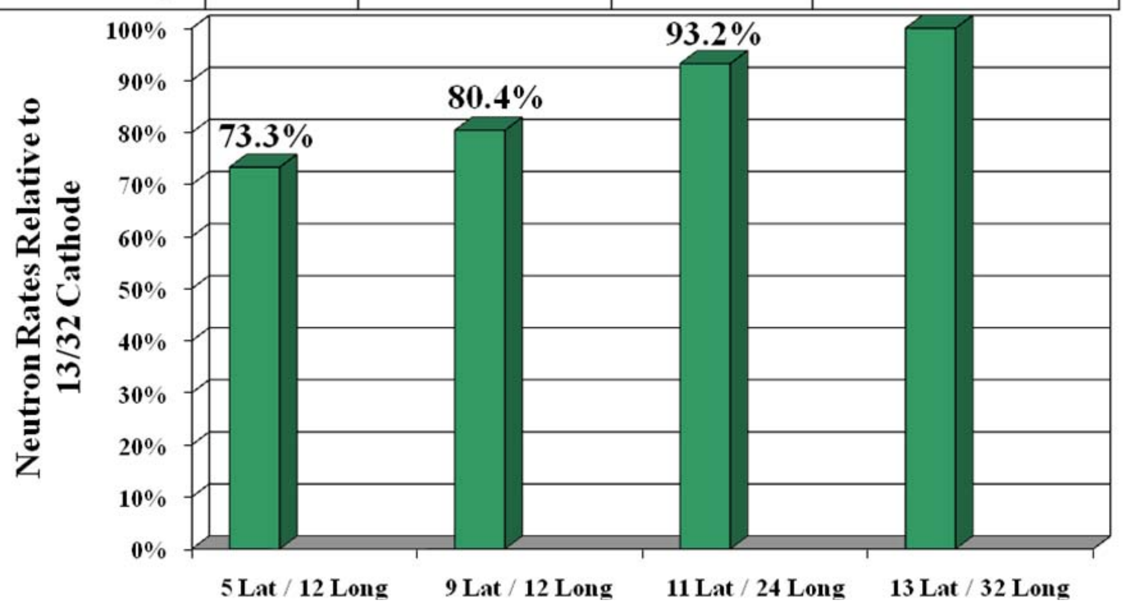

Figure 7.16 : Comparison of neutron production rates of all four cathodes relative to highest neutron producing cathode (13/32).

The experiments performed thus far have not determined the effect of the transparency and the number of potential wells independently of each other. All three cathodes constructed had different transparencies and different numbers of potential valleys. The 13/32 grid was constructed with the goal of trying to separate these two variables in order to try and determine the effects of each one. The intention was for the 13/32 grid to have a similar level of transparency as the 11/24 grid, but with more potential valleys. The 13/32 grid was built using a combination of 0.0762 cm diameter wire and 0.0508 cm diameter wire, while the 11/24 grid was made using only the 0.0762 cm diameter wire. By using this combination of thin and thick wire on the 13/32 cathode, a grid was able to made that had more holes but not at the cost of reducing the transparency. This was somewhat successful because the 13/32 grid had over 50 percent more potential valleys but had only a slightly lower transparency than the 11/24 grid (92.01% compared to 92.95%). Previous experiments conducted by Thorson and Demora, discussed in Chapter 3, indicated that transparency did not have a noticeable impact on neutron production rates, so more attention was typically paid to the number of potential valleys rather than the transparency during these experiments.

The results of the cathode studies conducted thus far seem to indicate that adding more wires to the cathode results in higher neutron production rates. An average increase in neutron rates of nearly 30 percent was measured between the least (5/12) and most (13/32) wired cathodes. The original cathode used in the IEC before these studies was the 11/24 cathode that was disabled by titanium coating, and a replica of this cathode was found to also produce lower rates than the 13/32 cathode. These studies have therefore not only resulted in a higher neutron producing cathode for HOMER than has ever before been used, but have also added insight into the operation of gridded IEC devices on the significance of the cathode design with regard to neutron production.

7.3.3 Separation between Anode and Cathode

Studies regarding the separation distance between the concentric spherical anode and cathode grids began as a result of an initial hypothesis that less separation between the grids would result in more fusion reactions in the system. The hypothesis was based upon the idea that if the distance between the grids was shortened, then there would be less distance over which parasitic charge exchange and dissociation reactions could occur and degrade the fast particle energy spectra. Experiments were planned to test this hypothesis, which involved varying the radius of the anode while keeping the cathode radius constant.

In order to conduct these experiments, a new 30 cm diameter anode was made to replace the 40 cm diameter anode that had been used up to that point. The 30 cm anode was originally designed to be a larger version of the 20 cm diameter 9/12 cathode, with which it was used in the W-12 configuration, so both the anode and cathode had the same number of latitude and longitude wires in order to attempt to line up the holes in the grids as much as possible. The construction of the 30 cm anode is shown in Figure 7.17. The construction method for the 30 cm grid was the same as the method for constructing the 20 cm diameter cathodes, except that hemispherical Styrofoam molds were used, which did not require the molds to be melted with acetone to use the grid.

Figure 7.17: Construction of 30 cm diameter anode.

The operation of the 20 cm cathode/30 cm anode configuration also required the introduction of a more rigid support system for our grids. Since there is a very large potential difference between the grids, there is an electrostatic force that tries to pull the grids together if they are not in the perfectly concentric equilibrium position. When the 30 cm anode was used, the gap between the grids had dropped to the point where the force at the higher voltage levels was strong enough to pull the anode towards the cathode, causing it to decrease the distance further between the grids until they eventually became close enough together to cause an arc and shutdown the system. This required an upgrade to HOMER in which stronger, more rigid supports for the anode were added.

Another improvement on HOMER that came about during the course of these experiments was a new method of positioning the anode in the chamber. Previously, the four support rods for the anode were attached to four independent swivel plates that rotated about a fixed point on the lid of the chamber. Since all four of these plates could be moved independently, it was very difficult to ensure that they were all in the same position each time, and correspondingly that the anode was positioned consistently in the same place. To remedy this, a circular jig was created from an aluminum plate that had preset tracks for the support rods. These tracks allowed for the rods to only travel in the radial direction with respect to the center of the cylindrical chamber so as to allow different anode sizes to be used, but the jig ensured that each support would always be positioned in the same place relative to the other supports. This added a significant level of repeatability to the placement of the electrodes. A photo of the current support system for the grids can be seen in Figure 7.18.

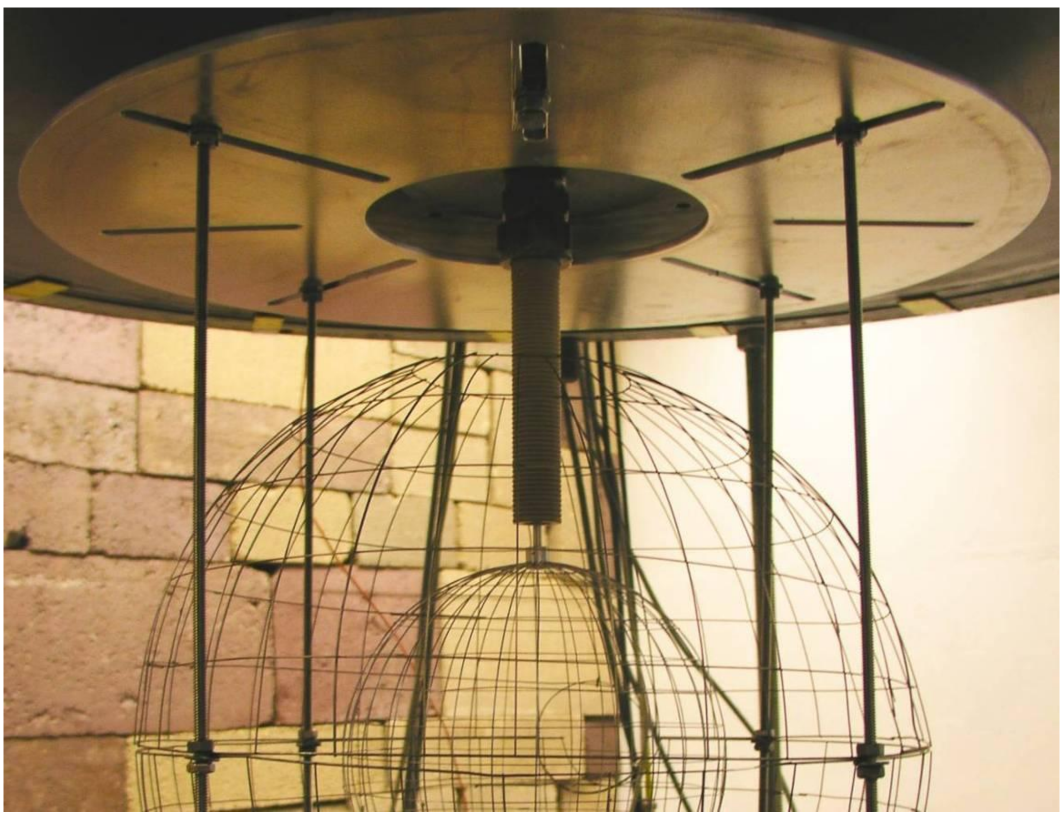

Figure 7.18 : Circular jig for grid support and repeatable positioning.

The results of varying the anode diameter are shown in Figure 7.19. The two configurations shown in the figure are nearly identical, the only difference being diameter of the anode used.

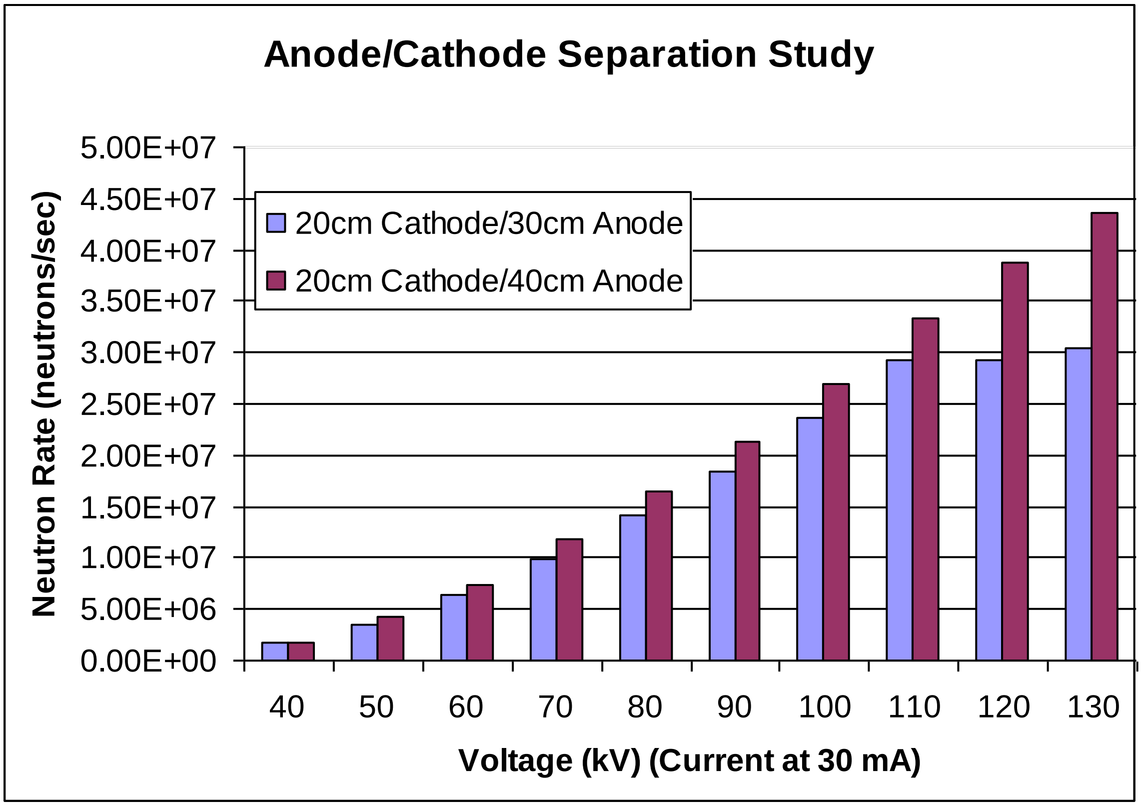

Figure 7.19: Comparison between 20 cm cathode/30 cm anode and 20 cm cathode/40 cm anode configurations.

As can be seen from Figure 7.19, the 20 cm cathode/30 cm anode configuration (20-30) yielded increasingly lower rates than our previous 20 cm cathode/40 cm anode configuration (20-40) as voltage was increased. The 20-40 configuration was found to have up to 40 percent higher neutron rates than the 20-30 configuration. This was in contradiction to the original hypothesis, but the experimental data added valuable insight to the theoretical models being created.

Another set of experiments was later performed, which compared the neutron rates between a 20 cm diameter cathode/40 cm diameter anode and a 20 cm diameter cathode/50 cm diameter anode configuration (20-50). The results are shown in Figure 7.20.

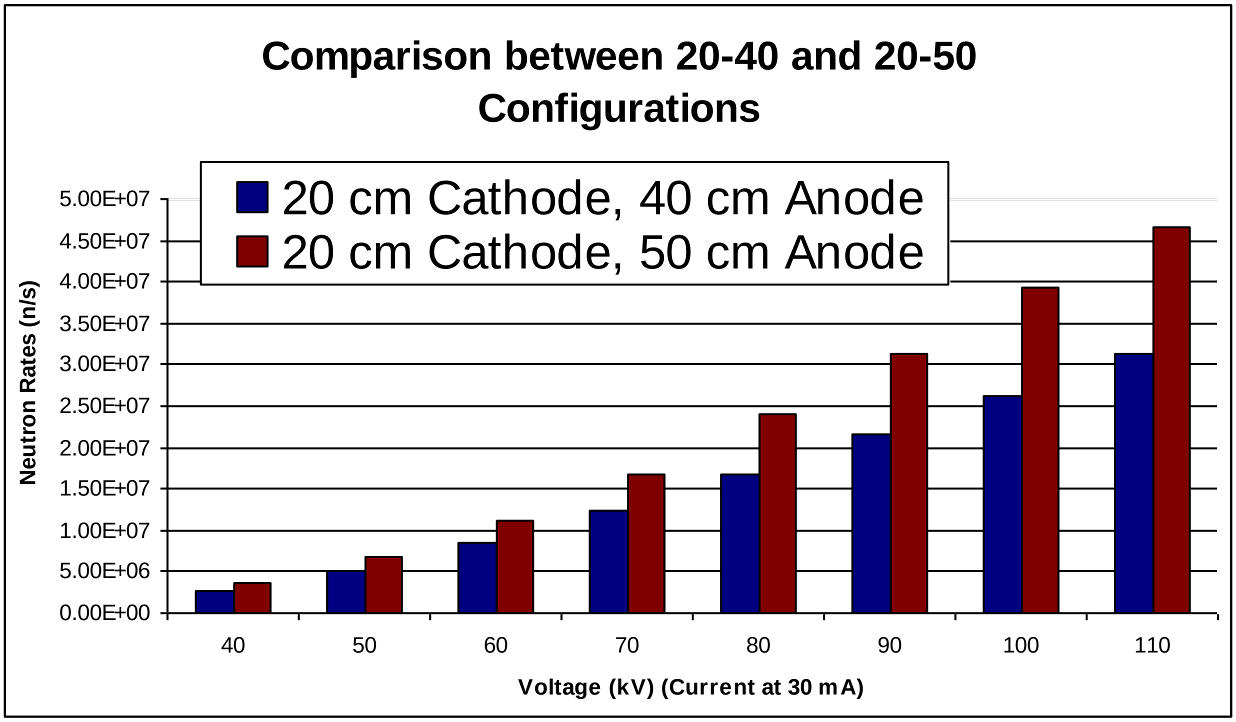

Figure 7.20 : Comparison between 20 cm diameter cathode/40 cm diameter anode and 20 cm diameter cathode/50 cm diameter anode configurations.

Once again, the larger electrode separation distance of the 20-50 configuration was found to result in higher neutron production rates than the smaller separation distance of the 20-40 configuration. In this case, the 20-50 configuration produced up to 50 percent higher rates than the 20-40 configuration.

The electrode grid separation studies indicate that in the mode in which HOMER is operating, if the cathode radius is held constant, then increasing the anode radius results in increased neutron production rates. There is almost assuredly a point at which increasing the anode radius further would result in a drop in neutron production due to atomic and molecular processes excessively softening the ion and neutral energy spectra. However, the 50 cm diameter anode is currently the largest sized spherical anode that could be fit into HOMER. Further study can be done by testing the effects of varying the cathode diameter while maintaining constant anode diameter, or by varying the diameter of both the anode and cathode. Previous experiments conducted by Radel and Wehmeyer discussed in Section 3.3 indicated that a 10 cm diameter cathode/50 cm diameter anode configuration (10-50) has lower neutron production rates than the 20-40 configuration. In this case, the larger separation distance of the 10-50 configuration did not increase neutron rates, which indicates that the absolute diameter of the cathode most likely has an important influence on the neutron production rates as well for pressure in the range of 2 mTorr and the voltage and current ranges in which HOMER is operated.

These studies regarding the separation distance between the electrodes evolked the use of the new Fusion Ion Doppler (FIDO) diagnostic developed by Boris [3]. FIDO is able to provide high resolution energy spectra of the fast particles in the IEC using the Doppler shift of the fusion products. This diagnostic allowed not only the neutron rates to be compared between the three cathode/anode configurations, but also allowed for the study of how the energy spectra of the fusion reactants changed as the anode diameter was varied. A more in depth discussion of FIDO and the results obtained from it can be found in a later chapter.

Chapter 7 References

1 Wehmeyer, A. L. (2005). The detection of explosives using an inertial electrostatic confinement D-D fusion device. (Masters thesis, University of Wisconsin – Madison)

2 , R. F. (2007). Detection of highly enriched uranium and tungsten surface damage studies using a pulsed inertial electrostatic confinement fusion device. (PhD dissertation, University of Wisconsin – Madison)

3 Boris, D. (2008). Diagnosing the high energy deuterium spectra in IEC devices using Doppler shifted fusion products. Proceedings of the 10th US-Japan IEC Conference, Kyoto, Japan

8 New High Voltage Feedthrough

In the summer of 2009, the high voltage power supply for the UW-Madison IEC Group was upgraded from a Hippotronics ® 200 kV, 75 mA supply to a 300 kV, 200 mA supply. The new supply was custom built for the IEC Group by Phoenix Nuclear Labs based out of Middleton, WI. The new supply made it possible to push the IEC devices to higher power levels than had ever before been achieved in the IEC community. Neutron rates have been shown to scale almost linearly on HOMER with both current and voltage up to the highest ranges achieved using the previous power supply, which were 165 kV and 68 mA. If rates continue to rise at this same rate, then it could be possible to raise the maximum neutron producing capabilities of HOMER by over 400 percent if the full capacity of the power supply could be utilized. However, in order to fully make use of the new supply, a new high voltage feedthrough design would have to be implemented.

In the past, the largest limitation on operating at high voltages has been high voltage arcing from the high potential of the cathode and the conducting rod to either the anode or more commonly the body of the chamber, both of which are grounded. High voltage arcing can occur through vacuum, plasma, dielectrics, or across surfaces. Arcs originate from high field points, particularly on any peaks or other features that extend towards ground and perturb the electric fields of the conductor causing a region of very localized, very large field concentrations. An arc can occur through a dielectric when the localized field strength surpasses the dielectric strength, which is capable of permanently damaging the dielectric material. The dielectric strength of the Boron Nitride (BN) insulator that surrounds the Molybdenum conducting rod is

66.9 kV/mm [1]. Section 7.2 details some of the various efforts that have been taken to minimize high field concentrations in the existing HOMER feedthrough.

These efforts allowed modest gains in operating capabilities at high voltages. However, the best way to minimize the probability of arcs at high voltages is to increase the separation distance between high voltage and ground. In the original feedthrough, the smallest separation between high voltage and ground occurs at the Swagelok ™ vacuum sealing nut, where there was only 1 cm of BN between the Molybdenum conducting rod and the grounded nut. This was the most common failure location from high voltage arcs through the dielectric for the BN stalks. Once an arc was able to blast a path through the BN creating what is known as a pin hole failure, the stalk was no longer of any use beyond 30 to 40 kV because the pin hole became the easiest path to ground and nearly all future arcs would take place there. Even arcs that are not able to blast through the BN are very troublesome when operating at high voltages, such as arcs across surfaces known as flash-over. These flash-over arcs can cause a sudden surge in current from the power supply, forcing the supply to shut down to protect itself. When operating at voltages on the order of 150 kV, these shutdowns can happen several times a minute, making high voltage operation very unstable and very difficult to collect useful data. Therefore, it is also necessary to maximize the minimum surface path length between high voltage and ground to minimize these surface arcs that plague high voltage runs.

The original HOMER feedthrough was constructed out of stainless steel and was entirely conductive. The solution to maximizing the distance between high voltage and ground was to switch to a non-conductive feedthrough, such that only the molybdenum rod and high voltage cable were at high voltages. This concept of using a mostly non-conductive feedthrough was first attempted on a different UW-IEC device known as SIGFE, constructed by Brian Egle [2]. A drawing of this feedthrough can be seen in Figure 8.1.

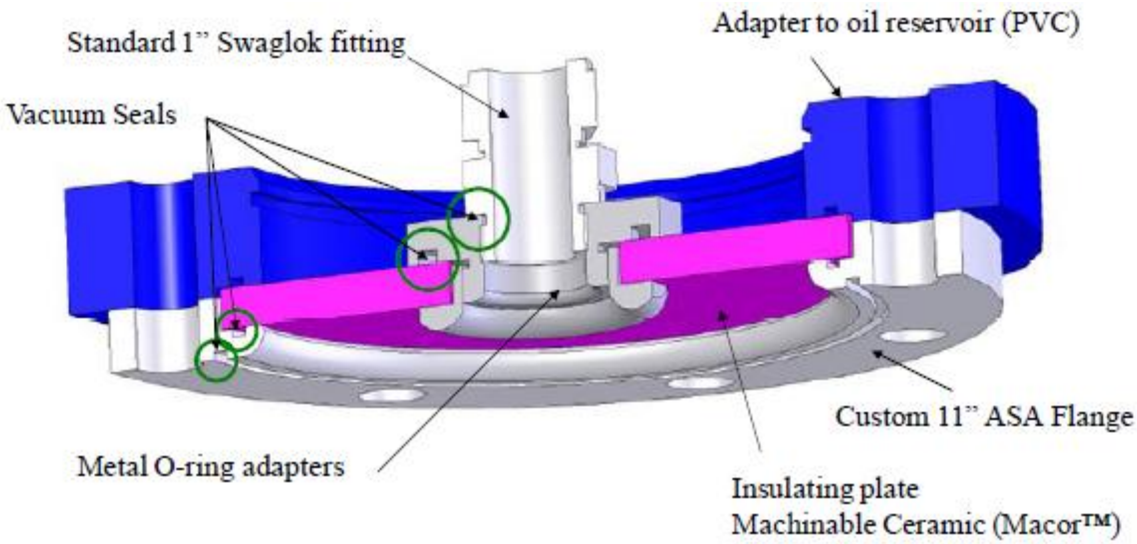

Figure 8.1 Drawing of non-conductive, isolated nut high voltage feedthrough design from SIGFE.

The concept for this design was to electrically isolate the Swagelok fitting around the BN stalk by placing it in the middle of a Macor ™ plate, which is an insulating machinable ceramic. The nut would then float at roughly half the potential of the high voltage conducting rod. Simulations were performed on this design using Maxwell 3D ®, which is a 3D electrodynamics modeling software, as well as the original HOMER feedthrough design. The simulations found that the new SIGFE feedthrough decreased the maximum field concentrations by a factor of 2.2 as compared to the original HOMER feedthrough. The SIGFE feedthrough was successfully tested to voltages up to -150 kV. One significant problem with this design however was that the Macor plate was prone to failure as a high vacuum interface. On two occasions, concentrated electron jets produced from the cathode of the IEC were believed to have hit the Macor plate, causing extreme heating of an isolated section that eventually led to a fracture in the plate. The fracture was then immediately exacerbated by the extreme pressure difference on the plate, causing the plate to crack and allowing the high voltage oil in the feedthrough to pour into the vacuum chamber. The Macor plate was eventually replaced by an aluminum plate to allow for operation at lower voltages on SIGFE.

The success of the non-conductive feedthrough concept on SIGFE led to the design of a similar concept on HOMER to be implemented to make use of the new 300 kV power supply. The goal was to utilize the ability to isolate the high voltage components and separate them as far from ground as possible while still maintaining structural stability and allowing operation in high vacuum and high heat. The new HOMER feedthrough had to meet a number of constraints:

1. Material – Non-conductive components had to be used to maximize distance between high voltage and ground.
2. Vacuum and Plasma Interface – For the vacuum facing components, materials could only be used that were vacuum compatible, mechanically strong enough to hold a microtorr of pressure, and able to survive exposure to plasmas and electron jets.
3. Vacuum Seal – A method of sealing the BN stalk in the feedthrough had to be developed without using conductive components.
4. Size – The space within which the entire HOMER experimental setup had to fit was constrained to the size of the shielded room in which HOMER resides, henceforth known as the Experimental Facility.

Quartz was chosen as the ideal vacuum interface barrier. Quartz has nearly the highest heat capacity of any industrial ceramic with an operable temperature limit of at least 1000 degrees Celcius, as well as a very high tensile strength of roughly 1000 psi allowing for excellent mechanical strength. The construction of a custom quartz feedthrough was commissioned with

Technical Glass Products, Inc. located in Painesville, OH. The final product can be seen in Figure 8.2.

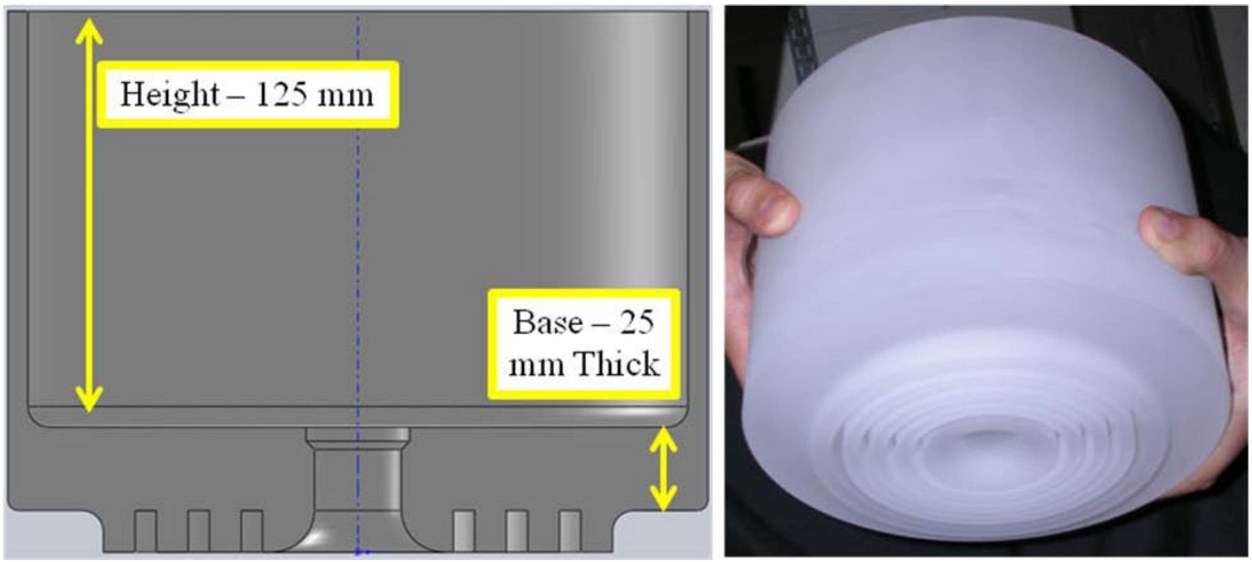

Figure 8.2 Quartz base for new HOMER high voltage feedthrough.

The quartz base is shaped like a bowl with a hole in the middle through which the BN stalk is placed. The bowl was created by first machining the bottom section from a solid cylinder of quartz. The cylindrical tower was then fused to the bottom section, making a solid bowl. The bottom of the quartz base is 25 mm thick, which is more than enough thickness to withstand the force of the vacuum pressure. Ridges were machined into the underside of the base in order to increase surface path length for high voltage arcs crossing over the surface. The minimum desirable surface path length for voltages up to 300 kV is approximately 38 cm. These ridges offer up to 9 cm of additional path length along the underside increasing the path from 9 cm to 18 cm, which translates into the ability to standoff approximately an additional 70 kV of potential as compared to not having them in place.

Another new feature was to remove the Swagelok seal all together and eliminate the last conductive component of the feedthrough outside of the Molybdenum rod. This was quite a challenge because there were no commercial methods for vacuum sealing the 2.5 cm diameter BN stalk in the feedthrough without using some sort of threaded metal compression system. The idea was eventually introduced to use an O-ring seal in which the compressive force was applied by a tower of PVC (Polyvinyl Chloride), which was driven down onto the O-ring by the force of a series of threaded rods located on the outside of the feedthrough body. A prototype was constructed to test this vacuum sealing method, a schematic of which can be seen in Figure 8.3 with a detailed view of the sealing mechanism in Figure 8.4.

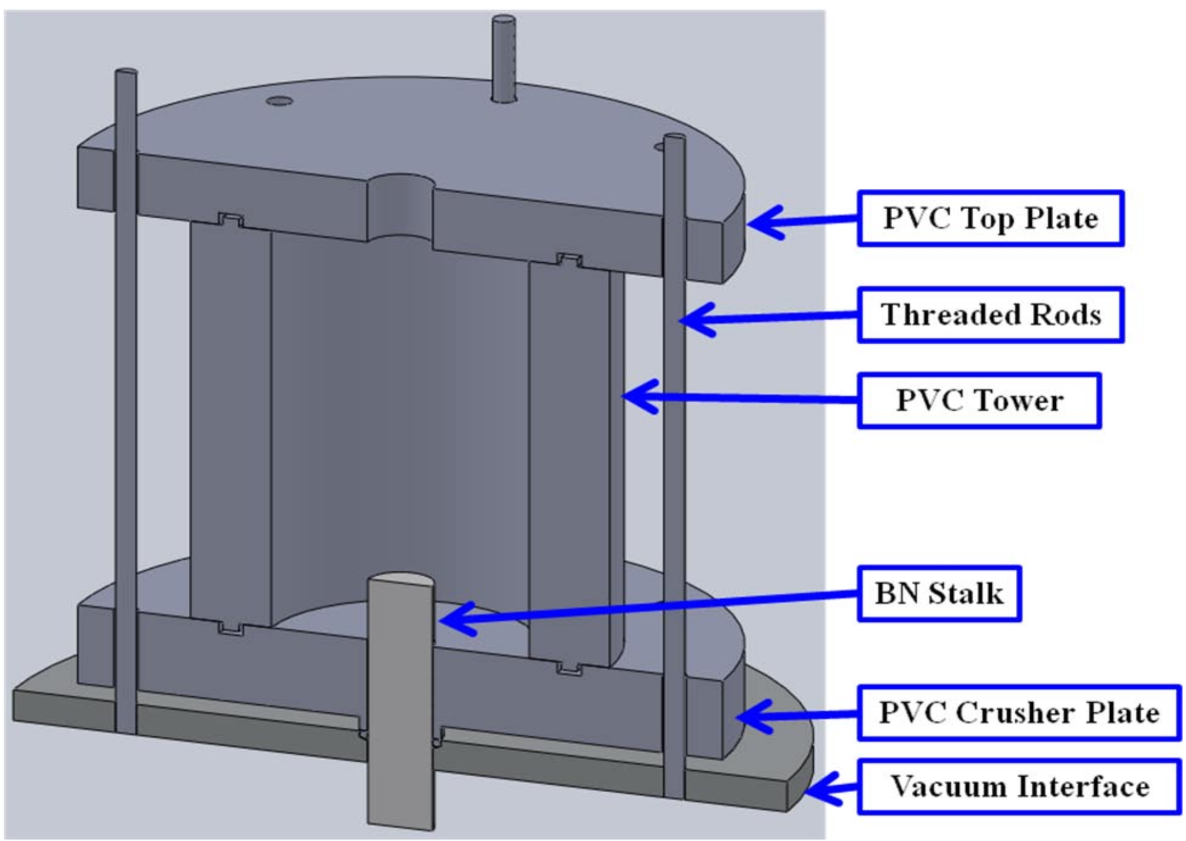

Figure 8.3 Prototype to test new vacuum sealing method for high voltage feedthrough.

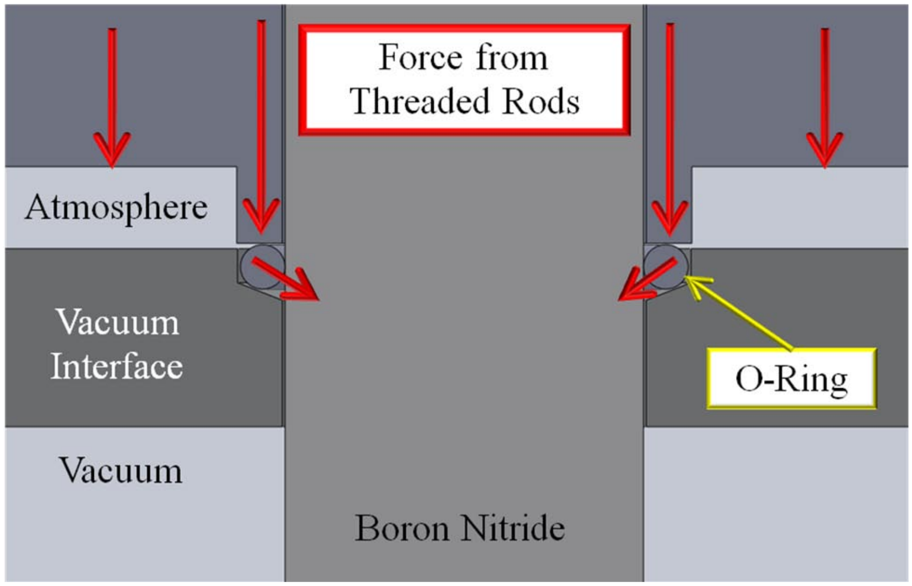

Figure 8.4 Schematic of vacuum seal around Boron Nitride stalk using a PVC tower to transmit a compressive force from a series of threaded rods to force the O-ring down the tapered groove to create a seal.

The prototype feedthrough successfully sealed down to a base pressure on the order of a microtorr with a solid 10 cm length of a 2.5 cm diameter BN rod in place. PVC was chosen as the primary building material for the atmosphere side of the new feedthrough because it had the best combination of mechanical and tensile strength, chemical resistance to the high voltage oil, dielectric strength (544 V/mm), machinability, relatively low cost, and it is self-extinguishing in case of fire. This method of vacuum sealing removes the metal fittings from around the BN stalk and takes the last conductive component outside of the main body of the feedthrough. After the successful testing of the prototype and the procurement of the quartz base, the final design for the feedthrough was completed and later constructed. The new high voltage feedthrough can be seen in Figure 8.5 and Figure 8.6.

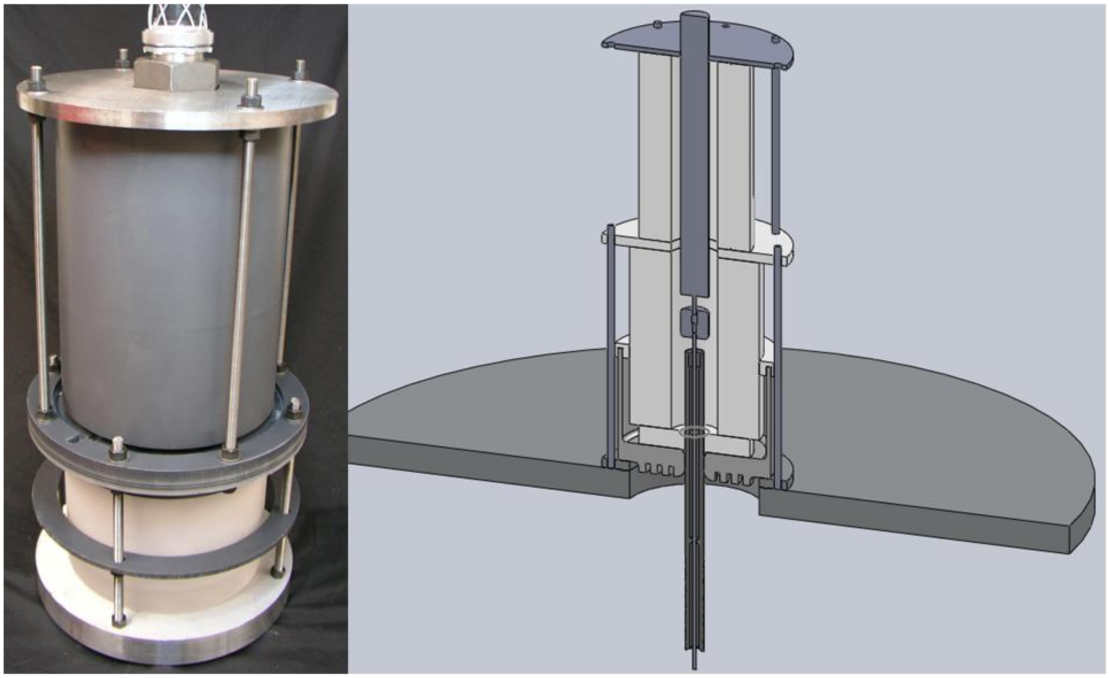

Figure 8.5 New HV feedthrough for HOMER designed for operation up to 250 kV.

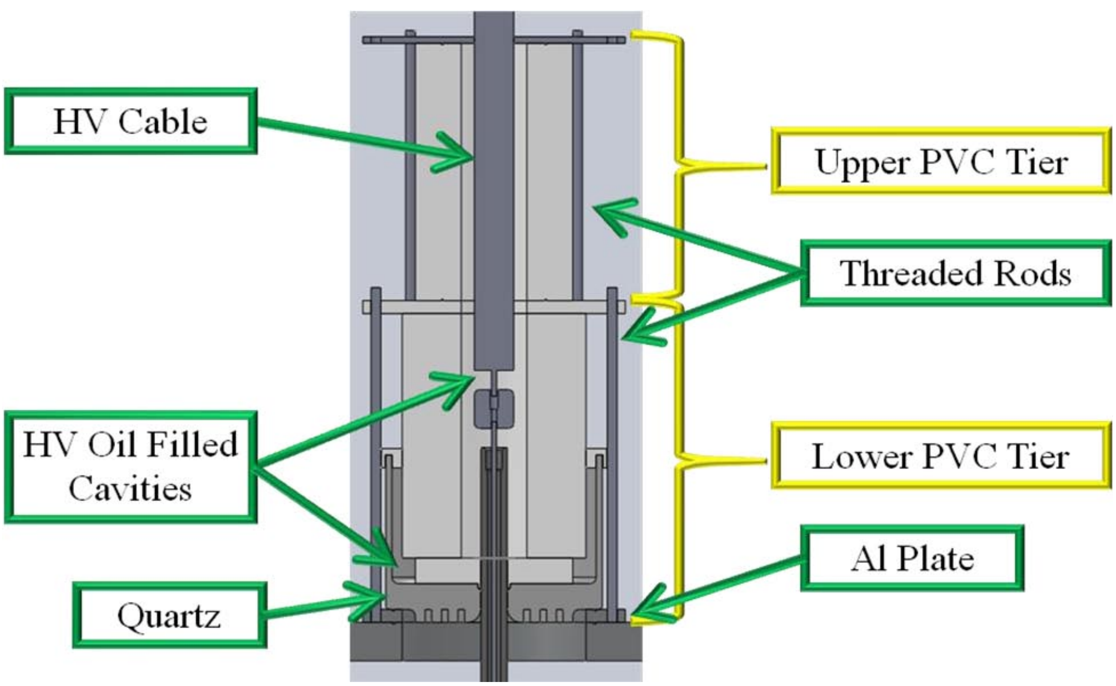

Figure 8.6 HV feedthrough divided into upper and lower tiers held together by threaded rods. Inner cavity surrounding HV cable filled with HV oil.

The central cavity surrounding the high voltage cable and other high voltage components is intended to be filled with high voltage oil. The oil has a high dielectric strength (12 kV/mm), and as a liquid it also has the valuable properties of being a self-healing substance if an arc occurs and it is better able to remove heat from the high voltage components. The ability to cool the high voltage components will prove critical at high power operation, and since the rest of the feedthrough body is made of PVC, which is not a good thermal conductor, a method has to be in place to allow heat to be removed from the system in an efficient manner. The option now exists to put a system in place to pump out the oil in the feedthrough as it is heated and pump in cool oil to effectively remove the heat from the central cavity. A thermocouple probe will also be necessary in this central cavity to keep a constant reading on the temperature of the system to ensure maximum thermal tolerances of the PVC as well as the O-Ring seal at the bottom of the central cavity have not been reached.

As can be seen from the figures, the final design is constructed using two separate tiers that are connected to each other using threaded rods and joining plates. This design is primarily due to a size constraint for the feedthrough dictated by the height of the Experimental Facility in which HOMER is located. The total height of the body of the new feedthrough is approximately 590 mm, compared to a height of roughly 310 mm for the original feedthrough (shown in Figure 7.6). The increase in height of the new feedthrough was necessary to allow for the increased surface path length required to standoff the new voltage range of 250 to 300 kV. The BN stalk then extends another 250 mm below the feedthrough. The distance between the lid of HOMER and the ceiling of the Experimental Facility is enough to allow the body of the feedthrough to be placed on top of HOMER, but is insufficient to allow for the new feedthrough to be put into place with the stalk extruding from the bottom. The high voltage cable also extends 380 mm into the feedthrough, which means that there must be sufficient height above the feedthrough to accommodate the cable length plus the bend radius of the cable. Therefore, the feedthrough was designed as two separate sections.

The bottom section is almost identical in basic design to the prototype shown in Figure 8.3, with the quartz base now acting as the vacuum interface. The bottom tier has its own set of four threaded rods to allowed it to be vacuum sealed independent of the top tier. This allows the bottom section to be fully assembled external to the Experimental Facility and then put into place on HOMER because its height is sufficiently small to fit within the boundaries of the Experimental Facility. The top tier is much simpler in design and consists primarily of a cylinder of PVC with a channel bored through the center through which the high voltage cable is placed. The high voltage cable is placed inside the top tier and then the assembly is secured into place on top of the bottom tier using a second set of four threaded rods after the bottom tier has already been placed on the lid of HOMER. This allows for a greater height, and therefore greater surface path lengths, while working within the spatial constraints of the Experimental Facility. The length of the BN stalk has also been increased from 300 mm in the original design to 400 mm in the new design, which allows for greater surface path length to reduce arcing.

Another effort aimed at increasing the total distance between the chamber lid and the Experimental Facility ceiling was to redesign the support system for HOMER in order to allow for the chamber to be dropped by an additional 125 mm. This was done by replacing the original fixed aluminum support structure for HOMER with a pre-assembled 80/20 ™ support system. A diagram of the new structure can be seen in Figure 8.7. The cylindrical section in the middle of the structure represents the turbopump assembly, which is attached to the bottom of HOMER and is the primary limiting factor on how low the chamber can be dropped. The additional 125 mm of height provided by the new supports allows for an increase in surface path lengths in the feedthrough that translate into up to 100 kV of additional high voltage standoff capability.

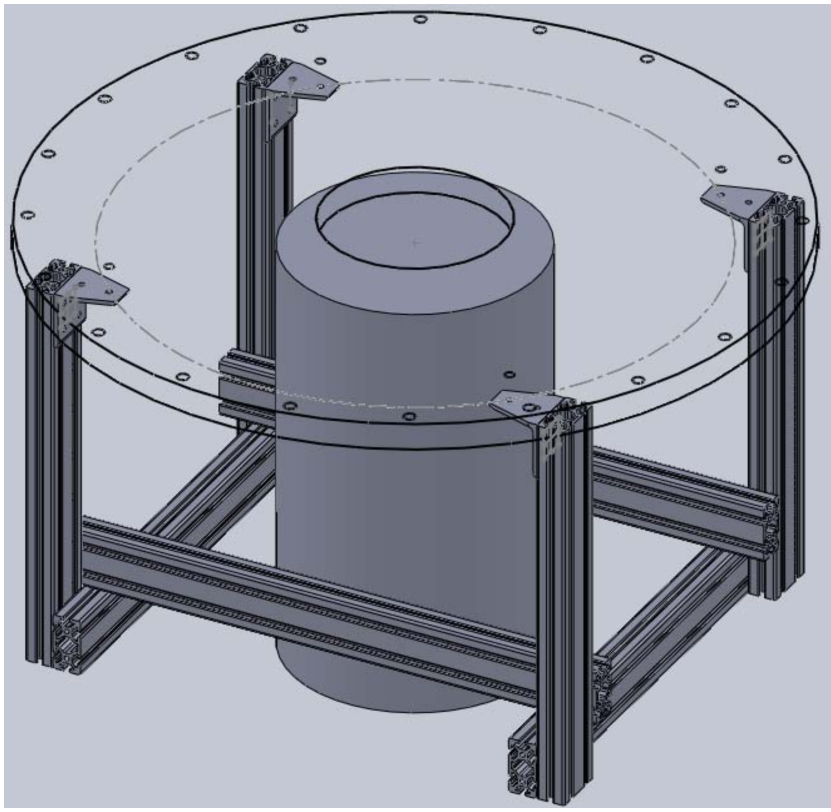

Figure 8.7 New support structure for HOMER allowing 125 mm of additional height for feedthrough.

Before the construction of the feedthrough, a series of Maxwell 3D ® simulations were performed on the original HOMER feedthrough and the new design. The results of these simulations can be seen in Figure 8.8. As was mentioned previously, the majority of all BN stalk failures on the original design occurred at the Swagelok nut, which is the location with the closest separation between high voltage and ground. When the maximum field concentrations at that location are compared to the analogous location on the new feedthrough in which the Swagelok nut and all other conductive and grounded components are removed, the maximum fields for the new design are a factor of approximately 3.5 lower. The simulations for the SIGFE design discussed previously noted a drop in field concentrations of 2.2, so this new design represents a further improvement in the high voltage standoff capabilities.

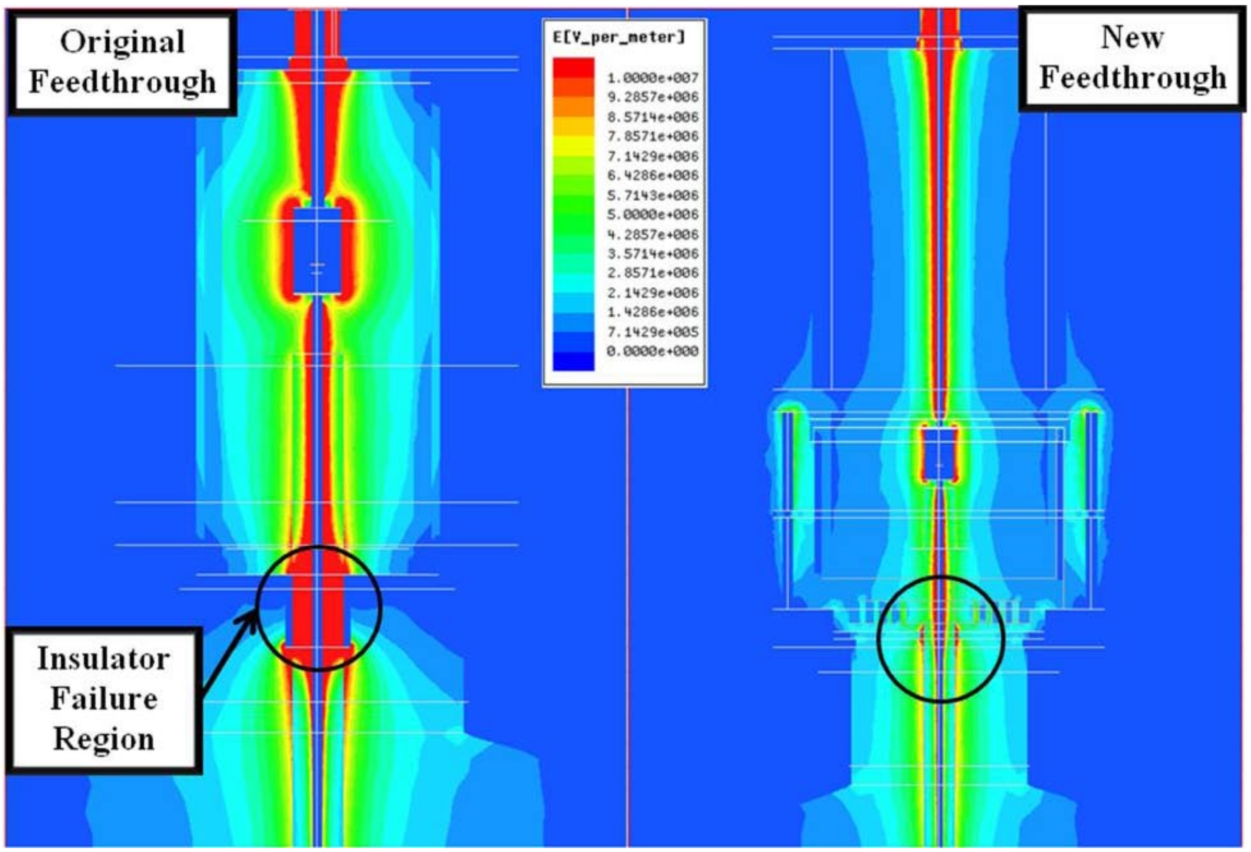

Figure 8.8 Maxwell 3D simulations of HOMER feedthrough designs. Drawings are not at the same spatial scale but use the same electric field scaling. Maximum field concentrations at the point of most previous stalk failures dropped by a factor or roughly 3.5 with the new design.

The minimum surface path length between high voltage and ground for the new design is 320 mm, which corresponds to a high voltage standoff capability of roughly 250 kV. The minimum surface path length in the original feedthrough was on the order of 100 mm, so the new design represents a significant improvement in the mitigation of flash-over arcs. The surface path length for the new feedthrough is still slightly less than the full length necessary to fully standoff 300 kV, but the existing length should still be capable of dramatically reducing the number of flash-over arcs that occur in the system and limit them to only the highest voltage operations.

Chapter 8 References

1 Saint-Gobain Ceramics, (2003). Combat® solid boron nitride: technical overview datasheet. Retrieved February 2, 2010, from www.bn.sain-gobain.com

2 Egle, B. J. (2010). Nuclear Fusion of Advanced Fuels Using Converging Focused Ion Beams. (PhD Dissertation – University of Wisconsin-Madison)

9 Fusion Ion Doppler (FIDO) Diagnostic

The Fusion Ion Doppler (FIDO) diagnostic is a tool developed by Boris [1] used to gather D-D fusion product and reactant energy spectra within a well defined solid angle view of the chamber without the high levels of background x-ray noise created in the IEC. The detection of the fusion products within a restricted view of the chamber is accomplished using a variant of the collimated proton detector setup. The standard collimated proton detection scheme involves a straight collimator channel with a proton detector at one end. Typically, one or several irises are put into place in order to control the number of particles reaching the detector. The length of the collimator and the diameter of the irises determine the size and shape of the solid angle in which protons can be collected. The longer the collimator or the smaller the irises, the more acute the angle of the conical observed volume becomes. The primary variation in FIDO is the shape of the collimator, which in this case is not a straight channel but rather an arm with roughly a 20 degree bend at the elbow. The development of the FIDO Diagnostic by Boris was instrumental to the construction and utilization of the Time of Flight (TOF) Diagnostic accomplished by the author, discussed further in Chapter 10. A schematic of the FIDO setup can be seen in Figure 9.1.

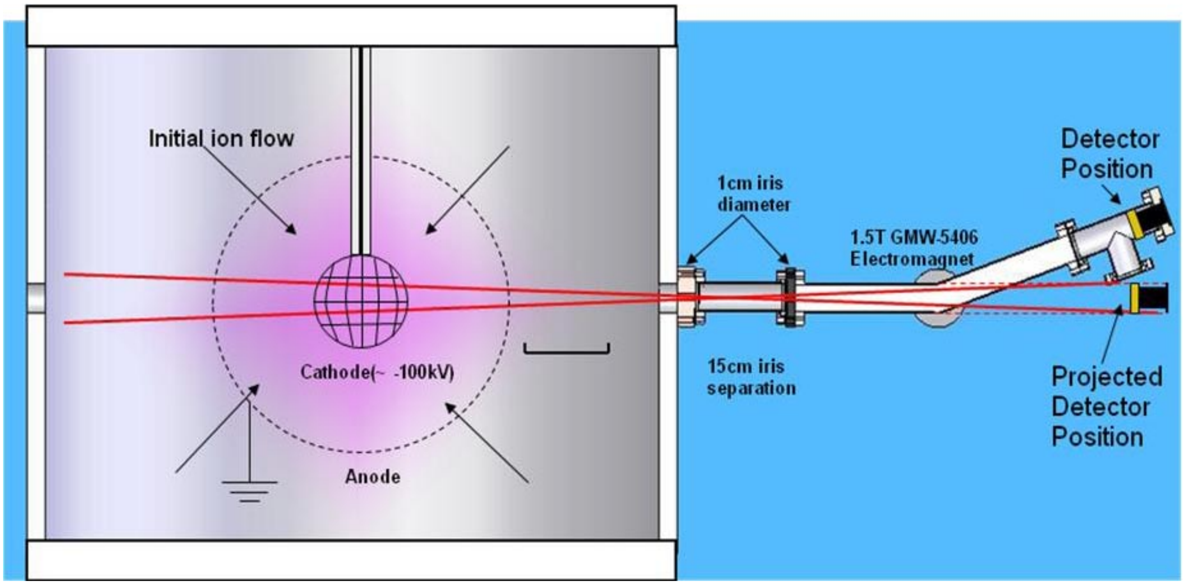

Figure 9.1 : Schematic of FIDO on HOMER including projection of solid angle view (red) of the chamber [1].

The bend in the collimator arm is the reason why FIDO is able to collect energy spectra with low levels of background noise. Typical collimated proton detector experiments conducted in the past by individuals such as Thorson or Masuda (see Chapter 2) have dealt with noise reduction by using a 25 μm thick lead foil in front of the detector, which is thick enough to stop most low energy x-rays, but not the 3.02 MeV protons emitted from the D-D reaction. However, the lead does cause slight distortions of the energy spectra of the protons that make it through the foil, which makes it difficult to get precise readings within a few hundred keV. The ability of the lead to attenuate x-rays also diminishes as the x-ray energy increases, making it difficult to block out high energy noise. FIDO accomplishes its noise reduction by moving the detector out of the line of sight of the x-rays by placing it at the end of the bended arm, allowing no direct path between the inside of the chamber and the detector face. However, this means that not only is there no direct path for the x-rays, there also is no straight line path for the fusion products to take to reach the detector face. This issue is resolved using a roughly 8 kG magnetic field, which bends the charged particles around the elbow of the arm and allows them to travel to the detector without colliding with any surface previous to reaching the detector. The detector used in FIDO is an Ortec Model BU-XXX-450-500-S Ultra Ion-Implanted Light Tight detector with an active area of 450 mm^2 and a minimum depletion depth of 500 µm. The detector also had a 300 nm thick Light Tight Coating, which was able to shield the detector from noise pollution from visible light photons. The detector has a Microdot ™ Female connector on the backside, which connects to a Microdot Male to Accufast ™ adapter that was custom made by Accuglass. The adapter then attaches to a quick release Klein Flange (KF) with a BNC type RF connector for a coaxial cable on the atmosphere side. The magnetic field is provided by a 1.5 T electromagnet with poles on either side of the elbow of the arm. A more detailed view of the arm and the placement of the magnet can be seen in Figure 9.2.

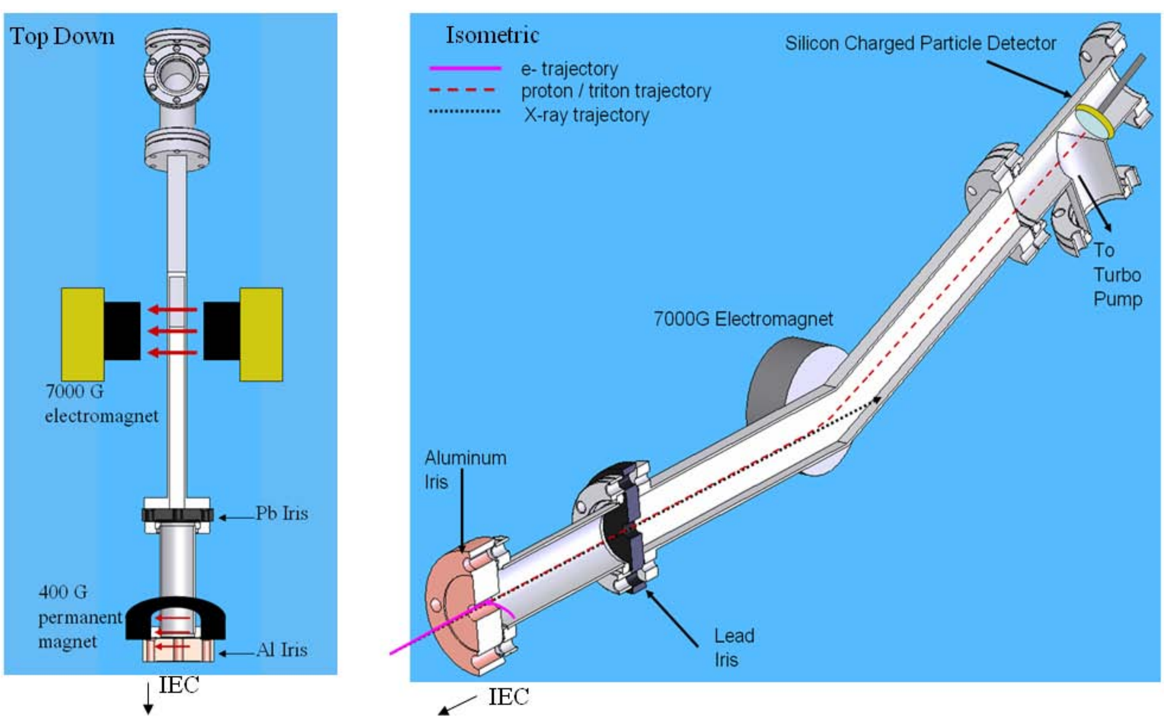

Figure 9.2 : Schematic design of FIDO arm by Boris and placement of electromagnet [1]

Previous computational modeling of the FIDO setup using the ion trajectory modeling software SIMION accomplished by Boris have found that at 8 kG, both the 3.02 MeV protons and 1.01 MeV tritons are able to be bent around the elbow and reach the detector face. Since x-rays have no charge, they will not experience any electromagnetic force and their only path to the detector is by scattering off the channel all the way up the arm. Preliminary testing of FIDO demonstrated a significant decrease in background noise in the energy spectra collected by the detector relative to the standard straight arm collimated proton detector. The comparison between the two configurations can be seen in Figure 9.3.

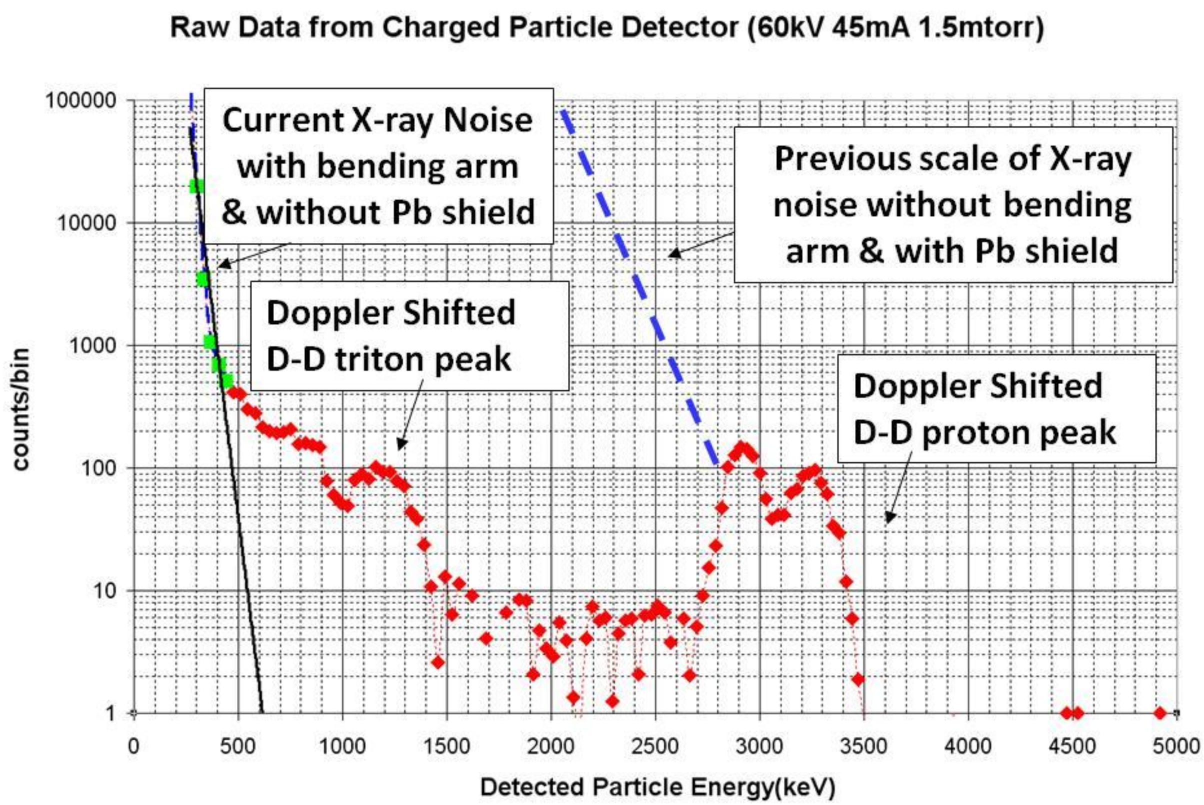

Figure 9.3 : Energy spectra collected by FIDO setup compared to noise level collected using standard straight arm collimator setup [1].

As can be seen from the above figure, the noise in the previous collimated detector setups completely overwhelmed the triton energy signature and permeated all the way up to the proton energy peak at 3.02 MeV, causing significant distortion of the proton peak such that the Doppler shift of the protons could never be discerned.

The Doppler shift of the fusion products is the result of the center-of-mass energy of the fusion reactants. The vast majority of fusion events occurring in the IEC device are believed to be a result of beam-background fusion, which occurs when fast deuterium ions or neutrals collide and fuse with a background neutral deuterium particle with almost no energy relative to the fast particle. The total velocity of the fusion reactants, v_t, is made up of the center of mass velocity, v_{cm}, and the velocity imparted by the energy of the fusion reaction, v_f, and the angle between the two, Θ. The center of mass velocity is a function of the mass and velocity of both reactant particles creating the fusion event:

$$v_{cm} = \frac{m_1 v_1 + m_2 v_2}{m_1 + m_2} \equiv \frac{m_1 v_1}{m_1 + m_2} \tag{9.1}$$

The last part of the equation is due to the assumption previously mentioned that the fast particles are primarily hitting neutral background particles, which would have a velocity (v_2) of roughly zero. The kinetic energy of the center of mass is then:

$$E_{cm} = \frac{1}{2}(m_1 + m_2) v_{cm}{}^2 = \frac{1}{2} \frac{m_1{}^2 v_1{}^2}{m_1 + m_2} \tag{9.2}$$

The energy available for fusion to occur is then:

$$E_{fus} = \frac{1}{2}\frac{m_1 m_2 v_1^{\ 2}}{m_1 + m_2} \equiv \frac{\mu_{12} v_1^{\ 2}}{2} \qquad \textbf{(9.3)}$$

Where μ_{12} is the reduced mass of the system. The center of mass and fusion product velocity components are then related by the Law of Cosines:

$$v_t = \sqrt{v_f^2 + v_{cm}^2 \pm 2 v_{cm} v_f \cos\Theta} \qquad \textbf{(9.4)}$$

The fusion velocity remains constant, but v_{cm} can vary depending on the energy of the reactant particles, which creates a range of possible values of v_t that takes a shape of a sphere in velocity space in which each variation of Θ creates a differential ring of thickness, $2\pi v_{cm} \cos\Theta\Big|_{\Theta}^{\Theta+\Delta\Theta}$, as shown in Figure 9.4.

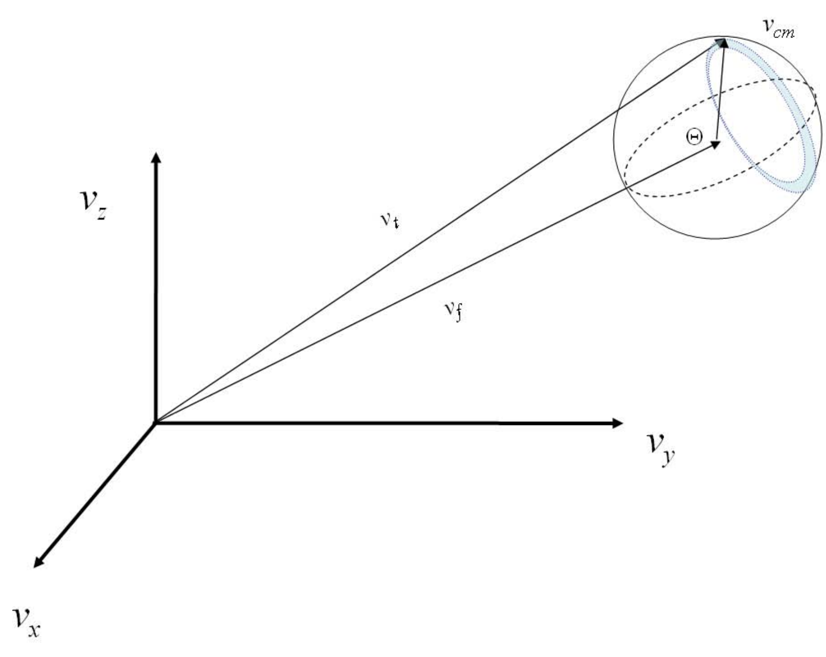

Figure 9.4 : Sphere traced out by variation of v_t in velocity space [1].

The collimation of the proton detector along the arm of FIDO acts to simplify this range of values significantly by forcing the detector to only be able to see the (cosΘ = ±1) fusion reactions. The collimator arm, along with the aid of the aluminum and lead 1 cm diameter irises shown in Figure 9.2, ensure that the detector only collects the energy spectra of those fusion products that are created within a narrow solid angle volume of the chamber. This allows only those particles travelling parallel to the length of the collimator arm to reach the detector. In order for the v_t of the fusion products to be in the direction parallel to the collimator channel, then v_{cm} and v_f must have been moving either nearly parallel or anti-parallel to the path of the collimator. The anti-parallel case occurs because every two-body fusion reaction involves two fusion products moving in the exact opposite direction of each other in the center of mass frame in order to conserve momentum, so v_{cm} could have been travelling on the anti-parallel path away from the detecting arm and one of the two fusion products would still be travelling in the direction towards the detector.

For this analysis, nearly all fast particles in the system are assumed to be moving in only the radial direction either towards or away from the center of the spherical symmetry. Even charge exchange and dissociation reactions that result in the creation of fast neutrals, which are no longer accelerated towards the center by electrostatic forces, will still result in the neutral continuing to move in the radial direction since that is the direction it was heading as a fast particle before the charge exchange occurred (further information on angle of deflection due to impact with background particles found in [1] Boris, *et al*). As a result, nearly all fast particles that enter the detector must have been traveling either parallel or anti-parallel to that line of sight. A small number of fusion events are able to form near the exact center of the device that occur as a result of a fast particle that was not travelling along this line of sight but are still able to create a reaction whose products are capable of reaching the detector. However, this event can only occur if the velocity of the reactants in the perpendicular direction to the line of sight of the detectors is sufficiently smaller than the parallel velocity to allow the reactants to still make it through both irises. The maximum perpendicular energy permitted for an event such as this to occur depends upon the diameter of the irises (d_{iris}) and the distance between the two irises (R_{iris}), which are related in the following manner:

$$E_{\perp} = E_{\parallel}\left(\frac{d_{iris}}{R_{iris}}\right)^2 \tag{9.5}$$

For the current settings of 1 cm diameter irises and 15 cm separation between the irises, the perpendicular energy of the reactants would have to be 1/225 of the parallel energy in order to allow their fusion products to be counted. Thus the cos(Θ) can be treated as $\pm$1. The resulting equation for v_t then becomes:

$$v_t = \sqrt{v_f^2 + v_{cm}^2 \pm 2v_{cm}v_f} \tag{9.6}$$

The Doppler Shift is the range of energies that the fusion product can have, defined by the magnitude of v_{cm}:

$$v_f - v_{cm} < v_t < v_f + v_{cm} \tag{9.7}$$

The proton and triton energies can be shifted either up or down depending on whether v_{cm} was moving parallel or anti-parallel relative to the line of sight of the detector. These upshifted and downshifted fusion products create two peaks that straddle the fusion energy of the fusion proton at 3.02 MeV and the triton at 1.01 MeV, as can be seen occurring for both the proton and triton signatures collected using FIDO shown in Figure 9.5.

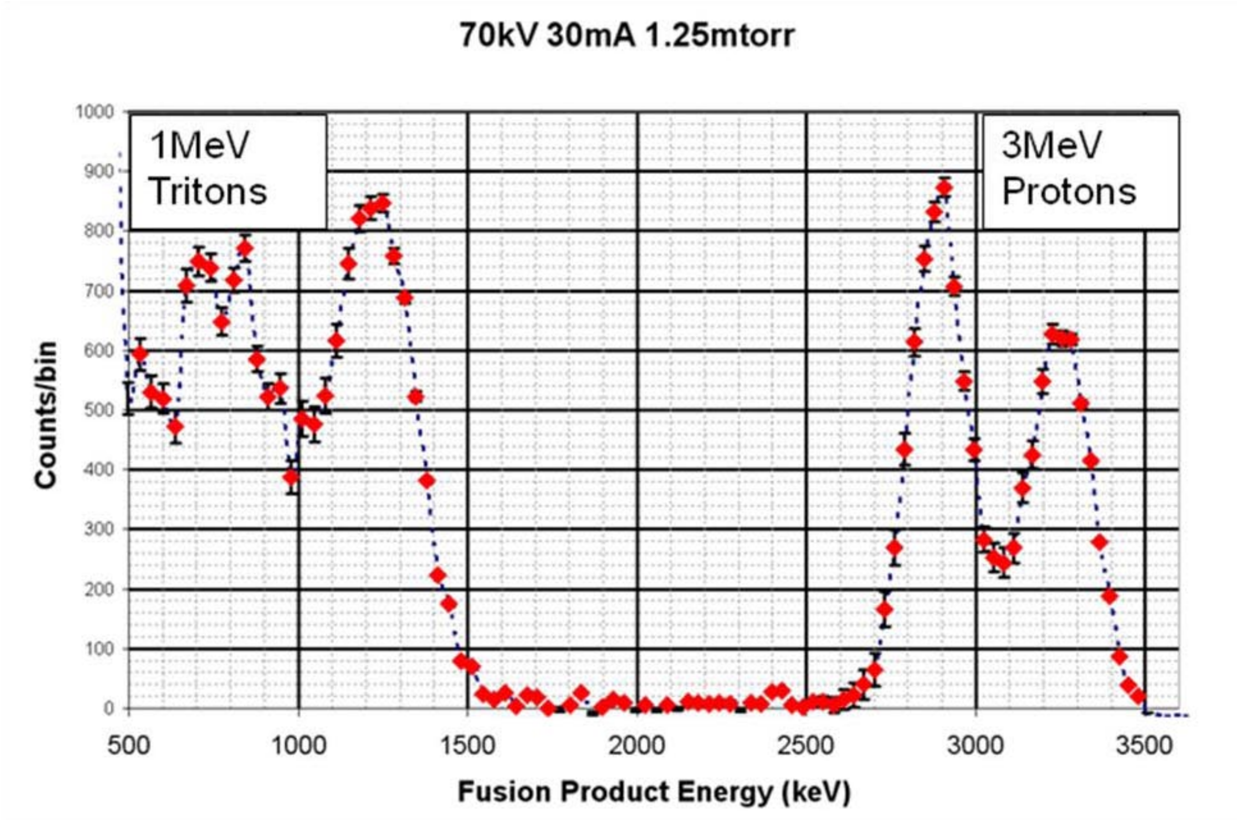

Figure 9.5 : Energy spectra of protons and tritons created by D-D fusion reaction collected by FIDO demonstrating the upshifted and downshifted Doppler peaks [1].

The ability of FIDO to discern these Doppler peaks and accurately measure the shift of the protons is what allows for the energy spectra of the fusion reactants to be back calculated. The energy of the particle collected by the detector is related to v_t by: $E_{detector} = ½\, m_{proton} v_t^2$. Using this relationship, the value of v_t for each particle collected by the detector can be calculated based on the energy of the detected particle. Since the energy imparted to the particle by the fusion reaction is a known constant, then v_{cm} can then also be calculated, which then provides the center-of-mass energy of the fusion reactants that created the event. This can then be taken a step further and the fusion cross sections, $\sigma_{fusion}(E_{\text{fast particle}})$, can be used to determine the likely number of particles in that solid angle view of the detector with that specific energy based upon the number of fast particles counted at that energy level divided by the corresponding probability of a particle with that energy creating a fusion event. A plot of the D(d,p)T fusion cross sections are shown in Figure 9.6.

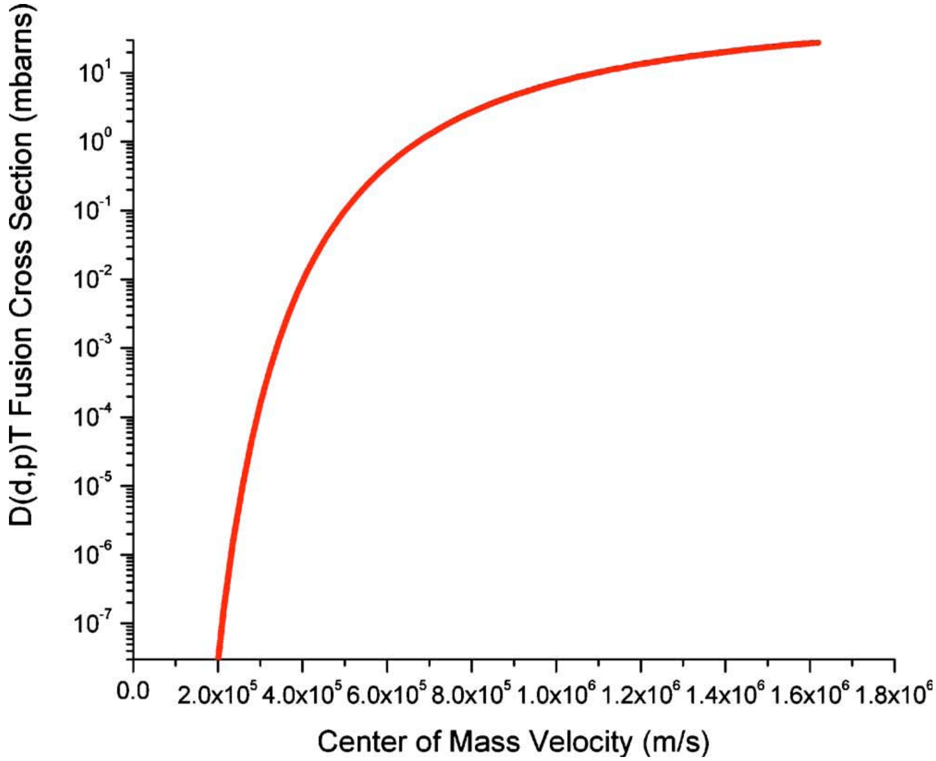

Figure 9.6: Plot of cross sections of D(d,p)T fusion reaction with respect to center of mass velocity of reacting deuteron.

The results of this back calculating are fusion reactant energy spectra similar to the one shown in Figure 9.7.

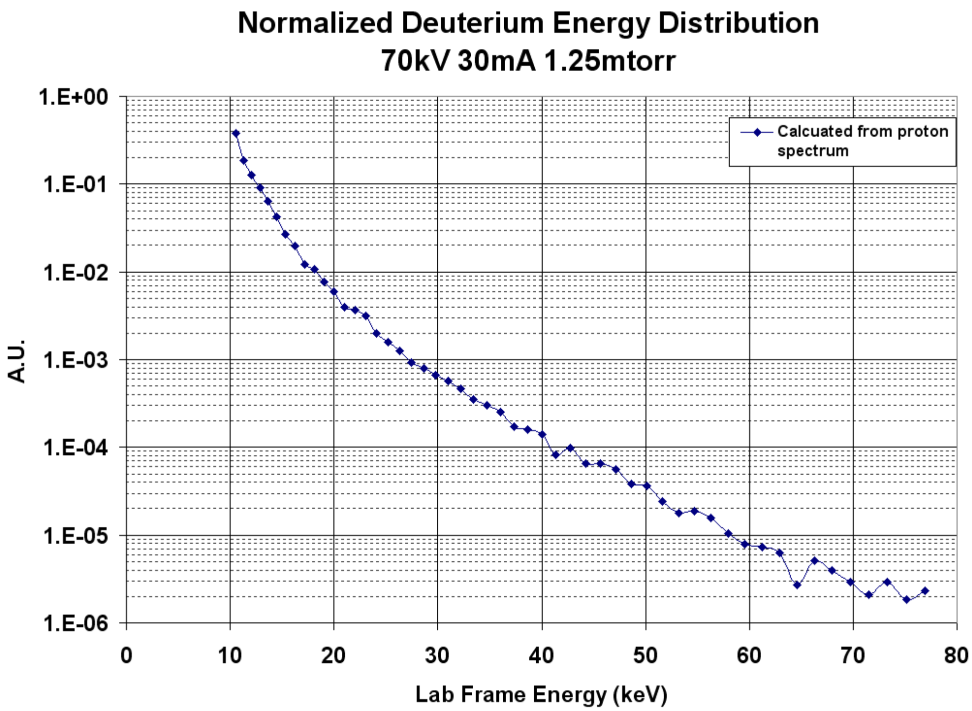

Figure 9.7 : Energy spectra of fusion reactants in HOMER collected by FIDO for settings of 70 kV, 30 mA, 1.25 mTorr (A. U. represents Arbitrary Units) [1].

The vertical axis of Figure 9.7 indicates the relative number of fast particles with a given lab frame energy. One may notice that although this spectrum was recorded at a cathode voltage of 70 kV, there are very few 70 keV fast particles creating fusion events. This is believed to be due primarily to parasitic charge-exchange reactions, which cause fast ions that have fallen only part way down the electrostatic potential hill to become fast neutrals while, along with ionization, creating cold ions that can only pick up at most the remaining energy of the potential hill below the birth point. This greatly degrades the energy spectra of the fast particles in the system. These findings provided important experimental benchmarks for the theoretical and computational models on charge exchange and atomic and molecular interactions being conducted by Emmert and Santarius (see Section 2.8).

The FIDO diagnostic was used by Boris to collect energy spectra for a range of voltage, current, and pressure conditions. It was also applied to the previously discussed optimization study on the separation distance between the electrodes of HOMER conducted by the author. As discussed in Section 7.3.3, a 20 cm diameter cathode was tested with anodes of diameter 30, 40, and 50 cm creating the 20-30, 20-40, and 20-50 configurations, respectively. In each case, neutron production rates and FIDO energy spectra were collected and compared. The neutron rates indicated that as the separation distance between the electrodes increased, the fusion rate increased. The energy spectra collected by FIDO helped to provide an explanation for this trend. Figure 9.8 shows the upshifted Doppler peak of the fusion proton portion of the energy spectra for all three configurations.

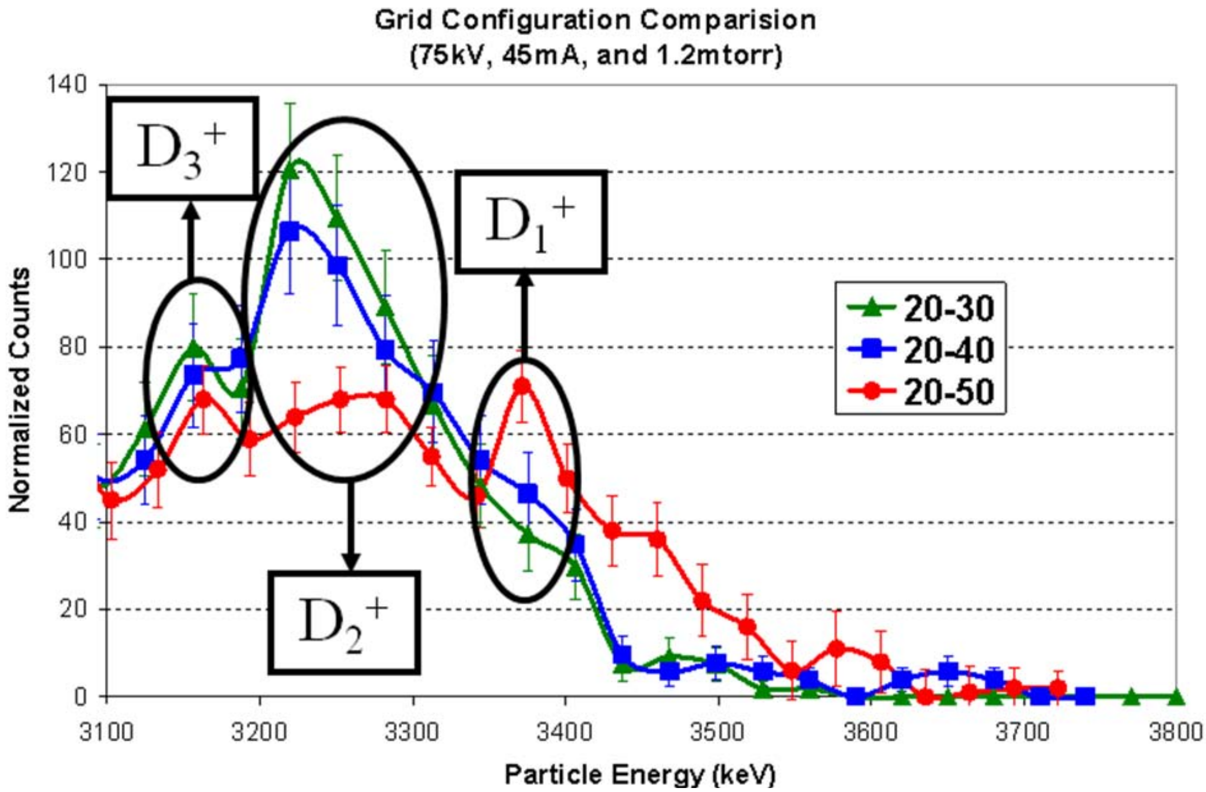

Figure 9.8 : Upshifted Doppler peak of the D-D fusion protons in HOMER at 75 kV, 45 mA, 1.2 mTorr for three different cathode/anode configurations with possible peaks due to different molecular ion species [2].

In the above figure there are three distinct peaks within the upshifted Doppler peak of the fusion protons. These peaks are believed to represent the three molecular ion species that make up the source region of the IEC. Previous experimental and theoretical research performed by Emmert and Boris [3] have shown that the source region is made up of, in order of increasing fraction of the source region, D_1^+, D_2^+, and D_3^+ molecular ions. The difference in mass between the three molecular ion species causes a slightly different Doppler shift to occur for the fusion proton depending on which molecular ion was responsible for the fusion event, because the ion's energy is equipartitioned among its atoms. The FIDO spectra have found that they create discrete peaks within the Doppler peak as shown above.

As the molecular ions are accelerated inward from the source region to the cathode, they experience collisions with background neutrals that can cause D_3^+ to break up into D_1^+ and D_2^+, and D_2^+ to break up into D_1^+ (see Figure 2.8). The distance between the electrodes and the pressure affects the probability that the molecular ions will experience collisions and subsequent dissociations, and the larger the distance, the more likely dissociation events will occur. Since the source region has been found to be made up primarily of D_3^+ molecular ions, then at close separation there would be a higher number of D_3^+ ions reaching the cathode intact. As the separation increased, then the relative number of D_3^+ ions reaching the core would decrease and more D_1^+ and D_2^+ ions would be created. This is exactly what was found to occur in the FIDO energy spectra seen above. The configuration with the shortest distance between electrodes, the 20-30 configuration, had the highest relative amount of D_3^+ ions out of the three configurations and the lowest amount of D_1^+ ions. Correspondingly, the configuration with the largest separation, the 20-50 configuration, had the lowest relative amount of D_3^+ ions and the highest number of D_1^+ ions.

The higher relative fraction of D_1^+ ions in the 20-50 configuration is believed to be the reason why it has the highest fusion rates of the three configurations. All three molecular ion species have the same charge, which means that they will experience the same magnitude of electrostatic force from the cathode potential. However, fusion occurs between one atom of the molecular ion and one atom of the background neutral molecule. Each of the molecular ion species gain the same energy from the electrostatic potential fields, but the molecular energy is split up among the energy of each atom in the molecule. Therefore, when fusion occurs with a

D_3^+ molecule, the atom of that molecule that actually fuses has only 1/3 the energy of the molecule as a whole. Similarly, the atoms of the D_2^+ molecule have only ½ of the total energy and the single atom of the D_1^+ species has the full energy imparted by the electrostatic potential fields. The atom of the D_1^+ species has the highest fraction of the full energy of the molecule of any of the molecular species. The fusion cross section for D-D increases with increasing incident atom energy, meaning that the higher energy atom of the D_1^+ ions will have a higher probability of creating a fusion event than atoms in the D_2^+ or D_3^+ molecular ions in the same electrostatic field. Therefore, since the 20-50 configuration creates the highest number of D_1^+ ions, it has the largest population of energetic atoms, resulting in it creating the largest number of fusion events, which is exactly what was confirmed by the neutron measurements of the three configurations.

The FIDO diagnostic has also been used in another important area of study, which is the profiling and potential contribution to fusion of the negative ions created in the IEC. Through the works of Boris, *et al*, at UW-Madison [4], the method of magnetic deflection of charged particles was used to verify the existence and importance of negative ions in an IEC device. Full details of the experimental methods can be seen in Ref. 4. The two primary means by which this study assumed that negative ions are created are through thermal electron capture and charge exchange reactions. Thermal electron capture occurs through the following reaction:

$$D_2 + e \rightarrow D_2^{-(m)} \rightarrow D^- + D \qquad \textbf{(9.8)}$$

In the above equation, $D_2^{-(m)}$ is a meta-stable state with a lifetime on the order of ~1 μs to ~1 ms. These thermal electron capture reactions are most likely to occur with electrons of less than 1 eV, and are believed to be most common near the cathode where a large number of thermal electrons are emitted from the cathode wires through ion impacts.

The cross sections for charge transfer reactions on the other hand are highest in the range of tens of keV. There are four primary means by which charge transfer can occur in the IEC, which are listed below:

$$D_3^+ + D_2 \rightarrow D^- + 2D^+ + 2D \qquad \textbf{(9.9)}$$

$$D_2^+ + D_2 \rightarrow D^- + 2D^+ + D \qquad \textbf{(9.10)}$$

$$D^{fast} + D_2 \rightarrow D^- + D^+ + D \qquad \textbf{(9.11)}$$

$$D^+ + D_2 \rightarrow D^- + 2D^+ \qquad \textbf{(9.12)}$$

These reactions are most likely to occur in the inter-grid and cathode regions of the IEC where the positive ions have sufficient energy to create the necessary charge exchange reaction when it impacts a background gas particle. When a positive ion is caught within the potential well created inside the anode, it will typically receive several passes back and forth across the well before it fuses or charge exchanges, which increases the path length of the ion and correspondingly increases the probability of a charge exchange reaction occurring.

The components of the FIDO diagnostic can be used to collect negative ions by reversing the direction of the magnetic field typically used to collect fusion products. The field typically used to collect fusion products is on the order of 8 kG. However, the field required to collect the negative ions, which have energy close to that provided by the cathode potential, is on the order of only 800 G. Experimental results were collected and compared to the contributions of the various birth mechanisms for negative ions discussed above, which is shown in Figure 9.9 [4].

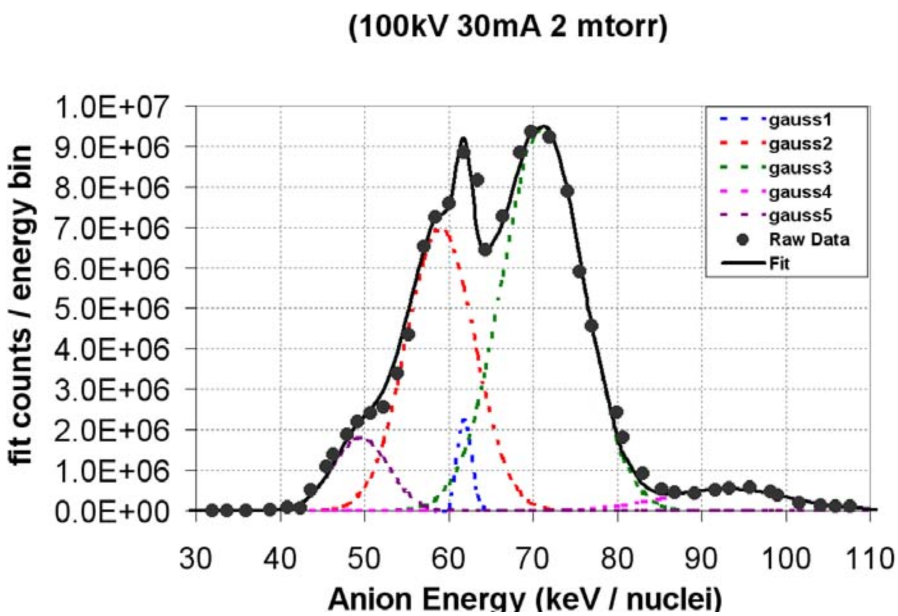

Figure 9.9 Negative ion spectra collected at 100 kV cathode potential, 30 mA cathode current, and 2 mTorr of background deuterium pressure using magnetic deflection method. Experimental results compared to sum of 5 gaussian curves, each representing a different birth mechanism for negative ions. Gauss 1, 2 and 3 are due to charge exchange reactions from D^{2+}/D^-, D^{3+}/D^-, and D^+/D^-, respectively. Gauss 4 is caused by thermal electron capture near the cathode. Gauss 5 represents the meta-stable state created by the thermal electron capture near the cathode.

The greatest contribution to negative ions appears to be from the various charge exchange reactions. The highest energy negative ions though are caused by the thermal electron capture near the cathode, where the negative ions would receive nearly the full energy of the potential well as they escape. In either case, the energy spectra of the negative ions appear to be much harder than that of the positive ions collected using FIDO. This indicates that the negative ions are much more likely to fuse when striking a background gas particle than the positive ions.

The evidence of negative ions was corroborated by Boris through the use of a Faraday trap. The Faraday trap was used to measure total negative ion current emitted from the system at two different locations. A 400 G magnetic field was applied at the entrance to the trap to deflect secondary electrons streaming out of the chamber from the cathode, but the field was low enough to not significantly deflect the negative ions. Using the Faraday trap, it was determined that as much as 1.5 mA of negative ion current could be emitted from the system for 30 mA of total cathode current. Although this only represents 5 percent of the total current of the system, the harder spectra of the negative ions could result in the negative ions being responsible for as much as 30 percent of the total fusion in the system.

The FIDO diagnostic has proven very useful thus far in expanding the understanding of the internal operations of a spherically gridded IEC device. Its ability to collect the charged particle energy spectra with great accuracy and very little background noise has allowed for energy spectra of not only the fusion products, but also the fusion reactants to be studied. FIDO has thus far been used for parameterization studies of the voltage, current, and pressure of HOMER and in optimization studies regarding the configuration of the electrodes. The experimental results thus far have helped advance theoretical and computational modeling of the IEC by adding benchmarks which can be used for comparison and validation of theoretical predictions. The confirmation of negative ions in the IEC and their importance to the fusion rates of the system were also a dramatic discovery and have led to a significant change in the way IEC devices are thought to work. The negative ions may have particular relevance to the spatial profiles collected by the author using the Time of Flight Diagnostic, which is discussed in Chapter 12.

There is still a great deal more work that can be done using FIDO to enhance the experimental and theoretical understanding of IEC operation, and there are various ways in which the diagnostic itself can be further optimized. One such advancement upon the original FIDO design has already been designed, constructed, and tested by the author. This is the

Adjustable FIDO Arm, which offers the potential to not only study D-D reactions, but also D-^{3}He using the existing electromagnets. The new Adjustable design also includes several additional noise reduction features, which can increase the voltage, current, and pressure range able to be scanned before the detectors are saturated with background noise. This new design is detailed in Chapter 10. As was already mentioned, the FIDO Diagnostic is also a key component of the Time of Flight Diagnostic constructed by the author and detailed in Chapter 11.

Chapter 9 References

1 Boris, D. R., Kulcinski, G. L., Santarius, J. F., Donovan, D. C., Piefer, G. R. (2010). Measureing D(d,p,)T fusion reactant energy spectra with Doppler shifted fusion products. Journal of Applied Physics, 107, 123305

2 Donovan, D. C. (2008). Optimization of an IEC fusion device to increase steady-state D-D neutron generation rates. Proceedings of 18th TOFE Meeting, San Francisco, CA

3 Boris, D., Emmert, G. (2006). Plasma characteristics of the ion source region in the University of Wisconsin IEC device. American Physical Society 48th Annual Meeting of the Division of Plasma Physcs, October 30, 2006

4 Boris, D. R., Alderson, E., Becerra, G., Donovan, D. C., Egle, B., Emmert, G. A., Garrison, L., Kulcinski, G. L., Santarius, J. F., Schuff, C., Zenobia, S. J. (2009) Deuterium anions in inertial electrostatic confinement devices. Physical Review E **80**, 036408

10 Adjustable FIDO Arm

Thus far, the FIDO diagnostic has only been used to study D-D fusion reactions. Since both products of the D-D fusion reaction have the same momentum, they can both use the same magnetic field and bend angle for the collimator channel. Another possible use for the FIDO system is to study the D-He^3 fusion reaction, which produces a 3.6 MeV Alpha particle and a 14.7 MeV proton. Using SIMION, it was found that the Alpha particle can be collected using the current setup with a 20 degree elbow on the collimator channel and a magnetic field of approximately 10.5 kG, which is within the capabilities of the current electromagnets. However, the 14.7 MeV proton would require a magnetic field of roughly 21.5 kG in order to achieve the same bend around a 20 degree elbow, which is beyond the capabilities of the current electromagnets. The solutions to capturing the fusion protons were to either obtain a new electromagnet with capabilities on the order of 25 kG, or to create a collimator channel with a smaller bend at the elbow. Obtaining a new electromagnet of the required capabilities was deemed prohibitively expensive, and the space and weight requirements for the new electromagnets would have required a series of additional upgrades and revisions to the current setup. Therefore, the option of obtaining a collimator channel with a smaller angle at the elbow was pursued.

The D-He^3 protons can be bent around a 10 degree elbow using an 8 kG magnetic field, and they can be bent around a 15 degree elbow using a 12 kG field. The first option was to construct a new collimator similar to the existing TOF arms, only with a shallower bend at the elbow. However, this would have required breaking vacuum in order to switch between studying D-D and D-He^3 fusion reactions. In order to minimize the changes to the vacuum environment between studies, it was desirable to find a method by which the angle of the elbow could be varied without having to break vacuum. The first option considered was to use a circular vacuum bellows flange, such as those available from Swagelok ®, which come equipped with the necessary Conflat 7 cm vacuum flanges commonly used on HOMER. However, the optimal cross section for the collimator channel is rectangular rather than circular because the minimum separation distance between magnet poles (located at the bending elbow of the collimating channel) and the maximum cross-sectional area of the channel is needed. Rectangular cross section bellows were somewhat more difficult to find from any of the standard vacuum component vendors.

Eventually, the idea was introduced to use a flexible waveguide assembly as the elbow since they often come with rectangular cross sections. There were several issues with waveguides that made it difficult to find the right design. First, most waveguide companies do not deal with ultra-high vacuum environments and were unable to rate their products to such low pressure specifications. Another common problem was that nearly all vendors made their waveguides almost exclusively out of copper beryllium or phosphor bronze. Neither of these alloys are ideal for either vacuum or plasma environments. Finally, MegaIndustries, Inc. based out of Gorham, ME agreed to make a 12.5 cm long flexible waveguide assembly out of 316 Stainless Steel with CF 7 cm flanges on both ends rated for ultra high vacuum. The inner dimensions of the rectangular cross section of the original fixed elbow collimator channel were 16 mm by 35 mm, and the outer dimensions were 19 mm by 38 mm. The corrugated section of the flexible waveguide has inner dimensions of 13.7 mm by 35.6 mm and outer dimensions of 18.1 mm by 40.1 mm. This results in a loss of only around 10 percent in the cross-sectional area of the channel by switching to the flexible waveguide, and offers a slight decrease in the minimum achievable separation of the magnet poles.

The manufacturer had had little previous experience corrugating stainless steel, and the product delivered was the first of a kind prototype. The end result was quite successful though and was effectively leak tested to a vacuum of less than 10^{-8} Torr. The flexible waveguide can be seen in Figure 10.1. The waveguide was also equipped with boundary bars on either side of the corrugated channel to ensure that the corrugated section bent only at the elbow in the center of the channel and also to limit the bend angle to less than 30 degrees so as to avoid any risk of breaking the vacuum seals on either end through over exertion.

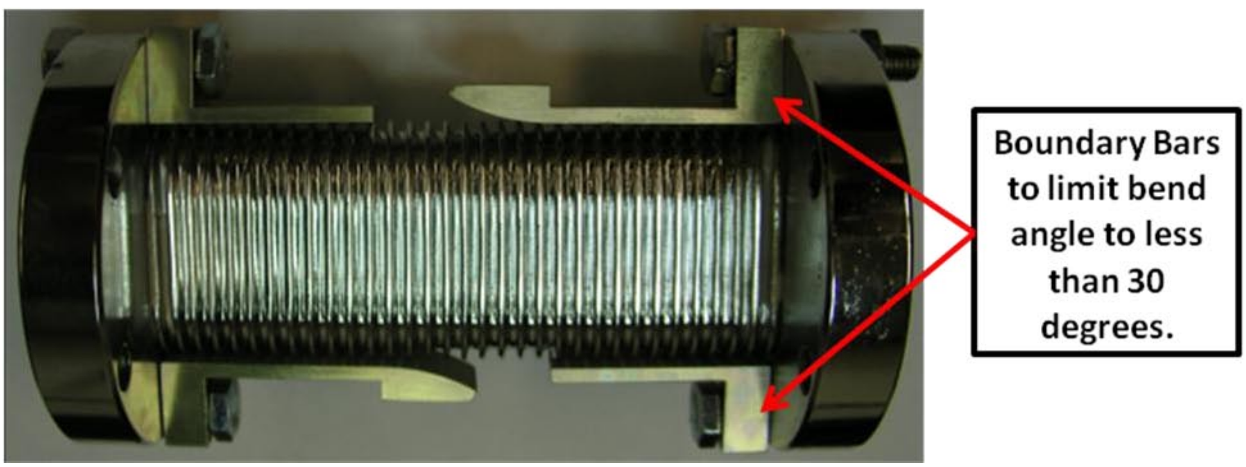

Figure 10.1 Flexible waveguide assembly created by MegaIndustries, Inc. Total length is 12.5 cm, corrugated section is made of SS 316, and both ends are mounted to 7 cm CF vacuum flanges.

One end of the flexible waveguide was then mounted to a 12.5 cm long CF 7 cm full nipple. The other end was mounted to another new feature for the adjustable arm assembly, an X-ray trap. The trap is essentially an empty aluminum box and matching lid, with O-ring seals around the lid and the ports on the front and back of the box in order to allow it hold a high vacuum. The box was machined from a solid block of aluminum. The lid is designed to fit the grooves of the box and be screwed down to create a tight O-ring seal. The trap can be seen in Figure 10.2.

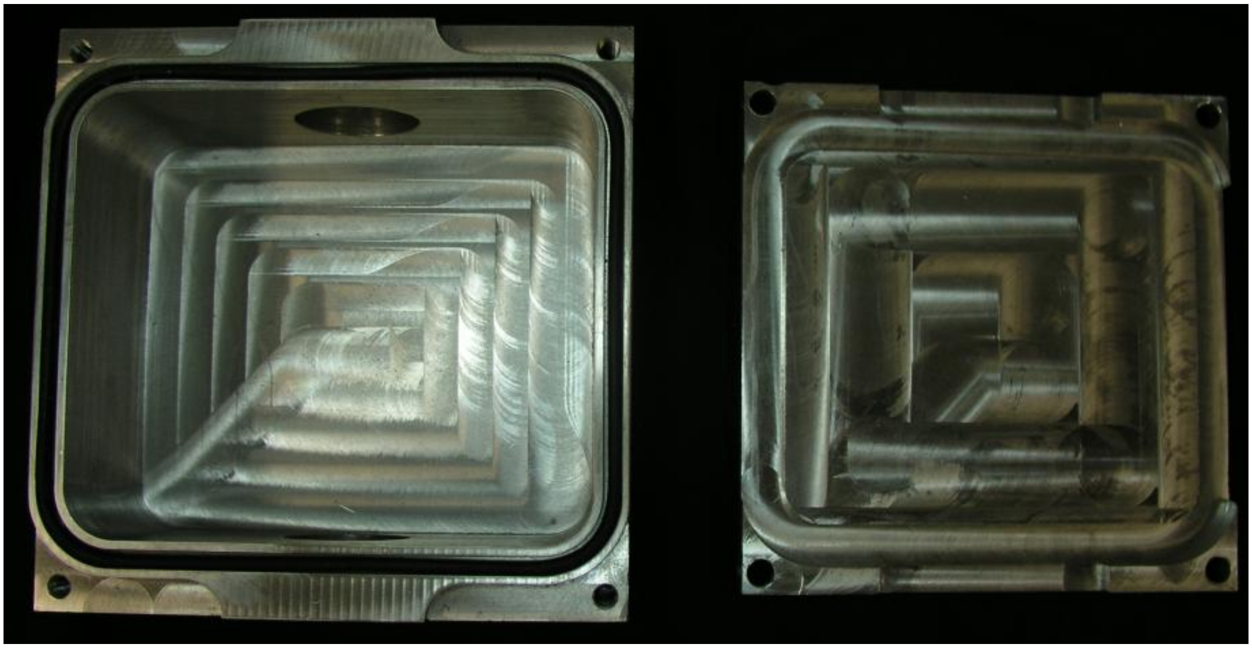

Figure 10.2 X-ray trap used in adjustable arm assembly. Constructed from aluminum, utilizes O-ring seals on the lid and all ports to seal the trap to high vacuum conditions.

The purpose of the X-ray trap is to allow a repository for x-rays bouncing around the collimator channel and prevent them all from being channeled directly towards the detector. X-rays created either inside the chamber or through electron impacts in the collimator channel are able to make several bounces before losing most of their energy. The collimator channel provides inner surfaces on which the X-rays can bounce and reach the detector. The trap is a meant to be a place where the X-rays can bounce around and lose most of their energy before reaching the detector. With the previous collimator channel, there were no direct lines of sight between the detector and the inside of the chamber, but there were paths that allowed for X-ray to take make a single bounce off the inner wall of the collimator channel and reach the detector. The X-ray trap eliminates those single bounce pathways and forces those X-rays to instead hit one of the back corners of the trap and take multiple bounces before finally reaching the detector.

Another feature of the adjustable arm assembly that helps to mitigate X-ray propagation is the corrugated section of the flexible waveguide. The inner surface of the corrugated section is filled with ridges, which only provide a path towards the detector if the X-ray strikes the peak of the ridge at the proper incident angle. At all other points on the ridge, the X-ray is more likely to be deflected at an angle away from the detector, back towards the chamber. Similarly, if an electron impacts one of the ridges on its way towards the detector, the resulting X-rays emitted from the impact are most likely to head away from the detector unless the electron impacted the small area on top of the ridge. As has already been mentioned, X-rays are believed to be a significant source of background noise in the FIDO setup. They are the primary limitation on the ability to study higher power or pressure levels because the increased background noise causes excessive pile up of low energy noise, crowding out genuine signals. There will always be a need for further advancement in the area of noise reduction as the FIDO diagnostic comes into greater use.

The complete adjustable arm assembly can be seen in Figure 10.3.

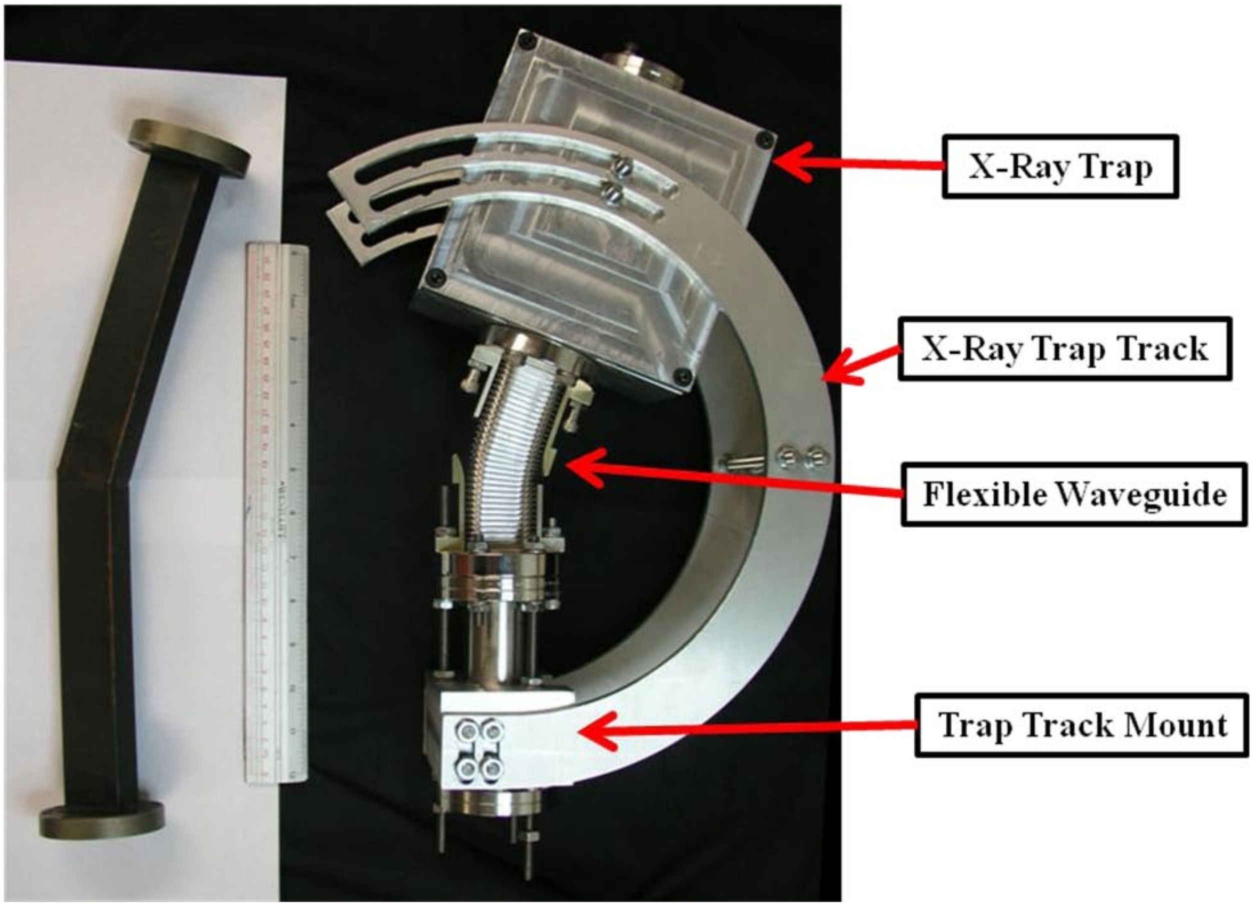

Figure 10.3 (Left) Previous collimator arm with 20 degree elbow. (Right) Adjustable Arm Assembly. Adjustable arm is roughly 5 cm longer than fixed arm.

The X-ray trap is mounted on a track, which allows it to traverse a path from -30 to +30 degrees relative to the normal axis of the section extruding from the chamber. Ridges were made in the track at 10 degree increments. The track is then connected to a mount, which fits around the CF 7 cm full nipple and is aligned and secured with the nipple using threaded rods to the vacuum flange on the outside of HOMER. The adjustable arm assembly is roughly 5 cm longer than the previous fixed arm, which causes a slight reduction in the amount of fusion products and background noise that are able to reach the detector.

The adjustable arm assembly is capable of reaching angles of 10 or 15 degrees, which are necessary for studying D-He^3 fusion. Other benefits of the adjustable arm include significantly more ease for studying negative ions as well as aligning the arms. Previously, in order to study negative ions it was necessary to rotate the electromagnet in order to reverse the direction of the magnetic field to bend negatively charged particles as opposed to positive ones. This was a bit of a challenge because it often required first removing the collimator arm from between the magnet poles, thereby breaking vacuum, and then using an engine hoist to lift and rotate the heavy electromagnet. The adjustable arm allows for the electromagnet to remain in the same position, and to simply drop the detector down to -20 degrees instead of +20 degrees without breaking vacuum. The new Adjsutable Arm design also has the possibility of simplifying the alignment used in the Time of Flight Diagnostic by dropping the elbow to 0 degrees, which is described in further detail in Section 11.4.

The adjustable arm was mounted directly to the chamber with additional support for the weight of the arm provided by a turnbuckle and threaded rod assembly, which is also used for alignment of the Time of Flight Diagnostic, discussed in Section 11.4. The mounted adjustable arm assembly can be seen in Figure 10.4. The diameter of the Trap Track was designed to be slightly larger than the electromagnets so as to ensure that the elbow was positioned as close to the center of the magnet poles as possible.

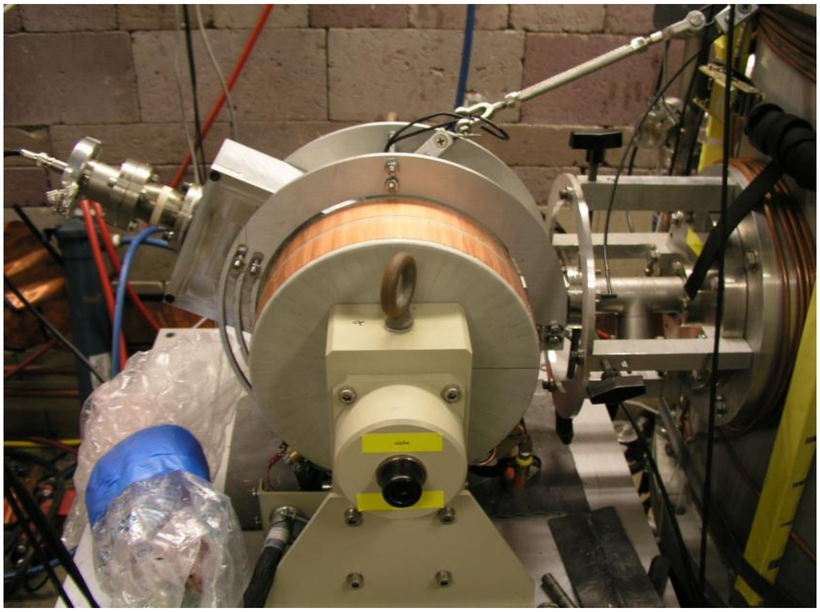

Figure 10.4 Adjustable arm assembly mounted on HOMER with additional support provided by the turnbuckle and threaded rods.

The assembly was able to seal down without significant difficulty to the same vacuum as the rest of HOMER, which was on the order of a microtorr of base pressure. FIDO scans were taken on the adjustable arm while varying such parameters as cathode potential, cathode current, background pressure, magnetic field, and bend angle of the elbow. The most immediate benefit of the adjustable arm that was noticed was its superior ability to collect protons at higher power levels as compared to the fixed arm. Background noise believed to be due primarily to X-rays created from Bremsstrahlung emission from electron and ion impacts cause significant pile up and dead time in the detectors, prohibiting the capture of genuine fusion products at these high noise levels. A dramatic increase in noise can be seen when the cathode potential is changed by as little as 10 kV. These effects can be seen in Figure 10.5 and Figure 10.6.

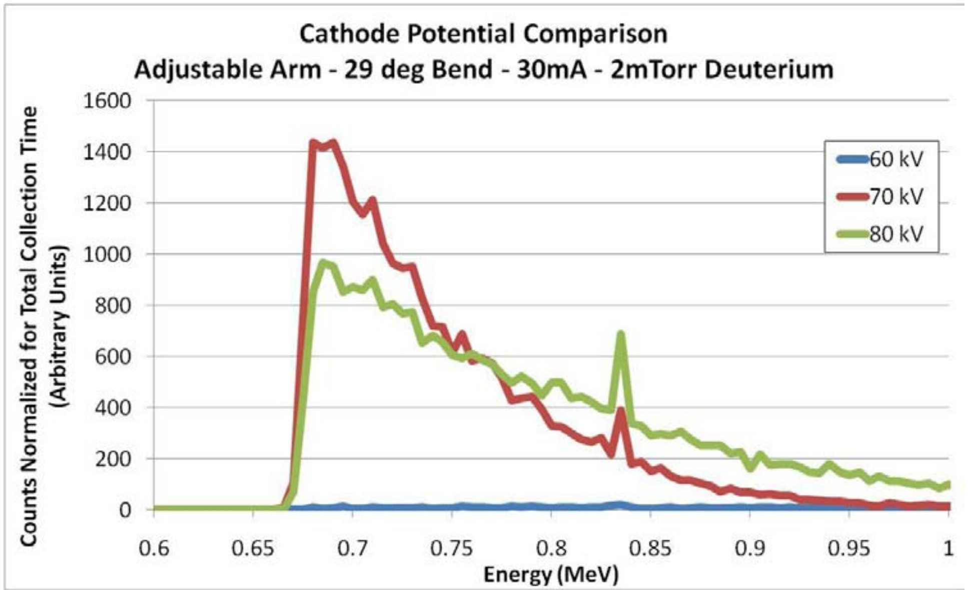

Figure 10.5 Comparison of energy spectra collected using adjustable arm assembly with bend angle of 29 degrees. Minimum trigger level for energy capture set to ~0.65 MeV. Close-up of spectra from 0.6 to 1.0 MeV to observe low energy noise.

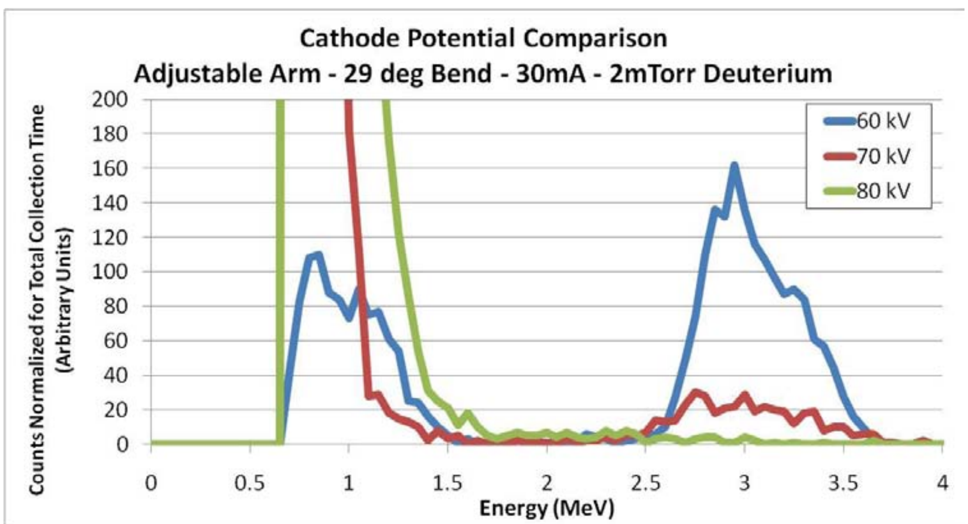

Figure 10.6 Same spectra as that shown in Figure 10.5, showing entire 0 to 4 MeV range demonstrating loss of genuine proton counts in the 2.5 to 3.5 MeV range when voltage and noise are increased.

Both figures represent the same three energy spectra collected using the adjustable arm assembly with a bend of 29 degrees. The minimum trigger level for signal capture was set at roughly 0.65 MeV, so as to better assess the higher energy noise caused as the cathode voltage is increased. Figure 10.5 focuses only on the portion of the spectra from 0.6 to 1.0 MeV in order to demonstrate the extent to which the background noise profile changes with the voltage. Figure 10.6 shows the entire spectra from 0 to 4 MeV, but looks more closely at the lower count sections of the curves to provide a clearer view of the proton peak between 2.5 and 3.5 MeV. At 60 kV of cathode voltage, the detector is still able to discern the proton peak rather clearly, centered around 3 MeV. When the voltage is increased from 60 to 70 kV, the number of counts below 750 keV increased by over two orders of magnitude. This dramatic increase in low energy noise saturated the counting ability of the detector and caused sufficient dead time to reduce the proton peak by over 80 percent. When the voltage was increased again from 70 to 80 kV, the total number of low energy counts does not change significantly because the detector was already saturated at 70 kV. However, for the 80 kV case, the noise peak extends to a higher range of nearly 1.5 MeV. This is most likely caused by an increase in the energy and amount of noise produced leading to greater pileup in the detector, which results in the detector mistaking the noise for higher energy signals. This further increase in noise reduced the proton peak to the point where it was no longer recognizable.

This case demonstrates how severe the issue of background noise is on the operating ability of the charged particle detectors, and therefore upon the capabilities of the FIDO and TOF diagnostics. Similar situations arise as the cathode current or background deuterium pressure are increased. These results are plotted in Figure 10.7, Figure 10.8, and Figure 10.9. In each figure, there is a clear point at which low energy noise (0 to 2 MeV counts) dramatically increases and saturates the counting ability of the detector, which corresponds to an immediate drop in the fusion protons collected (2 to 4 MeV counts) that are drowned out by the near total dead time.

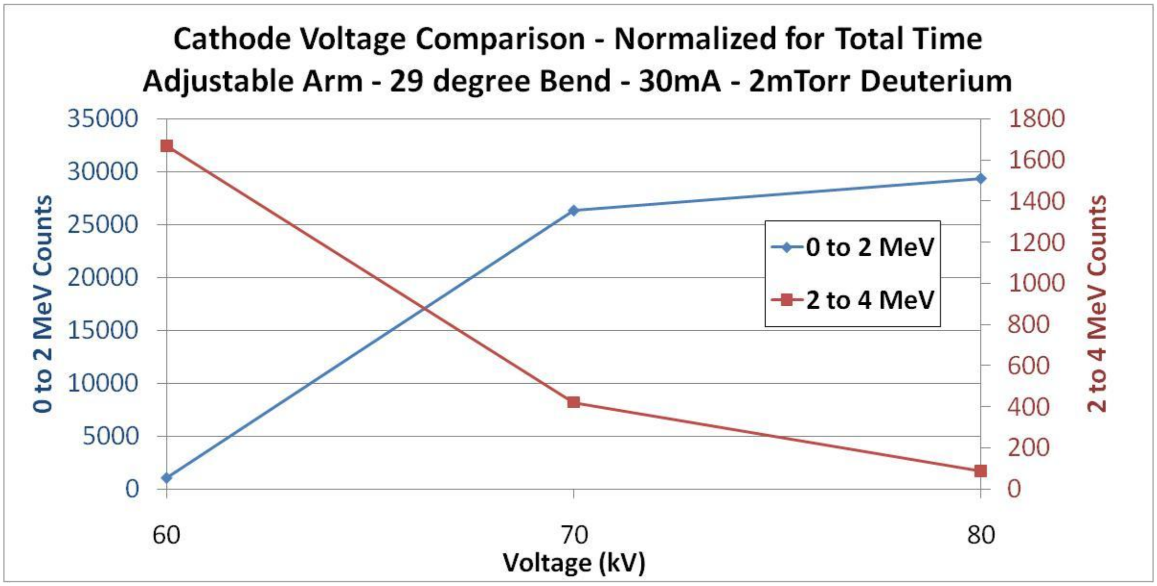

Figure 10.7 Comparison of counts collected from cathode voltage scan. Counts from 0 to 2 MeV are primary location for low energy background nose. Counts from 2 to 4 MeV represent actual counts from fusion protons.

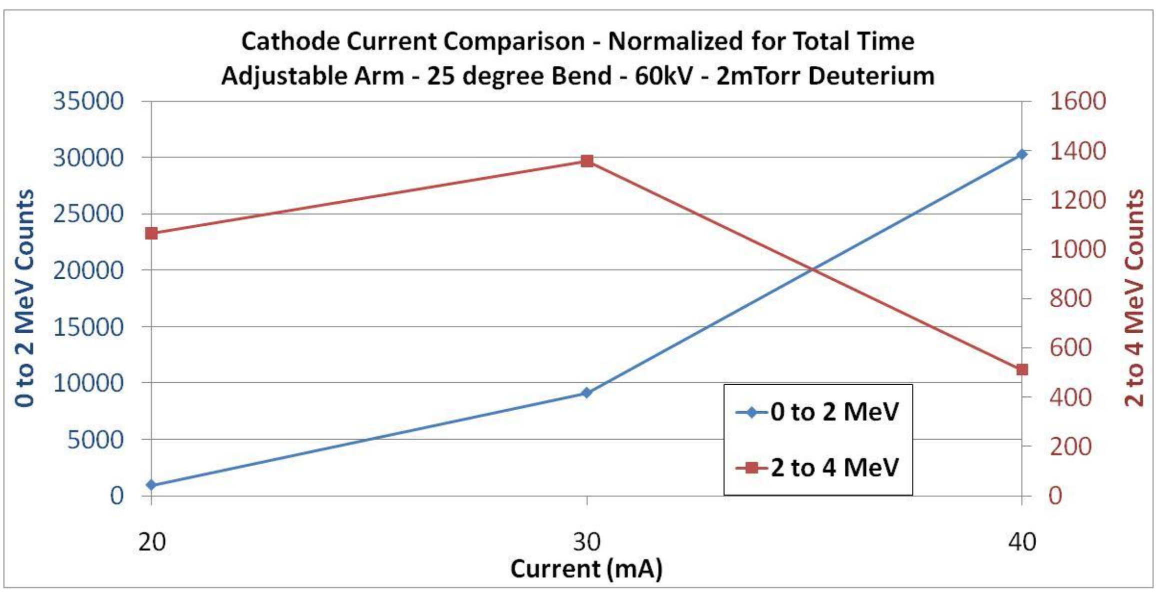

Figure 10.8 Comparison of counts collected from cathode current scan.

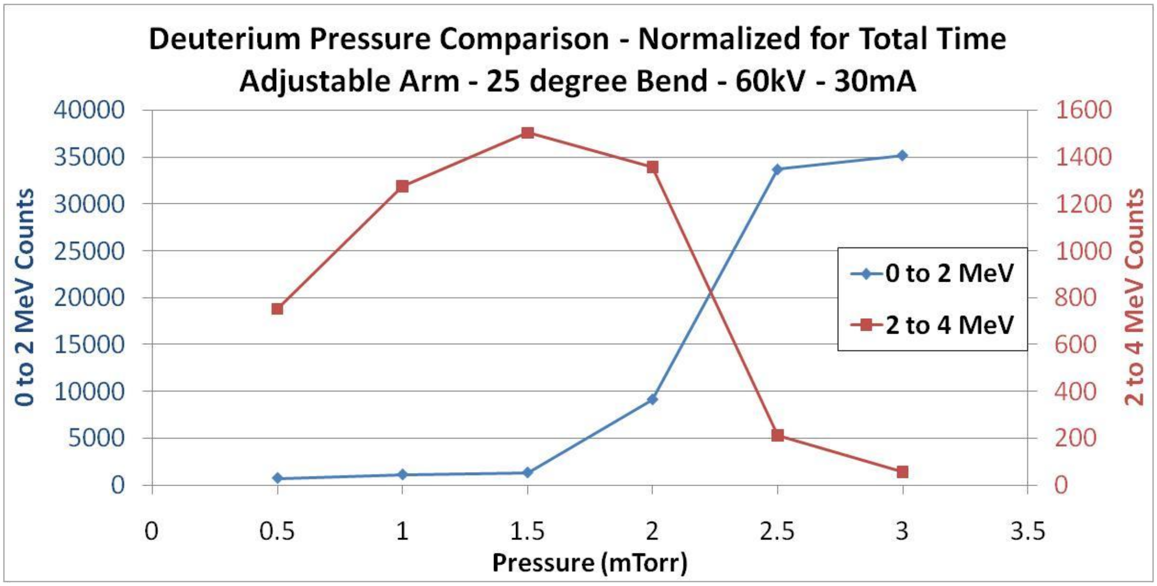

Figure 10.9 Comparison of counts collected from background deuterium pressure scan.

The figures shown above were all taken using the adjustable arm assembly. As was mentioned, one of the largest benefits of the adjustable arm over the fixed arm was that it demonstrated superior counting ability of fusion products at higher noise levels as compared to the fixed arm. The mitigation of noise was also seen to improve as the angle of the elbow was increased from 20 to 29 degrees. Table 10.1 shows the counts for the various configurations tested, divided into low energy noise counts (0 to 2 MeV) and genuine fusion proton counts (2 to 4 MeV). The counts were taken at 60 kV, which was already beyond the useable range for the fixed arm because it was saturated with noise at this level. The maximum cathode voltage level the fixed arm could reach before saturation of the detector for this particular configuration was 45 kV.

Collimator Channel	Elbow Bend Angle (degrees)	0 to 2 MeV Counts	2 to 4 MeV Counts
Fixed	20	29448	19
Adjustable	20	30246	94
Adjustable	25	20156	372
Adjustable	27	18431	668
Adjustable	29	9119	1268

Table 10.1 Energy spectra collected at 60 kV, 30 mA, 2 mTorr Deuterium. All counts are normalized for the same total collection time. Magnetic field at which each one of these configuration was set was first predicted by SIMION and then confirmed as the ideal point experimentally.

The direct comparison between the fixed arm at 20 degrees and the adjustable arm at 20 degrees shows that the adjustable arm appears to have collected on the order of 5 times as many fusion protons as the fixed arm. With all other parameters the same, this is likely due to the combination of the X-ray trap and corrugated interior of the elbow of the flexible waveguide, both of which were implemented with the hopes of reducing the amount of X-rays that could reach the detector. As the angle of the adjustable arm is increased, the low energy noise gradually decreases and the number of protons collected increases. The magnetic field used at the elbow for each degree of bend was first simulated using SIMION and then confirmed experimentally by performing scans over a range of magnetic fields to determine the optimal point. Each case represents the counts able to collected at the optimal magnetic field setting. By increasing the angle of the elbow from 20 to 29 degrees, the amount of low energy noise dropped by at least 70 percent (possibly more since the detector was saturated for the 20 degree case) and the number of fusion protons collected increased by a factor of over 66.

This represents a significant increase in the counting ability of the diagnostic at this voltage level provided by the versatility of the adjustable arm. It must also be noted though that as the angle of the elbow is increased, the magnetic field required to bend the fusion products also increases. This causes a greater beam spreading when the particles reach the detectors, due to the range of energies of the products caused by the Doppler shift. This is particularly important for the D-D fusion tritons, which experience much more spreading than do the protons because of their lower velocity. This issue is discussed further in Section 11.3, and may require both of the magnets to be set to different fields in order to focus on capturing either down or up shifted products because of the broader spreading of the tritons. The width of the beam spreading increases for a given cathode potential as the bend angle of the adjustable arm is increased.

This is a noted improvement in the capabilities of the system to take the maximum point before detector saturation from 45 kV with the fixed arm at 20 degrees up to 60 kV with the adjustable arm at 29 degrees. Unfortunately, as can be seen in Figure 10.5 and Figure 10.6, when the voltage is further increased from 60 to 70 kV on the adjustable arm at 29 degrees, the background noise increases dramatically and once again saturates the detector. This provides a demonstration of how important gains can be made in fighting background noise issues that plague the system, but continued efforts to combat these noise problems will almost certainly always be needed with a diagnostic system such as this.

11 Time of Flight (TOF) Diagnostic

11.1 TOF Diagnostic is an Advancement upon FIDO Diagnostic

The Time of Flight (TOF) Diagnostic was first proposed by Piefer and Boris and utilizes the FIDO setup [1], and later developed by Boris and Donovan, and finally constructed and utilized by Donovan. A single FIDO diagnostic setup is capable of producing energy spectra from the charged particles that are created by fusion reactions occurring within the volume of the solid angle cone traced out by the line of sight of the detector setup as it looks into HOMER. The TOF diagnostic consists of two identical FIDO diagnostic setups, each one placed on opposite sides of HOMER. This creates a line of sight through the two FIDO arms that travels directly through the center of HOMER, and though the origin of the spherical symmetry of the electrodes. A schematic of the TOF setup can be seen in Figure 11.1.

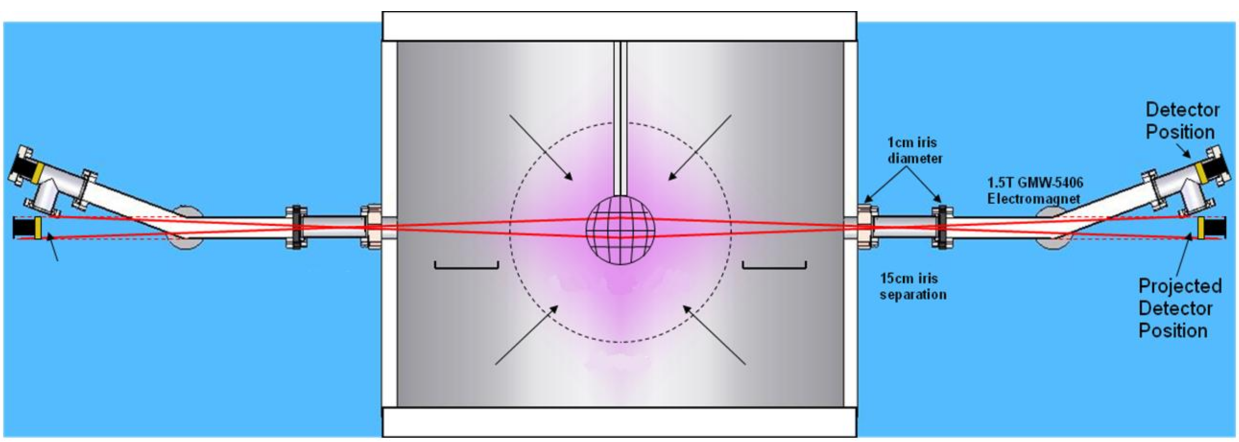

Figure 11.1 : Schematic of TOF setup includes two identical FIDO diagnostic setups on opposite sides of HOMER.

The products of the D-D fusion reaction travel in the exact opposite direction of each other in the center of mass frame in order to conserve the momentum of the reaction. As a result, whenever a fusion reaction occurs in the line of sight of the detectors and the products and reactants travelled in a path either parallel or anti-parallel to the line of sight of the detectors, each of the fusion products travelling in opposite directions will be detected by one of the two detectors, which are on opposite ends of HOMER. This also results in the collected particles always having opposite shifts from each other, since whenever the center-of-mass is travelling towards one detector (up-shift) it will inherently be travelling away from the other detector (down-shift).

The FIDO diagnostic is equipped to measure the energies of the arriving fusion products. Another addition required to create the TOF diagnostic was the Nuclear Instrumentation Module (NIM) fast timing circuitry, which is described in further detail in a following section. These electronics allow for the detection of the exact moment (within a nanosecond) at which a charged particle impacts the surface of the detector. Both FIDO detectors are connected to this circuitry. If a fusion event occurs with the proper directionality in the line of sight of both detectors, then each detector should collect one of the two fusion products. The speed at which the fusion products are moving allows them to traverse the length of the chamber and detector setup in less than a few hundred nanoseconds, so that as soon as one product is detected on one detector, the second product should be detected less than approximately 300 ns later on the opposite detector. Collection of the two counts from the same event on opposite detectors is known as coincidence counting, and is a common technique in radiation detection methods.

The D-D fusion proton has an energy of 3.02 MeV, while the triton has an energy of 1.01 MeV, and the proton also has one third the mass of the triton. This results in the fusion proton moving at three times the velocity of the fusion triton. This velocity changes slightly with the magnitude of the Doppler shift, and correspondingly the direction and magnitude of the reactant center-of-mass energy. Due to the size of HOMER and the length of the collimator arms on the FIDO diagnostics, and for the energy ranges which are being studied, there is no point along the line of sight of the detectors in the chamber at which a fusion event could occur that would allow for the triton of a fusion reaction to reach one of the detectors before the proton reached the opposite detector. Therefore, when looking for coincident D-D fusion product counts in HOMER, one detector must always be triggered to pick up the fusion proton since it will always arrive first, and the second must then look immediately after for the triton. A schematic of this reaction can be seen in Figure 11.2.

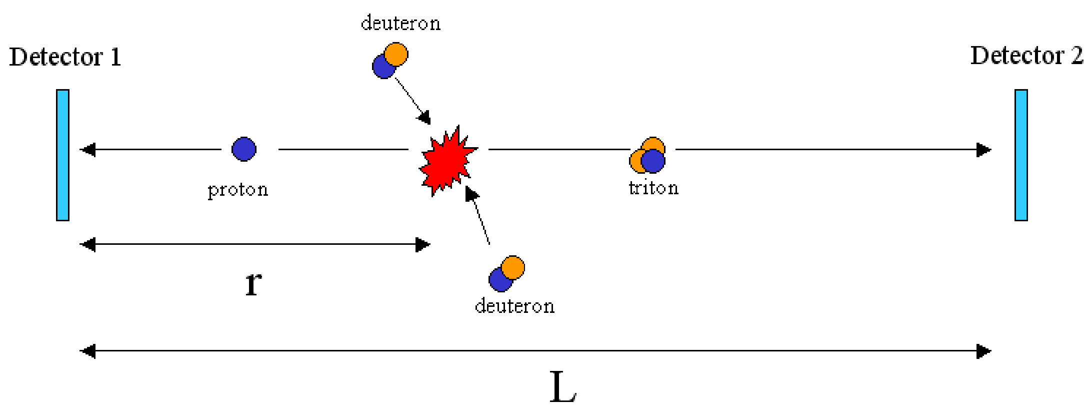

Figure 11.2 Schematic diagram of coincidence capture of D-D fusion proton and triton by detectors positioned on opposite sides of the reaction.

The time at which both products of the same fusion reaction reached their detectors then provides the difference in arrival times, which is also equal to the difference in the times of flight of both particles, $\Delta t = t_P - t_T$. The time of flight is the amount of time it takes for the fusion product to reach the detector after the fusion reaction occurred. The energy of both of the particles was also collected, so based upon the known fusion energy and the measured magnitude of the Doppler shift, the velocity at which the proton, v_p, and the triton, v_t, were both moving is known. The total length between the detectors is a constant value and is denoted by *L*, and the distance between West Detector and the position where the fusion reaction occurred is *r*. The time difference can then be written as:

$$\Delta t = t_T - t_P = \frac{L - r}{v_T} - \frac{r}{v_P} \tag{11.1}$$

This equation can then be rearranged to provide the only unknown quantity, *r*:

$$r = \frac{\frac{L}{v_T} - \Delta t}{\frac{1}{v_P} + \frac{1}{v_T}} \tag{11.2}$$

Using this method, the TOF diagnostic is capable of determining the location in the chamber where a fusion event occurred along with the energies of the fusion products and reactants. The TOF setup is the first diagnostic ever created that is capable of measuring both spatial and energy profiles of a radially symmetric IEC device. This setup is also capable of collecting the profiles with far less interference and background noise than any other similar diagnostics utilized in the past.

11.2 TOF Data Collection

11.2.1 Energy and Timing Electronics

The accuracy and precision of the data collected by the TOF diagnostic is most dependent upon the accuracy of the energy and timing electronics used. The majority of the electronics used for this experiment were purchased from ORTEC. As was described in the previous section, the TOF setup consists of two identical FIDO setups on opposite sides of HOMER. Each FIDO setup includes an Ametek Silicon Charged Particle Detector, which is used to collect the fusion products after they are bent around the elbow of the collimator arm. Once the particles reach the detectors, the energy of the particle and the moment of arrival are collected by the detector, then sent through a series of electronics before finally reaching a computer-based data acquisition program for recording. The diagram of the electronics can be seen below in Figure 11.3.

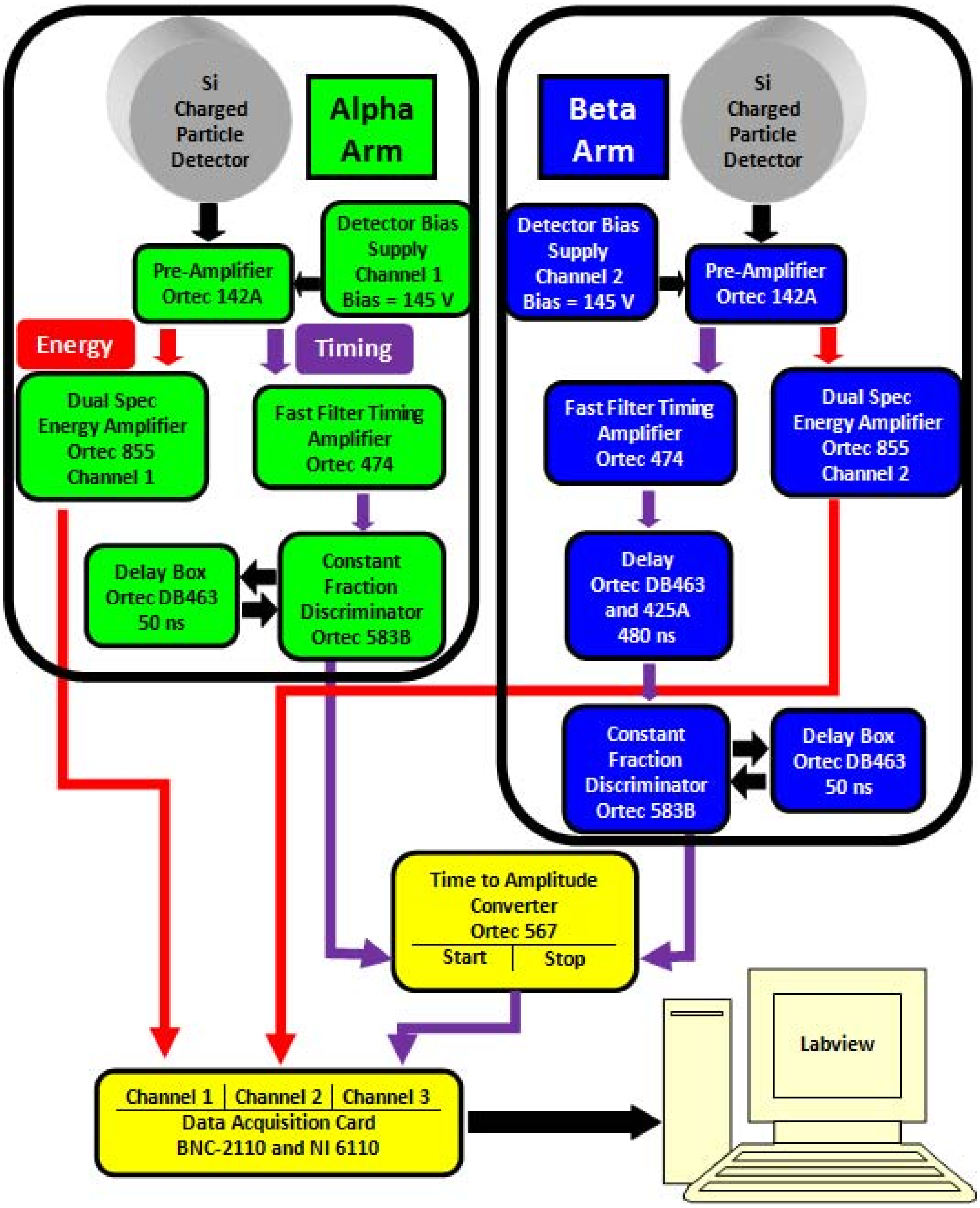

Figure 11.3 Block diagram of TOF Electronics showing separate electronics for Alpha and Beta sides of TOF diagnostic and indicating difference between electronics designated for timing resolution and energy resolution.

Both FIDO arms that make up the TOF diagnostic use the same type of Silicon Charged Particle Detectors, which were described previously in the description of the FIDO diagnostic.

The detectors are powered by a 145 V bias voltage, which is produced by a bias supply that sits in the NIMBIN (the rack which contains all of the modular nuclear instrumentation electronics). The bias voltage is sent through the Ortec 142A Pre-Amplifier, which is then connected to the back of the detector. The Pre-Amplifier acts as a gateway for both the bias voltage going into the detector, as well as the voltage signals created by an incoming particle leaving the detector. When a particle is collected on one of the detectors, a roughly 10 pA signal is immediately sent to the Pre-Amplifier and divided into both the timing and energy resolution branches.

The energy resolution branch is concerned foremost with transmitting a precise signal height that is proportional to the energy of the incoming particle. The energy signal is typically on the order of 10 to 15 microseconds wide and can take up to a microsecond to be properly transmitted, and it is able to measure incoming energies with an accuracy of roughly $\pm$ 5 keV. The timing branch has the opposite concern in that it does not require as exact of a signal height to be transmitted, but rather it is intended to produce the signal as quickly as possible. The timing branch will produce a signal with amplitude of ~50 mV, a width of ~50 ns, and a rise time of 5 to 10 ns. The timing branch of the Pre-Amplifier can reliably produce a signal to an accuracy of approximately $\pm$ 2 ns.

This 2 ns timing resolution of the Pre-Amplifier is currently the largest source of inaccuracy in the TOF electronics, and therefore is responsible for the spatial resolution achievable. A 2 ns error in the timing measurements corresponds to approximately $\pm$ 2 cm of minimum spatial resolution. The primary source of noise in the Pre-Amplifier is due to a phenomenon called timing jitter [2]. Jitter is caused by small, random fluctuations in the voltage signal produced by the Pre-Amplifier due to broadband thermal noise. An example of this effect can be seen in Figure 11.4. More advanced Pre-Amplifiers exist that allow for thermoelectric cooling of the electronics, thereby minimizing the jitter to a level on the order of several hundred picoseconds. This will be described further in the Future Works chapter as a possible upgrade, which would allow for finer spatial resolution of the diagnostic.

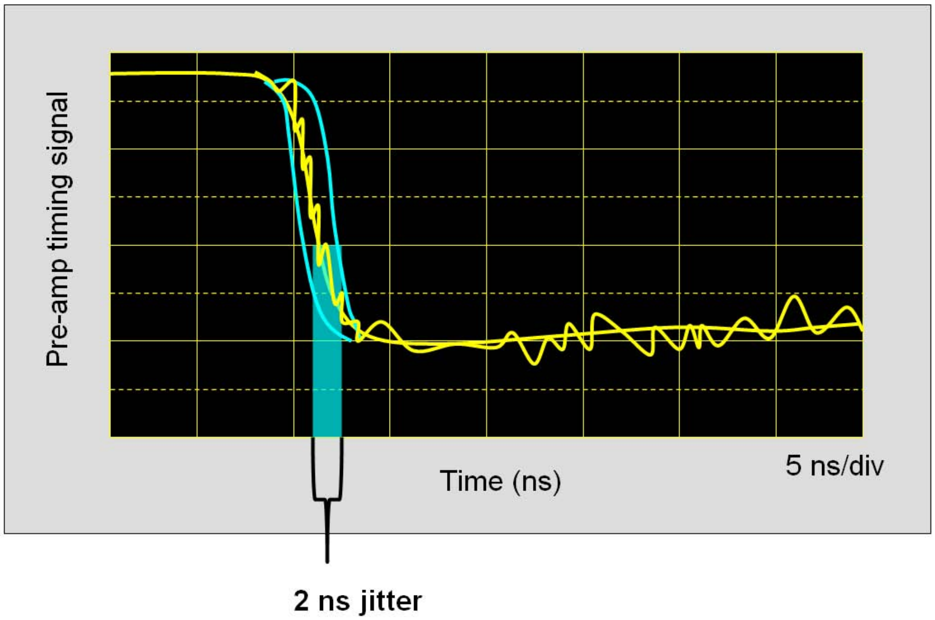

Figure 11.4 Timing jitter of Pre-Amplifier caused by thermal noise in circuitry. Jitter causes a level of uncertainty in the timing signal of approximately 2 ns.

Another common source of noise in the Pre-Amps is a result of high frequency signal transmission through the casing of the Pre-Amp from any other electronics nearby. The high voltage power supply that supplies the cathode potential is a particularly strong source of high frequency noise that is able to conduct its way to nearly anything in contact with the chamber. As a result, the Pre-Amps must be kept well insulated at all times and the casing cannot be allowed to make any conductive paths with any other equipment, which includes the table on which it sits. To resolve this issue, the Pre-Amps were wrapped in insulating plastic and placed on plastic blocks to ensure no harmful signal transmission reached the electronics.

After the Pre-Amplifier, the timing and energy branches take separate paths, as shown in the electronics diagram. The energy branch alone is what makes up the FIDO diagnostic. It heads to the Ortec 855 Dual Spec Energy Amplifier to be amplified to the proper signal height. The Energy Amplifier is calibrated using an Am-241 Alpha source, which produces 5.486 MeV (85.2%) and 5.443 MeV (12.8%) Alpha particles. The Am-241 source is obtained from the UW Reactor Laboratory. Accurate calibration of the Energy Amps is essential because it will have a strong impact on the minimum resolution of the TOF diagnostic. The accuracy of the calibration is on the order of 10 to 20 keV, which offers a slightly lower minimum resolution than the jitter caused by the Pre-Amps. However, if the Pre-Amps were to be upgraded, then the calibration would become a primary concern for increasing resolution of the diagnostic, and a more accurate means of calibration would need to be implemented. The output of the energy amplifier is a single pulse between 0 and 10 V, roughly 15 microseconds wide, with a height proportional to the energy of the particle incident on the detector that created the signal. The Energy Amp is calibrated such that 1 V of signal represents 1 MeV of incident particle energy.

The timing branch takes a separate path to the Ortec 474 Fast Filter Timing Amplifier. The Timing Amp is intended to amplify the signal coming out of the Pre-Amp, apply filters for optimal pulse shaping for input into the next piece of electronics in the chain, and optimize the signal-to-noise ratio of the system. As was mentioned previously, the timing branch of the Pre-Amp output is intended to produce a signal quickly, but not necessarily with an amplitude that is as closely matched to the energy of the particle as the energy output of the Pre-Amp is capable of producing. The height of the timing output signal is still roughly proportional to the energy of the incoming particle, however there is not an exact calibration that can be made. This makes the calibration of the Timing Amps slightly more difficult because they have to be set such that they do not artificially exclude actual signals and mistake it as noise. This calibration is not concerned with transmitting proper signal amplitude since only the arrival time of the signal is relevant not the height, but rather with screening out unnecessary noise. The calibration of the Timing Amp is accomplished by collecting the energy and timing outputs of the Pre-Amp together, and then determining what the minimum likely energy of an actual signal may be. This allows the minimum threshold of the Timing Amps for incoming signals to be set such that unnecessary noise signals can be ignored and true counts can be collected.

The output of the Timing Amp is a signal with amplitude in the range of 0 to $\pm$5 V, with a rise time of less than 10 ns. Since the timing output of the Pre-Amp does not produce signals with consistent amplitudes, an undesirable effect called Amplitude Walk can arise [2]. Most timing logic electronics require a triggering signal in order to initiate a pulse, and this trigger typically involves an input signal reaching a certain magnitude. If two signals have different amplitudes, they will both reach the trigger amplitude at different times, even if both signals originated at the same moment. The difference between the times when both signals reach the necessary trigger amplitude is known as Amplitude Walk. A demonstration of this effect can be seen in Figure 11.5.

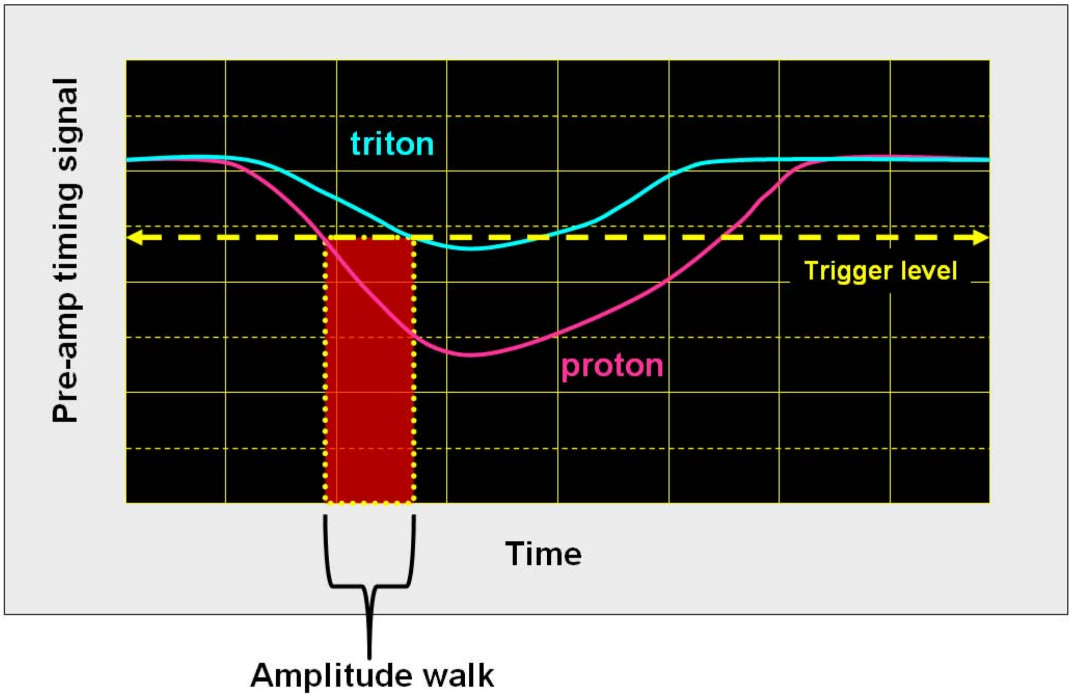

Figure 11.5 Example of Amplitude Walk involving two signals of different amplitudes originating at the same moment. The difference between when each signal crosses the trigger level is shown in red, and represents the extent of the Walk.

The next component in the electronics chain exists to counteract this effect, which is the Ortec 583B Constant Fraction Discriminator (CFD). The CFD is what allows the ability to reliably time off the same point of the output of the Timing Amp, rather than allowing the trigger point to rely on amplitude and rise time. The CFD works by cloning the incoming signal and slowing the copy by an imposed delay. This delay can be seen in the electronics diagram adjacent to the CFD, and can be varied depending on the width of the incoming signal. The original signal is then attenuated causing it decrease in amplitude, and then the two signals are added back together. The sum of the two signals creates a shape that will cross the trigger level at the same moment every time, rather than having the cross point dependent on signal amplitude. The moment the signal crosses the trigger level, a single logic pulse of constant amplitude is produced. A step by step diagram of this process can be seen in Figure 11.6. The CFD is effectively able to decrease the impact of the Amplitude Walk from 5 to 10 ns down to less than 75 ps.

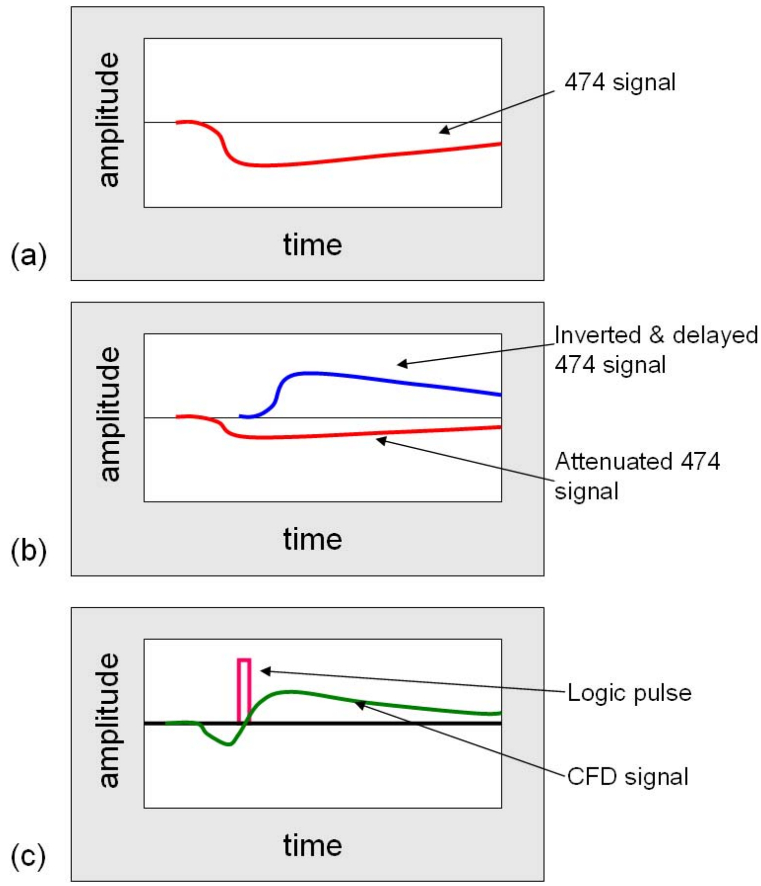

Figure 11.6 Sequence of events in an Ortec 583B Constant Fraction Discriminator. (a) Incoming signal from Timing Amp. (b) Signal is cloned and one copy is delayed while the other copy is attenuated. (c) Two copies are added together, producing a single logic pulse at a repeatable moment in time indifferent of original signal amplitude.

The output of the CFD is then sent into the final piece of nuclear instrumentation electronics, which is the Time to Amplitude (TAC) Converter. The TAC essentially acts as a sophisticated stopwatch, with a start gate and a stop gate. The TAC awaits a signal at the Start Gate, which must be greater than a minimum threshold set on the front panel of the TAC. Once the gate is opened, the TAC will wait for a pre-determined length of time, which can be anywhere from 50 ns to 1 ms, although for this setup the window is typically set to either 500 or 1000 ns. The Start signal is provided by the CFD output from the side marked as the Alpha Arm in the electronics diagram, making the Alpha Arm the trigger for all coincident event collections. The TAC will not accept any more signals from the Start Gate as long as the time window is open. If the window stays open for the preset length of time and no Stop signal is received, then the TAC resets itself and produces no output signal. If a signal is received at the Stop Gate before the time window closes, then the TAC will produce an output signal in the form of a single square wave 5 microseconds wide, with amplitude between 0 and 10 V that is proportional to the fraction of the time window that has passed. The resolution of the TAC is less than 50 ps for the time ranges considered in these experiments.

After the timing and energy signals have been properly filtered and amplified by the nuclear instrumentation electronics, the final signals are sent to the National Instruments Data Acquisition Card, Model NI 6110 with BNC-2110 BNC Adapter, for transmission to the data collection software. The DAQ card has a sampling rate of up to 5 million samples per second and has an input range of $\pm$0.2 to $\pm$42 V. The number of samples collected can be varied as well as the sampling rate, which together determine the length of time a signal is recorded after a triggering event is received. The type of event required to trigger the DAQ card can also be programmed to require a rising or falling slope, an analog or digital signal, and a minimum signal height that must be reached before a signal is recorded. The DAQ card is shown on the electronics diagram as having three channels, each taking a separate signal. Channels 1 and 2 accept the amplified energy signals from the Alpha and Beta Arms respectively. Channel 3 accepts the TAC signal, which gives the difference in arrival times between the signals on the

Alpha and Beta Arms. The DAQ card only records the inputs from the three channels when it receives a trigger signal. For this setup, Channel 1 has been set as the trigger, which means that Channels 2 and 3 can only be collected during a pre-designated length of time after a signal is detected on Channel 1. As was mentioned, Channel 1 collects the energy levels from the counts on the Alpha Arm detector, which by itself represents the capability of the FIDO diagnostic. If a coincident event occurs and the Beta Arm collects the opposing signal, which then makes it through to the TAC, then all three signals will be collected creating a complete coincident event capture. A complete coincident event can be seen in Figure 11.7.

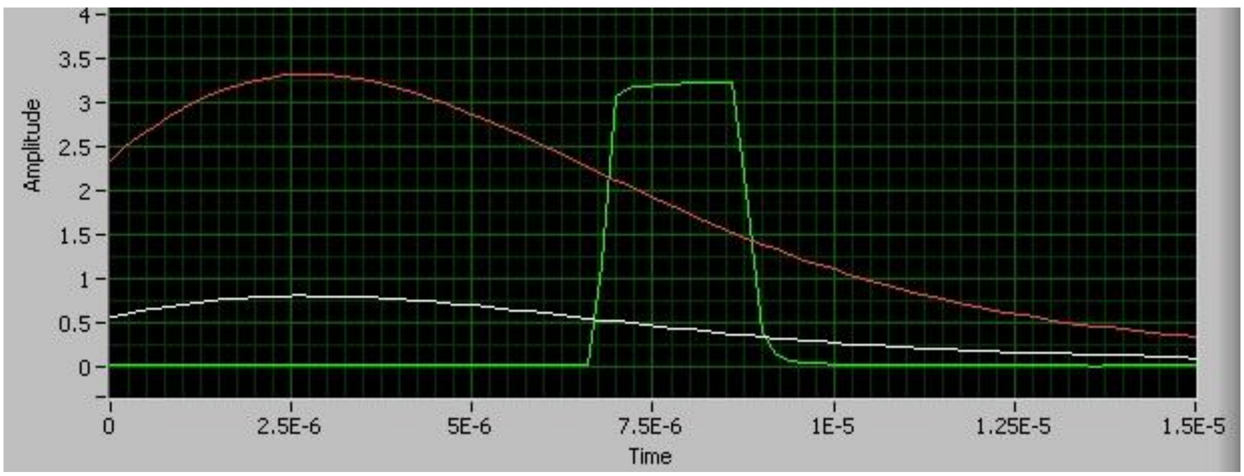

Figure 11.7 Complete coincident capture event. Red line is energy signal of upshifted proton. White line is energy signal of downshifted triton. Green line is TAC signal, with height proportional to difference in arrival times of fusion products.

The timing signal makes it through the electronics faster than do the energy signals (microseconds compared to hundreds of nanoseconds). Therefore, in order to ensure that the TAC arrives after the Alpha Arm energy signal so that it can be captured, the TAC utilizes a built in delay feature to artificially delay the TAC output signal by ~7 microseconds. The DAQ card is able to detect the incoming Alpha Arm energy signal on Channel 1 in less than a microsecond after the signal originates. Since the energy signals have a rise time of roughly 2.5 microseconds and the Beta Arm energy signal is arriving within less than 250 ns of the Alpha signal, there is no need to artificially delay the Beta Arm signal in order to allow it to be captured in the same event as the Alpha Arm signal.

Both the TAC and DAQ card require a single source to act as the trigger, and therefore will not allow both the Alpha and Beta Arms to initiate the collection of a count. As was mentioned, all fusion reactions within the IEC chamber for the parameters that are being examined will cause the fusion proton to arrive at a detector before the fusion triton. The original setup therefore allowed for only the Alpha Arm to initiate signals, and forced the Alpha Arm to always be the proton collecting arm and the Beta Arm had to always be the triton collecting arm. It was originally believed that in order to allow for both arms to act as triggers, then a second TAC and DAQ card would have to be implemented to allow for triggering off of both sides equally. However, an advancement was made to the electronics configuration to allow for both arms to initiate coincidence event captures without requiring the purchase of a second set of electronics.

A delay was put into place on the Beta Arm between the Timing Amp and the CFD (shown in the electronics diagram), which artificially held back the timing signal from the Beta detector by a preset length of time. This meant that if a fusion reaction caused a proton to arrive at the Beta Detector first, then the timing signal from that proton could be delayed before it reached the TAC so that the signal from the triton reaching the Alpha Detector could reach the TAC first and open the Start Gate. The delayed proton signal would then arrive at the Stop Gate after a period of time equal to the length of the imposed delay minus the actual difference in arrival times of the two fusion products at their respective detectors. If the opposite case occurs and the proton arrives at the Alpha Detector, the triton will arrive at the Beta detector and produce a time signal that will also be artificially delayed, thereby causing the Beta timing signal to reach the Stop Gate of the TAC after a period of time equal to the length of the imposed delay plus the actual difference in arrival times of the fusion products. This calculation of the actual delay can be seen below, in which T is the time difference recorded by the TAC, t_i is the imposed delay on the Beta Arm, and Δt is the actual difference in arrival times of the fusion products.

Proton on Alpha Arm $$T > t_i \Rightarrow \Delta t = T - t_i \quad \textbf{(11.3)}$$

Proton on Beta Arm $$T < t_i \Rightarrow \Delta t = t_i - T \quad \textbf{(11.4)}$$

The total length of the delay was measured by splitting the signal leaving the Alpha Timing Amp, then sending one side through the Alpha CFD. The other side replaces the signal from the Beta Detector at the point where it enters the Beta Delay and the Beta CFD. The split signals then rejoin at the TAC where the Alpha branch reaches the Start Gate and the Beta branch reaches the Stop Gate. This allowed the TAC to trigger off of the same signal every time, and the length of the delay measured by the TAC was then equal to the exact length of the combined delay of the Ortec DB463 and 425A, as well as all of the connecting cables and electronics. Measurement of the delay in this way is necessary because the additional cables and electronics can result in as much as ~40 ns of additional delay that must be taken into account in order to maintain a temporal resolution of less than 5 ns.

By allowing both arms to act as triggers, the counting rate of the TOF diagnostic was effectively doubled by this new configuration, which was achieved without having to purchase a second set of electronics. Data taken with this new configuration is routinely checked to ensure that both arms are collecting nearly equal amounts of protons since the device should be symmetric on both sides. The data typically demonstrates a disparity of no more than 5 percent between counts collected on both sides.

11.2.2 Troubleshooting Detectors and Electronics

During the course of refining the diagnostic setup, a variety of noise signals and detector efficiency problems arose. The TOF Diagnostic involves very precise timing and energy signals, and any loss of integrity of the signals will inevitably affect the resolution of the diagnostic. There has not been a need for such a high level of precision in the UW IEC Laboratory's diagnostics in the past, and therefore various aspects of the experimental setups were not prepared to meet the requirements for low electronics noise and had to be upgraded.

The grounding for the entire laboratory was redesigned in order to provide a single, uniform ground point for the IEC chamber and all attached components. When components of the chamber are attached to different grounds, slight differences in the ground potentials can cause destructive feedback loops through the various components, and these loops can give rise to low level noise. Permanent conduction paths were set up between the chamber body and the chamber lid, and then between the chamber lid and the feedthrough body. Previously, these components were separated by rubber O-ring seals and did not have ideal conductive contact. Copper plates and metal braids have now been installed to create a clear conductive path between all components and keep them all at the same ground potential. Poor contact between surfaces can lead to charge buildup, which could then reach a sufficiently high magnitude to cause a discharge. Discharge is a significant concern in this system because the power supply is supplying tens of kilovolts of potential to the feedthrough and charged particles are constantly striking all of the inner surfaces of the chamber and the anode. This can allow charge to buildup on the feedthrough body and/or on the lid if they are not properly grounded. Discharges can then send significantly large voltage spikes to anything connected to the system, which can then ripple through all of the TOF electronics and distort signals.

Isolation of the TOF components is important to minimize the amount of noise created in HOMER that is capable of interfering with the data acquisition. The NIMBIN containing most of the electronics was isolated using a SOLA Constant Voltage Transformer. The purpose of the transformer was to eliminate any sudden spikes in voltage from the power outlet that could be transmitted to the NIMBIN, and then the rest of the electronics held within. The detector mounts are secured into place using nylon bolts behind a ceramic standoff, which is capable of holding back at least 10 kV. The preamplifers are very sensitive to electronics noise even through the outer casing. To mitigate this, the preamplifiers was wrapped in lead to shield against x-rays, then plastic to keep them from contacting any conductive surfaces, and then they were placed on plastic blocks to further increase the distance between the casing and any conductive pathway. The placement of the coaxial cables is also an important concern as their insulating shielding is not entirely impenetrable to signal leakage. Many of the cables were remade to ensure that there were no breaks or kinks, then their paths were rerouted to avoid proximity to any other sources of high frequency noise in the room, particularly the high voltage power supply, the electromagnets and their power supplies, and the vacuum pumps.

The detectors also presented their own issue relating to the efficiency of high energy particle capture. After prolonged usage of the detectors during a run (on the order of hours), a phenomenon would occur in which the maximum particle energy able to be collected would gradually decrease. At the beginning of a run, the detectors could measure at least 3.5 MeV protons, but at the end they were unable to measure above 3 MeV, and the maximum would continue to fall the longer they were operated. After ceasing operation and waiting from 6 hrs to several days, the detectors would once again operate normally, until they were used for a sufficiently long period of continuous operation for the effect to return. The overall rate of collection of particles would also decrease. This then led to a significant decrease in the probability of collecting both particles of a fusion event, and the TOF diagnostic would essentially stop counting and become unusable. The detectors had received an estimated combined proton and neutron fluence of 10^6 to 10^7 particles/cm^2. The typical radiation damage threshold for silicon is on the order of 10^{13} to 10^{14} protons or neturons/cm^2, so it seemed unlikely that the detectors were radiation damaged.

The detectors were eventually returned to the manufacturer, Ortec-Ametek, and an analysis was performed. These charged particle detectors typically start out with a leakage current in the range of 50 nanoamps, but the anlaysis found that the detectors were producing leakage currents on the order of microamps. This very large increase in leakage current was causing a voltage drop across the preamplifier that was nearly equal to the amount of potential applied from the external bias supply. This essentially meant that the detectors were not receiving any bias towards the end of a run, and therefore would be unable to measure high energy particles. This problem was remedied by decreasing the value of the resistor in the Preamplifer by a factor of 10 from 100 megaohms to roughly 10 megaohms, thereby decreasing the voltage drain caused by the leakage current to drop by a factor of 10 as well and significantly increase the amount of bias reaching the detector. This then allows the detectors to operate for a much longer period of time before the leakage current once again becomes an issue. Changing the resistance in the preamplifer has an unfortunate consequence, which is that it decreases the resolution of the transmitted signals. However, the resolution was only decreased from ~8 keV to around 10 to 12 keV, which was deemed within the tolerances of this experiment.

High leakage currents are typically indicative of radiation damage to the detectors. However, as mentioned, the detectors have been exposed to a fluence that should be roughly six orders of magnitude below the damage threshold. The reason for why the damage is occurring more quickly in this case may have to do with the exposure to hydrogen. Exposure to hydrogen gas is particularly degrading to the detectors because, if the hydrogen diffuses into any components of the detector and reacts with trapped oxygen, then chemical reactions can occur that can potentially break down some of the binding compounds that hold the various layers of the detector together [3]. This could produce a higher leakage current in the same manner as typical radiation damage through poor contact between the various layers of the detector. The exact effects of hydrogen on silicon charged particle detectors are still not particularly well understood. However, it has been confirmed that the detectors are being damaged in the timeframe that they have been used in the IEC, which is on the order of two years. The lifespan of the detectors can be increased by actively cooling them during use. It is recommended that, in the future, the detectors be outfitted with a vacuum-capable cooling setup, which is further discussed in the Future Works Chapter.

11.2.3 Labview Data Acquistion

Once the signals have made it through the DAQ card, they are finally sent to a custom made file in LabVIEW for collection and analysis. LabVIEW, which is short for Laboratory Virtual Instrumentation Engineering Workbench, is a program created by National Instruments for the purpose of data collection, both active and passive control of instrumentation, and automation of processes. As was mentioned, the trigger for the DAQ card to initiate a signal capture event comes from the Energy Signal of the Alpha Arm. As a result, every time a signal is detected on the Alpha Arm it triggers the DAQ card and a count is collected on Labview, regardless of whether there are any coincident events occurring on the other two channels. The Alpha Arm Energy Signal alone is what makes up the FIDO diagnostic, so this method of triggering allows for FIDO data to be collected simultaneously with the TOF data.

Single event captures for FIDO happen on the order of 10 to 20 times per second. Since it is significantly more difficult to capture both products of a fusion event as opposed to just one, genuine coincidence event captures occur at a far slower pace, roughly 1 count every 45 seconds. As a result, less than approximately 0.2% of all FIDO counts collected will also involve a coincidence event capture from the other two channels on the DAQ card. This necessitates a series of filters to sort through the large amounts of data and pick out the genuine coincident events. Another important reason for filtering is due to the large amount of background noise from x-rays, visible light photons, thermal noise, and other sources that impact the detector, causing false signals.

The background noise levels typically increase as cathode potential, ion current, or background pressure is increased. As the background levels of low energy noise increase, there is a higher probability of pile up in the detector. This is caused when the noise is coming in faster than the detector is able to sweep out the charge carriers in the detector junction, causing the smaller noise signals to be added together to create a single large noise peak. The constant influx of noise can also cause significant dead time. Dead time is the time during which a detector is unable to collect new signals because it is still busy sweeping the charge carriers from the previous signal out of the band gap of the semiconductor. If there is significantly more noise than there are genuine fusion products counts, then the noise will cause so much dead time that the counts will be unable to be detected and only noise will be collected. A further description of how various noise sources impact the counting ability of Silicon charged particle detectors can be found in Ref 2, 4, and 5. By taking the detector out of the line-of-sight of the chamber, the background noise levels were able to be significantly decreased. However, depending on the operating conditions, background noise can still cause false signals up to 500 keV. If a genuine fusion product count is received on the Alpha Arm and opens the Start Gate of the TAC, then it is possible for a noise signal of sufficient size to reach the Stop Gate before the time window closes on the TAC, thereby creating an output signal from the TAC that does not represent a true coincident event.

The first filter applied to data collected in LabVIEW checks the size of all three of the incoming signals. As for the energy signals coming in on Channels 1 and 2, the minimum and maximum possible energies for fusion products depend on the maximum possible shift, which is dependent upon the operating cathode potential. For the cathode potentials studied thus far, a maximum shift of 600 keV is more than enough to encompass all possible fusion products. The energy signals on Channels 1 and 2 are evaluated to determine if they are less than 0.4 MeV (lowest possible energy of a downshifted triton) or greater than 3.6 MeV (highest possible energy of an upshifted proton). As for the TAC signal on Channel 3, all signals below 0.2 V would correspond to less than 20 ns of delay between particle arrivals, which is not possible for fusion events taking place inside the chamber given the current electronics setup, therefore all signals below 0.2 V are considered electronics noise and they are filtered out.

Next, the length of the delay provided by the TAC is evaluated to determine on which arm the proton from a coincident event should have arrived. As shown in Equations (11.3) and

(11.4), if the time difference measured on the TAC is greater than the imposed delay on the Beta Arm, then the proton had to arrive on the Alpha Arm, and if the TAC measurement is less than the delay, then the proton had to arrive on the Beta Arm. The TAC height is cross referenced with the energies measured on Channels 1 and 2 to ensure that the proton is showing up on the proper arm and the triton is showing up on the other arm. A particle is considered to be a proton if it has energy within 2.4 to 3.6 MeV, and it is a triton if the energy is between 0.4 and 1.6 MeV.

The last filter checks whether the magnitude and direction of the Doppler shifts of the two fusion products correspond to each other properly. Since the two detectors are on opposite sides of the same fusion reaction, the center-of-mass from the reactants would always be heading towards one detector (up shift) and away from the opposite detector (down shift), except in the cases of a center-of-mass velocity that is entirely perpendicular to the line of sight of the detectors or a fusion event between two fast particles of the exact same energy and opposing directions. Therefore, when both particles are collected on opposite sides of the device, they must have opposite and nearly equal shifts. The magnitude of the shifts are not exactly the same due to the way in which the center-of-mass velocities and fusion velocities are combined together (see Equation (9.6)), causing the upshifted particle to have up to a 25 keV larger shift than the downshifted particle, for the cathode potentials that are being studied. The filter checks the energies of the proton and triton and ensures that one product is upshifted and the other is downshifted, and checks whether the magnitudes of the shifts are within 200 keV of each other. The 200 keV limit was determined to encompass the natural difference in magnitudes as well as the maximum possible error in measuring particle energy inherited from the calibration of the Energy Amps.

The data acquisition hardware and LabVIEW filters represent a significant improvement in the reliability of the data collected compared to when the experiment began. The first proof of principle experiments performed in 2009 and published in Boris [4] were accomplished by measuring TAC height using an oscilloscope without the accompanying Alpha and Beta Arm energy signals. Since the energy signals were not collected with the TAC signals, the exact energies, and therefore the exact velocities, of the fusion products were not known. Instead, an average Doppler shift of 200 keV was applied to all particles, which greatly decreased the spatial resolution of the resultant radial profiles. Transitioning from recording coincident counts on an oscilloscope by hand to an automated collection system allowed for a dramatic increase in the rate of collection. The ability to collect the Alpha and Beta Energy signals along with the TAC signal brought about a much higher level of confidence in the results. The energies could now be used to create the filters to properly screen out false coincidence counts caused by background noise interference. Also, the spatial resolution of the profiles could be greatly increased because an exact energy could now be used to calculate particle velocity rather than using an average value for the Doppler shift.

11.3 TOF Magnetic Fields

Both FIDO setups require their own 1.5 T Electromagnet and matching power supplies. The magnets used for these experiments were GMW Model 5403 76MM Electromagnets, which are variable gap, water-cooled dipole magnets. The magnetic field produced is dependent upon the input current and distance between the 76 mm diameter pole faces. The figure below plots the field strength as a function of both of these variables.

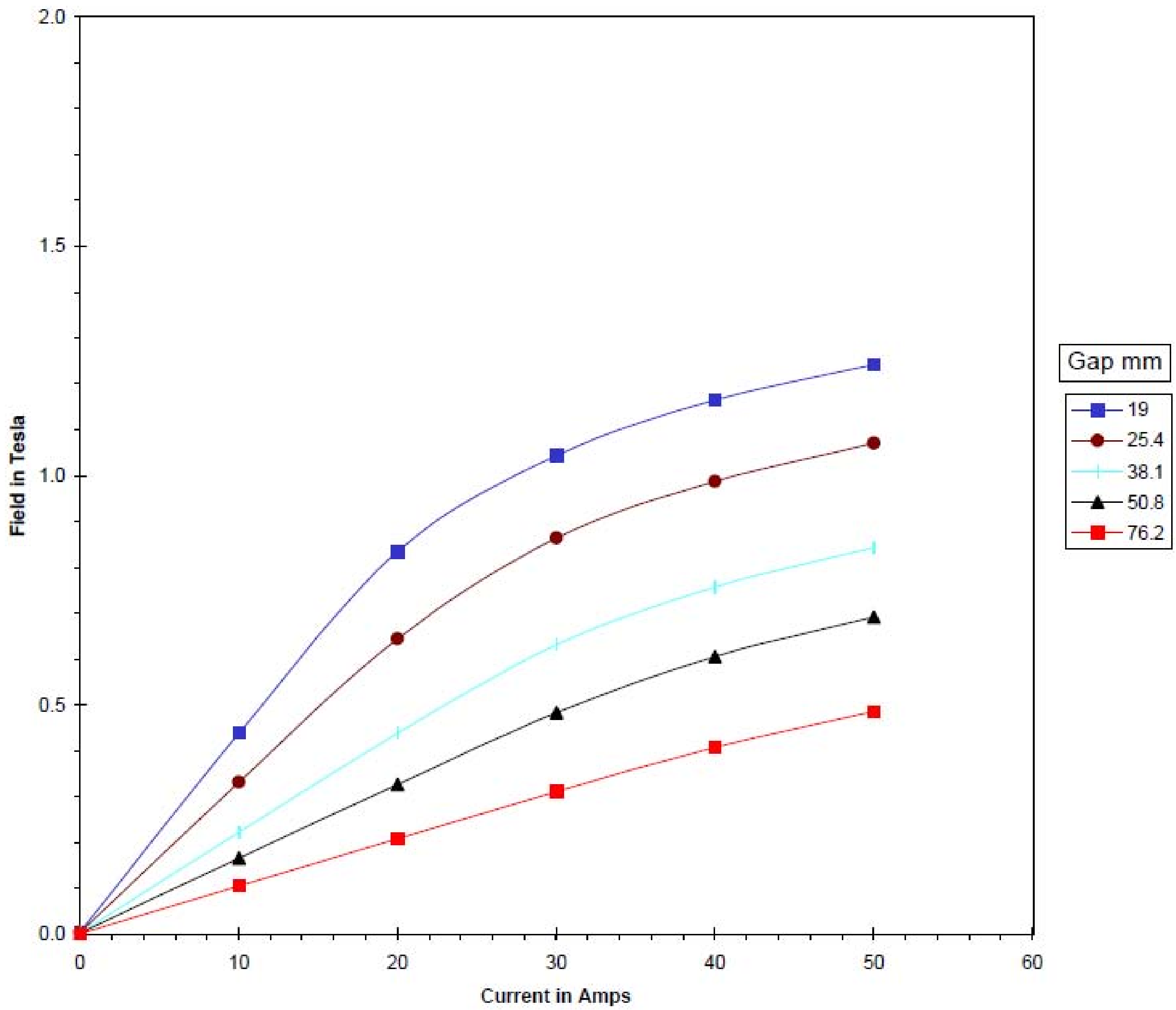

Figure 11.8 Field strength of GMW 5403 Electromagnets as a function of both input current and separation between the magnet poles. [6]

As can be seen from the figure above, the maximum achievable magnetic field drops off quickly as the distance between the magnet poles is increased. This is a prime reason why a rectangular cross section was used as opposed to a circular cross section for the collimator channel. It allows for the best combination of the minimum distance between the magnet poles and the maximum cross sectional area through which particles are able to pass through the collimator channel.

The electromagnets require 50 A of current to reach their full magnetic field strength. For this purpose, 4 HP Agilent 6032A Power Supplies were used. These supplies have a range of 0-50 A, 0-60 V, and 1000-1200 W of power. The electromagnets have a resistance of approximately 0.5 Ohms, which means that a single supply could not meet the power requirements of a single magnet. Therefore, a set of coupled supplies was used for each electromagnet to reach the necessary 50 A of current, with each pair consisting of a master and a slave supply.

The optimal field at which to run the electromagnets was first determined by simulation using the SIMION ® software package, which is used to simulate charged particle trajectories in applied electric or magnetic fields. The simulation can be seen in Figure 11.9.

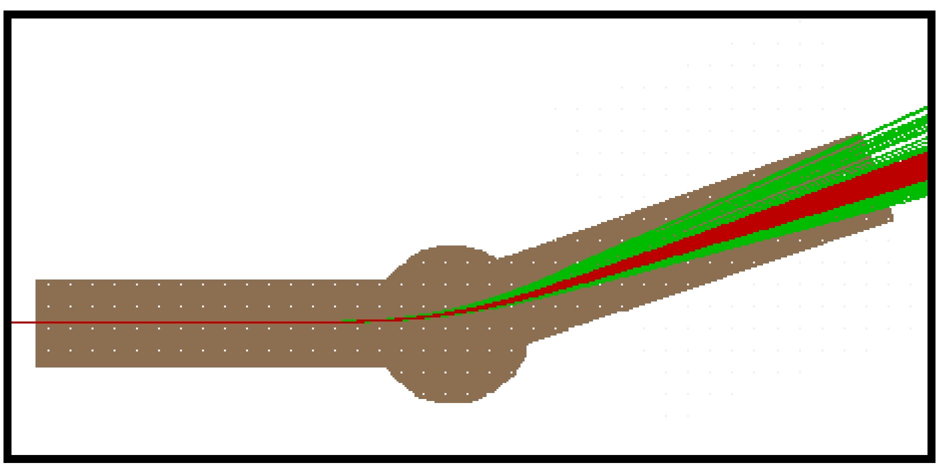

Figure 11.9 SIMION simulation of D-D fusion products traveling through the collimator channel of the TOF arm with a 20 degree bend and an 8.5 kG magnetic field applied at the elbow. The green lines represent D-D fusion tritons with energy between 0.5 and 1.5 MeV and the red lines are the protons with energy between 2.5 and 3.5 MeV, to encompass the full range of upshifted and downshifted particles.

The figure includes the collimator channel with a 20 degree bend, and the 76 mm diameter magnet poles at the elbow. The magnetic field for this simulation is 8.5 kG, which allows the optimal final trajectories for the fusion products to reach the detector at the end of the channel. The fields vary between 8.2 kG near the edge of the poles to 8.5 kG in the center. As can be seen from the simulation, the fusion tritons experience quite a bit more spreading than the fusion protons due to the lower energy of the tritons. The field must be accurately applied in order to ensure that the products are not being over or under bent causing them to be lost to walls of the collimator channel.

The simulation was then tested experimentally, and the energy spectra of the fusion products and the rate of coincident count collection were compared for a range of magnetic fields. The fields were varied from 7.25 to 8.75 kG. The optimal rate of coincident count collection was found to be at a measured value of approximately 8.25 kG using a Bell 5070 Gaussmeter at a point inside the poles just outside of the collimator channel. This matches very closely with the field that SIMION predicted would be near the edge of the poles to correspond to a max field of 8.5 kG at the center. The ratio of upshifted to downshifted protons and tritons were also compared over this range of magnetic fields to ensure that a significant percentage of either up or down shifted fusion products were not being lost to the wall. The ratio between up and down shifted protons varied by less than 5 percent over the range examined. The ratio of up and down shifted tritons varied by a larger amount, on the order of 15 to 20 percent, which was to be expected since the simulation predicted that tritons would have a much broader range of trajectories due to their lower energies. For the low cathode potentials at which these results were collected, the Doppler shift does not appear to be large enough to significantly skew the collection of fusion products by placing both magnets at the same field. However, as higher potentials are studied, the shifts will increase and it may then become necessary to apply different magnetic fields and study the up shifted and down shifted products separately in order to ensure that the entire range of particles are being collected and analyzed.

11.4 Alignment of TOF Arms

Proper alignment of the TOF arms is critical to ensure maximum rate of coincident count collection. If the elbows in the collimator channels of each FIDO were straightened, the length from the chamber wall to the detector face would be roughly 55 cm. The total distance between both detector faces through the chamber is approximately 2 meters. Determining the extent to which the detectors are misaligned can be thought of the overlapping area of two circles, with each circle having the same diameter as the detector face, as shown in Figure 11.10.

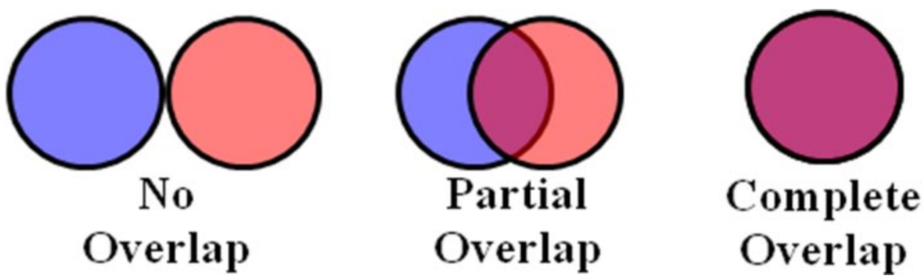

Figure 11.10 Alignment of TOF arms is dependent on the area of overlap of the detector faces in each arm.

The area of the overlapping region can be calculated using the equation below, where A is the overlapping region of the two circles, R is radius of each circle (in this case equal to the radius of the detector face), and d is the distance between the center of each circle.

$$A = 2R^2 \cos^{-1}(\frac{d}{2R}) - \frac{1}{2} d\sqrt{4R^2 - d^2} \tag{11.5}$$

This distance between the center of the circles is dependent on the extent to which the arms are misaligned. Originally, the only support for the arms was the ConFlat 7 cm vacuum flange that connects the arms to the rest of the chamber. This can allow the arms to sag slightly on the end farthest from the chamber, which is detrimental to alignment. To combat this effect, a support system was constructed that utilizes threaded rods positioned at four points around the flange to allow the arm to be lifted and pushed into a plane of proper alignment. In addition, a steel cable and turn buckle assembly was attached to the end of the arm to alleviate the additional weight of the arm. A picture of this assembly can be seen in Figure 11.11.

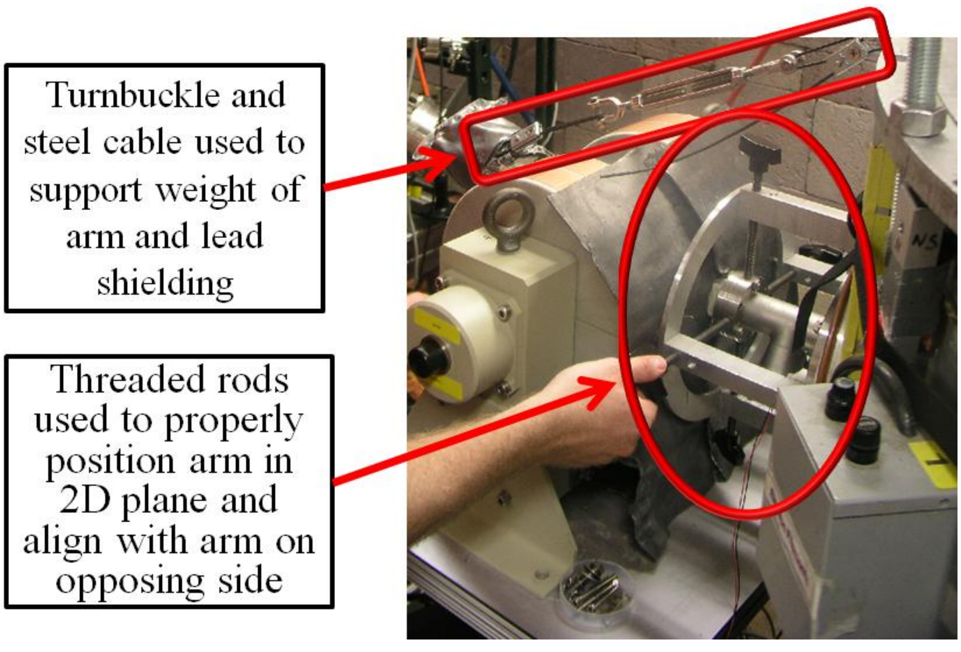

Figure 11.11 Rigid support structure and turnbuckle assembly used to properly align TOF arms.

In order to utilize this alignment system, there must be some means of experimentally determining the alignment of the system. This was accomplished using a combination of laser diodes and photodetectors. Two laser diodes were mounted in the assembly shown in Figure 11.12.

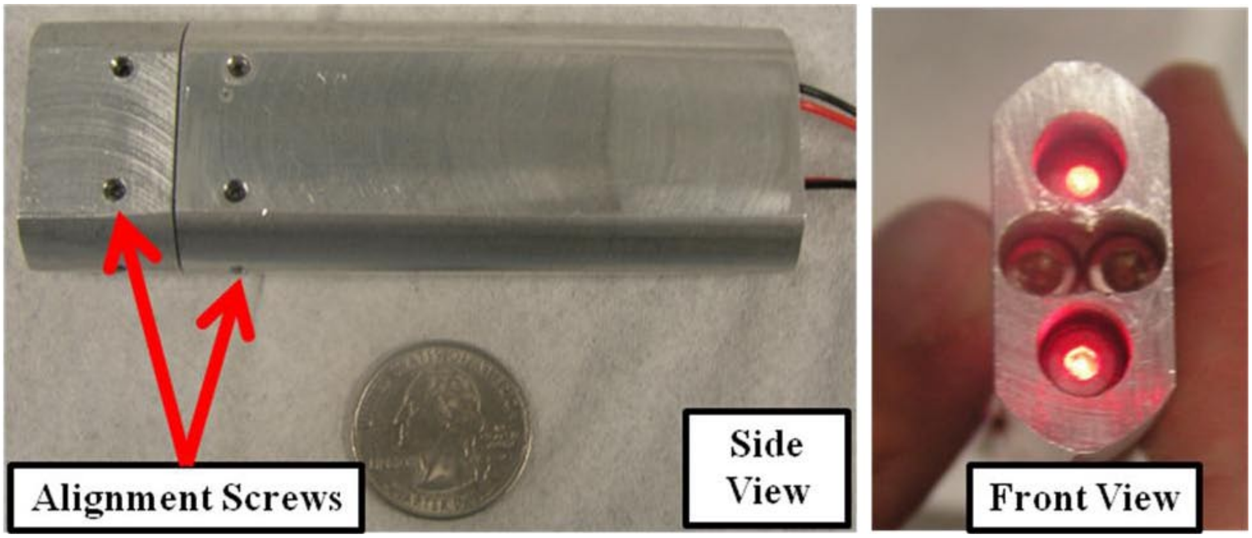

Figure 11.12 Laser diode carriage for alignment system. Alignment screws used to align laser diodes for straight line of sight out of carriage.

The carriage was constructed from two sections with O-rings placed in between. The O-rings surround the laser diodes, and the alignment screws on both sides of the O-rings allow for the diodes to be pushed and held in proper alignment with the carriage so that the lasers shoot straight out from the carriage. This additional degree of precision was required to compensate for any imperfections in the machining of the carriage as well as for the imperfections of the laser diodes. The photodetectors were mounted in a similar carriage of the same overall length. However this carriage was made from one solid piece because the O-ring assembly was unnecessary since the detectors only needed to capture the light, which could be done over a wide range of incident angles. The two carriages were then aligned with each other using a system external to HOMER before they were implemented. The assembly can be seen in Figure 11.13.

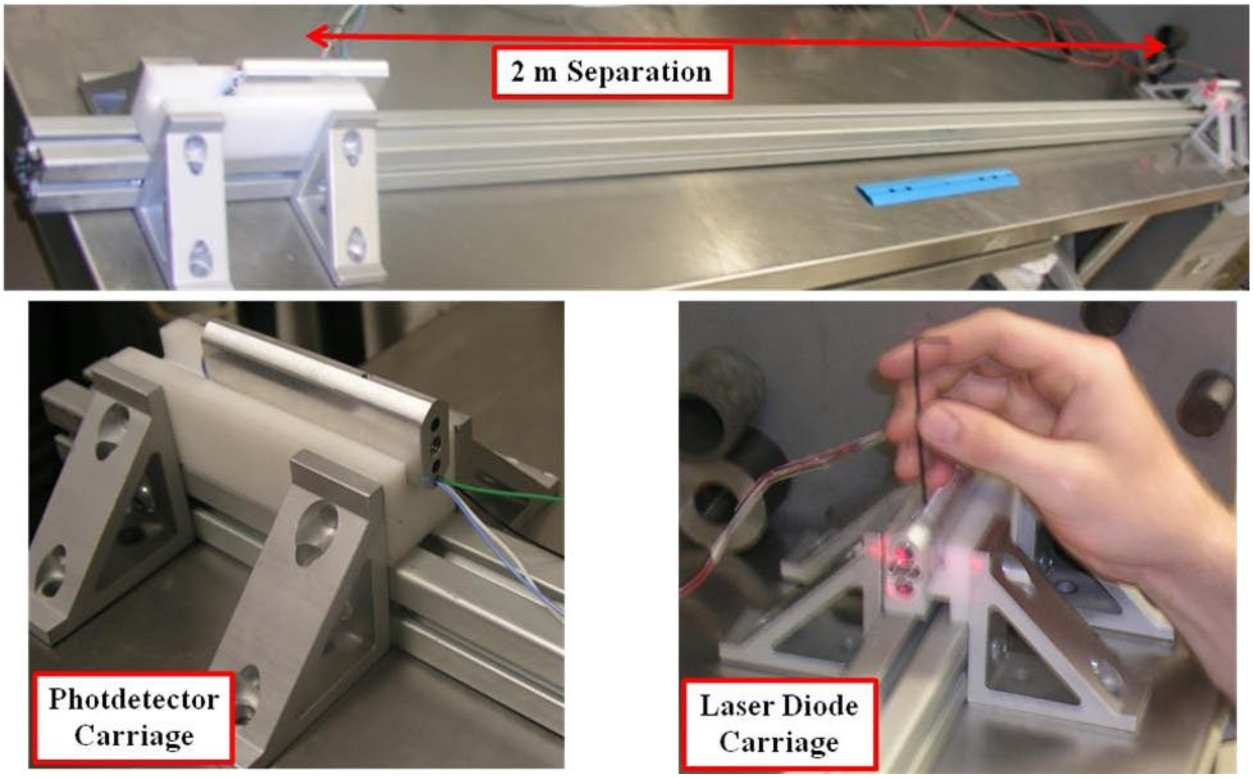

Figure 11.13 System used for aligning laser diodes in carriage before use on HOMER. Separation between carriages is 2 meters, approximately equal to distance between detectors on HOMER. Laser diode carriage photo demonstrates alignment of laser diodes using alignment screws.

Once the carriages are aligned, they are slipped inside the collimator arms while the chamber is at atmosphere. The carriages are designed to fit snuggly inside the collimator channel. The output of the photodetectors are monitored using a Tektronix Oscilloscope. The threaded rods and turnbuckle assembly are then used to adjust the arms until the laser light produces a signal on the photodetectors. The carriages are then removed from the arms and the system is pumped down to vacuum.

The detector faces can go from complete overlap to no overlap if d goes from 0 to $2r$. The distance between the circles is dictated by the angle by which the arm sags from its mounting on the chamber wall. Based upon the dimensions of the collimator channel, the arm could be sagging by as much as 1.75 degrees and still have a clear, although greatly diminished line of sight to the opposing detector. These calculations assume we have a straight collimator channel and that one of that the opposing arm is properly aligned to demonstrate the deleterious effect that occurs even if only a single arm is misaligned. Without any proper alignment, this can lead to an active overlap area of the detector as low as 20 percent. The diameter of the photodetectors used in the alignment system is less than 1 cm. For a separation distance of 2 meters between the laser diodes and the photodetectors, they must be aligned to less than 0.4 degrees in order to receive a signal. This corresponds to an overlap area of the detector faces of at least 80 percent. That is nearly a factor of 4 increase in the minimum reliability of overlap area of the detectors, and correspondingly of coincident event capture capabilities.

The new Adjustable FIDO Arms could ideally make aligning the arms on either side of the chamber much easier by now allowing the elbow to be dropped to 0 degrees and mounting the alignment lasers and photodetectors on the back end of the collimator assemblies. As was mentioned, the laser and photodetector carriages were designed to fit snuggly inside the collimator channel. However, they had to be inserted from the chamber side, which required opening the entire vacuum vessel to align the arms. The carriages were also so closely sized to the inside of the collimator channel that they could often become lodged in the arm and required a great deal of effort to remove them. Now, the carriages can be mounted in a specially designed holder that mounts directly on the back of the X-ray trap, shown in Figure 11.14. This greatly simplifies the alignment procedure. Since the carriages are now also moved from before the elbow in the original fixed collimator channel to behind the X-ray trap in the adjustable assembly, a higher degree of alignment is achievable because the laser diodes and photodetectors are placed farther apart, and therefore must be aligned to a higher degree of accuracy in order for the laser light to be detected on the opposite side by the photodetectors.

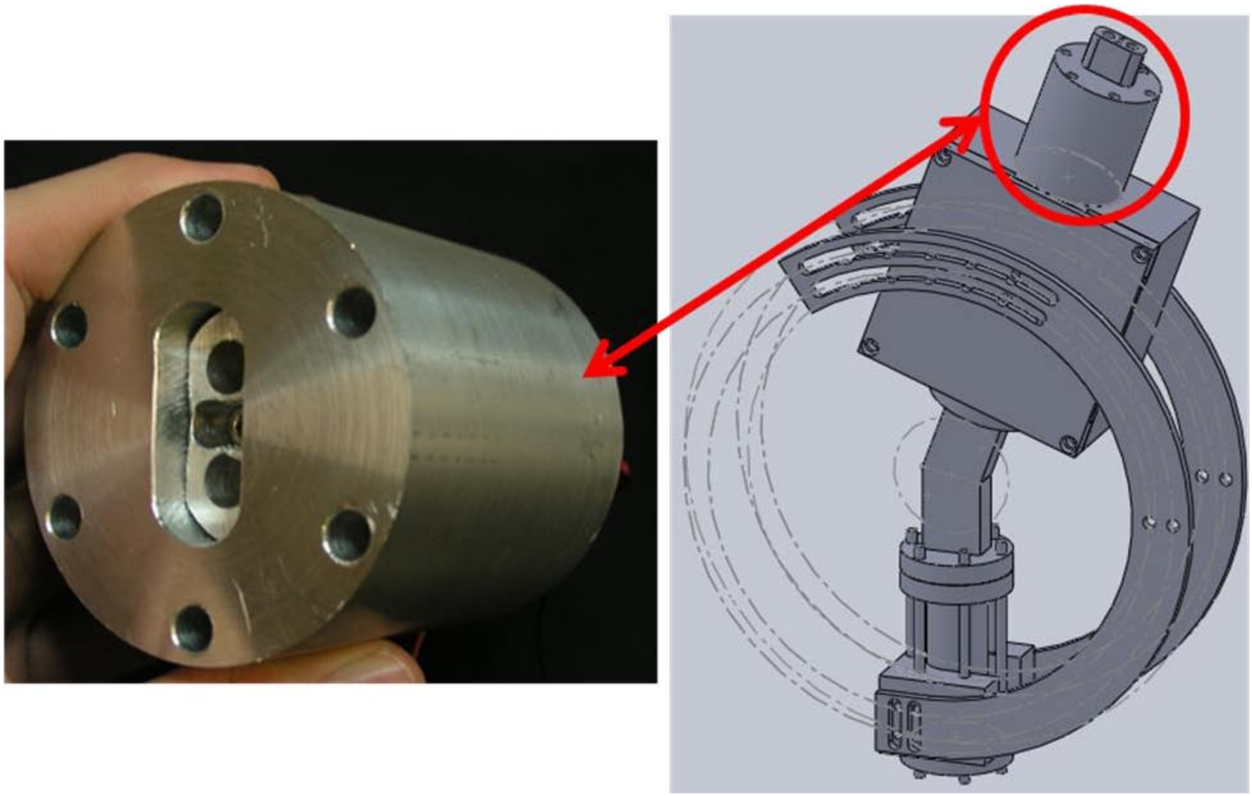

Figure 11.14 Holder for laser and photodetector carriages to be mounted on the back end of the X-ray trap for aligning TOF arms.

Chapter 11 References

1 Piefer, G. R., Boris, D. R. (2007). Coincidental time of flight diagnostic for spatially resolving fusion reactions. Invention Disclosure Report, Provisional Patent Application

2 G. F. Knoll (2000), *Radiation Detection and Measurement*, John Wiley and Sons Inc., New York, NY

3 Personal Communications with Ortec-Ametek Technical Support (January 2011)

4 Boris, D. R. (2009). Novel Diagnostic Approaches to Characterizing the Performance of the Wisconsin Inertial Electrostatic Confinement Plasma, (PhD Dissertation, University of Wisconsin-Madison)

5 Ametek Advanced Measurement Technology (2010). Introduction to Charged Particle Detectors, Web based publication found at www.ortec-online.com

6 GMW (2004). User’s Manual for Model 5403 76MM Electromagnet, Available via GMW website: http://www.gmw.com

12 TOF Experimental Results

The Time-of-Flight Diagnostic has been used to study a variety of parameters including cathode voltage, background deuterium pressure, electrode configurations, concentricity of electrodes, cathode design, and filament configurations. The results discussed in this section will begin with a data set taken at 60 kV cathode potential, 30 mA cathode current, 2 mTorr background deuterium pressure, 20 cm diameter cathode, and 50 cm diameter anode. The spatial profile of fusion events created by the raw data from the TOF diagnostic for this configuration is shown below in Figure 12.1.

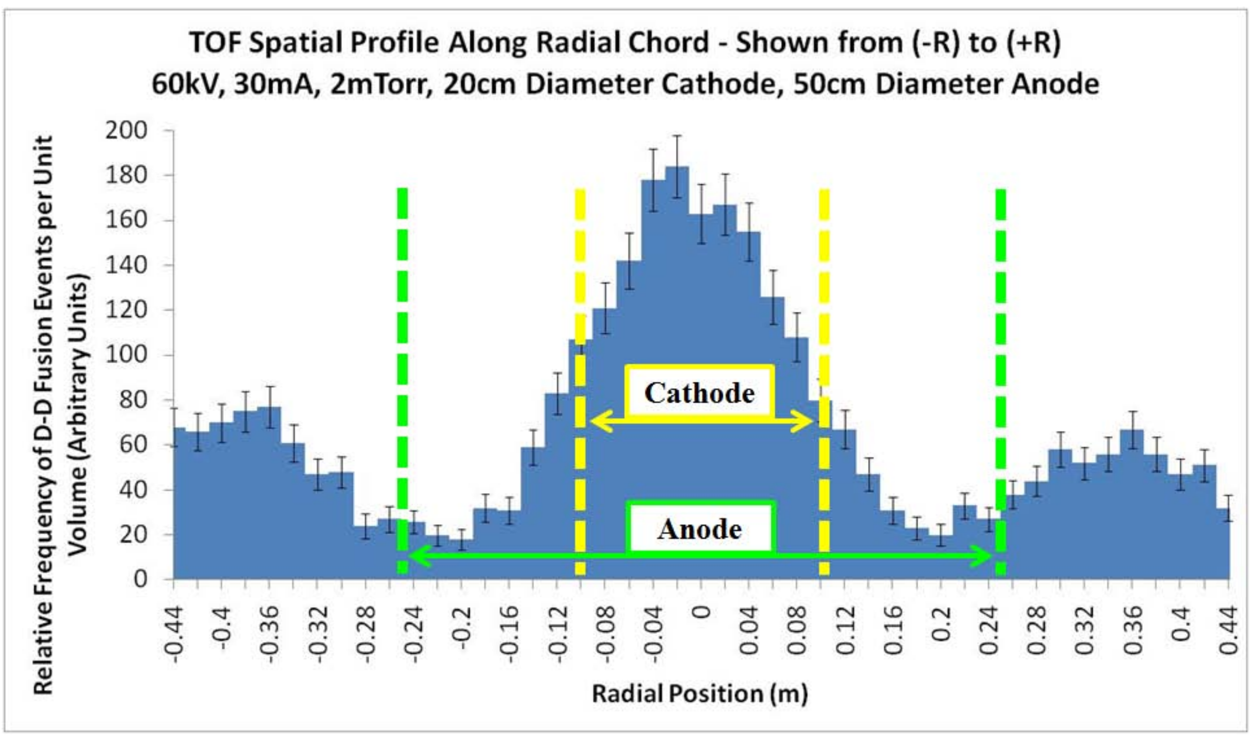

Figure 12.1 TOF spatial profile from raw data extending from (-R) side of chamber to (+R) side of chamber along radial chord. Boundaries of cathode in yellow; boundaries of anode in green.

The data set above contains nearly 3500 counts of fusion events, which was collected at a rate of approximately one count every 45 seconds, resulting in a total of roughly 45 hours of operation time. The rate of data collection for the TOF Diagnostic is dramatically slower than the single-armed FIDO Diagnostic, which collects at roughly 10 to 20 counts per second at the same settings. This difference in counting rates reflects the much lower probability of simultaneously capturing both fusion events of the same reaction as compared to catching only one. The spatial bins along the horizontal axis are 2 cm wide and extend from the (-R) side of the chamber at r = -45 cm to the (+R) side of the chamber at r = +45 cm. The size of the spatial bin was determined based upon the magnitude of the uncertainty in the energy and timing electronics, as well as the accuracy of the charged particle detectors in an environment of constant low energy x-ray noise. The vertical axis of the plot represents the number of coincident counts from D-D fusion events collected in each spatial bin, which is effectively equivalent to the concentration of fusion events per unit volume.

12.1 Analysis of TOF Spatial Profile

As was mentioned, the data displayed in Figure 12.1 was collected using a 20 cm diameter cathode, a 50 cm diameter anode, and the inner diameter of HOMER is 91 cm. The r = 0 point is positioned in the exact center of the chamber, and the cathode and anode are positioned symmetrically about the origin. As can be seen in the results, there is a high level of symmetry about the origin. A comparison of the contributions to the total counts from the same regions on either side of the origin can be seen in Table 12.1 for the raw data in Figure 12.1. Another item of symmetry regarding this data set involves the number of protons and tritons collected on each detector. As was discussed in Section 11.2, the diagnostic setup allows both protons and tritons to trigger the data collection electronics. Of the nearly 3500 events captured in the above data set, 51% were collected from protons reaching West Detector and 49% were collected from protons reaching East Detector. This extra level of symmetry offers some validation that the diagnostic setup is working effectively and that both sides of the diagnostic are collecting data at nearly equal rates.

	r = [-R:0]	**r = [0:R]**
Abs(r) = [0:45 cm]	50.8% $\pm$ 1.3%	49.2% $\pm$ 1.3%
Abs(r) = [0:10 cm]	23.8% $\pm$ 0.9%	23.4% $\pm$ 0.9%
Abs(r) = [10:25 cm]	8.7% $\pm$ 0.5%	9.8% $\pm$ 0.6%
Abs(r) = [25:45 cm]	18.3% $\pm$ 0.8%	16.1% $\pm$ 0.7%

Table 12.1 Percentage of total counts from r = -45 cm to r = +45 cm existing on each side of the origin for given regions of r for raw data.

The high level of symmetry across the device from (-R) to (+R) allows the spatial profile seen in Figure 12.1 to be folded in on itself about the origin, thereby creating a radial profile from r = 0 to r = R. The resulting radial profile can be seen in Figure 12.2. The radial profile can then be divided into regions based upon the boundaries of the electrodes and the wall of the vacuum chamber. The region inside the cathode (radius 10 cm) is the Core, the region between the cathode and the anode (radius 25 cm) is the Inter-Grid, and the region between the anode and the chamber wall (inner radius 45.5 cm) is the Source. The region beyond the chamber wall is considered to be inside the arm of the TOF diagnostic.

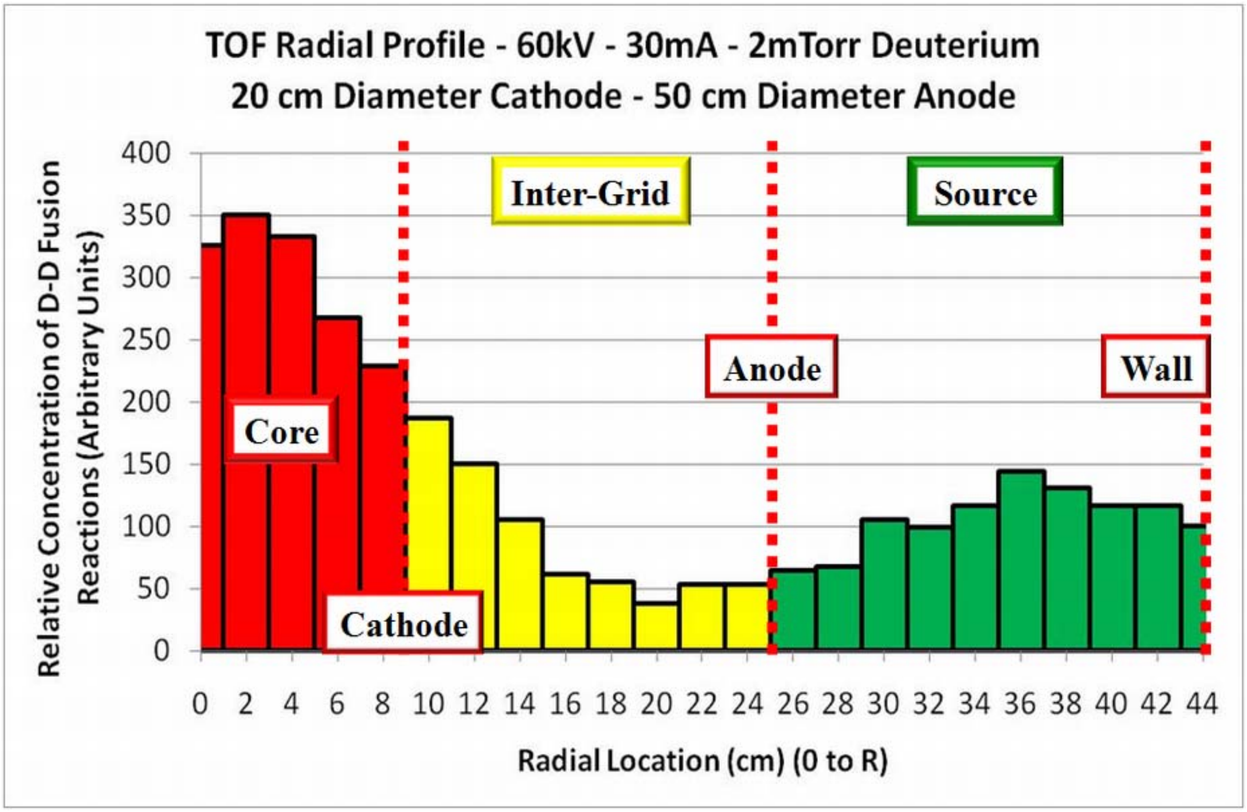

Figure 12.2 TOF Radial Profile created by folding Spatial Profile [-R:+R] in on itself about the origin to create a profile from [0:R]. Radial Profile is divided into regions, determined by the radii of the electrodes and the inner wall of the vacuum chamber.

The vertical axis of the radial profile represents concentration of fusion events per unit volume. The highest concentration of fusion events takes place in the Core near the center of the cathode. This conforms with the original theory of the IEC devices that the positive ions are being accelerated towards a central focus where they will fuse. However, the distribution of counts throughout the core demonstrates how HOMER does not create a single point focus, but rather a region of fusion inside the cathode. The concentration of fusion is highest in the center of the cathode, but remains high throughout the Core region. The electrostatic potential across the Core is ideally constant, though in reality there will be some fluctuations in potential due to the holes in the grids in which potential valleys can form. This region of constant field causes the ions to remain at a constant energy as long as they travel inside the Core. Because both the background deuterium pressure and fusion reactant velocity are roughly constant throughout the Core, the probability of a fusion event between a fast particle and a background atom is therefore also constant throughout the Core. The only factor that would make fusion in the exact center of the Core more likely is the geometric convergence of the device, which should cause an increasingly higher concentration of fast fusion reactants as the origin is approached. The fact that the peak in counts is so wide within the core would indicate that the current electrode design is not achieving optimal convergence.

The issue of core convergence in a spherically convergent ion focus such as the IEC has been analyzed by individuals such as Krall and Rosenberg [1]. Their work detailed much of the theoretical result of collisional effects between ion-ion and ion-background interactions, which can result in thermalization of the ion velocities and can cause ions to take on non-radial trajectories. More recent research conducted by McGuire [2] demonstrated using PIC code modeling of IEC systems with a single cathode that extensive defocusing of the fusion reactant beam lines occurs as the particles travel back and forth in the potential well. This was believed to be due in part to small angle collisions with background particles that caused the fast particles to assume slightly non-radial trajectories that eventually became chaotic after several passes. The most significant reason for the defocusing that was found from this computer modeling was the existence of the high voltage stalk, which offers a strong perturbation to the spherical symmetry of the device. The result of the PIC code modeling for a singly gridded IEC device with a stalk can be seen in Figure 12.3. As is evident in the figure, even when the system starts with tightly focused ion beams from the source region, they quickly can become defocused and chaotic within the core as they are slightly deflected from radial trajectories and recirculated in the well. This modeling assumed nearly constant particle energy of 50 keV, while in the case of HOMER there is likely to be a wide spectrum of particle energies, dominated primarily by lower energy particles in the range of 10 keV, as was first predicted theoretically by Emmert and Santarius [3] and later observed by Boris using the FIDO Diagnostic [4] (see Chapter 9) and compared with the theoretical modeling [5, 6]. These lower energy particles would be even more susceptible to assuming slightly non-radial trajectories and would only exacerbate the diffusion of the core. The PIC modeling shown in Figure 12.3 is also performed at a much lower pressure (10^{-10} Torr) than HOMER's typical operating range (2 mTorr), which means that HOMER would have a higher probability of collisions with background particles. These effects are most likely responsible for the broadening of the peak in fusion concentration seen in the Core in the radial profile from a single sharp peak to an extended region of high fusion rates throughout the cathode.

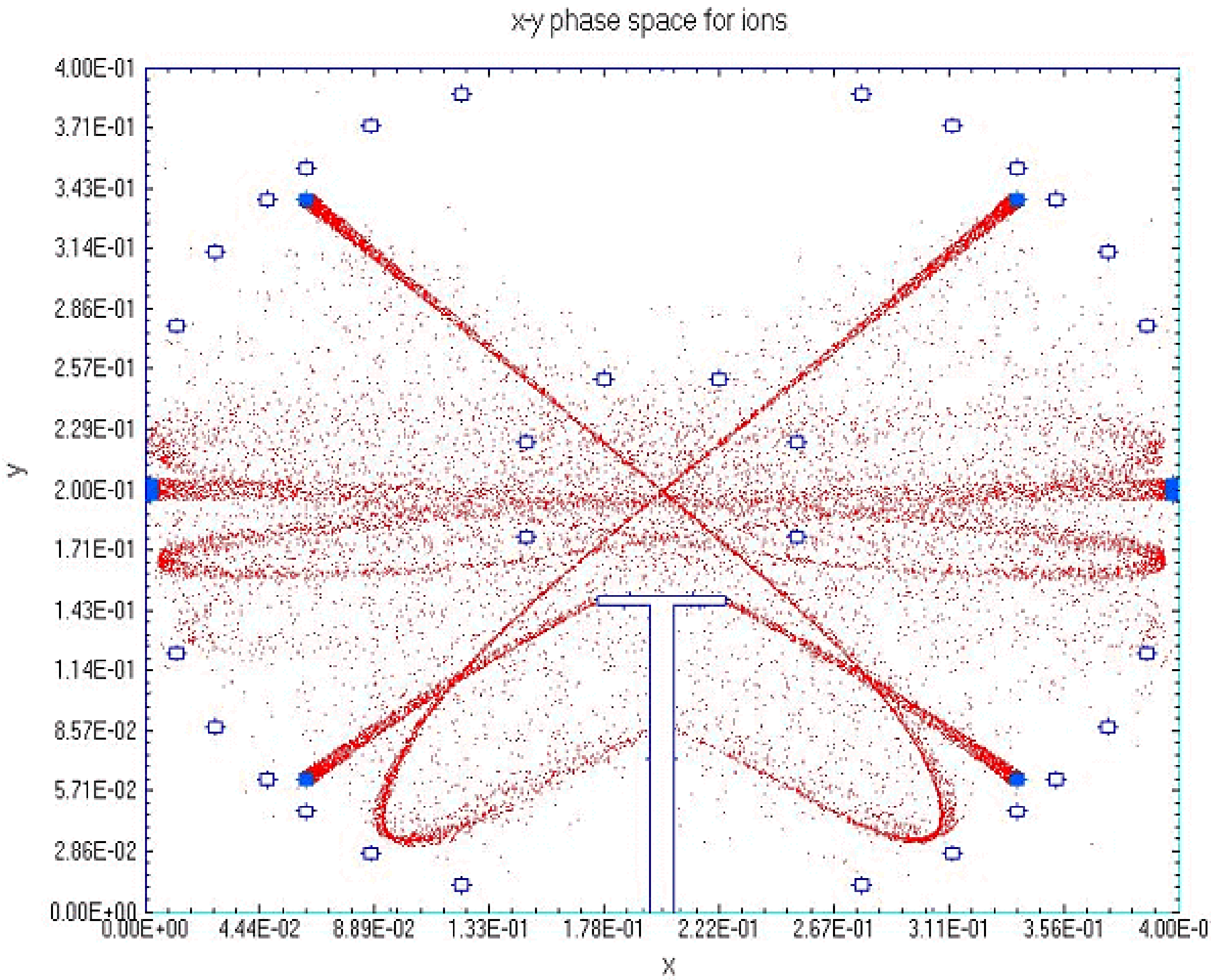

Figure 12.3 PIC Modeling of singly gridded IEC device with high voltage stalk in place. Cathode potential is 50 kV, background deuterium pressure is 10^{-10} Torr, cathode diameter is 10 cm, anode diameter is 40 cm. System begins with six distinct ion sources producing focused beams, which become defocused as they approach the center of the device. [2]

Proper convergence is essential for optimizing fusion between fast particles because the concentration of fast ions in the device has been estimated to be at least four orders of magnitude less than the concentration of background particles. If beam-beam fusion was dominating the system, then there would most likely be a very distinct peak in the center of the cathode where the fast particles are converging. Previous research conducted on HOMER using alternative diagnostic methods, described in Section 2.5, has indicated that beam-beam fusion most likely makes up a very small portion of the total fusion in the device as compared to beam-background fusion. The lack of a large spike in counts in the center of the cathode indicates that the system is not achieving an optimal convergence of beam-beam fusion at the center of the device. Beam-beam fusion may still be occurring elsewhere in the Core, though the probability of a fast ion colliding with another fast ion is significantly lower if they are not converging towards a central focus and have to rely merely on the chance of overlapping trajectories as they travel throughout the Core region.

The concentration then drops steadily as r increases until the anode is reached. At around the anode, a previously unexpected phenomenon occurs in which the concentration suddenly begins to rise again as r increases and extends into the Source region. Spatial profiles have been made of HOMER with similar electrode grid configurations in the past by Thorson [7], Cipiti [8], and Murali [9]. These methods involved using a single charged particle detector and measuring the total number of protons collected within the cone of view while varying the line of sight of the detector (Thorson and Cipiti) or while varying the size of an eclipse disc in front of the detector (Cipiti and Murali) to measure the contribution from the remaining region. In these cases, D-D fusion protons were detected in measurable quantities outside of the anode indicating that fusion is indeed occurring in the Source region. Analyses were then conducted to determine approximately how much each region contributed to the total fusion in the chamber. None of these previous methods determined that a profile existed such as the one found with the TOF Diagnostic, in that there was a drop in fusion up to the anode and then a subsequent increase in the Source region.

One issue with the previous method of determining spatial profiles was that some assumption had to be made about the profile of the device in order to perform the analysis. In the case of Thorson's work, the assumption was made that the shape of the fusion counts inside the cathode could be modeled by a polynomial function, and that outside the cathode there was a constant $1/r^2$ fall off in fusion. Based upon the knowledge available at the time, this was considered to be an accurate assessment of the profile. Another assumption that was made, particularly in the work of Cipiti, was that there was a nearly uniform amount of fusion occurring with background particles throughout the chamber. As the cones of view of the detectors cut through an off axis slice of the sphere, it would pass through both the high count region and low count region at different points in the sphere, making it very difficult to distinguish between them. Instead, the high and low concentration regions would be collected in the same cone and averaged together over the entire collection volume. This would effectively smooth out any peaks in counts and simply add to a rise in overall counts throughout the region. The TOF Diagnostic offers the first method of empirically collecting individual fusion events and determining location based upon measurements of timing and velocity. None of the same assumptions about the spatial profile of the device have to be used in order to perform the analysis. This could offer a potential explanation for why this phenomenon has not been seen before using some of the previous diagnostic methods.

When the shape of the TOF Radial Profile was discovered, a variety of tests were performed on the diagnostic to determine if the peak of counts in the Source region could somehow be a feature of the diagnostic and not actually reflective of what was happening in the device. The TOF electronics were all tested and confirmed to be functioning within acceptable parameters. The detectors were re-calibrated using a different Am-241 source from the UW Reactor Lab, and were found to be functioning. The electronics and detectors for each of the TOF Arms were switched to ensure that slight variations in operational abilities of the components were not causing discrepancies, and no change was seen in the profile. Significant consideration was also given to the possibility that the region of view of the diagnostic could somehow be preferentially seeing more or less of certain fusion reactions in the device based on location in the viewable region, as well as the energy and trajectories of the fusion reactants and products. This possibility was taken into consideration and is discussed further in Section 12.4. There has been no indication that reactions are somehow significantly more likely to be seen in the Source region that could allow for there to be an artificial increase in counts in that area.

As was discussed in Section 11.2, a set of delays was used to allow both arms of the TOF diagnostic to collect protons and initiate the capture of a coincident event, which effectively doubled the collection rate from the original setup in which only one arm was capable of collecting protons. This also allows TOF profiles to be collected from proton initiated capture events from two different sides of the chamber and be added together to create the total profile, effectively seeing the same region of the chamber from opposite sides. As has already been said, the disparity between the number of coincident events captured by each arm is less than 2 percent of the total, demonstrating excellent symmetry in the collection capabilities. The profiles created from the two arms were compared and both of the spatial profiles showed peaks in the Source region on both sides of the origin. This helped to remove concerns that the peaks were simply a manifestation of the TOF collimator channels' line of sight that provided preferential view that the detectors may have to one side of the chamber over the other, which could have potentially lead to an artificial skewing of the results. Scans were also taken with the delays removed altogether, reverting the system back to having the ability to only collect from one side, at half the collection rate. Profiles were collected from both arms individually acting as the triggering proton collection arm, and in both cases the Source region counts continued to show up on both sides of the origin. Once these methods for confirming the validity of the profiles were conducted, the analysis continued as to why these profiles would take such a shape.

At the time when the experiments of Thorson, Cipiti, and Murali were performed, the only recognized explanation for how fusion reactants could have sufficient energy to fuse beyond the anode was due to charge exchange reactions. These occur between fast positive ions and background neutrals, thereby creating a cold ion and a fast neutral that would then be capable of continuing its trajectory out of the potential well without being slowed, allowing the neutral to maintain enough energy to fuse with a background deuterium atom in the source region. The high energy neutrals would be created somewhere in the potential well and stream away from or through the center, presumably creating a $1/r^2$ falloff as they moved towards the walls of the chamber. A new type of fusion reactant has since been discovered that may have relevance to fusion in the Source region, which are the negative ions, discussed in Chapter 9. Negative ions gain energy from the electrostatic potential well in the opposite direction as the positive ions, and therefore speed up as they travel from the Core through the Inter-Grid towards the Source region. Unlike the positive ions, which are able to recirculate back and forth in the potential well, the negative ions are accelerated out of the well and therefore only receive a single pass. The positive ions are at their maximum energy when traveling through the Core, and therefore have the highest probability of fusing in that region. The negative ions reach their maximum energy when they have left the outer boundary of the potential well, which means their highest probability of fusing is in the Source region. The Inter-grid is primarily a transit region for both positive and negative ions as they are either speeding up or slowing down, but neither type of ion reaches its full energy, and therefore its highest probability of fusing, until leaving the potential well. Because of this, the negative ions offer a possible explanation for why there would be a drop in counts in the Inter-Grid and then a sudden increase in counts in the Source region. The directions of increasing energy for positive and negative ions are shown in Figure 12.4. High energy neutrals are also streaming radially in both directions throughout the chamber.

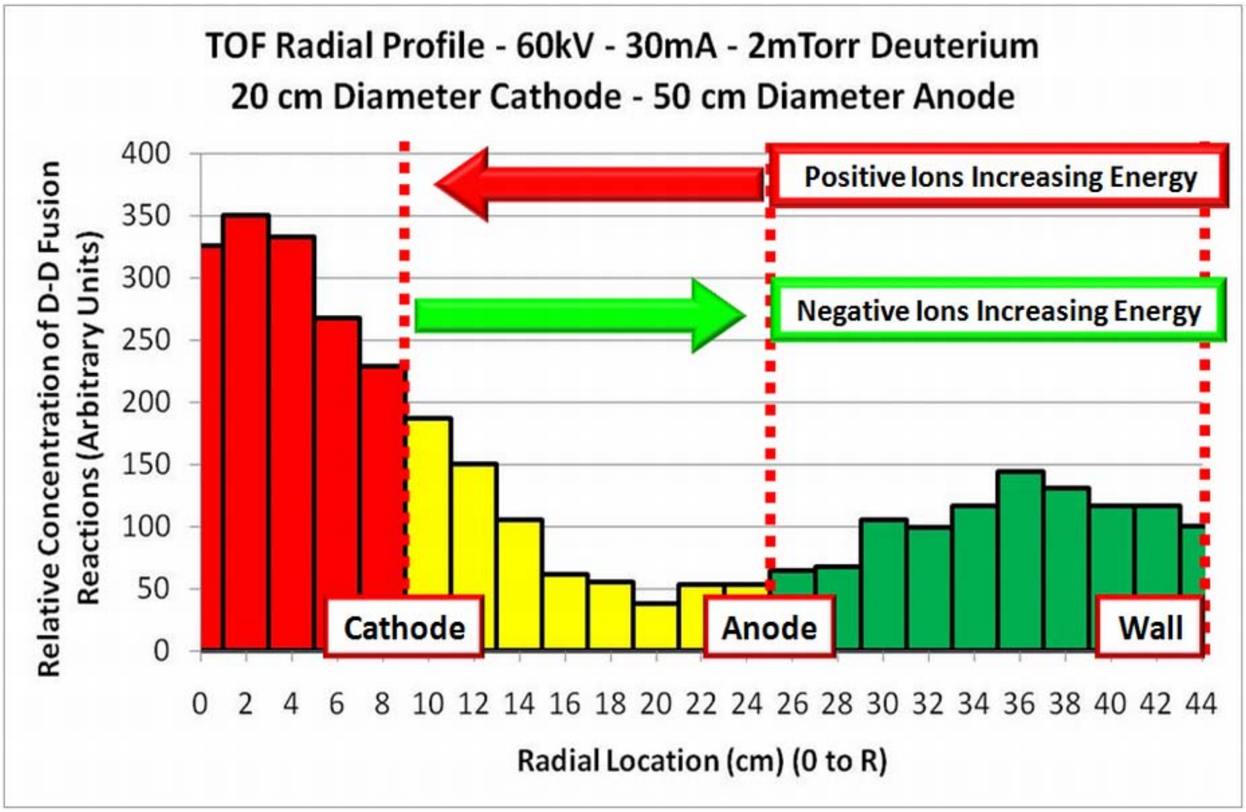

Figure 12.4 TOF Radial Profile shown with direction of radial trajectories of the three known fusion reactants occurring in the IEC device: positive ions, negative ions, and high energy neutrals. Neutrals are not affected by the potential well and maintain a constant energy throughout the device once they are created.

The discovery of negative ions in IEC devices occurred rather recently by Boris [10], and there is still a great deal that is unknown about their behavior and impact on the operation. Unfortunately, while the FIDO and TOF diagnostics are able to determine the location of a fusion event and the energy of the fusion reactants, they are incapable of empirically determining the charge of the fusion reactants that created the fusion event. There are several issues with the theory that negative ions are responsible for the increase in Source region fusion that are as of yet not fully understood. The first issue is whether there are a sufficient number of negative ions streaming out of the potential well to bring about such a large rise in fusion events in the Source region. Because the positive ions are able to recirculate in the potential well, they are potentially given a somewhat longer length over which to travel, thereby giving a higher probability of fusing than the negative ions, which accelerate directly out of the chamber. The negative ions would also be emitted somewhat radially from the chamber, which would cause their paths to diverge as they traveled through the Source region, lowering the concentration per until volume as r increases. Initial estimates of negative ion current leaving the potential well collected using a Faraday cup have indicated that it is possible that only around 5 percent of cathode current goes into creating negative ions [10], while positive ion current has been estimated to be on the order of 30 percent. However, the energy spectra collected from negative ions have indicated that the average energy of negative ions may be as much as three to four times higher than that of the positive ions. For the energy ranges in which the data set discussed here was collected to create the radial profile, that difference in energy between the positive and negative ions could result in more than an order of magnitude increase in the D-D fusion cross-section. This could allow for a relatively small population of negative ions to have a much larger contribution to the total fusion rates due to their harder spectra.

Another issue with the Source region counts is why the counts only begin to pick up at the anode and do not reach full height until 5 to 10 cm into the Source region. Theoretically, the potential well created by the electrodes would ideally have finite barriers at the boundaries of the cathode and anode. In this model, the potential reaches its lowest point at the cathode radius and remains constant throughout the cathode, and the potential reaches its highest value (ground) at the anode radius and the potential should remain constant throughout the region outside of the anode. Based on this model, because the potential does not change outside of the anode, there should be no additional electrostatic force to continue to accelerate or decelerate the ions in the Source region. Therefore, the ion velocity should be constant throughout the Source region beginning at the anode radius and correspondingly so should the probability of fusion. The question then arises as to why do fusion rates continue to increase beyond the anode if the negative ions should have theoretically reached their maximum velocity at the anode radius. As was mentioned previously, there is also believed to be a significant flux of high energy neutral particles streaming radially outward into the Source region, but these particles are not affected by the potential well and therefore should have a uniform probability of fusing throughout the source region.

In the experiment, however, the electrodes are made from highly transparent spherical wire grids, which do not form perfect boundaries for the potential well. The holes in the grid are likely to cause slight perturbations in the potential around the anode in which the electric fields extend slightly into the Source region, causing a non-uniformity in the potential of the Source region. This would extend the boundary of the potential well beyond the anode radius. The cross-sections for D-D fusion in the energy ranges which are being considered here (10-60 keV) can vary quite a bit over slight changes in reactant energy. As little as 5 keV can result in two to three factor increases in the probability of fusion. This could provide a possible explanation why the fusion concentration measured in the TOF profiles continues to increase for an additional 5 to 10 cm beyond the boundary of the anode. An experiment that could be accomplished on HOMER in the future that could help to answer this question would be to install a moveable emissive probe in the Source region to study the vacuum potential. Ideally, the probe would be capable of moving radially to determine the extent of the potential variation from the anode boundary to the wall. Movement in the polar and azimuth directions could also be beneficial to effectively map out the potential profile around one of the holes in the anode to determine how it might be effecting the potential profile, and possibly the fusion reaction rate, in the Source region. The negative ions in the source region are currently being examined by Alderson [11]. Through the use of a moveable Faraday Cup, the current of negative ions at various locations in the Source region is being measured. As this work continues to evolve, it will help to explain how the negative ions may be impacting the fusion rates in the Source region.

12.2 Effect of Concentricity of Electrodes on Spatial Profile

Another experiment that was performed was to determine the effect on the spatial profile from a non-concentricity in the electrodes. Ideally, the cathode is to be placed in the exact center of the anode in order to create the most symmetric potential well possible. However, the realities of experimental setups typically dictate that perfect concentricity of the electrodes is not always achieved. There is a desire to determine in what way and to what extent this imperfection could affect the spatial profile. To do this, data was taken using the 20 cm diameter cathode, 50 cm diameter anode configuration, in which the cathode was placed 1 cm out of alignment from the exact center of the anode. After a data set was taken in this position, the grids were rotated by 180 degrees and another data set was collected. The grid mounting system, as described in Section 7.3.3, is completely dependent on the position of the lid of the chamber. Therefore, to take a data set of the opposite side, the lid simply had to be lifted and rotated by 180 degrees and sealed back in place. The reason why two data sets were taken of the same configuration from opposite sides was to add an additional check on the accuracy of the diagnostic. After the first data set was taken with a non-concentric cathode, it appeared that the core had been shifted slightly to one side. To ensure that this was not simply a fault in the diagnostic, the opposite view was taken, and this resulted in the core being shifted to the other side. The data can be seen in Figure 12.5.

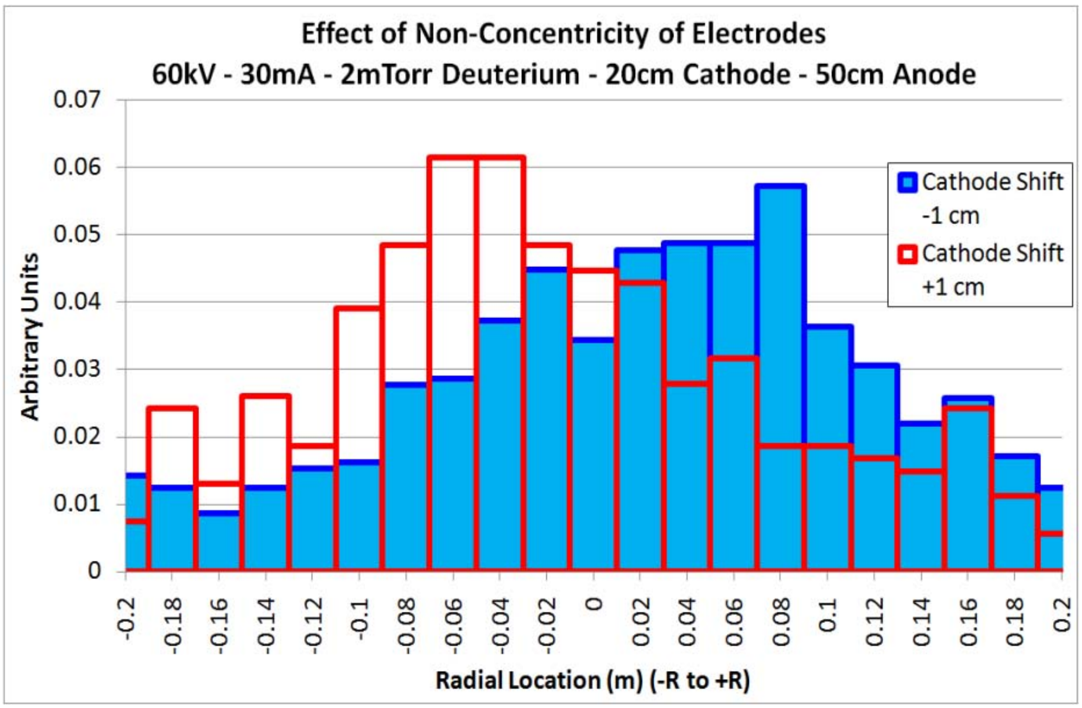

Figure 12.5 Close-up of spatial profile focusing on shift in Core region of 20 cm diameter cathode, 50 cm diameter anode configuration due to cathode misalignment of 1 cm. Cathode shift of +1 cm implies cathode is moved closer to the +R side of the chamber, and vice versa. Profiles are overlayed, with pink representing the +1 cm shift, blue representing the -1 cm shift, and purple representing the region of overlap between the two profiles.

A 1 cm misalignment of the cathode results in one side of the cathode being 14 cm from the anode, while the other side is 16 cm from the anode. As can be seen from the data, when the cathode is shifted 1 cm in one direction, the peak in counts in the Core region shifts towards the opposite direction by approximately 5 cm. The peak in counts in the Core appears to favor the side of the cathode that has the largest distance between the electrodes. This trend could potentially be related to experiments conducted previously using both neutron detectors and the FIDO diagnostic, which examined the difference in fusion rates between configurations with the same size cathode but different size anodes. These experiments, described in further detail in Section 7.3.3 and Chapter 9, compared neutron production rates for three configurations involving a 20 cm diameter cathode with 30, 40, and 50 cm diameter anodes. The neutron rates were found to increase as the anode diameter, and hence the separation distance between the electrodes, was increased. The FIDO data indicated that the larger grid separation resulted in a higher fraction of D_3^+ ions, which are believed to dominate the ion population in the Source region, being converted into D_1^+ ions, which have a higher probability of fusing because of their higher energy due to their lower mass. This may explain why the peak in counts in the Core favors the side of the cathode with the largest separation between electrodes. This case also demonstrates how even a small misalignment of the electrodes can result in a disproportionate shift in the Core of the device.

The issue of rotating the lid to test the accuracy of the diagnostic also yielded interesting results. As was mentioned, the electrodes in the two cases shown in Figure 12.5 are in the same position relative to each other, the lid was simply lifted and rotated allowing the entire configuration to be rotated without disturbing the electrodes. All other operating conditions were held the same, so the only feature that has changed with regard to what the TOF diagnostic sees is that the cathode asymmetry is now on the opposite side. When the two data sets are overlayed, they appeared to be mirrored quite well about the origin at r = 0. This indicates that the spatial dimensioning is reasonably accurate such that the diagnostic was able to identify the center of the chamber as the point about which the rotated system is reflected. This also adds validation to the precision of the device in that it was capable of detecting the peaks on the order of centimeters as they show up at nearly the same position on either side of the origin.

12.3 Perturbations to Spherical Symmetry of HOMER

When attempting to convert a spatial profile [-R:+R] created by the TOF diagnostic into a radial profile [0:R], symmetry about the device is an important consideration. If the spherically gridded IEC is analyzed in a standard spherical (r, θ, φ) coordinate system, then the TOF diagnostic is only capable of collecting a radial profile along a single chord through the origin of the spherical symmetry, which corresponds to only a single value of θ and φ on either side of the origin. The fusion concentration at a given value of r may vary as the position is rotated around the sphere in either the altitudinal or azimuthal directions. The issue of asymmetry in the electrodes has already been discussed, as well as the computational modeling of the effect of the high voltage stalk in perturbing the radial trajectories of the reactants. There are a number of other features of gridded IEC devices, and HOMER in particular, that must also be taken into consideration. Several of these issues that will be discussed here are dips in the potential well between electrode grid wires and location of the tungsten filament ion sources.

12.3.1 Microchannels Created in Potential Valleys between Cathode Wires

Ideally, the potential well would be created by a completely transparent and totally uniform conducting sphere. In reality, a compromise between the two features must be made, resulting in the use of highly transparent and conductive grids. The field around the spherical grid is largely uniform on the order of tens of kilovolts, but slight drops in the potential will invariably occur in the holes between wires. The magnitude and profile of the drop is dependent upon the size and shape of the grid hole. Charged particles are then capable of preferentially falling into these potential valleys and traveling in them through the electrodes, creating microchannels or “spokes” emitting from the cathode. Because the cathode is at a large negative potential, the microchannels would be a region of slightly less negative potential, causing negatively charged particles to preferentially move into them. The highest concentration of negative particles currently believed to exist in these channels is electrons created near the cathode from ion impacts with the cathode wires, ionization of background gas within the Core region, or through thermal emission of the hot tungsten metal. The recently discovered negative ions would also be preferentially driven into these channels. Negative ions can be created near the cathode from electrons in that region ionizing background gas and through charge exchange reactions between fast ions or neutrals traveling through the core and background deuterium. The cross sections for these reactions can be seen in Figure 12.6 and Figure 12.7. Once the electrons fall into these microchannels, they would immediately be accelerated radially away from the cathode. Along the way they have the possibility of ionizing background deuterium, thereby creating positive ions, which would then be drawn in the opposite direction back towards the core. In this manner, the microchannels are theoretically capable of acting as preferential pathways for counter streaming currents of positive ions, negative ions, and electrons.

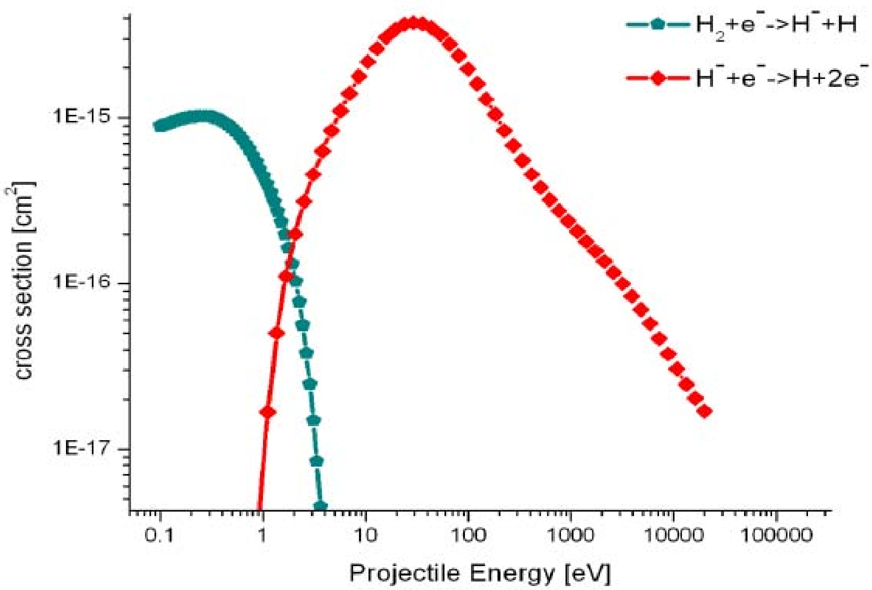

Figure 12.6 Probability of negative ion creation from cold electrons (less than 10 eV) and negative ion neutralization from electrons. [12]

.

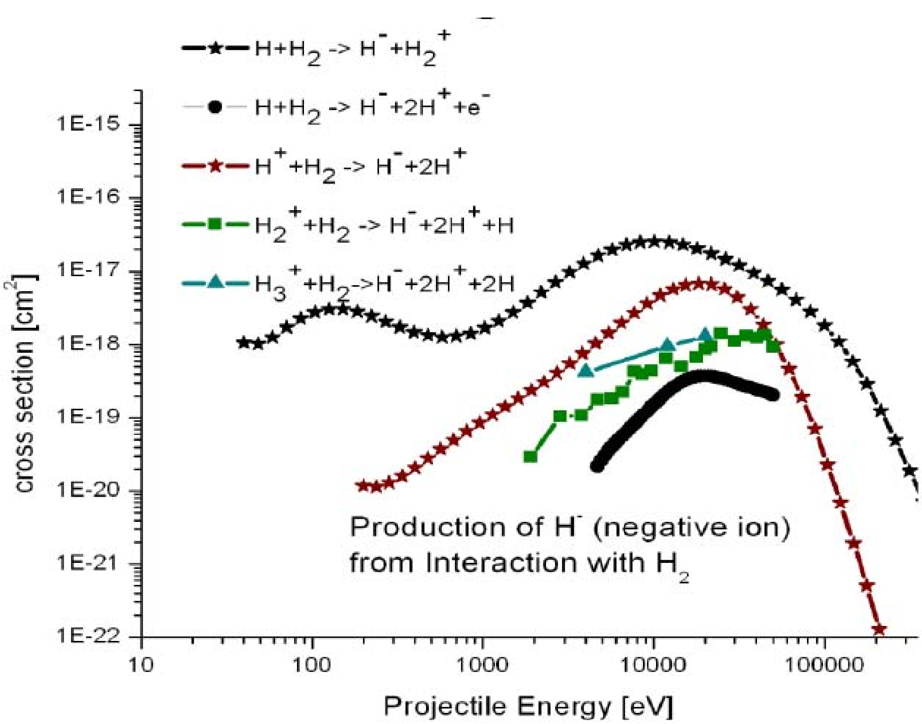

Figure 12.7 Probability of negative ion formation from various charge exchange and atom impact reactions. [13] [14] [15]

The existence of these microchannels in IEC devices has been theorized for some time, and experiments have been performed on HOMER before to try and characterize the channels. Research conducted by Murali, *et al.* [16] on HOMER involved rotating the cathode at controlled angular increments and measuring the variation in proton counts collected by a detector that was held at a fixed position facing the cathode. The results demonstrated that when the proton detector was aligned with a cathode wire, the proton count rates were on the order of 40% lower than the rates for when the detector was aligned with a hole. Similar experiments were conducted recently utilizing both the FIDO and TOF diagnostics to monitor the variation in fusion product count rates as different views of the cathode were studied. Two different cathodes were used in these studies, both of which were of the latitude/longitude configuration. The first grid consisted of 11 latitude and 24 longitude wires, and is known as the 11/24 grid. The second grid consisted of 6 latitude and 16 longitude wires, and is known as the 6/16 grid.

A key difference between these grids other than the number of wires is that the 11/24 grid included a wire at the equator while the 6/16 grid had no wire at the equator. The microchannels are believed to be emitted from the center of the holes in the grids in a direction normal to the surface of the sphere. Therefore, if the grid has a wire at the equator, then the microchannels will only be emitted above and below the equator and continue to move radially outward away from the midplane. The line of sight of the charged particle detectors in the diagnostics is parallel to the midplane created by the equator of the cathode, which means the detectors would not be able to get a direct view of one of the microchannels when observing the 11/24 grid. The 6/16 grid was constructed without an equator wire so as to produce microchannels that would be emitted directly from the midline, and therefore would be capable of being collected by the diagnostics. Drawings of the grids and the microchannels can be seen in Figure 12.8 and Figure 12.9.

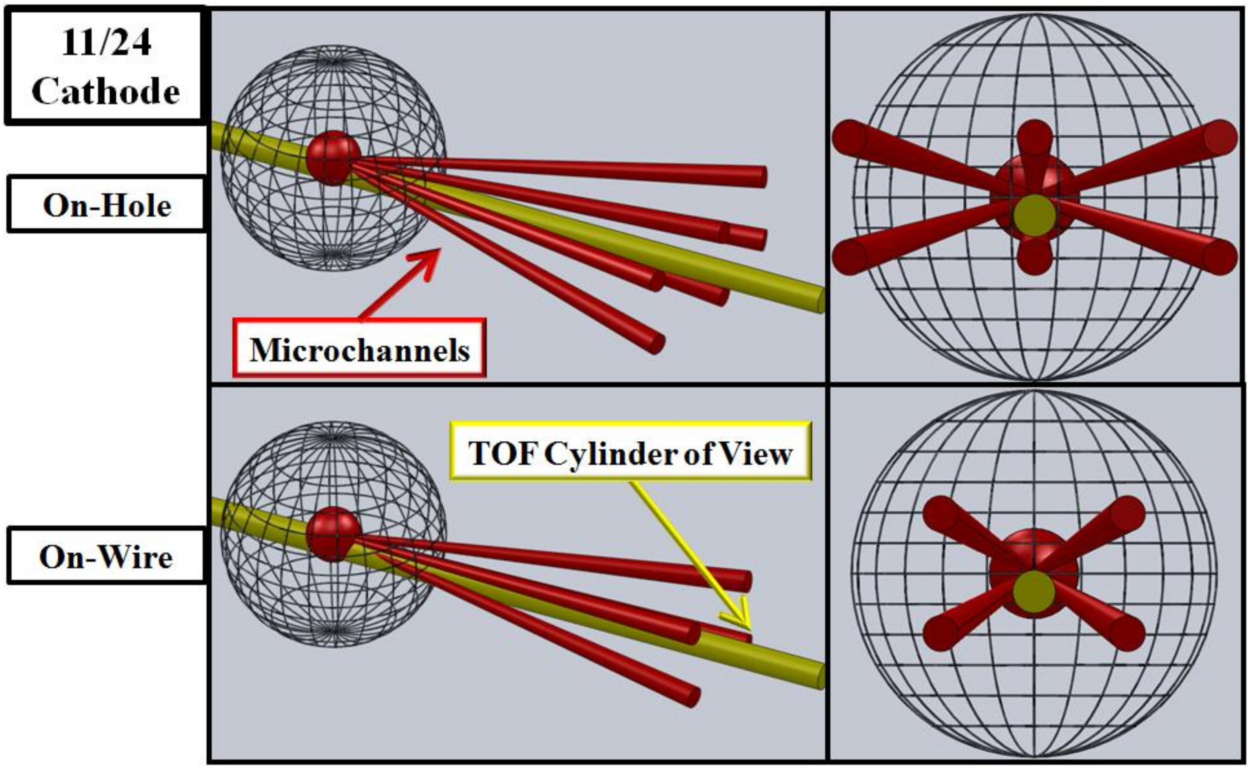

Figure 12.8 Schematic view of 11/24 Cathode with microchannels (red) extending from holes in grid and the view of the TOF diagnostic shown (yellow). Microchannels extend above and below the TOF Cylinder of View due to existence of equator wire.

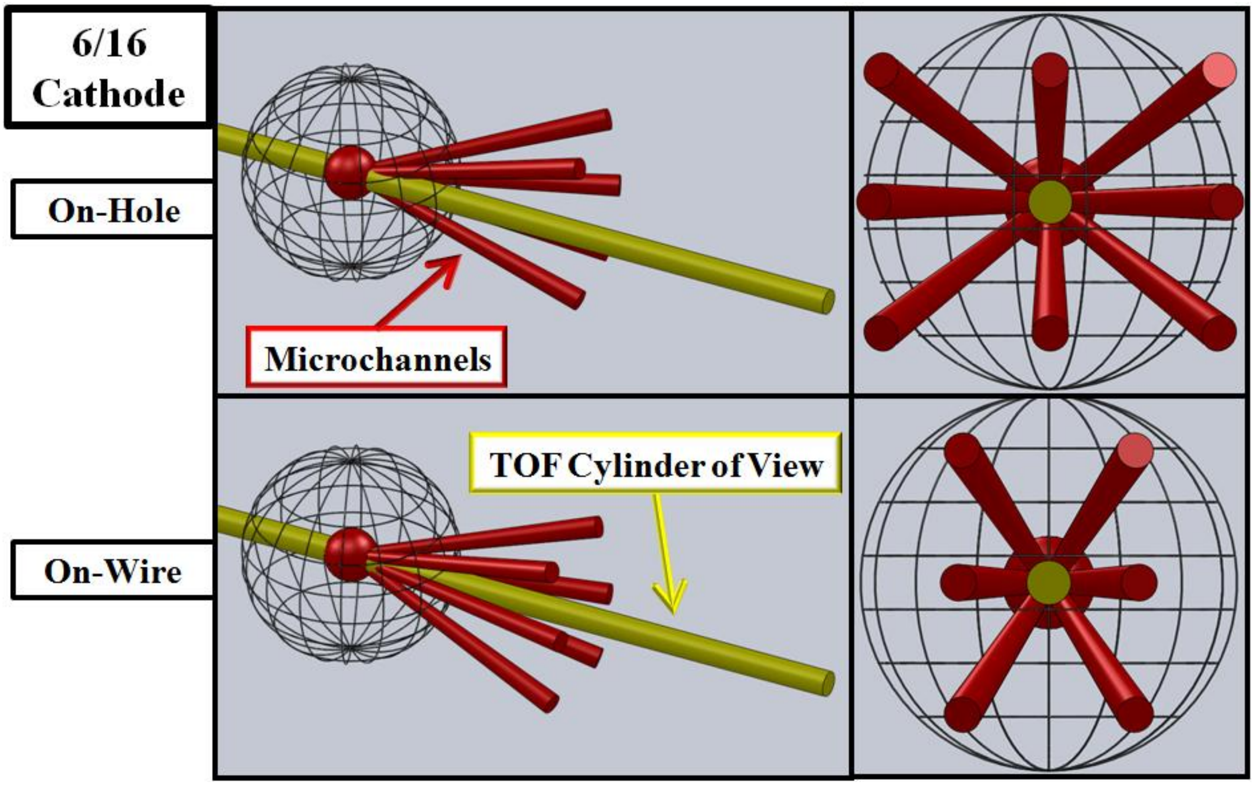

Figure 12.9 Schematic view of 6/16 Cathode with microchannels (red) extending from holes in grid and the view of the TOF diagnostic shown (yellow). Microchannels extend directly from midplane of grid because there is no equator wire.

The cylinder of view of the TOF Diagnostic is dictated by the diameter of the face of the charged particle detector, which is 2.4 cm. The view of the charged particle detectors in the FIDO and TOF diagnostics was slightly below the equator for the 11/24 Cathode, which encompassed both the center of the cathode and the center of the ring of holes below the equator. As is described in Section 7.3.2, the cathode has a molybdenum nut woven into the top of the grid, which is then fixed into place on the molybdenum conducting rod of the feedthrough by a pin that is placed through a hole in the nut and a hole in the rod. Previously, the only way to change the height of the cathode relative to the chamber was to move the Boron Nitride stalk surrounding the molybdenum conducting rod up in the feedthrough. This involved breaking the vacuum seal and oil barrier and risking damaging the stalk, and it was also a one way movement because the top of the stalk was covered in high voltage oil and could not be moved back down into the vacuum. When the new 6/16 cathode was constructed, a new feature was added to allow more versatility in positioning the cathode in the chamber. The height of the molybdenum nut on the top of the grid was increased from 12.5 mm to 25 mm and through holes were placed every 2.5 mm up the nut. This allowed the cathode to be moved up or down by slight increments in order to achieve the optimal position with regard to the view of the diagnostics. The new molybdenum nut design is shown in Figure 12.10.

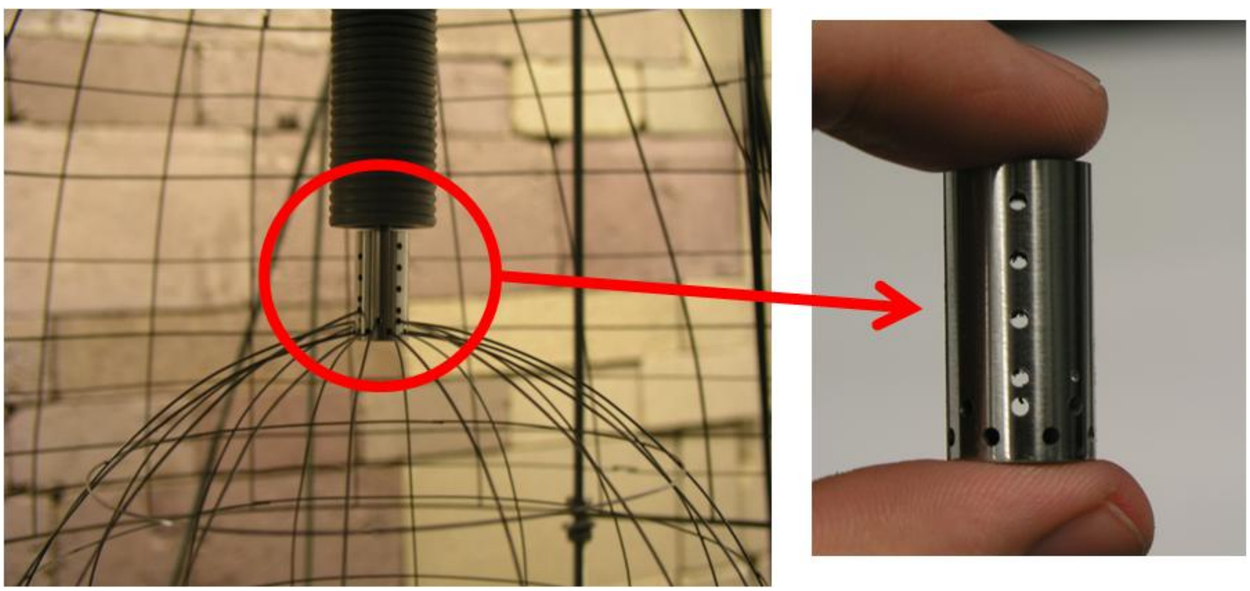

Figure 12.10 Molybdenum not on 6/16 Cathode was made larger (25 mm) than previous designs (12.5 mm) and included through holes at increments of 2.5 mm to allow minor height adjustments of cathode to better align the midplane of the cathode with the diagnostics.

The new design for the molybdenum nut on the 6/16 Cathode allowed the grid to be placed at a chosen height, which allowed the view of the diagnostics to be lined up directly with the equator of the grid. Because the 6/16 Cathode had no wire at the equator, this could then allow the diagnostic to look directly down one of the microchannels. Between the two different cathodes, data sets were taken at a total of four different views, which are shown in Figures Figure 12.8 and Figure 12.9. These consist of On-Wire and On-Hole views for both cathodes. FIDO and TOF data was taken for all four of these views and compared. The FIDO data indicated that for the 11/24 Cathode, the D-D fusion proton count rate was nearly equal for the On-Hole and On-Wire cases. This would seem to indicate that neither view was receiving the full path of a microchannel, and thus neither would be able to capture the increased fusion rates. This was to be expected because the microchannels were believed to be emitted from the surface of the cathode sphere with trajectories above and below the detectors line of sight, which would have forbidden the diagnostics from seeing the full microchannel. The FIDO data taken on the 6/16 Cathode however, indicated that the proton count rate for the On-Wire view was approximately 45% of the proton count rates when the diagnostic was looking at the On-Hole view. This appears to be an indication that the diagnostic was successfully able to capture a view of a microchannel emitted from the 6/16 Cathode. The identifying feature of these microchannels is an increased fusion production rate, which would add evidence in favor of the theory that the microchannels are regions of higher populations of fusion reactants. The estimates here for the difference in proton count rates between on and off microchannel view for the detector compare reasonably well to the previous work done by Murali [16]. The reason why the FIDO diagnostic was able to observe a larger drop in rates for the On-Wire case could be due to the differences in the cathodes used in the experiments. Also, the FIDO diagnostic has proven to be far more reliable at measuring fusion product count rates than previous collimated proton detector setups used on HOMER in the past due to its significant noise reduction capabilities [4], so the new data may simply indicate a more accurate count rate because it is not hindered by high energy noise signals that plagued the previous setups.

Radial profiles of these setups were also created using data collected from the TOF diagnostic. Two sets of direct comparisons were made between the On-Hole and On-Wire views of the 11/24 and 6/16 Cathodes, the results of which are shown in Figures Figure 12.11 and Figure 12.12 and Tables Table 12.2 and Table 12.3.

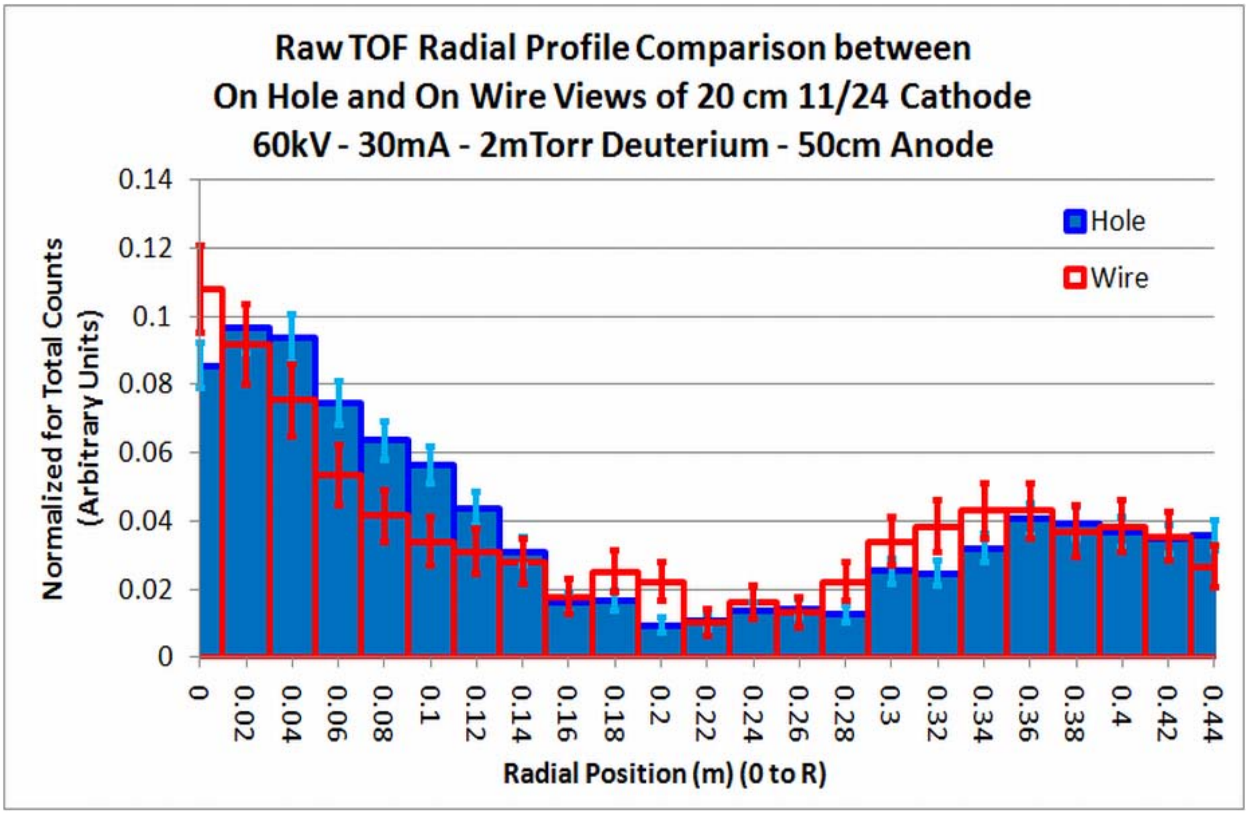

Figure 12.11 Comparison of weighted radial profiles created from TOF data collected on 11/24 Cathode with TOF view centered On-Hole and On-Wire of cathode.

	Core		Inter-Grid		Source	
Hole	46%	±1.6%	20%	±1.1%	34%	±1.4%
Wire	42%	±2.6%	19%	±1.8%	39%	±2.6%

Table 12.2 Comparison of raw number of counts collected in each region of radial profiles for 11/24 Cathode.

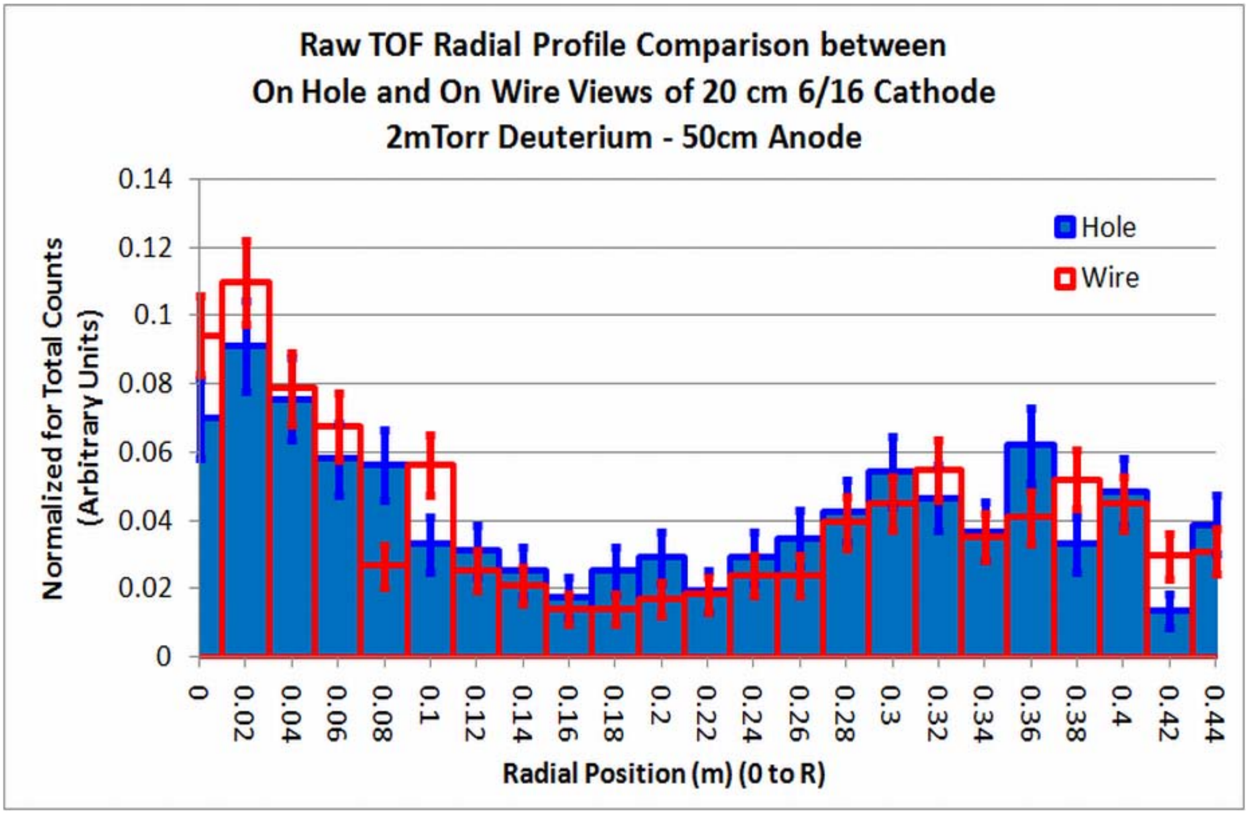

Figure 12.12 Comparison of weighted radial profiles created from TOF data collected on 6/16 Cathode with TOF view centered On-Hole and On-Wire of cathode.

	Core		Inter-Grid		Source	
Hole	36%	$\pm$2.7%	19%	$\pm$1.9%	45%	$\pm$3.0%
Wire	39%	$\pm$2.4%	17%	$\pm$1.6%	44%	$\pm$2.5%

Table 12.3 Comparison of number of counts collected in each region of radial profiles for 6/16 Cathode.

The data sets collected for both cathodes indicate that the radial profiles do not differ greatly between the On-Hole and On-Wire cases. For the 6/16 Cathode, the rate of data collection was over twice as fast for the On-Hole case as compared to the On-Wire case. However, because the radial profiles are largely within error bars of each other, this would indicate that the fusion concentrations increased nearly uniformly across the chamber. This would be possible if the microchannels contained higher concentrations of fusion reactants, but roughly the same relative concentration of fusion reactant species at each radial location. Also, because the fusion reactions in the chamber are believed to be dominated by beam-background collisions, and the background gas pressure is uniform throughout the device, then a roughly doubling of fusion reactants uniformly along a radial chord through the chamber would translate into a uniform doubling of fusion events along the radial chord as well.

From the four views studied using the FIDO and TOF diagnostic, several features of the microchannels can be interpreted. The two views of the 11/24 Cathode studied were believed to be looking slightly above the microchannels being emitted from the ring of holes directly below the equator. If these microchannels assumed a trajectory normal to the surface of the sphere, then they would have continue moving farther away from the midline as they travelled outward radially, thereby further taking it out of the line of sight of the detector. The fact that the FIDO proton count rates between the On-Hole and On-Wire view of the 11/24 cathode were nearly the same indicates that the microchannels do assume a somewhat concentrated trajectory such that they are not capable of being detected from a position on the perimeter of the chamber unless a direct view down the microchannel was achieved. This direct view was believed to be achieved with the On-Hole view of the 6/16 Cathode, which indicates that these microchannels could contain fusion concentrations at nearly twice the rates of the off-channel locations.

These microchannels obviously create perturbations to the ideal spherical symmetry of the IEC device. Much is still unknown of the exact shape these microchannels assume as they continue radially away from the center of the chamber. Particularly whether they remain a concentrated beam, or possibly that they begin to diverge as they leave the anode as space charge effects and collisions gradually drive them apart. Further study into these microchannels would benefit from a comprehensive mapping of the spherical potential profile of the IEC device, because variations in the potential are the most likely driving factor for the creation and trajectories of these microchannels. This could be done both through computation modeling using packages such as Ansoft Maxwell 3D, but would also require measurements of the vacuum potential using moveable emissive probes for correlation between the theoretical modeling and experimental conditions. These studies would have multiple other benefits to the understanding of the IEC, which will be discussed further in the Future Works chapter. At the moment, the unknown profile and contribution of these microchannels to the total fusion production rates hinder any ability to convert the radial profiles into representative volume scaled fusion rate profiles, which would indicate total fusion contributed from each increasingly larger radial shell in the device.

12.3.2 Position of Tungsten Filament Ion Sources

Another perturbation to the spherical symmetry about the chamber is the positioning of the tungsten filament ion sources. The original filament configuration consisted of six filaments, which were organized into three columns of two filaments. The two filaments in each column were placed equidistant above and below the midline of the chamber. The three columns of filaments were placed 120 degrees apart around the cylindrical chamber. However, the six-filament configuration was not symmetric about the position of the TOF diagnostic arms. A drawing of the filament positions can be seen in Figure 12.12.

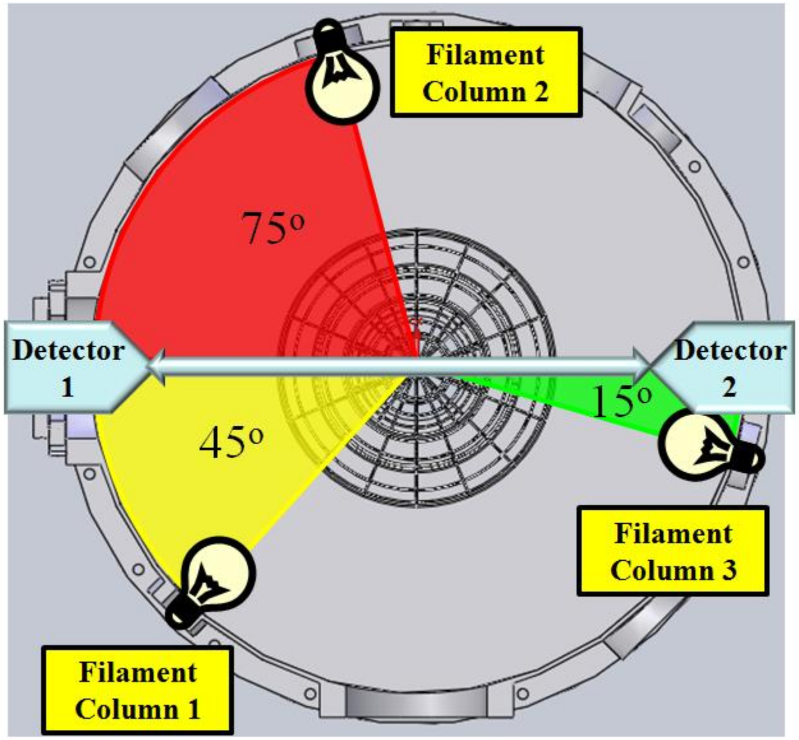

Figure 12.13 Position of three filament columns in Six Filament configuration with regard to position of TOF diagnostic arms.

As can be seen from the figure, the filament columns were not evenly placed around the TOF diagnostic arms. In order to ascertain the effect of the filaments on the symmetry of the device, FIDO data was taken for all the various permutations of the 3 columns. Only the columns were tested because the two rows that made up the three columns were symmetric about the midplane of the sphere and the midline of the arms. A total of seven combinations of the filament columns were tested. The eighth possible combination would have been to have all three columns turned off, which does not allow operation of the device. The relative FIDO proton collection rates using West Detector for the seven configurations can be seen in Table 12.4.

Filament Columns On	FIDO Proton Collection Rates using West Detector
1, 2, 3	1.00
2, 3	1.00
1, 3	1.48
1, 2	0.74
1	1.00
2	0.54
3	1.54

Table 12.4 Comparison of FIDO proton collection rates for various combinations of filament columns in Six Filament configuration. Proton collection rates are normalized to case when all filaments are on. All configurations were operated at the same cathode current and voltage.

All the data in the table was collected for the same cathode current and voltage levels, and all other operating conditions were held constant. The neutron production rate for the system as a whole stayed relatively constant for all configurations. The FIDO data indicates that there can be quite a large variation in the fusion proton collection rates from the view of West Detector depending on which filaments are operated. Of the seven combinations of filament columns, the highest rates all involved configurations that included Column 3, and the lowest rates all involved Column 2. Not only did Column 2 alone have the lowest overall rate, but when it was included with the other two columns it actually managed to hinder the rates of Columns 1 and 3 when they operated together. This data demonstrates how the location of the ion sources can have a strong impact on the spatial distribution of fusion events around the device.

The reason why the location of the filaments could have such a large impact on the proton collection rates at a specific location most likely has to do with the current of fusion reactants created near the filaments, which are then accelerated into the potential well. The electrons emitted from the tungsten filaments are likely producing higher concentrations of fusion reactants near the filaments. These reactants would then fall into the potential well and travel back and forth along a trajectory that extends directly from the filaments to the core. In the case of Column 3, the trajectory created would point almost directly at West Detector, and the fusion reactants heading in that direction would impart their center-of-mass contribution to the fusion products and preferentially direct them towards the detector. This would likely explain why West Detector saw the highest count rates with Column 3 operating. However, Column 2 would create fusion reactant trajectories that were nearly perpendicular to the line of sight of West Detector. This would cause the fusion products to be preferentially directed out of the line of sight of the detector, causing West Detector to see fewer fusion products from Column 2 operating alone.

The filaments are all powered by a single supply, which means that the power is divided up somewhat evenly (depending on the resistance of each filament) among the filaments in use. Therefore, when Column 2 is used along with any of the other filament columns, the other columns receive less of the total power provided by the supply because they are forced to share that power with Column 2. In this manner, Column 2 not only adds little to West Detector's line of sight but can actually make it more difficult to collect fusion products from reactants created from the other two filament columns when operated with them. The overall neutron rates remain the same for each configuration, indicating that total fusion rates for the system are constant. This is reasonable considering the cathode is operating at the same current and voltage so roughly the same total number of fusion reactants are being created and fusing, they are simply happening in different locations depending upon the configuration of the filaments in use.

Complete TOF data sets were not able to be taken for each of the seven filament configurations, but smaller sets with several hundred counts each did not show any dramatic changes in the spatial distribution of particles. The original data set shown in Figure 12.1 was also collected using the six filament configuration with all three filament columns in use, and was shown to be reasonably symmetric. The TOF diagnostic is less sensitive to subtle variations in symmetry due to the fact that it involves considerably smaller counts than the FIDO diagnostic, and therefore has poorer statistics. However, as the counting ability of the TOF diagnostic increases over time and the accuracy of the device increases, subtle variations due to asymmetries in the device will become more pronounced. Therefore, it was decided to be a prudent measure to redesign the filament configuration so as to make them more symmetric with regard to the diagnostic. The new filament configuration can be seen in Figure 12.14.

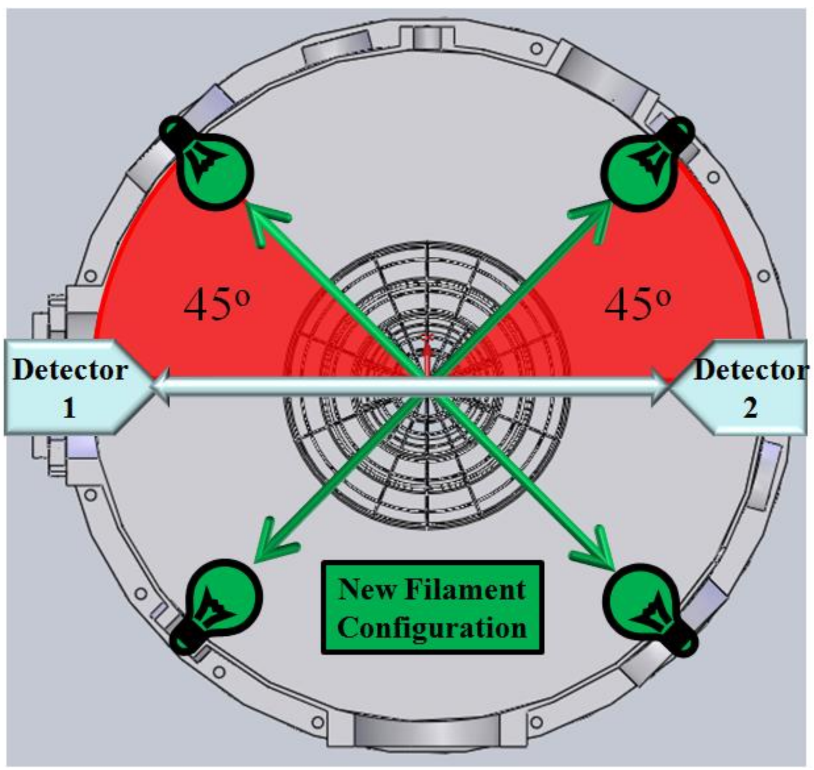

Figure 12.14 New eight filament configuration is divided into four columns of two filaments each and is now symmetric about the TOF diagnostic arms.

The repositioning of filaments in the chamber is primarily dependent on the availability of existing vacuum ports. Luckily, there were four columns of ports, each located at 45 degrees from the diagnostic arms, with two ports in each column, both equidistant from the midline of the chamber. Various port adapters had to be machined to facilitate the transition, and two new filaments holders had to be built. The new configuration should alleviate some of the concern about achieving symmetry regarding the spatial profiles collected with the TOF diagnostic. However, the fact that the filaments can have such a strong influence on the observations of local concentrations of fusion events around the chamber once again hinders the ability to accurately convert radial profiles collected using the TOF diagnostic into representative volume scaled profiles, which would indicate contribution to total fusion in the chamber from each radial shell. Ideally the ion source will continue to evolve in the experiment to become more uniform about the device, such as by using a single tungsten wire ion source that wraps around the entire chamber. Attempts such as these have been made on similar IEC devices [17], however they were typically deemed to be less reliable in normal use and often required a high level of maintenance. There are likely still options for improvement on these designs in order to obtain a more robust, uniform ion source around the device. In any case, as the TOF diagnostic continues to improve in accuracy, the location of the ion sources will invariably have to be taken into consideration when analyzing spatial profiles.

12.4 Weighting Factor Calculation

Another important aspect of the analysis is to take into account the probability of fusion event capture by the TOF Diagnostic throughout the region of view between the detectors. Some locations in the chamber are more likely than others to produce a fusion event with products capable of reaching both detectors. This probability is determined by the position of the fusion event and the trajectories of the fusion products, which is influenced by the energy and trajectory of the fusion reactants. Any imbalance in probability of event capture across the device must be calculated and compensated for using a weighting factor that can be combined with the raw data to properly calibrate the results. Because the TOF Diagnostic only measures coincident counts, the calculation of the weighting factor is based upon the probability of capture of both fusion products by the TOF detectors. This section details how this weighting factor was calculated and how it can affect the raw data collected by the diagnostic.

This discussion will begin with defining a coordinate system in which to perform the analysis. The device is intended to act as a spherically convergent focus, but for these calculations the analysis will be performed in a Cartesian (x, y, z) coordinate plane. This coordinate system can be seen in Figure 12.15. The x-axis represents the line that travels between both detectors on opposite sides of the chamber, if the collimator arms were flat rather than bent at the elbow. The $x = 0$ point is located at the center of the chamber. The angular θ direction exists in the x-y plane in which $\theta = 0$ points in the direction of $+x$ and $\theta = \pi/2$ points in the $+y$ direction. The angular φ direction exists in the y-z plane in which $\varphi = 0$ points in the $+y$ direction and $\varphi = \pi/2$ points in the $+z$ direction. In this manner, any trajectory emitting from the origin of the (x, y, z) coordinate plane can be created as a combination of θ and φ.

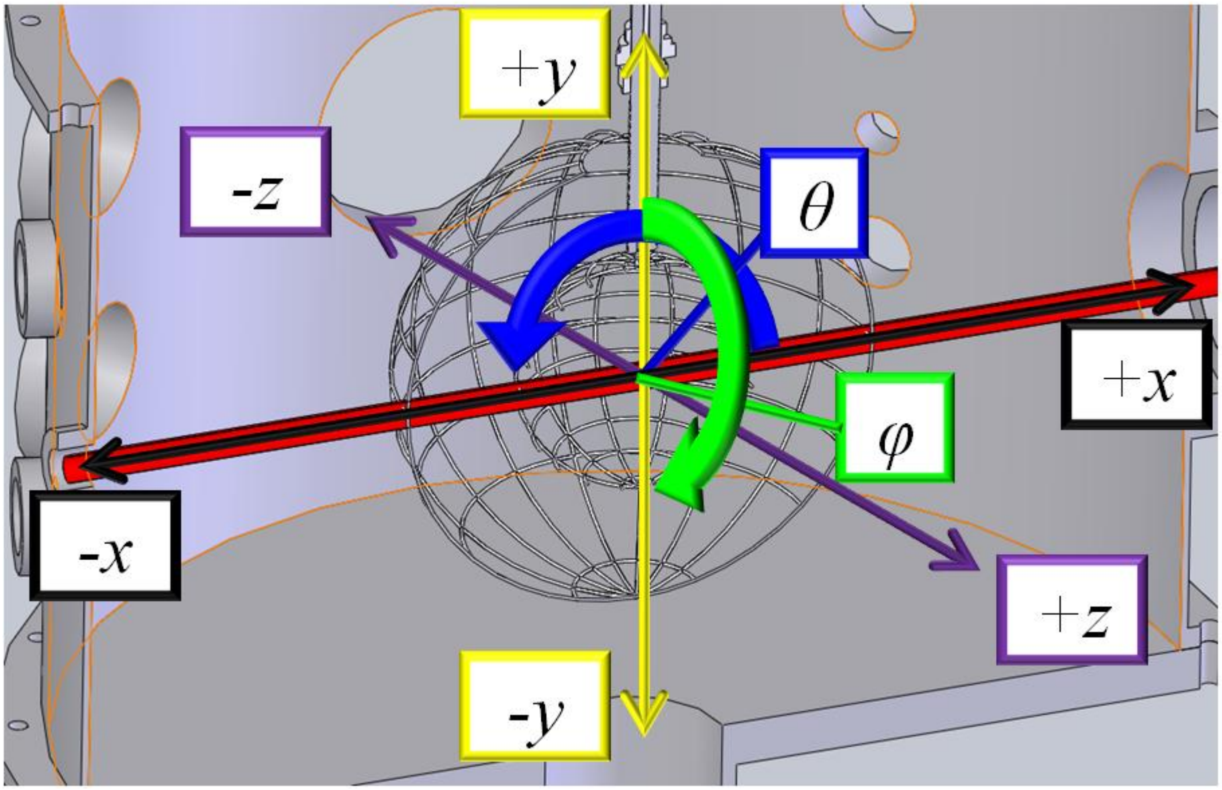

Figure 12.15 Cartesian coordinate system used in weighting factor calculations. Red chord represents region of view of TOF diagnostic.

The first stages of the analysis will take place entirely in the x-y plane, which is shown in Figure 12.16. This figure shows the region of view created by the two detectors. Each detector creates a cone of view within the chamber. The angle of that cone is dependent upon the radius of the detector face (r_{det} = 1.2 cm), the inner radius of the collimator channel (r_{CF} = 1.7 cm), and the distance from the entrance of the collimator channel to the detector face (L_{west} for West Detector and L_{east} for East Detector). These quantities are demonstrated in a close-up view of the x-y plane shown in Figure 12.17. The angles of the cones of view of each detector are denoted by α_{cone} for West Detector and β_{cone} for East Detector, and can be calculated as follows:

West Detector Cone of View

$$\alpha_{cone} = \tan^{-1}\left(\frac{r_{\det} + r_{CF}}{L_{west}}\right) \tag{12.1}$$

East Detector Cone of View $$\beta_{cone} = \tan^{-1}\left(\frac{r_{\det} + r_{CF}}{L_{east}}\right) \tag{12.2}$$

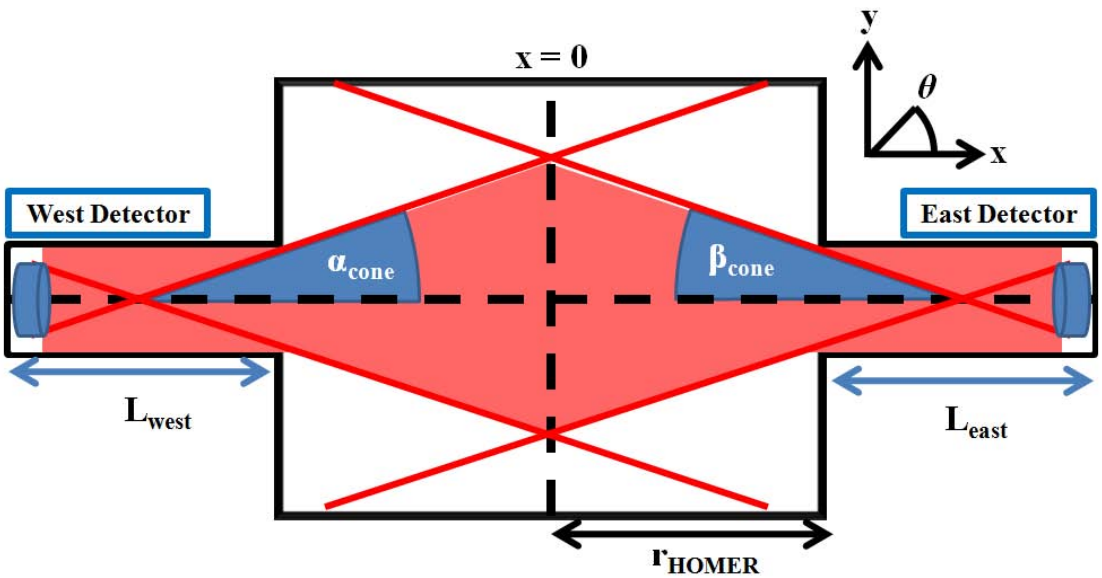

Figure 12.16 Side view of HOMER representing the *x*-*y* plane. Not drawn to scale. Yellow lines indicate the boundaries of the region of view of each detector within the chamber. All (*x, y*) positions within the red area can be seen by both detectors.

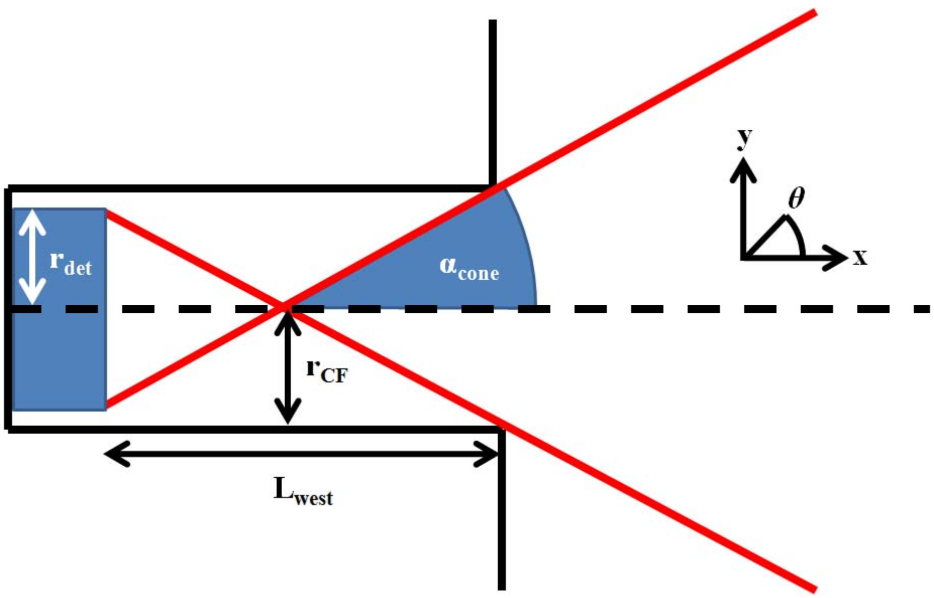

Figure 12.17 Close-up of collimator arm and detector. Not drawn to scale. The inner radius of the collimator channel, r_{CF}, is slightly larger than the radius of the detector face, r_{det}. The size of the cone of view of the detector is determined by the radius of the detector, the inner

radius of the collimator channel, and the length from the entrance to the detector face in the collimator channel.

While the FIDO setup is only concerned with the view of one detector, the TOF Diagnostic requires both detectors to pick up a fusion product. Therefore, the region of view of the TOF Diagnostic is the overlapping region of the cones of view of each detector. The two collimator arms in the TOF Diagnostic are slightly different lengths. L_{west} is 56.9 cm long while L_{east} is 50.5 cm long. This causes the angle of the cone of view of West Detector to be slightly smaller than the angle for East Detector. This then results in the convergence of the two cones occurring at a position slightly to the right of the origin at $x = +2.8$ cm. These discrepancies in the lengths of the arms and the angles of the cones have all been taken into account in the calculations discussed here.

This calculation is intended to determine the probability of capturing both products of a fusion reaction occurring at every (x, y, z) position within the viewable region between the detectors. This probability is determined by the trajectories of the fusion products when they are emitted from the position of the fusion event. The trajectories are dependent upon the mass, velocity, and trajectory of each of the fusion reactants that created the fusion event, as well as the angle of emission that the products take after the fusion event. The fusion products are emitted isotropically in the center-of-mass frame in exact opposite directions in order to conserve the momentum of the reaction. Because the products are emitted in any direction in the center-of-mass frame with equal probability, the total probability of coincident event capture is dictated by the fraction of the sphere of isotropic fusion product emission that is taken up by trajectories that will allow both fusion products to reach a detector. In the lab frame, the center-of-mass contribution from the fusion reactants will alter the total velocities of the fusion products and cause them to take trajectories that may not be exactly opposite. Therefore, for every position in which the probability of capture is being calculated, the source conditions must include the properties of the fusion reactants in order to properly calculate the final trajectories of the fusion products to determine if they will be able to reach the detectors.

In order to perform these calculations over a range of parameters, a MATLAB script was created, which can be seen in full in the Appendix. This code has a total of 9 inputs that are used to determine the probability of event capture, which are: the position of the fusion event in the (*x*, *y*) plane (*x_position*, *y_position*), masses of the fusion reactants (multiple of mass of deuterium atom, *m_d*) (*m_1*, *m_2*), energies of the fusion reactants (keV) (*E_1*, *E_2*), angle of fusion reactant trajectory in theta direction (degrees) (*ang_theta_1*, *ang_theta_2*), angle of proton emission in the theta direction (*ang_theta_p*). As was mentioned, this analysis begins with only examining the fusion reactions occurring the (*x, y*) plane shown in Figure 12.16, so no *z*-position is entered. We are only considering D-D fusion reactions here, so *m_1* and *m_2* are both equal to the mass of a deuterium atom. It has been estimated that the probability of ion-ion fusion reactions is at least three to four orders of magnitude lower than the probability of ion-background fusion reactions in the IEC due to the significantly higher fraction of background particles than ions in the device. Therefore, it is typically safe to assume that the fusion reactions dominating in the chamber are ion-background reactions, meaning *E_2* would be zero and *ang_theta_2* is irrelevant.

The angles of the fusion reactants are based on the same coordinate system shown in Figure 12.15, in which the origin has been transposed to the given (*x, y*) location. The MATLAB script has the option of calculating *ang_theta_1* based upon the (*x*, *y*) position and assuming purely radial symmetry so that all of the reactants are on a straight line trajectory towards or away from the exact center of the chamber. The chamber is almost certainly not experiencing perfect radial symmetry in which all trajectories are moving towards or away from the exact center of the chamber. Theoretical and computational research on this subject is described further in Section 12.1. However, trajectories close to radial are typically expected throughout the device.

The angle of the proton emission is also based on this transposed coordinate system and represents the angle in which the fusion proton is emitted before the center-of-mass contribution is taken into account to calculate the total fusion proton velocity. In this definition, the fusion proton is equally probable of emitting at every angle in the theta and phi directions. Only the angle of proton emission needs to be entered because, in this frame, the triton will be moving in the exact opposite direction in the center-of-mass frame so *ang_theta_t* will be (*ang_theta_p* + 180 degrees) and similarly in the phi direction.

The center-of-mass velocity of the combined system from the two reactants is calculated in both the *x* and *y* directions based on the masses, energies, and trajectories of the reactants, as shown in Equations (12.3) to (12.7).

Reactant Velocity	$v_{(1/2)} = \sqrt{2 * \frac{E_{(1/2)}}{m_{(1/2)}}}$	(12.3)
Reactant Velocities in x-direction	$v_{(1/2)x} = v_{(1/2)} * \cos(ang\_theta\_(1/2))$	(12.4)
Reactant Velocities in y-direction	$v_{(1/2)y} = v_{(1/2)} * \sin(ang\_theta\_(1/2))$	(12.5)
Center of Mass Velocity in *x*-direction	$v\_cm\_x = \frac{m_1 * v_1 * \cos(\theta_1) + m_2 * v_2 * \cos(\theta_2)}{m_1 + m_2}$	(12.6)
Center of Mass Velocity in *y*-direction	$v\_cm\_y = \frac{m_1 * v_1 * \sin(\theta_1) + m_2 * v_2 * \sin(\theta_2)}{m_1 + m_2}$	(12.7)

The velocities of the reactants must then be converted from the Lab Frame into the Center-of-Mass (CM) Frame.

Reactant Velocities in CM Frame
$$u_{(1/2)(x/y)} = v_{(1/2)(x/y)} - v_{cm(x/y)} \tag{12.8}$$

The total energy available for fusion (E_{fus}) is equal to the sum of the reactant energies in the center of mass frame. This is the energy that is used to determine the probability of fusion in the cross-section tables. This value is then added to the Q values of the fusion reaction, which in the case of the proton-triton branch of D-D fusion is 4.03 MeV. This sum is then divided between the two fusion products based upon their masses to give the proton and triton velocity in the CM Frame. The relevant definitions appear in Equations (12.9) to (12.12).

Energy Available for Fusion in CM Frame
$$E_{fus} = \frac{1}{2} * m_1 * (u_{1x}^2 + u_{1y}^2) + \frac{1}{2} * m_2 * (u_{2x}^2 + u_{2y}^2) \tag{12.9}$$

Total Energy of Fusion Products in CM Frame
$$E_{fus\_total} = E_{fus} + Q \tag{12.10}$$

Energy of D-D Fusion Proton in CM Frame
$$E_p = \left(\frac{m_t}{m_p + m_t} \right) * E_{fus\_total} \tag{12.11}$$

Energy of D-D Fusion Triton in CM Frame
$$E_t = \left(\frac{m_p}{m_p + m_t} \right) * E_{fus\_total} \tag{12.12}$$

Finally, the energies of the fusion products are used to determine the velocity of the products in the CM Frame. The fusion products are emitted isotropically in the CM Frame, so all trajectories are equally likely, and the product trajectories are always in opposite directions. The velocities of the products are then converted from the CM Frame back to the Lab Frame in order to determine if their trajectories will reach the detectors, using Equations (12.13) to (12.16).

Velocities of Fusion Products in CM Frame	$u_{(p/t)} = \sqrt{2 * \frac{E_{(p/t)}}{m_{(p/t)}}}$	(12.13)
Velocities of Fusion Products in x-direction of CM Frame	$u_{(p/t)x} = u_{(p/t)} * \cos(ang\_theta\_(p/t))$	(12.14)
Velocities of Fusion Products in y-direction of CM Frame	$u_{(p/t)y} = u_{(p/t)} * \sin(ang\_theta\_(p/t))$	(12.15)
Velocities of Fusion Products in Lab Frame	$v_{(p/t)(x/y)} = u_{(p/t)(x/y)} + v\_cm\_(x/y)$	(12.16)

Once the velocities of each of the fusion products have been calculated including the center-of-mass contributions of the reactants, it must be determined whether the trajectories of the products are capable of being collected, which is done by performing three tests. With nearly equal setups on both sides of the *x*-axis, the direction of the product velocity along the *x*-axis determines which collimator channel and detector the product is capable of reaching. First, the (*x*, *y*) position of the fusion event is confirmed to be within the region of view of both detectors. Next, the *y*-position of the product at the entrance of its respective collimator channel is calculated to determine that it is within the radius of the channel, and therefore able to enter. Last, the *y*-position of the product at the detector face is calculated to determine whether it is within the radius of the detector face. If both products pass all three tests, then the fusion event is capable of being collected for that combination of conditions.

In order to determine the total probability of fusion event capture at a given (*x*, *y*) position and the pre-chosen reactant conditions, all possible trajectories of the fusion products about the isotropic sphere of emission must be considered in order to determine what fraction of those trajectories can allow both fusion products to reach the detectors. This requires checking every combination of angles in both the theta and phi directions. To do this, a loop is created in the MATLAB script in which the 360 degrees of the theta direction are divided up into a number (n) of equal angular increments, and the before-mentioned calculations are performed for every incremental *ang_theta_p* value around the theta direction. If a coincident event is able to be captured for a given value of *ang_theta_p*, then another loop is created in which equal angular increments in the phi direction are added to the trajectories, which gives the final trajectories a component in the z-direction. By adding a component in the z-direction, that reduces the velocity in the x and y directions in order to maintain the same total velocity, as shown in Equation (12.17).

Total Fusion Product Velocity $$v_{(p/t)} = \sqrt{v_{(p/t)tx}^2 + v_{(p/t)ty}^2 + v_{(p/t)tz}^2} \qquad (12.17)$$

The angular increments in the phi direction scan that plane from 0 to 5 degrees. The maximum possible angle of a fusion proton in the phi direction that could still allow both products to reach a detector has been estimated to be less than 1 degree, so by scanning to 5 degrees all possible trajectories that are capable of reaching the detectors will almost certainly be included. For every increment of phi, the distance travelled in the z-direction (Δz) for both the proton and triton is calculated to determine if both of their trajectories will continue to pass into their respective collimator channel and through the detector face. A diagram of this scanning process over the phi and theta directions can be seen in Figure 12.18.

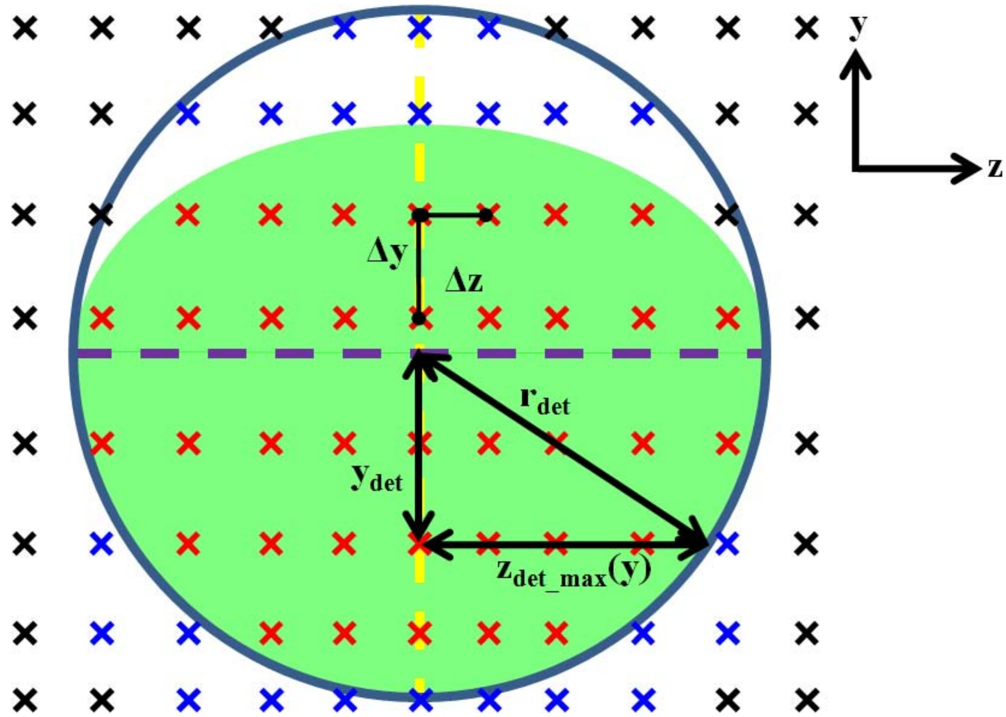

Figure 12.18 Front view of detector face in the *y-z* plane. Green region represents the actual region of that detector face that is capable of collecting coincident events from a single (*x,y*) location. Red marks indicate fusion product trajectories that were calculated and found to be capable of producing detectable coincident events. Blue marks indicate when a fusion product is capable of reaching one detector but the opposing product cannot reach the other detector. Black marks indicate neither fusion product could be captured. $z_{det\_max}(y_{det})$ represents the maximum distance to the boundary of the detector face at a given *y* position on the face. Δy and Δz are the distance travelled in the *y* and *z* direction, respectively, for every increment of theta and phi, respectively.

In the figure, the distance between $z = 0$ and the boundary of the detector face at the position on the face in the *y*-direction where the fusion product trajectory intersects (y_{det}) is given by:

$$z_{\mathrm{det\_max}}(y_{\mathrm{det}}) = \sqrt{r_{\mathrm{det}}^2 - y_{\mathrm{det}}^2} \tag{12.18}$$

A similar calculation is performed at the entrance to the collimator channel to determine the maximum distance in the *z*-direction to the boundary of the channel wall. The position of the fusion products in the *y-z* plane at each of their respective entrances to the collimator channels and the detector faces are calculated to determine that both products have made it into the channel and reached the detector for the values of phi and theta. For every increment of phi that successfully results in a coincident event capture, the same position is added on the opposite side of the *z*-axis because the detector face is symmetric about $z = 0$. In order to scan over the entire range of all combinations of theta and phi, it would require a total of n^2 calculations for every (x,y) position, where *n* once again is the number of equal increments in which the phi and theta directions are divided. By only performing calculations in the phi direction if a coincident count was possible in the theta direction, and by only scanning the phi direction over a 5 degree range, the number of calculations is dramatically reduced. This allows for higher values of *n* to be calculated, which leads to greater resolution in the calculation and a more accurate estimate of the total coincident capture probability at a given position.

The calculation described thus far has derived the fraction of the total isotropic sphere of fusion product emission that contains trajectories that will allow for both fusion products to be captured by detectors on opposite sides of the chamber, which is equivalent to the total coincident event capture probability at that location. Next, two additional sets of loops are created in the MATLAB script in order to perform this same calculation over a range of values in the *x* and *y* directions. This data can then be used to create a 3D plot in which the axes are: x-position, y-position, and total probability of coincident event capture. This plot can be seen in Figure 12.19. For this figure, the CM velocity is set to zero for illustrative purposes, which means that the plot Lab Frame and the CM Frame are the same. The position $x = 0$ represents the center of the chamber, and the boundaries in the *x*-direction are at $\pm$ 0.5 meters, which is slightly beyond the walls of the chamber. The *y*-axis only goes from -1.2 cm to +1.2 cm, which in this case encompasses the entire region of view of the TOF Diagnostic inside the chamber.

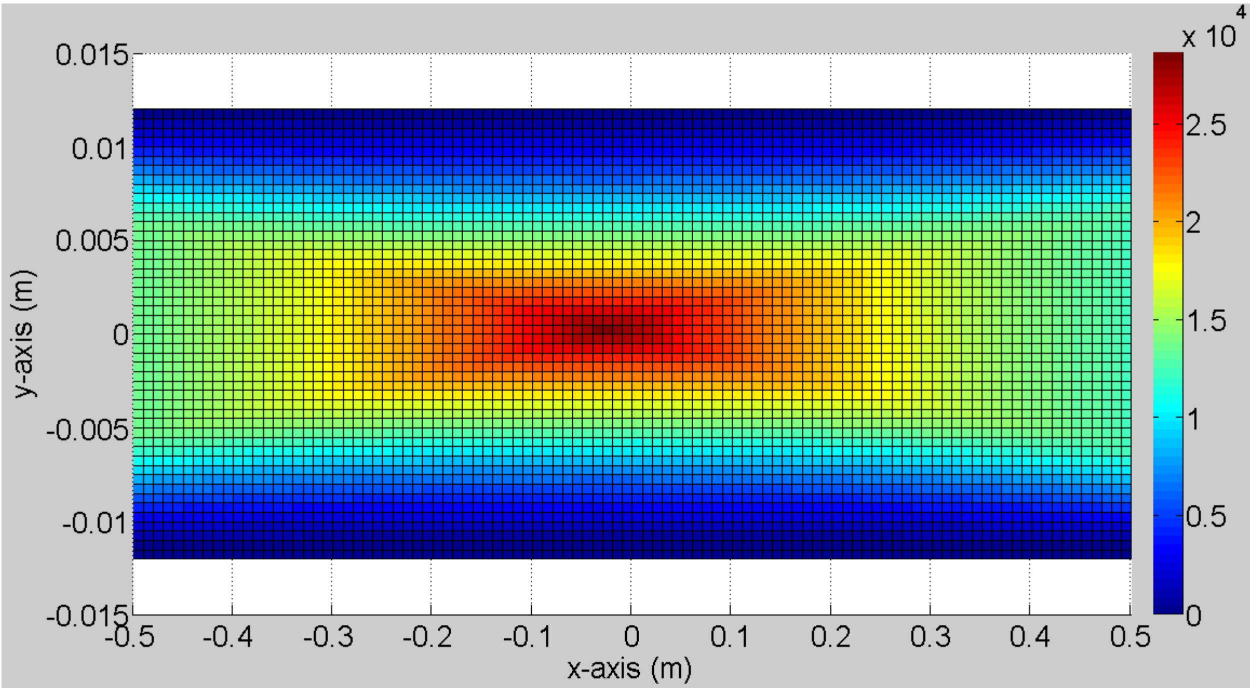

Figure 12.19 Horizontal axis represents positions along the x-axis, vertical axis is position along the *y*-axis, and the color indicates the probability of coincident event capture at the given (*x*,*y*) position (red is highest probability, blue is lowest in arbitrary units). This plot represents the probability when both reactants have zero energy.

As can be seen from Figure 12.19, the highest probability of fusion event capture occurs near the exact center between the detectors, and decreases as the distance is increased in both the *x* and *y* directions. It is also interesting to note that for y-positions near the top and bottom boundaries of the plot, the probability of fusion event capture actually increases as the *x*-position strays farther from the center and the *y*-position remains constant. This effect is demonstrated in Figure 12.20. In the figure, there is assumed to be no center-of-mass velocity contribution, so all fusion product trajectories are in opposite directions. The size of the cone of collectable trajectories emanating from a given (*x*,*y*) position is dictated by the angular spread, γ. At $x = 0$, the cones are symmetric about an axis that is parallel to the x-axis. However, as the (*x*,*y*) position moves away from the *x* and *y* axes, the cones become symmetric about an axis that is no longer parallel to the x-axis. The figure demonstrates how it is possible for the size of the cone of detectable trajectories to increase as the distance from $x = 0$ in the x-direction is increased and the position on the y-axis remains constant.

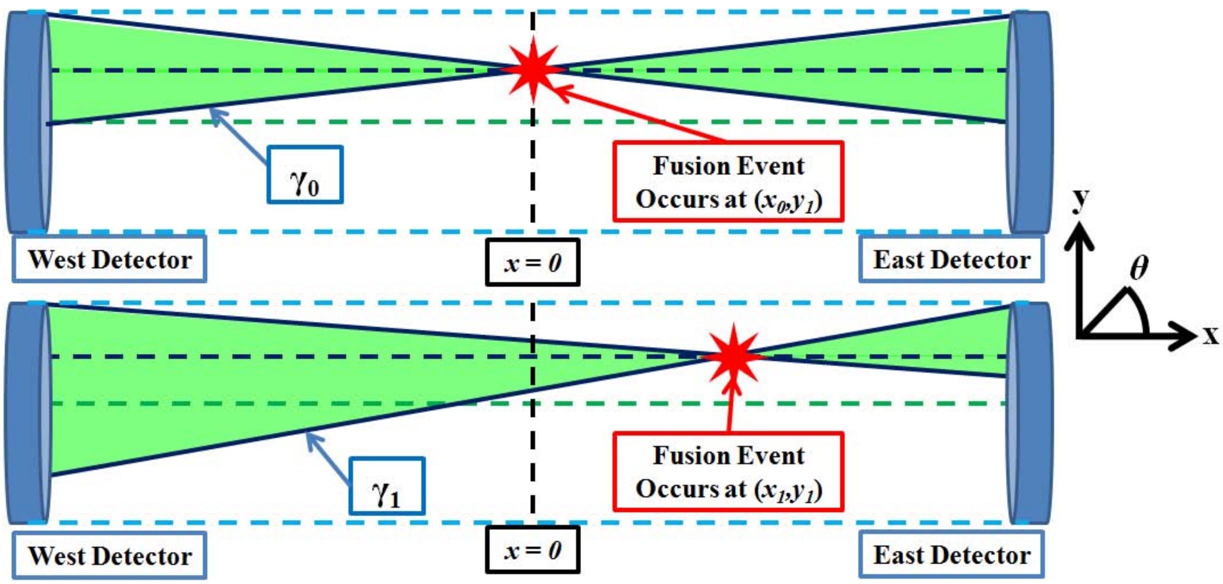

Figure 12.20 Diagram of region of view between detectors with a fusion event occurring at (x_0,y_1) (Top) and (x_1,y_1) (Bottom). Assuming zero center-of-mass contribution so all fusion product trajectories are exactly opposite of each other. Size of cone of collectable region defined by angular spread of cone (γ). Figures demonstrate how size of cone can increase as the distance is increased along the x-direction while the y-position remains constant.

The total coincident event capture probability over the x-y plane shown in Figure 12.19 provides only a single slice of the total volume made up by the region of view between the TOF detectors. In order to take into account the entire volume, the values in the x-y plane must be rotated about the x-axis, creating a cylinder. This is done by multiplying the total probability factor at every (x,y) position by 2*π*Abs(*y_position*) to give the combined probability factor of all positions at the same radius $\left(\sqrt{y^2+z^2}\right)\sqrt{y^2+z^2}$ from the x-axis for a given *x_position*. This is once again assuming spherical symmetry about the device. When this is applied to the data in Figure 12.19, the result can be seen in Figure 12.21. The total volume capture probability factor can then be summed over all values of *y* for a given position in *x*. This sum creates the cumulative probability factor as a function of the position along the *x*-axis.

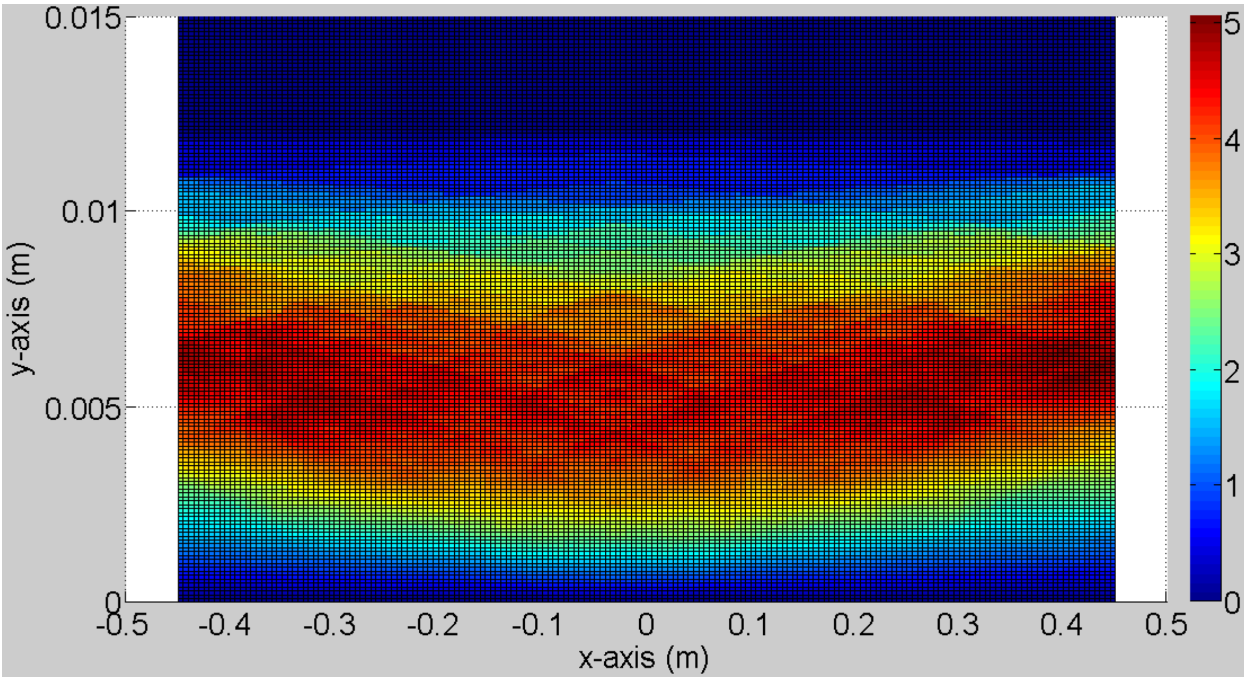

Figure 12.21 Total capture probability factor in (*x*,*y*) plane multiplied by (2*π**y_position*) in order to convert the plane into a total volume capture probability factor. Note that y-axis only extends from 0 to 1.5 cm because the position on the y-axis is equivalent to a radial location when it is wrapped around the *x*-axis. Also note that color bar is using a different scale of arbitrary units than was seen in Figure 12.19.

The total capture probability was shown in Figure 12.19 to be highest near the center point between the detectors. However, when the results are compensated for the total volume of the region of view between the detectors, as is shown in Figure 12.21, the radial distance from the x-axis will influence the total volume probability factor and causes the radial positions farther from the axis to have a higher contribution to the cumulative sum. When this volume contribution was taken into account, the cumulative probability of the sum of all *y_positions* at each *x_position* across the *x*-axis was found to be nearly constant, with a variation on the order of less than a percent. This indicates that when there is assumed to be no contribution from the reactant energy, the probability of coincident event capture is roughly uniform across the device.

The contribution of the energies of the fusion reactants to the final trajectories of the fusion products is nearly insignificant throughout the majority of the region of view between the detectors. This is because the fusion reactants are typically assuming radial trajectories, and for much of the TOF region of view the angle of these trajectories are nearly parallel to the axis that runs between the detectors. It is only when the *x_position* comes within roughly 10 cm of the origin that the fusion reactants are able to assume sufficiently non-parallel trajectories to begin to influence the probability of capture of the fusion products. Figure 12.22 and Figure 12.23 demonstrate the probability of fusion event capture in the *x*-*y* plane for the case of 10 keV deuterium atoms moving along strictly radial trajectories and fusing with stationary deuterium atoms. The energy of the fusion reactants was chosen based upon the energy spectra collected by the FIDO Diagnostic, which indicated a high concentration of fusion reactants with energy on the order of 10 to 20 keV.

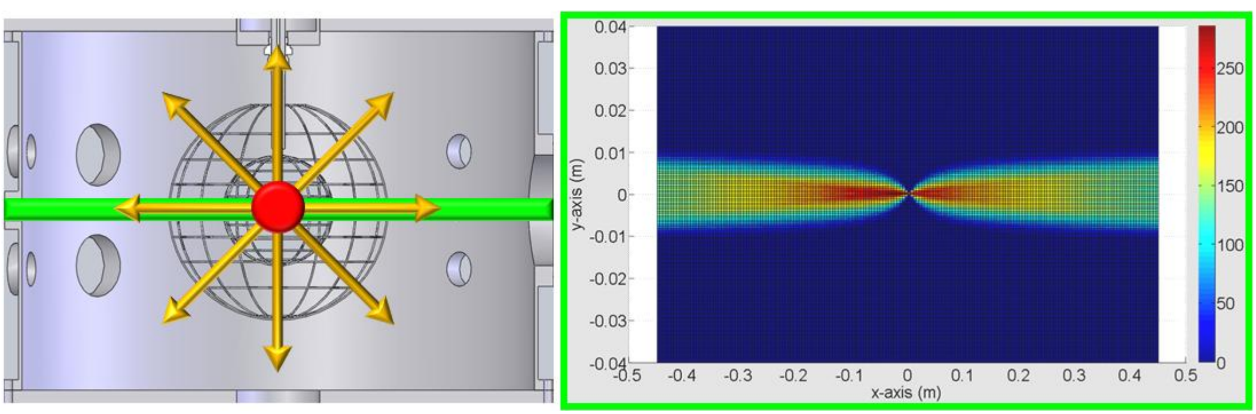

Figure 12.22 Probability of fusion event capture in the *x*-*y* plane for 10 keV deuterium atoms with purely radial trajectories moving away from the origin fusing with stationary deuterium atoms. Plot on right only includes region of view of the TOF Diagnostic and is not drawn to scale (*x*-axis extends from -45 cm to +45 cm while *y*-axis only extends from -4 cm to +4 cm).

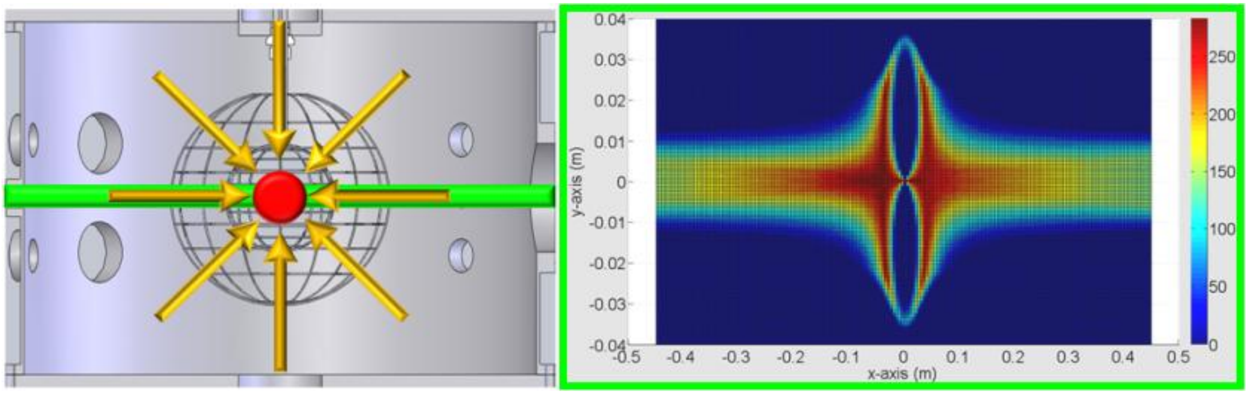

Figure 12.23 Probability of fusion event capture in the *x-y* plane for 10 keV deuterium atoms with purely radial trajectories moving towards the origin fusing with stationary deuterium atoms. Plot on right only includes region of view of the TOF Diagnostic and is not drawn to scale (*x*-axis extends from -45 cm to +45 cm while *y*-axis only extends from -4 cm to +4 cm).

Figure 12.22 demonstrates the effect of fusion reactants moving away from the origin, while Figure 12.23 represents reactants moving towards the origin. Therefore, a particle originating in the Source region will first move towards the origin, corresponding to Figure 12.23, and then when it reaches the center it will begin moving away from the origin, corresponding to Figure 12.22. These plots only demonstrate significant differences from Figure 12.19 once positions within around 10 cm from the origin along the *x*-axis are reached. Along the *y*-axis at *x* = 0, the purely radial trajectories are perpendicular to the line of sight between the detectors. These perpendicular trajectories cause the maximum deflection of the fusion products away from the region of view of the detectors, which makes them much less probable to collect except near the outer edges of the TOF region of view. The figures also demonstrate that near the *y*-axis, particularly on the outer edges of the region of view, fusion reactions are more likely to be detected from reactants moving towards the origin as opposed to away from the origin.

The plots shown are assuming that the chamber is assuming perfect radial symmetry and that all reactant trajectories converge towards a single focal point. However, the actual experiments are not achieving perfect radial convergence. More likely, the reactants are all converging towards a focal region around the center of the cathode. Because of this, the trajectories of the fusion products will not be exactly equal to purely radial trajectory, but instead there will be a range of trajectories above and below the ideal that encompass most of the reactants. The MATLAB script has shown that if the core is as much as a centimeter wide or off-axis from the exact center of the chamber, then the increased probability of event capture near the origin will drop significantly. This appears to be validated from the TOF spatial profiles taken, which are lacking a sharp peak at the center of the device, and instead appear to have a pileup of counts throughout the cathode. The trajectories were modified to better reflect the realities of the experiment. The plots developed from these cumulative probability factors created using the MATLAB script have demonstrated a slightly higher probability of event capture in a region localized to the Core. A weighting factor can then be used to compensate for this by devaluing the counts in the Core region with respect to the rest of the chord of view. The results of this can be seen in Figure 12.24.

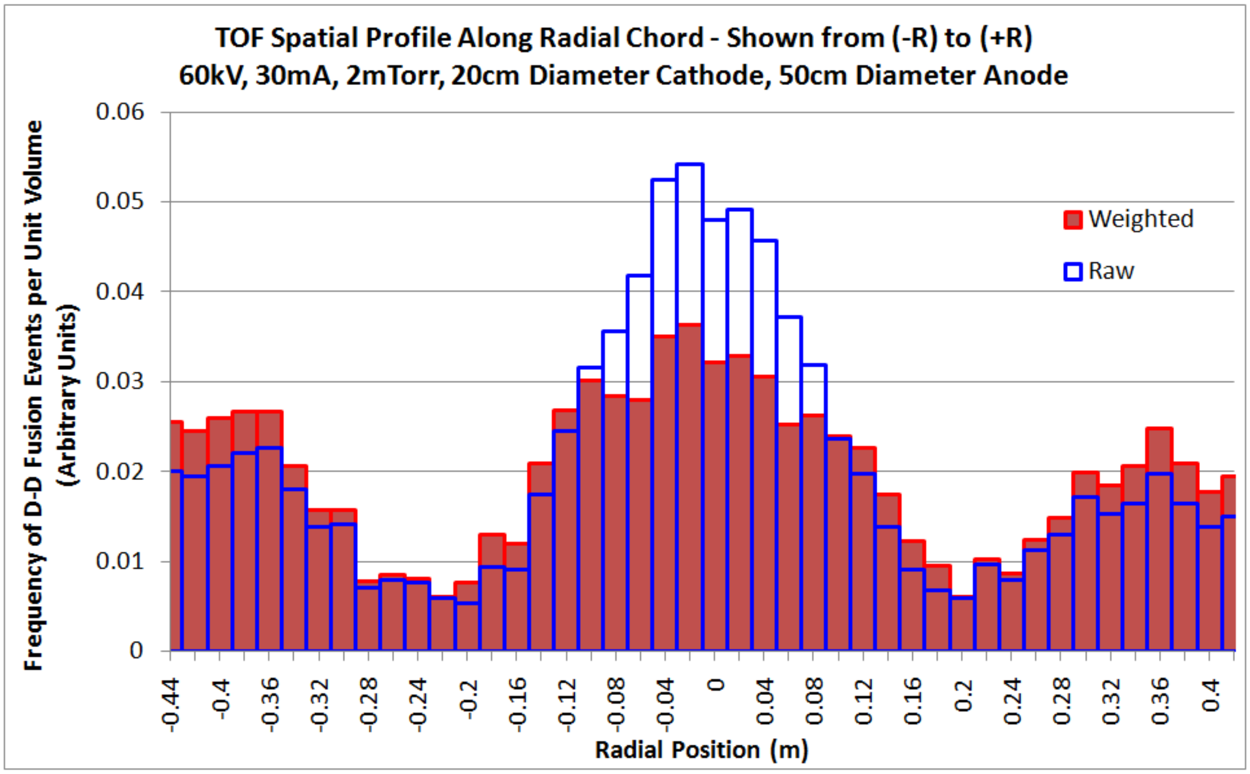

Figure 12.24 TOF Spatial Profile demonstrating effect of the weighting factor derived using the MATLAB script on the Raw Data. The weighting factor devalues the counts in the Core to compensate for a slightly higher probability of fusion event capture in the Core region.

This weighting factor was developed using estimates for the extent to which the focus of convergence of the fusion reactants is spread over a region near the center of the cathode rather than existing as a single point. The exact level of convergence of the device is dependent upon the shape of the potential well, which is influenced by the shape and design of the anode and cathode as well as the high volt stalk, and also the extent to which collisions with other particles manage to cause slightly non-radial trajectories of the fusion reactants. This weighting factor will likely evolve over time as better estimates of the Core convergence are developed, which will affect the extent to which the Core is weighted relative to the rest of the chamber. However, qualitatively the profile is unlikely to change dramatically as the weighting factor calculations become more precise. All indications are that any changes in probability of event capture across the device are limited to the Core region because only there do the fusion reactant trajectories have a large enough perpendicular component to significantly affect the final trajectories of the fusion products. Therefore, while the counts in the Core region may rise or fall slightly as more is learned about the Core convergence, the fall in counts in the Inter-Grid region and subsequent rise in the Source region does not appear to be an artifact of the detectors' view of the chamber. This adds further confirmation that this newly discovered rise in counts in the Source region is a genuine feature of the spatial profile of the device.

Chapter 12 References

1 Rosenberg, M., Krall, N. A. (1992). The effect of collisions in maintaining a non-Maxwellian plasma distribution in a spherically convergent ion focus. Physics of Plasmas B, Volume 4, Number 7, 1788-1794

2 McGuire, T.J., Sedwick, R.J. (2008). Numerical Predictions of Enhanced Ion Confinement in a Multi-grid IEC Device, AIAA-2008-4675, AIAA/ASME/SAE/ASEE JPC, 44th Annual meeting, Hartford, CT

3 Emmert, G. A., Santarius, J. F. (2006). Multiple-Ion Species Effects in IEC Modeling. Bulletin of the American Physical Society, Volume 51, Number 7, 166

4 Boris, D. R., Kulcinski, G. L., Santarius, J. F., Donovan, D. C., Piefer, G. R. (2010). Measuring D(d,p,)T fusion reactant energy spectra with Doppler shifted fusion products. Journal of Applied Physics, 107, 123305

5 Emmert, G. A., Santarius, J. F. (2010). Atomic and Molecular Effects on Spherically Convergent Ion Flow I: Single Atomic Species. Physics of Plasmas, 17, 013502

6 Emmert, G. A., Santarius, J. F. (2010). Atomic and Molecular Effects on Spherically Convergent Ion Flow II: Multiple Molecular Species. Physics of Plasmas, 17, 013503

7 Thorson, T. A. (1996). Ion flow and fusion reactivity characterization of a spherically convergent ion focus. (PhD dissertation, University of Wisconsin – Madison)

8 Cipiti, B. B. (2004). The fusion of advanced fuels to produce medical isotopes using inertial electrostatic confinement. (PhD dissertation, University of Wisconsin – Madison)

9 Krupakar Murali, S., Cipiti, B. B., Santarius, J. F., Kulcinski, G. L. (2006). Study of fusion regimes in an inertial electrostatic confinement fusion device using the new eclipse disc diagnostic. Physics of Plasmas, 13, 053111

10 Boris, D. R., Alderson, E., Becerra, G., Donovan, D. C., Egle, B., Emmert, G. A., Garrison, L., Kulcinski, G. L., Santarius, J. F., Schuff, C., Zenobia, S. J. (2009). Deuterium anions in inertial electrostatic confinement devices. Physical Review E **80**, 036408

11 Alderson, E. C. (2010). Theoretical and Experimental Studies of Negative Ions in IEC Devices at UW-Madison. Proceedings of 12th US-Japan Workshop on IEC Fusion, Osaka, Japan

12 Hickman, A. P. (1991). Dissociative attachment of electrons to vibrationally excited H_2. Physical Review A, Volume 43, Number 7, 3495-3502

13 Williams, J. F., Dunbar, N. F. (1966). Charge Exchange and Dissociation Cross Sections for H1+, H2+, and H3+ Ions of 2 to 50 keV Energy Incident Upon Hydrogen and the Inert Gases. Physical Review, Volume 149, Number 1, 62-69

14 Alvarez, I., Cisneros, C. (1976). Negative-ion formation from dissociative collisions of H2+, H3+, and HD2+ in H2, He, and Xe. Physical Review A, Volume 14, Number 2, 602-607

15 Barnett, C. F. (1990). Collisions of H, H2, He, and Li Atoms and Ions with Atoms and Molecules. Atomic Data for Fusion, Volume 1, ORNL-6086

16 Murali Subramanian, K. M. (2004). Diagnostic Study of Steady State Advanced Fuel (D-D and D-He3) Fusion in an IEC Device. (PhD dissertation, University of Wisconsin-Madison)

17 Egle, B. J. (2010). Nuclear Fusion of Advanced Fuels Using Converging Focused Ion Beams. (PhD Dissertation – University of Wisconsin-Madison)

13 Conclusions

The work described in this thesis has spanned a variety of subjects within the field of IEC research. It began with expanding upon the proof-of-principle experiments of detecting nitrogen-based explosives using a steady-state D-D neutron flux. After designing and testing various advancements to the detection setup, it was deemed most beneficial to further optimize the neutron source in order to increase the total neutron flux available for detection. This led to a series of experiments examining the effect on neutron production rates from various system parameters, as well as the design and configuration of the electrodes. Significant advancements were also made in the high voltage capabilities of the UW IEC laboratory. The design and construction of a new 300 kV high voltage feedthrough now provides the possibility of being able to fully utilize the capabilities of the 300 kV power supply, that has before now been unable to be used to its full capacity.

The optimization experiments began with using the neutron detector as the primary diagnostic for evaluating the change in total fusion rates in the system, but then evolved into using more precise diagnostics, namely the Fusion Ion Doppler (FIDO) Diagnostic, to study the reasons behind why certain parameters affected the total fusion rates of the system. Improvements were designed and constructed for the FIDO Diagnostic, primarily in the form of the Adjustable FIDO Arm, which has the potential of expanding the capabilities of this tool from only studying D-D fusion to also having the ability to examine D-^{3}He without breaking vacuum. The emphasis on diagnostics continued with the design and construction of the Time of Flight (TOF) Diagnostic. This was a first of its kind tool on an IEC device, and over the last several years it has been taken from concept to full implementation. Methods for proper alignment, data acquisition, and analysis have all been developed in order to increase the reliability and collection capabilities of this tool. Spatial profiles have already been collected using this tool and have revealed interesting and previously unknown results about the distribution of fusion events throughout the UW spherically gridded IEC device.

13.1 Detection of Explosives

The work with explosives detection began after the initial proof-of-principle experiments had been conducted by Wehmeyer [1]. A variety of improvements were made to the detector setup based upon the lessons learned from the original experiments with the goal of decreasing the necessary interrogation time and increasing the reliability of the system.

- Three NaI detectors were used for gamma ray capture, as opposed to one in the original experiments.
- The detectors were moved from behind the interrogation sample to a position beside the sample in the same plane, which allowed for detectors to avoid much of the thermalized neutrons that are necessary for nitrogen activation but detrimental to detection in NaI detectors due to activation of the iodine.
- Detector shielding was improved from originally utilizing lead bricks to individually wrapping each detector in lead sheets on all sides, minimizing x-ray penetration through gaps in the shielding.
- Improved shielding reduced x-ray noise on detectors sufficiently to allow the hydrogen gamma ray peak at 2.22 MeV to be clearly detected, which aids in

calibration of the data and can be used to help identify the properties of the interrogation sample.

- Computational modeling was implemented to determine optimal moderator thickness so as to allow the ideal combination of the maximum number of thermal neutrons to reach the sample with the minimum amount of scattering or capture of neutrons before reaching the sample.

These new improvements were tested with the IEC device and were able to produce nitrogen signatures above background. However, it was deemed that the greatest gains could be made with a higher flux of neutrons. Efforts then began to study the effects of various parameters on the neutron production rates in order to maximize the total neutron flux.

13.2 Optimization of the IEC with regard to Neutron Production Rates

Various parameters of the IEC device were studied in order to determine an optimal configuration with regard to producing maximum D-D neutron fluxes. This then evolved into an in-depth examination of how and why these parameters had such effects.

- D-D neutron production rates were recorded with regard to cathode voltage, cathode current, and background deuterium pressure.
- The high voltage capabilities were increased through improved methods of component cleaning, machining of high voltage surfaces, cooling of the chamber, and utilization of a new design for the insulating Boron Nitride stalk surrounding the high voltage conductor.

- The design of the cathode was studied. Four different cathodes were created for this purpose, with neutron production capabilities varying by roughly 25%.
- A new method of cathode construction was developed utilizing Styrofoam spheres, providing an inexpensive and easily alterable template.
- Molybdenum nuts were utilized in the construction of the cathodes to allow the cathode to be easily placed on the high voltage stalk in a repeatable position and orientation while enduring the high temperatures at that location.
- The effect of varying anode diameter while maintaining constant cathode diameter was studied, involving three different anode/cathode configurations and requiring the construction of a new 30 cm diameter grid. A better configuration was found, which offered a 50% increase in neutron production capabilities.
- A new method for hanging and positioning the anode was developed that allowed for a significant increase in the mechanical strength of the electrode supports (preventing the anode from pulling towards the cathode for the 30 cm anode configuration) and the accuracy of the positioning of the anode with regard to the cathode and the rest of the chamber.
- The FIDO Diagnostic developed by Boris [2] was utilized during the optimization studies and was used to determine how the variation of system parameters affected the fusion reactant energy spectra and dominant reactant species.
    - The study of the variation of the anode diameter revealed particularly valuable information regarding the importance of dissociation of D_3^+ ions into D_1^+, and its effects on the total fusion rates.

These optimization studies coincided with the acquisition of a new 300 kV power supply, which necessitated dramatic improvements to the high voltage capabilities of the laboratory for full utilization. Also, during the optimization studies, the development and utilization of the FIDO diagnostic was able to demonstrate the important role of diagnostics in these experiments and led to the development of the TOF Diagnostic.

13.3 Design and Construction of 300 kV High Voltage Feedthrough

The high voltage power supply of the UW IEC Laboratory was upgraded in the summer of 2009 from a 200 kV, 75 mA supply to a 300 kV, 200 mA supply. The highest cathode voltage previously achieved on a UW IEC device was 185 kV, with maximum operable levels typically limited to 150 to 160 kV. The existing stainless steel high voltage feedthrough was deemed unable to make use of the new high voltage capacities of the new supply. A new concept for the feedthrough was designed, utilizing nearly all non-conductive material outside of the high voltage components. The new design had to meet quite a few requirements including: ability to standoff 300 kV, utilize non-conductive components, act as a vacuum barrier and plasma surface, and fit within the space provided within the experimental facility.

- Quartz was chosen as the vacuum barrier and plasma interface due to its high dielectric strength, mechanical strength, and heat capacity. A custom made quartz container was designed by the author and then constructed by an outside quartz machining firm.
- A method of vacuum sealing the high voltage insulating stalk in the feedthrough without using conductive material near the high voltage components was designed.

- The method of vacuum sealing the feedthrough was tested using a prototype, and was found to hold vacuum of at least a microtorr.
- The feedthrough was designed to be constructed as two separate tiers, which provided a much longer surface path length within the feedthrough while still allowing it to fit within the spatial dimensions of the operating facility.
- A new support structure was constructed for HOMER, allowing the chamber to be dropped by an additional 12.5 cm, which then increased the maximum allowable height of the feedthrough.
- The feedthrough design was modeled using the electromagnetic software package, Maxwell 3D. The results indicated that the new design offered a factor of 3.5 reduction in maximum electric field concentrations as compared to the old design.
- The minimum surface path length within the feedthrough was increased from 10 cm in the old design to 32 cm in the new design, which dramatically decreased the probability of flash-over arcs occurring.
- The new feedthrough design has been constructed and is ready for testing. The full test is awaiting the completion of the rebuilding of the high voltage resistor barrel which operates between the supply and the IEC devices, which is scheduled to be completed in 2011.

The D-D neutron production rates in the IEC have been shown to scale nearly linearly with cathode voltage and current, therefore full utilization of the voltage capabilities of the new power supply could lead to at least a 50 percent increase in our maximum recorded neutron production rates. This is particularly valuable for studying D-^{3}He and ^{3}He-^{3}He fusion, which require higher reactant energies for fusion than do D-D. This new feedthrough design will be an essential component of the high voltage system and will take the IEC devices to power levels never before achieved on gridded IEC devices in the global community.

13.4 Adjustable FIDO Arm

All previous experiments using the FIDO Diagnostic involved the study of D-D fusion products. The electromagnets used in the setup are incapable of producing the magnetic fields required to bend the 14.7 MeV protons created in the D-^{3}He fusion reaction around the 20 degree elbow of the fixed FIDO collimator channel. The solution was to either purchase a new magnet or decrease the angle of the elbow. The cost of a sufficiently strong magnet was deemed prohibitively expensive, so the only option that remained was to decrease the angle of the elbow.

- SIMION computational modeling was performed to determine that existing magnet was powerful enough to bend 14.7 MeV protons around a 15 degree elbow, but not 20 degrees.
- A design for a collimating arm was created to allow adjustment of the elbow angle while under vacuum to avoid perturbing the system between D-D and D-^{3}He operation.
- The adjustable elbow was commissioned to a waveguide manufacturing firm in order to create a first of its kind prototype for a flexible corrugated section with a rectangular cross-section (necessary to combine minimum width between magnet poles and maximum cross-section area) capable of reaching at least a microtorr vacuum and made out of stainless steel with a bend angle between -30 and +30 degrees.

- An x-ray trap was added behind the elbow in order to minimize x-rays created inside the chamber from reflecting down the collimator channel and into the detector. Interior surface of corrugated flexible elbow also acts to minimize propagation of x-rays down the collimator channel by minimizing surface area facing the detector from which the x-rays could scatter.
- The adjustable arm was constructed and tested on HOMER. It was able to reach at least a microtorr vacuum and was successfully used to collect FIDO data over a range of elbow angles and magnetic field strengths.
- The adjustable arm proved to be superior at capturing D-D fusion protons at higher power levels than the fixed arm. The x-ray trap and corrugated elbow provided a factor of 5 increase in proton counting rates. Increasing the elbow angle from 20 to 29 degrees allowed a further factor of 13 increase in counting rates, resulting in a total increase of a factor of 66 in D-D fusion proton collection rates over the fixed arm for the higher power levels.
- The adjustable arm can also be moved to -20 degrees and used with a much lower magnetic field strength to study negative ions.
- The ability to vary the angle of the elbow also allows various forms of background noise from x-rays and other particles to be better isolated and studied in order to determine their cause and how to mitigate them.
- A second adjustable arm identical to the first has been constructed in order to allow for the TOF Diagnostic to be used to study D-^{3}He fusion.

The Adjustable FIDO Arm represents an innovative advancement in the capabilities of the FIDO Diagnostic. D-^{3}He fusion has been an important area of study for the UW IEC

Research Group, and it is prudent to ensure that as many diagnostic tools as possible are available to properly study it. Minimizing background noise from x-rays and other particles reaching the detectors will always be a priority for both the FIDO and TOF diagnostics because they are the primary limiting factor on the rate of data collection. The adjustable arms have already demonstrated superior noise reduction capabilities at higher power levels. They will continue to be used in the future to examine the causes of various forms of background noise in order to better understand how to mitigate those sources.

13.5 Time of Flight Diagnostic and Spatial Profiling

The final work discussed in this thesis is the design, construction, and utilization of the first Time of Flight Diagnostic to be used on an IEC device. The idea for the diagnostic was first proposed in 2007 by Piefer and Boris [3], and was made possible by the successful development of the FIDO Diagnostic by Boris [2]. Since 2009, the author of this work has taken the TOF Diagnostic from concept to full implementation and used the tool to obtain the first spatial profiles of an IEC device from direct measurements of fusion product arrival times and velocities.

- The first spatial profile from the TOF diagnostic was obtained in fall of 2009 using an oscilloscope to measure differences in arrival times of fusion products. However, the timing measurements used to create the profile were collected without particle energy, and the rate of collection was roughly one count every 4 to 5 minutes. Without measuring particle energies, the validity of the timing measurements was unable to be confirmed to correspond to genuine coincidence events, and would have contained a higher level of false counts.

- An alignment system was constructed to ensure TOF arms on opposite sides of the chamber were aligned to less than half a degree, which offered the potential for up to a factor of 4 increase in counting ability.
- A computer based data acquisition setup was implemented utilizing a custom made LabView program for data collection and processing.
    - The particle energies from one arm were constantly collected while searching for coincidence counts, allowing FIDO to be operated simultaneously with the TOF diagnostic.
    - Coincidence counts can now be collected along with both particle energies and the difference in arrival times, allowing the velocity to be directly calculated from the particle energy as opposed to using an average particle energy as had been done previously.
    - LabView program allowed various filters to be applied to the collected data, which compared the energy and magnitude of the Doppler shifts of the fusion products to confirm that the time difference corresponds to a genuine coincident fusion event, thereby greatly reducing the number of false counts.
- Extensive refurbishing of HOMER and the TOF electronics occurred in order to minimize electronics noise. This included redesign of grounding, isolation of electronics, redirecting paths of cables, and creating proper conductive paths to reduce discharges in the system.
- The innovative use of timing delays in the electronics allowed both TOF arms to collect fusion protons (as opposed to just one in the original setup) without requiring the purchase of a duplicate set of TOF electronics and data acquisition hardware.

This effectively doubled the rate of data collection and provided views of the same region of HOMER from opposite sides of the chamber, thereby adding another check on the symmetry of the diagnostic.

- A weighting factor calculation was derived in order to compensate for the variance in the probability of capture of both products of a fusion event based on the position of the event within the viewable region of the diagnostic and the energy and trajectory of the fusion reactants.
- The largest data set was collected at 60 kV, 30 mA, 2 mTorr Deuterium with 20 cm diameter cathode, 50 cm diameter anode. The data was collected at a rate of roughly 1 coincident count every 45 seconds.
    - Spatial profile demonstrated excellent symmetry about the center of the chamber.
    - The highest concentration of fusion events was found in the Core region inside the cathode. The lack of a prominent peak within the cathode indicated that the current single cathode system is not achieving optimal convergence of particles at a single focus within the device.
    - The density of fusion events appear to reach a minimum value near the anode radius, but then unexpectedly increase again as the radius increases beyond the anode. The counts beyond the anode are believed to be a result of high energy neutrals and the recently discovered negative ions fusing with the background gas.

- The effect of non-concentricity of the electrodes was studied and found that as little as a 1 cm misalignment of the cathode from the center of the anode can result in a shift in the position of the peak in counts in the Core.
    - The peak in concentration of fusion events shifts to the side of the cathode with the largest gap between the electrodes. This conforms well with the previously discussed experiments on the effects of varying anode diameter while keeping cathode diameter constant, which found that fusion rates were higher for larger distances between the electrodes because of a greater portion of D_3^+ ions breaking up into D_1^+ ions.
    - These experiments also demonstrated the accuracy and precision of the TOF diagnostic because when the electrodes were rotated by 180 degrees, the spatial profiles were mirrored about the origin at $r = 0$, and the peaks occurred within a centimeter of each other on either side of the origin.
- Microchannels created by potential variations in the cathode grid were studied in order to determine how they may be affecting the spherical symmetry about the IEC device.
    - Initial experiments were performed on a latitude/longitude cathode grid with a wire at the equator. Spatial profiles were collected for a view directly on a wire or on a hole of the grid and found to be nearly the same. The rate of D-D fusion proton collection was roughly the same, indicating microchannels were located above and below the TOF line of sight.
    - A new cathode grid was constructed without a wire at the equator. Spatial profiles taken on a hole and on a wire were nearly the same again, but the rate

of proton collection on the hole between the wires was more than twice as high as on the wire, indicating the microchannels do appear to be localized chords of higher fusion concentrations directed normal to the surface of the cathode sphere and corresponding to the holes in the cathode.

- The filament ion source position was studied in order to determine how the locations of the ion sources could affect local concentrations of fusion reactions.
  - Initial filament configuration consisted of three columns of filaments, which were placed symmetrically about the chamber but not symmetric about the TOF arms.
  - All combinations of the filament columns were studied at the same settings and while the total neutron production rate for the system stayed nearly constant, it was found that the column closest to the axis of the TOF arms produced the highest rate of D-D fusion proton collection within the view of the detector, while the column farthest away produced the lowest proton collection rates. This indicated that the location of the filaments do have localized effects on the distribution of fusion events.
  - A new four column filament design was constructed and implemented, which is symmetric about the chamber and symmetric about the TOF arms.

The Time of Flight Diagnostic represents what may be the most accurate method thus far attempted on an IEC device to determine the spatial distribution of fusion events. During the course of this work, significant progress has been made in taking this instrument from the drawing board to a fully implemented research tool. Improvements have been made in a variety of areas to increase the rate of data collection as well as the reliability of the data collected.

Extensive work has taken place not only in constructing this diagnostic, but also in upgrading much of the experimental setup of HOMER and the surrounding facility to accommodate a diagnostic with such a high level of sensitivity and accuracy. Methods of data collection and analysis have been developed that work to ensure that the profiles produced from the diagnostic are reliable and representative of what is physically occurring in the device. Over 500 hours of operation time have been spent running with the TOF diagnostic, studying a variety of parameters and configurations to gauge the capabilities of this tool and ensure its accuracy in all domains of operation.

This research only represents the beginning of what this technology is capable of accomplishing. Advancements to further increase the data collection rates and decrease the background noise will expand the capabilities of these diagnostic tools, which are vital to optimize the performance of IEC devices. This work has provided the UW IEC laboratory and the global IEC community with a new tool with which to further the understanding and subsequent utilization of IEC devices.

Chapter 13 References

1 Wehmeyer, A. L. (2005). The detection of explosives using an inertial electrostatic confinement D-D fusion device. (Masters thesis, University of Wisconsin – Madison)

2 Boris, D. R., Kulcinski, G. L., Santarius, J. F., Donovan, D. C., Piefer, G. R. (2010). Measuring D(d,p,)T fusion reactant energy spectra with Doppler shifted fusion products. Journal of Applied Physics, 107, 123305

3 Piefer, G. R., Boris, D. R. (2007). Coincidental time of flight diagnostic for spatially resolving fusion reactions. Invention Disclosure Report, Provisional Patent Application

14 Recommendations for Future Work

Significant progress has been made in a variety of areas of study regarding spherically gridded IEC devices during the course of this work. Many of these areas still have more that can be learned by further research. The expense and time required for these recommendations vary, and the paths described are merely suggestions from the author as to areas that may benefit from further study.

14.1 Explosives Detection

An explosives detection setup has been constructed at the UW IEC Laboratory that utilizes an improved detector and shielding configuration as well as moderator thickness than the original proof-of-principle experiments. When the new 300 kV high voltage power supply is able to be fully utilized after the completion of the various high voltage component upgrades in the laboratory over the next year, the IEC will then be capable of reaching higher neutron fluxes than have previously been achieved in an IEC device. These higher fluxes could then be used in combination with the new detector and moderator setup to bring about a significant decrease in the interrogation time and the necessary interrogation sample size for detection. Another potential improvement to the detector setup would be to utilize heavy water as opposed to paraffin wax as the moderator. Heavy water has the benefit of thermalizing neutrons without capturing them, which offers a higher thermal neutron flux reaching the interrogation sample for activation of the nitrogen than other moderating material.

14.2 Cooling during High Voltage Operation

A complete prototype of the 300 kV feedthrough described in this work has been constructed and assembled. The first tests will occur once the various other high voltage components for the laboratory that will allow for the full utilization of the new power supply are completed, ideally sometime in 2011. One of the biggest concerns during high power operation is proper cooling of components. The 300 kV, 200 mA power supply has the capacity to create an enormous amount of heat over a relatively small area, so all heat sensitive components must be properly monitored. The high voltage components in the feedthrough are surrounded either by high voltage oil, boron nitride, or vacuum. The high voltage oil will be the primary means by which heat is removed from the components on the atmosphere side of the feedthrough. A thermocouple will need to be installed in the oil to monitor temperature over long periods of operation at high power. It may then be deemed necessary to install an active cooling setup in the feedthrough by constantly pumping out hot oil and replacing it with cool oil, particularly to avoid excessive heating of the rubber O-ring vacuum seal around the boron nitride. Cooling lines channeling chilled water may also be an option, but it is essential to make sure that the minimum direct path and surface path between high voltage and ground inside the feedthrough is not significantly altered.

The primary cooling mechanisms for HOMER are copper tubing, channeling chilled water wrapped around the outer surface of the chamber, and air cooling from fans. In the past, this has allowed approximately 10 to 15 minutes of operation at power levels in the range of 10.5 kW (175 kV and 60 mA) before the temperature rose high enough to begin to endanger the rubber vacuum seals on the chamber. Significant improvements will need to be made to the cooling of HOMER in order to utilize the full 60 kW capacity of the new power supply for any appreciable period of time. Additional cooling lines may be added to the surface of HOMER, but in order to achieve the necessary level of cooling a more drastic strategy will most likely need to be taken to either achieve better thermal contact between the cooling lines and the body of the chamber or to install a full chamber water cooling jacket. It may also be necessary to upgrade the rubber gaskets on the chamber to higher heat capacity copper seals.

14.3 Background Noise reduction in FIDO and TOF Diagnostics

The primary limiting factor of using the FIDO and TOF diagnostics to study higher cathode current, cathode voltage, or background pressure is the dramatic increase in low-energy noise that occurs as the current, voltage, or pressure is increased. As was detailed in Chapter 10, with as little as a 10 kV increase in cathode potential, the amount of low energy background noise can increase by several orders of magnitude. This causes the dead time on the detectors to increase to the point that they are unable to measure genuine fusion products. The Adjustable FIDO Arm was able to increase the voltage range over which the diagnostic was able to measure D-D fusion protons. However, further advancements will be needed if the diagnostics are used at voltages approaching or surpassing 100 kV. The background noise is believed to consist primarily of x-rays created in the chamber and reflecting down the arm to the detectors. Other sources of noise are likely created by impacts in the arm from deuterium neutrals and ions as well as electrons, which then release x-rays and secondary electrons in the arm. Depending on where these particles impact within the arm, they have the potential of creating electrons or ions through charge exchange reactions in the arm that can then reach the detector. The x-ray trap on the adjustable arm is an ideal location to perform an analysis of how the various forms of noise are propagating their way to the detector because the trap is easy to open and modify. One option is to line the interior of the trap with an x-ray absorbing material, or a material with a lower secondary electron emission coefficient. Another possibility is to place permanent magnets with fields on the order of a few hundred gauss along the top and/or bottom of the trap. This field would not be sufficient to significantly affect fusion products, but would be enough to deflect electrons and low energy ions that were created in the arm and have trajectories that would otherwise reach the detector.

Another potential design for the collimator channels of the diagnostics would be to create an arm with a beam dump for the x-rays and neutral particles streaming out of the chamber. This design can be seen in Figure 14.1 This design was originally considered at the same time as the adjustable arm. The adjustable arm was chosen as the model to build because it offered the greatest versatility for use between D-D, D-^{3}He, and negative ion study. However, this beam dump design may be desirable to study high power D-D fusion by limiting the amount of x-rays and other low energy particles capable of reaching the detectors. The design shown includes ports at angles of 20 degrees for the D-D fusion products, -20 degrees to study negative ions, and 0 degrees to be used in aligning with the arm on the opposite side of the chamber for TOF measurements. There is also an additional port at 90 degrees, which could be used for a turbopump if differential pumping of the arm is deemed necessary.

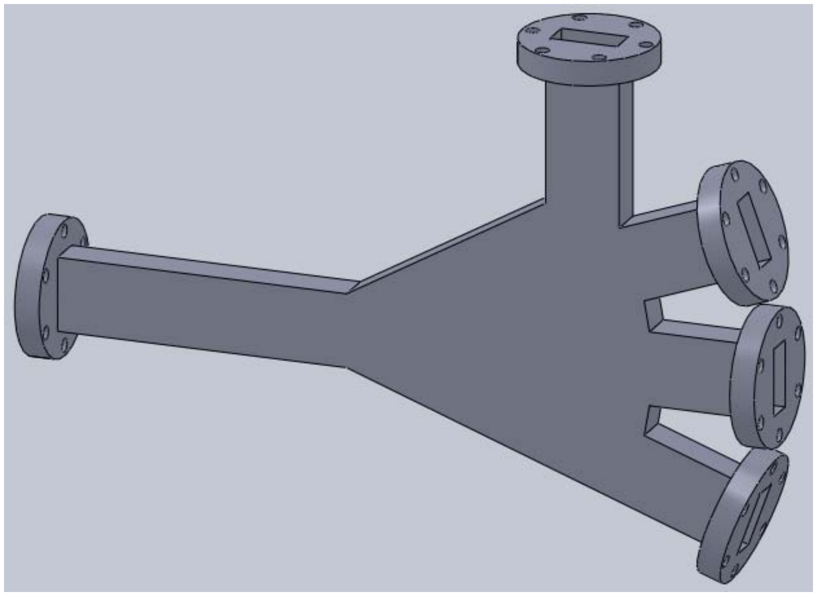

Figure 14.1 Design for collimator channel of FIDO diagnostic with beam dump. Includes ports at angles of -20 degrees for negative ion study, 0 degrees for alignment with opposite arm, 20 degrees for D-D fusion product study, and 90 degrees for an optional turbopump.

14.4 Upgrades to FIDO and TOF Components

The detectors used in the FIDO and TOF diagnostics are silicon charged particle detectors. These detectors operate most efficiently in the range of -30 to +25 degrees Celsius. The detectors are placed at the end of the collimator arms, which are significantly displaced from the plasma in the chamber and any heat source. However, it is still estimated that the detectors may be operating in the range of 20 to 25 degrees Celsius. Operating at the higher end of the temperature range causes the leakage current of the detectors to increase, which then decreases the bias voltage able to be applied across the detector junction. If the detectors are damaged by radiation or other sources such as hydrogen implantation, then the leakage current will already be at a high level and the increased temperature will only exacerbate the problem. Therefore, it would be beneficial to construct a method for cooling the detectors while in vacuum in order to ensure that they do not get above the 10 to 15 degree range. This could be accomplished using thermoelectric cooling through the Peltier Effect. Thermoelectric coolers known as Peltier blocks can be placed in contact with the detectors while in vacuum, and through the application of a voltage difference they are capable of transferring heat away from the detectors to a heat sink. This method avoids the complications involved in trying to utilize chilled water or Freon loops in vacuum, which can also cause vibrational effects from the flowing fluid that can negatively impact the operation of the detectors.

The accuracy of the timing electronics is one of the largest influences on the resolution of the spatial profiles created by the TOF diagnostic. In the current chain of timing electronics, the Ortec 142 Preamplifier is the least accurate component and dictates the error for the entire setup. An improvement on these Ortec models would be an actively cooled preamp, which would reduce the low level noise sufficiently to provide an increase in the resolution. One such model is the A250CF CoolFET ® Charge Sensitive Preamplifier from Amptek, Inc. These preamps are thermoelectrically cooled to -50 degrees Celsius using the Peltier effect described above, and are currently recognized as one of the lowest noise preamplifiers available. Another improvement that could be made to the electronics is to upgrade the coaxial cables from singly shield to doubly shielded. Double shielded coaxial cable indicates two layers of outer conductor shielding, in which one layer is typically a metalized foil and the other is a metallic braid. Double shielded coaxial cable is often somewhat more expensive and less flexible than single shielded, but it can offer a significant decrease in signal leakage into and out of the cable. This is particularly relevant in the types of high sensitivity experiments described here in which even miniscule noise leakage into the coaxial cables can cause severe perturbations to the transmitted signal.

14.5 Combine TOF Spatial Profiles with Fusion Reactant Energy Spectra

The current TOF setup is capable of collecting the energy of both fusion products for each coincident event. This allows the energy of the reactants to be calculated based upon the Doppler Shift of the products. This is capable of producing a three axis spatial profile of the IEC device with radial position, concentration of fusion reactions, and fusion reactant energy spectra. This would be a very important asset to understanding the distribution of reactant energy throughout the device. Unfortunately, the collection rates for the current setup are still prohibitively low to allow sufficient data to be collected in each spatial bin in a reasonable length of collection time to allow for reactant energy distributions to be generated. Typical FIDO data analysis involves the collection of hundreds of thousands of fusion products in order to produce fusion reactant energy spectra. The TOF has a much lower probability of capturing both products of a fusion reaction as opposed to just one, which makes the TOF collection rates nearly three orders of magnitude lower than the FIDO collection rates. The total data collected on TOF is then divided into a large number of spatial bins across the device, further reducing the number of counts available for analysis in each bin.

Gains can still be made in the collection rates of the TOF diagnostic, particularly if the voltage and current are able to be increased. However, as mentioned previously, this must be met with sufficient noise reduction methods to allow data collection at higher current and voltage levels. The TOF diagnostic will most likely never come close to producing the level of counts used in standard FIDO analyses. On the other hand, with another order of magnitude gain in collection rates and sufficiently long collection time, the TOF spatial profiles may yield sufficient counts in the higher concentration regions to provide an acceptable level of statistics for a fusion reactant energy analysis.

14.6 Mapping of Source Region Electrostatic Potential using Emissive Probes

Several issues have arisen during this work that may be influenced by the electrostatic potential structure outside of the anode. The first is the question of why does the rise in counts in the Source region only begin to increase at the anode radius and not reach their full height until 5 to 10 cm beyond the anode. One potential explanation is that the anode is not forming a perfect potential well and that field leakage beyond the anode is causing the potential in the Source region to be non-uniform. Variations in the potential will then affect the energy of the charged particles, and therefore their probability of fusing. Another issue that was brought up was the existence of microchannels emanating from the holes in the cathode at trajectories normal to the surface of the sphere. It is still unknown what the precise shape these microchannels assume will be as they extend radially outward. If these high concentrations of fusion reactants in the microchannels diverge as they move radially outward, then that would affect the distribution of fusion events around the device and perturb the spherical symmetry. It would be beneficial to measure the fluxes of ions and neutrals at various locations throughout the Source region. It may also be possible to determine the location of the microchannels in the Source region by measuring subtle variations in the space charge concentrations from these higher concentrations of electrons and ions.

The vacuum potential profile in the Source region can be measured using an emissive probe. The probe would need to have the capability to move radially between the anode and the chamber wall. Ideally, the probe would be capable of moving in the polar and azimuthal directions as well in order to map out the potential profile surrounding an anode hole to determine the extent of the potential leakage and the boundary of the potential well. This would most likely pose somewhat of a challenge because HOMER has a limited number of vacuum ports available, and they are not necessarily in the ideal positions to place such a diagnostic. Nevertheless, if the Source region is in fact where a significant portion of the fusion reactions are occurring in the IEC, then a more thorough understanding of the potential structure of this region would be quite valuable.

14.7 TOF Weighting Factor Calculation

The spatial profiles created from the data produced by the TOF Diagnostic are only as accurate as the method used to analyze the data. The weighting factor calculation is a very important aspect of that analysis and is responsible for compensating for any artificial preferences the diagnostic has for seeing reactions involving certain energies, trajectories, and locations within the region of view of the detectors. The method for calculating the weighting factor detailed in Chapter 12 is primarily based on determining the fraction of all possible fusion product trajectories that can produce products capable of reaching both detectors. The zero order calculation involving no center-of-mass contribution from the reactants demonstrated almost no variation in the cumulative probability of event capture along the axis between the detectors. Initial investigation into the effect of adding in non-zero reactant energies has demonstrated that the energy and trajectories of the fusion reactants can influence the probability of event capture within the core region, particularly very near to the center of the chamber where particle trajectories are able to have a significant velocity component perpendicular to the axis between the detectors. As the precision of the diagnostic and the level of counting statistics increase, the influence of the reactant energies on the final product trajectories will need to be revisited to determine whether they are affecting the accuracy of the interpretation of the post-processing of the measurements. Further computational modeling of the system would most likely need to take place at that point to determine a cumulative probability factor for every location within the region of view between the detectors that factors in the mass, velocity, and direction of each fusion reactant. A locus of possibilities for the position along the axis between detectors and the velocities of the fusion reactants can be calculated within measurement tolerances to compensate for the realities of the experiment, in which the reactants do not always assume perfectly radial trajectories. Most of these other factors are interpretation considerations. However, in order to derive a weighting factor based on the properties of the fusion reactants, certain assumptions will invariably have to be made about the dominant ion species, average reactant energy, likely particle trajectories, and other factors based upon the position within the device. These assumptions must be made carefully so as to avoid artificially perturbing the data based on misconceptions about the structure.

14.8 FIDO and TOF Analysis of D-^{3}He Fusion

The new adjustable arm discussed in this work has the capability of decreasing the bend angle of the collimator channel to 15 degrees. The ion tracking software SIMION has been used to determine that the current electromagnets are capable of producing a sufficiently strong magnetic field (~12 kG) to bend the 14.7 MeV protons of the D-^{3}He fusion reaction to this angle to reach the detector at the end of the arm. This will allow FIDO to be used for the first time to study D-^{3}He protons. A second adjustable arm has already been constructed, which allows for

TOF to also be used to study D-^{3}He. The D-D fusion products travel with the same charge and momentum and therefore experience the same amount of deflection from the magnetic field. However, the 3.6 MeV alpha particle (charge +2) and the 14.7 MeV proton (charge +1) of the D-^{3}He reaction have the same momentum but different charge, which means they each require a different magnetic field to be bent properly around the elbow of the collimator channel. The +2 charge on the alpha particle makes it easier to bend, which allows the angle of the collimator elbow to be increased and has been shown to decrease the amount of background noise capable of reaching the detector.

Because the two arms must be operated at different magnetic fields and/or placed at different bend angles, one arm of the diagnostic must always capture protons and the other must always capture alpha particles in a TOF setup studying D-^{3}He. This means that it will not be able to utilize the improvement on the D-D collection setup allowing both arms to collect equally, so the collection rates will be cut in half for D-^{3}He. The fusion cross-section for D-^{3}He surpasses that for D-D at ~130 keV deuterium projectile energy. This means that a higher cathode potential would be required for efficient data collection but that D-^{3}He counting rates could theoretically exceed those of D-D. This once again would require further advancement in reducing background noise levels of x-rays and other low energy particles in order to allow data to be collected at higher cathode potential without prohibitively high amounts of dead time.

14.9 Time-of-Flight Using “Tagged Neutrons”

The Time-of-Flight Diagnostic could potentially be used with the explosives detection setup in order to determine not only the existence of explosive material, but also the exact location. Roughly half of D-D fusion reactions create a 2.45 MeV neutron and a 0.82 MeV helium-3 particle. This method could also potentially be used with the D-T fusion reaction, which creates a 14.1 MeV neutron and a 3.5 MeV alpha particle, but that would require working with tritium, which has relatively high radioactivity, and would also require greater shielding to protect against the high energy neutrons. As is described in this work, the D-D neutron can be used to activate the nitrogen atoms in explosive material, producing a characteristic 10.83 MeV gamma ray. There is a method known as "tagging" the neutrons, which involves capturing the He-3 particle moving in the opposite direction and using its arrival time and velocity to determine when the fusion reaction occurred, and therefore when the neutron began its journey towards the interrogation sample.

If the gamma ray produced by the neutron activation can also be captured, the difference in arrival times of the He-3 fusion product and the gamma ray, along with their respective velocities, can be used to determine when and where the neutron interacted with the nitrogen atom that created the gamma ray. With a sufficiently large number of coincident counts, this method could be used to trace out the region that is occupied by the nitrogen-based explosives. This technique has been demonstrated successfully by other research groups in the past, one of which can be found in Ref [1]. This method would require significantly higher counting statistics than what is used for either the TOF Diagnostic or explosives detection experiments alone, and therefore is not feasible with the current setup. However, as the research progresses and the counting ability of the TOF Diagnostic, the optimization of the explosives detection setup, and the increase in the neutron flux of the IEC source continues, this method could become a valuable tool for locating clandestine materials.

Chapter 14 References

1 Lunardon, M., Nebbia, G., Pesente, S., Romagnoli, G.M., Viesti, G. (2003). A large area scanning system using 14 MeV neutron tagged beams for non-destructive assays. Nuclear Instrumentation and Methods in Physics Research B, 213 (2004), 544-547

Appendix A - TOF Weighting Factor Calculation

Written in MATLAB Version 7.

```
% This MATLAB Script is intended to calculate the probability of coincident
% event capture for the UW IEC Research Group Device HOMER using the TOF
% Diagnostic.  The code begins by caculating the total probability of
% capture at every position on a place between the detectors, and then sums
% all the values along the axis between the detectors to create a
% cumulative weighting factor for the entire device.  This script has the
% capability to input energy, trajectory, and mass for two different
% reactants.  Using loops, it then scans through all possible directions of
% emission for the fusion products and calculates their final trajectories
% to determine if the final products can be captured by the detectors.
%
% Mass of proton (kg)
m_p=1.672621637e-27;
% Mass of deuteron (kg)
m_d=3.3444969725816e-27;
% Mass of triton (kg)
m_t=5.0082709417778e-27;
% Q Value from D-D Fusion (eV)
E_fus_DD=4.03e6;
% Conversion between eV and J
conv_eV_J=1.60217646e-19;
% Length of Alpha Arm (m)
L_alpha=0.5695;
% Length of Beta Arm (m)
L_beta=0.5052;
% Inner Radius of HOMER (m)
r_HOMER=0.47625;
% Total Length between Detectors
L_total=L_alpha+L_beta+2*r_HOMER;
% Area of Detector Face (m^2)
A_det=450e-6;
% Radius of Detector Face (m)
r_det=(A_det/pi)^0.5;
% Inner Radius of CF Nipple (m), which is equal to inner radius of
% collimator channel
r_CF=0.01740027;
% Alpha Arm Viewing Cone Angle (radians)
ang_alpha_cone_rad=atan((r_det+r_CF)/L_alpha);
% Alpha Arm Viewing Cone Angle (degrees)
ang_alpha_cone_deg=ang_alpha_cone_rad*180/pi;
% Beta Arm Viewing Cone Angle (radians)
ang_beta_cone_rad=atan((r_det+r_CF)/L_beta);
% Beta Arm Viewing Cone Angle (degrees)
ang_beta_cone_deg=ang_beta_cone_rad*180/pi;
% Distance (m) from center of chamber where cones converge (negative number
is
% on alpha side, positive is on beta side)
d_cone_conv=(L_total*tan(ang_beta_cone_rad)/(tan(ang_alpha_cone_rad)+tan(ang_
beta_cone_rad)))-(L_alpha+r_HOMER);
% Radius (m) of Disc at convergence of Alpha and Beta Cones of View
```

```
r_alpha_cone_conv=(d_cone_conv+L_alpha+r_HOMER)*tan(ang_alpha_cone_rad)-
r_det;
r_beta_cone_conv=(-d_cone_conv+L_beta+r_HOMER)*tan(ang_beta_cone_rad)-r_det;
r_cone_conv=(r_alpha_cone_conv+r_beta_cone_conv)/2;
% Number of steps into which 360 degree isotropic emission plane of fusion
% products is divided in theta plane. Higher number of steps results in
better precision.
n=3600;
% theta angular step size for isotropic emission.
n_ang=360/n;
n_rad=2*pi/n;
% Number of steps in zeta direction into z-plane dicated by theta angular
% step size.  Distance into z plane is determined by (Distance along
% x-axis)*tan(zeta)
zeta_max_deg=5;
zeta_step_deg=n_ang;
zeta_steps=round(zeta_max_deg/zeta_step_deg);
MC_emis=zeros(n,27);
% Energy of Reactant Particle 1 (eV)
E_1=0;
% Mass of Reactant Particle 1 (number of deuterium atoms)
m_1=m_d;
% Angle of Particle 1 (degrees)
ang_theta_1_manual=0;
% Energy of Reactant Particle 2 (eV)
E_2=0;
% Mass of Reactant Particle 1 (number of deuterium atoms)
m_2=m_d;
% Angle of Particle 1 (degrees)
ang_theta_2=0;
% Velocity of Particle 1 (m/s)
v_1=((2*E_1*conv_eV_J)/(m_1))^0.5;
% Velocity of Particle 2 (m/s)
v_2=((2*E_2*conv_eV_J)/(m_2))^0.5;
% Calculate for a range of y_positions
y_position_step_size=0.0001;
y_position_min=-0.015;
y_position_max=0.015;
axis_1_steps=round(abs(y_position_max-
y_position_min)/y_position_step_size)+1;
% Calculate for a range of x_positions
x_position_step_size=0.005;
x_position_min=-0.45;
x_position_max=0.45;
axis_2_steps=round((abs(x_position_max-
x_position_min))/x_position_step_size)+1;
% Setup necessary matrices for the loops
plot_1=zeros(axis_1_steps+1,axis_2_steps+1);
plot_1_vol=zeros(axis_1_steps+1,axis_2_steps+1);
plot_1_vol_values=zeros(axis_1_steps,axis_2_steps);
plot_1_vol_test=zeros(axis_1_steps+1,axis_2_steps+1);
plot_1_vol_test_values=zeros(axis_1_steps,axis_2_steps);
plot_1_angles=zeros(axis_1_steps+1,axis_2_steps+1);
plot_1_angles_values=zeros(axis_1_steps,axis_2_steps);
for k=1:axis_2_steps
```

```
    x_position=x_position_min+x_position_step_size*(k-1)
    plot_1(1,k+1)=x_position;
    for j=1:axis_1_steps
        y_position=y_position_min+(j-1)*y_position_step_size;
        plot_1(j+1,1)=y_position;
        % plot_1_angles is a matrix that contains the angle of a purely
        % radial trajectory at every (x,y) position.
        plot_1_angles(1,k+1)=x_position;
        plot_1_angles(j+1,1)=y_position;
        plot_1_angles(j+1,k+1)=atan(abs(y_position/x_position))*180/pi;
        plot_1_angles_values(j,k)=atan(abs(y_position/x_position))*180/pi;
        % Radius of Alpha Cone at x_position (m)
        r_alpha_cone_x=(L_alpha+r_HOMER+x_position)*tan(ang_alpha_cone_rad)-
r_det;
        % Radius of Beta Cone at x_position (m)
        r_beta_cone_x=(L_beta+r_HOMER-x_position)*tan(ang_beta_cone_rad)-
r_det;
        % Test whether (x,y) position is within the cone of view of both
        % detectors.
        if (abs(x_position)<=r_HOMER)
            if (y_position<=r_alpha_cone_x) && (y_position<=r_beta_cone_x)
                test_inside_cones=1;
            else test_inside_cones=0;
            end;
        else
            if (y_position<r_CF)
                test_inside_cones=1;
            else test_inside_cones=0;
            end;
        end;
        % Angle of Particle 1 (degrees)
        ang_theta_1_manual=0;
        % Angle at position assuming radial trajectory.
        if (x_position>0) && (y_position>0)
            ang_radial=atan(abs(y_position)/abs(x_position))*180/pi;
        else
            if (x_position<0) && (y_position>0)
              ang_radial=(pi-(atan(abs(y_position)/abs(x_position))))*180/pi;
            else
                if (x_position<0) && (y_position<0)
                  ang_radial=(pi+(atan(abs(y_position)/abs(x_position))))*180
                  /pi;
                else
                    if (x_position>0) && (y_position<0)
                      ang_radial=(2*pi-
                      (atan(abs(y_position)/abs(x_position))))*180/pi;
                    else
                        if (x_position>0) && (y_position==0)
                            ang_radial=0;
                        else
                            if (x_position==0) && (y_position>0)
                                ang_radial=90;
                            else
                                if (x_position<0) && (y_position==0)
                                    ang_radial=180;
```

```
                        else
                            if (x_position==0) && (y_position<0)
                                ang_radial=270;
                            else
                                if (x_position==0) && (y_position==0)
                                    ang_radial=ang_theta_1_manual;
                                end;
                            end;
                        end;
                    end;
                end;
            end;
        end;
    end;
end;
% If particle is moving towards the center, add 180 to ang_radial,
% if particle is moving away from center, then add nothing.
ang_theta_1=ang_radial;
% Center of Mass Velocity of Combined Reactants in x-direction
% (m/s) in Lab-Frame
v_cm_x=(m_1*v_1*cos(ang_theta_1*pi/180)+m_2*v_2*cos(ang_theta_2*pi/18
0))/(m_1+m_2);
% Center of Mass Velocity of Combined Reactants in y-direction
% (m/s) in Lab-Frame
v_cm_y=(m_1*v_1*sin(ang_theta_1*pi/180)+m_2*v_2*sin(ang_theta_2*pi/18
0))/(m_1+m_2);
% Velocity of Reactant 1 in the x-direction in the Lab-Frame
v_1_x=v_1*cos(ang_theta_1);
% Velocity of Reactant 1 in the y-direction in the Lab-Frame
v_1_y=v_1*sin(ang_theta_1);
% Velocity of Reactant 2 in the x-direction in the Lab-Frame
v_2_x=v_2*cos(ang_theta_2);
% Velocity of Reactant 2 in the y-direction in the Lab-Frame
v_2_y=v_2*sin(ang_theta_2);
% Velocity of Reactant 1 in the x-direction in the CM Frame
u_1_x=v_1_x-v_cm_x;
% Velocity of Reactant 1 in the y-direction in the CM Frame
u_1_y=v_1_y-v_cm_y;
% Velocity of Reactant 2 in the x-direction in the CM Frame
u_2_x=v_2_x-v_cm_x;
% Velocity of Reactant 2 in the y-direction in the CM Frame
u_2_y=v_2_y-v_cm_y;
% Total Energy of Fusion Products (J) in CM Frame
E_fus_total=0.5*m_1*(u_1_x^2+u_1_y^2)+0.5*m_2*(u_2_x^2+u_2_y^2)+E_fus_
DD*conv_eV_J;
% Total energy of D-D fusion proton (J) in CM Frame
E_p_f=(m_t/(m_p+m_t))*E_fus_total;
% Total velocity of D-D fusion proton (m/s) in CM Frame
u_p_f=(2*E_p_f/m_p)^0.5;
% Total energy of D-D fusion triton (J) in CM Frame
E_t_f=m_p/(m_p+m_t)*E_fus_total;
% Total velocity of D-D fusion proton (m/s) in CM Frame
u_t_f=(2*E_t_f/m_t)^0.5;
MC_emis_vol=zeros(zeta_steps+1,(n+1));
% Begin loop to scan over all possible trajectories of the fusion
```

```
% products in the theta direction in the CM frame.
for i=1:n
    % Angle of D-D fusion proton emission in lab frame (deg)
    ang_theta_p_deg=(i-1)*360/n;
    ang_theta_p_rad=ang_theta_p_deg*pi/180;
    MC_emis(i,1)=ang_theta_p_deg;
    MC_emis_vol(1,i+1)=ang_theta_p_deg;
    % Angle of D-D fusion triton emission in lab frame (deg)
    ang_theta_t_deg=ang_theta_p_deg+180;
    if (ang_theta_t_deg>=360)
        ang_theta_t_deg=ang_theta_t_deg-360;
    end
    ang_theta_t_rad=ang_theta_t_deg*pi/180;
    MC_emis(i,2)=ang_theta_t_deg;
    % Velocity of proton in x-direction from fusion energy alone
    % (m/s) in CM Frame
    u_p_x=u_p_f*cos(ang_theta_p_rad);
    MC_emis(i,3)=u_p_x;
    % Velocity of proton in y-direction from fusion energy alone
    % (m/s) in CM Frame
    u_p_y=u_p_f*sin(ang_theta_p_rad);
    MC_emis(i,4)=u_p_y;
    % Total proton velocity in x-direction (m/s) in Lab Frame
    v_p_t_x=u_p_x+v_cm_x;
    MC_emis(i,5)=v_p_t_x;
    % Total proton velocity in y-direction (m/s) in Lab Frame
    v_p_t_y=u_p_y+v_cm_y;
    MC_emis(i,6)=v_p_t_y;
    % Total Magnitude of Proton Velocity (m/s) in Lab Frame
    v_p_t=(v_p_t_x^2+v_p_t_y^2)^0.5;
    MC_emis(i,7)=v_p_t;
    % Total Energy of Proton (eV) in Lab Frame
    E_p_t=0.5*m_p*v_p_t^2/conv_eV_J;
    MC_emis(i,8)=E_p_t;
    % Angle of proton in Lab Frame
    ang_p_t_rad=atan(v_p_t_y/v_p_t_x);
    ang_p_t_deg=ang_p_t_rad*180/pi;
    MC_emis(i,9)=ang_p_t_deg;
    % Velocity of triton in x-direction from fusion energy alone
    % (m/s) in CM Frame
    u_t_x=u_t_f*cos(ang_theta_t_rad);
    MC_emis(i,10)=u_t_x;
    % Velocity of triton in y-direction from fusion energy alone
    % (m/s) in CM Frame
    u_t_y=u_t_f*sin(ang_theta_t_rad);
    MC_emis(i,11)=u_t_y;
    % Total triton velocity in x-direction (m/s) in Lab Frame
    v_t_t_x=u_t_x+v_cm_x;
    MC_emis(i,12)=v_t_t_x;
    % Total triton velocity in y-direction (m/s) in Lab Frame
    v_t_t_y=u_t_y+v_cm_y;
    MC_emis(i,13)=v_t_t_y;
    % Total Magnitude of Triton Velocity (m/s) in Lab Frame
    v_t_t=(v_t_t_x^2+v_t_t_y^2)^0.5;
    MC_emis(i,14)=v_t_t;
```

```
% Total Energy of Triton (eV) in Lab Frame
E_t_t=0.5*m_t*v_t_t^2/conv_eV_J;
MC_emis(i,15)=E_t_t;
% Angle of triton in Lab Frame
ang_t_t_rad=atan(v_t_t_y/v_t_t_x);
ang_t_t_deg=ang_t_t_rad*180/pi;
MC_emis(i,16)=ang_t_t_deg;
% Distance (m) the proton traveled in the y_direction as it went
% from the fusion event to the Collimator Channel Entrance.
if (v_p_t_x<0)
    x_p_CF=r_HOMER+x_position;
else
    x_p_CF=r_HOMER-x_position;
end;
delta_p_CF=x_p_CF/abs(v_p_t_x)*v_p_t_y;
if x_p_CF<0
    x_p_CF=0;
    delta_p_CF=0;
end
MC_emis(i,17)=delta_p_CF;
% Position (m) of the proton at the CF in the y-direction.
y_position_p_CF=y_position+delta_p_CF;
MC_emis(i,18)=y_position_p_CF;
% Distance (m) the proton traveled in the y_direction as it went
% from the fusion event to the detector.
if (v_p_t_x<0)
    x_p_det=r_HOMER+L_alpha+x_position;
else
    x_p_det=r_HOMER+L_beta-x_position;
end
delta_p_det=x_p_det/abs(v_p_t_x)*v_p_t_y;
MC_emis(i,19)=delta_p_det;
% Position (m) of the proton at the detector in the y-direction.
y_position_p_det=y_position+delta_p_det;
MC_emis(i,20)=y_position_p_det;
% Test whether proton made it past CF and into detector.
if (abs(y_position_p_CF)<r_CF) && (abs(y_position_p_det)<=r_det)
    test_p=1;
else test_p=0;
end
MC_emis(i,21)=test_p;
% Distance (m) the triton traveled in the y_direction as it went
% from the fusion event to the CF.
if (v_t_t_x<0)
    x_t_CF=r_HOMER+x_position;
else
    x_t_CF=r_HOMER-x_position;
end;
delta_t_CF=x_t_CF/abs(v_t_t_x)*v_t_t_y;
if x_t_CF<0
    x_t_CF=0;
    delta_t_CF=0;
end
MC_emis(i,22)=delta_t_CF;
% Position (m) of the triton at the CF in the y-direction.
```

```
y_position_t_CF=y_position+delta_t_CF;
MC_emis(i,23)=y_position_t_CF;
% Distance (m) the triton traveled in the y_direction as it went
% from the fusion event to the detector.
if (v_t_t_x<0)
    x_t_det=r_HOMER+L_alpha+x_position;
else
    x_t_det=r_HOMER+L_beta-x_position;
end
delta_t_det=x_t_det/abs(v_t_t_x)*v_t_t_y;
MC_emis(i,24)=delta_t_det;
% Position (m) of the triton at the detector in the y-direction.
y_position_t_det=y_position+delta_t_det;
MC_emis(i,25)=y_position_t_det;
% Test whether triton made it past CF and into detector.
if (abs(y_position_t_CF)<r_CF) && (abs(y_position_t_det)<=r_det)
    test_t=1;
else test_t=0;
end
MC_emis(i,26)=test_t;
% Test whether both proton and triton reached detectors.
test_capture=test_inside_cones*test_p*test_t;
MC_emis(i,27)=test_capture;
% Distance from center line to collimator channel boundary at
% y_position_p_CF and y_position_t_CF
z_CF_y_p_CF=(r_CF^2-y_position_p_CF^2)^0.5;
z_CF_y_t_CF=(r_CF^2-y_position_t_CF^2)^0.5;
% Distance from center line to detector boundary in z-direction
% at y_position_p_detector and y_position_t_det
z_det_y_p_det=(r_det^2-y_position_p_det^2)^0.5;
z_det_y_t_det=(r_det^2-y_position_t_det^2)^0.5;
% Loop now calculates trajectories in the z-plane by adding a
% zeta angular component to the trajectories.  The loop only
% begins if a coincidence count was successfully detected in
% the theta direction, and then will begin moving off the (x-y)
% plane by angular increments until zeta_max is reached.  All
% succesful counts in the z-plane are then doubled because the
% counts are symmetric about the x-y plane and will be equally
% likely to occur on the opposite side of the x-y plane.
if test_capture==1
    for m=1:zeta_steps
        % Define angle in zeta direction (extending into z
        % plane) which goes from 0 to 90 degrees
        ang_zeta_p_deg=(m-1)*zeta_step_deg;
        ang_zeta_p_rad=ang_zeta_p_deg*pi/180;
        ang_zeta_t_deg=ang_zeta_p_deg+180;
        ang_zeta_t_rad=ang_zeta_t_deg*pi/180;
        MC_emis_vol(m+1,1)=ang_zeta_p_deg;
        % Determine depth into z-plane at CF and detector
        z_p_CF=abs(x_p_CF*tan(ang_zeta_p_rad));
        z_t_CF=abs(x_t_CF*tan(ang_zeta_t_rad));
        z_p_det=abs(x_p_det*tan(ang_zeta_p_rad));
        z_t_det=abs(x_t_det*tan(ang_zeta_t_rad));
        % Determine if position in the z-plane is within the
```

```
                    % boundaries of the detector and collimator channel for
                    % both proton and triton.
                    if z_p_CF<=z_CF_y_p_CF
                        z_p_CF_test=1;
                    else
                        z_p_CF_test=0;
                    end
                    if z_t_CF<=z_CF_y_t_CF
                        z_t_CF_test=1;
                    else
                        z_t_CF_test=0;
                    end
                    if z_p_det<=z_det_y_p_det
                        z_p_det_test=1;
                    else
                        z_p_det_test=0;
                    end
                    if z_t_det<=z_det_y_t_det
                        z_t_det_test=1;
                    else
                        z_t_det_test=0;
                    end
                   MC_emis_vol(m+1,i+1)=z_p_CF_test*z_t_CF_test*z_p_det_test*
                   z_t_det_test;
                end
            end
        end;
        weight_coinc=sum(MC_emis,1);
        weight_coinc=weight_coinc(1,27);
        plot_1(j+1,k+1)=weight_coinc;
        cum_vol_test=sum(MC_emis_vol(2,2:n+1));
        % Sum all the successful captures of coincident events for the
       % single (x,y) position calculated.
       cum_vol=sum(MC_emis_vol(2,2:(n+1)))+2*sum(sum(MC_emis_vol(3:zeta_steps
       ,2:(n+1))));
        plot_1_vol_test_values(j,k)=cum_vol_test;
        plot_1_vol_values(j,k)=cum_vol;
    end
end
font_size=20;
font_size_title=15;
if (ang_theta_1==ang_radial)
    direction_1='Away from Core';
else
    if (ang_theta_1==ang_radial+180)
        direction_1='Towards Core';
    else direction_1=ang_theta_1;
    end
end
dlmwrite('MC_emis_01.txt', MC_emis, 'delimiter', '\t', 'precision', 6);
dlmwrite(['TOF Weighting Factors - M1=',num2str(m_1),' -
E1=',num2str(E_1),'eV - ang_theta_1=',num2str(direction_1),' -
M2=',num2str(m_2),' - Resolution=',num2str(n),'.txt'], plot_1, 'delimiter',
'\t', 'precision', 6);
plot_1_vol(1:axis_1_steps+1,1)=plot_1(1:axis_1_steps+1,1);
```

```
plot_1_vol(1,1:axis_2_steps+1)=plot_1(1,1:axis_2_steps+1);
plot_1_vol(2:axis_1_steps+1,2:axis_2_steps+1)=plot_1_vol_values(1:axis_1_step
s,1:axis_2_steps);
plot_1_values=plot_1(2:axis_1_steps+1,2:axis_2_steps+1);
x_axis_values=zeros(axis_2_steps,1);
for i=1:axis_2_steps
    x_axis_values(i,1)=plot_1(1,i+1);
end
y_axis_values=plot_1(2:axis_1_steps+1,1);
plot_1_sum=sum(plot_1_values);
plot_1_diam=zeros(axis_1_steps+1,axis_2_steps+1);
plot_1_diam_mult=zeros(axis_1_steps+1,axis_2_steps+1);
% Multiply every (x,y) position by 2*pi*y_position, which is equivalent to
spinning the (x,y) plane about the x-axis in order to create the
% total volume between the detectors, which is theoretically symmetric
% about the x-axis.
for i=1:(axis_2_steps+1)
    for j=1:(axis_1_steps+1)
        plot_1_diam_mult(j,i)=abs(plot_1(j,1));
        plot_1_diam_mult(1,i)=plot_1(1,i);
        plot_1_diam_mult(j,1)=plot_1(j,1);
        plot_1_diam(j,i)=plot_1(j,i)*2*pi*plot_1_diam_mult(j,i);
        plot_1_diam(1,i)=plot_1(1,i);
        plot_1_diam(j,1)=plot_1(j,1);
    end
end
plot_1_diam_values=plot_1_diam(2:axis_1_steps+1,2:axis_2_steps+1);
plot_1_diam_sum=sum(plot_1_diam_values);
dlmwrite('plot_1_vol.txt', plot_1_vol, 'delimiter', '\t', 'precision', 6);
dlmwrite('plot_1_vol_test.txt', plot_1_vol_test, 'delimiter', '\t',
'precision', 6);
figure
axes('FontSize',font_size)
surf(x_axis_values,y_axis_values,plot_1_vol_values)
xlabel('x-axis (m)','FontSize',font_size)
ylabel('y-axis (m)','FontSize',font_size)
colorbar('fontsize',font_size)
title(['TOF Weighting Factors Volume - M1=',num2str(m_1),' -
E1=',num2str(E_1),'eV - ang_theta_1=',num2str(direction_1),' -
M2=',num2str(m_2),' - Resolution=',num2str(n)],'FontSize',font_size_title)
saveas(gcf,['TOF Weighting Factors Volume - M1=',num2str(m_1),' -
E1=',num2str(E_1),'eV - ang_theta_1=',num2str(direction_1),' -
M2=',num2str(m_2),' - Resolution=',num2str(n),'.fig']);
figure
axes('FontSize',font_size)
plot_1_vol_sum=sum(plot_1_vol_values);
plot(x_axis_values,plot_1_vol_sum)
xlabel('x-axis (m)','FontSize',font_size)
ylabel('Probability Factor (Arb.Units)','FontSize',font_size)
title(['TOF Weighting Factors Volume Sum - M1=',num2str(m_1),' -
E1=',num2str(E_1),'eV - ang_theta_1=',num2str(direction_1),' -
M2=',num2str(m_2),' - Resolution=',num2str(n)],'FontSize',font_size_title)
saveas(gcf,['TOF Weighting Factors Volume Sum - M1=',num2str(m_1),' -
E1=',num2str(E_1),'eV - ang_theta_1=',num2str(direction_1),' -
M2=',num2str(m_2),' - Resolution=',num2str(n),'.fig']);
```

```
plot_1_vol_diam=zeros(axis_1_steps+1,axis_2_steps+1);
plot_1_vol_diam_values=zeros(axis_1_steps,axis_2_steps);
plot_1_vol_diam(1:axis_1_steps+1,1)=plot_1_vol(1:axis_1_steps+1,1);
plot_1_vol_diam(1,1:axis_2_steps+1)=plot_1_vol(1,1:axis_2_steps+1);
for i=2:(axis_2_steps+1)
    for j=2:(axis_1_steps+1)
        plot_1_vol_diam(j,i)=plot_1_vol(j,i)*2*pi*plot_1_diam_mult(j,i);
    end
end
plot_1_vol_diam_values(1:axis_1_steps,1:axis_2_steps)=plot_1_vol_diam(2:axis_
1_steps+1,2:axis_2_steps+1);
figure
axes('FontSize',font_size)
surf(x_axis_values,y_axis_values,plot_1_vol_diam_values)
xlabel('x-axis (m)','FontSize',font_size)
ylabel('y-axis (m)','FontSize',font_size)
colorbar('fontsize',font_size)
title(['TOF Weighting Factors Vol Diam - M1=',num2str(m_1),' -
E1=',num2str(E_1),'eV - ang_theta_1=',num2str(direction_1),' -
M2=',num2str(m_2),' - Resolution=',num2str(n)],'FontSize',font_size_title)
saveas(gcf,['TOF Weighting Factors Vol Diam - M1=',num2str(m_1),' -
E1=',num2str(E_1),'eV - ang_theta_1=',num2str(direction_1),' -
M2=',num2str(m_2),' - Resolution=',num2str(n),'.fig']);
figure
axes('FontSize',font_size)
plot_1_vol_diam_sum=sum(plot_1_vol_diam_values);
plot(x_axis_values,plot_1_vol_diam_sum)
xlabel('x-axis (m)','FontSize',font_size)
ylabel('Probability Factor (Arb.Units)','FontSize',font_size)
title(['TOF Weighting Factors Vol Diam Sum - M1=',num2str(m_1),' -
E1=',num2str(E_1),'eV - ang_theta_1=',num2str(direction_1),' -
M2=',num2str(m_2),' - Resolution=',num2str(n)],'FontSize',font_size_title)
saveas(gcf,['TOF Weighting Factors Vol Diam Sum - M1=',num2str(m_1),' -
E1=',num2str(E_1),'eV - ang_theta_1=',num2str(direction_1),' -
M2=',num2str(m_2),' - Resolution=',num2str(n),'.fig']);
dlmwrite('plot_1_vol_diam.txt', plot_1_vol_diam, 'delimiter', '\t',
'precision', 6);
```